

Department of Exploration Geophysics

**Electrical Formation Factor of Beach Sands and Clay-sand
Mixtures from Experimental and Digital Rock Physics**

Mohammed Ali Garba

**This thesis is presented for the Degree of
Doctor of Philosophy
of
Curtin University**

July 2017

Declaration

“To the best of my knowledge and belief this thesis contains no material previously published by any other person except where due acknowledgment has been made.

This thesis contains no material which has been accepted for the award of any other degree or diploma in any university.”

Signature:

Date: 29/06/2017

Abstract

Electrical properties of rocks are important parameters for well-log and reservoir interpretation. Laboratory measurements of such properties are time-consuming, difficult, if not impossible in some cases. Being able to compute them from 3D images of small samples will allow generating massive data in a short time, opening new avenues in applied and fundamental science. To become a reliable method, the accuracy of this technology needs though to be tested. In this study, I developed a comprehensive and robust workflow, starting with clean sand from several beaches of the Perth Basin (composed of quartz and carbonates), then adding clay (kaolinite) to the sand (in case of the Cottesloe clay-sand sample). Electrical conductivities were first carefully measured in the laboratory at 1 kHz (conduction quasi-ohmic) at ambient conditions, using a two, copper-electrode system. A range of porosities spanning from a minimum of 0.26 to 0.33 to a maximum of 0.39 to 0.44, depending on the samples, was achieved by compacting the samples in a way that reproduces natural packing of sand. Characteristic electrical formation factor versus porosity relationships were then obtained for each sand type (the laboratory measurements serve as a benchmark for the digital computations). 3D micro-computed tomography images of each sand sample were acquired at different resolutions. Image processing was done with Avizo Fire 9 using global thresholding method and up to 174 sub-samples of sizes from $(200)^3$ to $(700)^3$ voxels in this research work 1 voxel is equal to $(2.6\mu\text{m})^3$. After segmentation, the images were used to compute the effective electrical conductivity of the sub-cubes using a Finite Element conductivity code (Free software from NIST; Garboczi, 1998) as well as formation factor. For both clean sand and clay sand samples, a good agreement between laboratory measurements and computation from digital cores was found, as long as the sub-cube size REV is reached that is between $(1300\mu\text{m})^3$ and $(1820\mu\text{m})^3$, which, with an average grain size of $160\mu\text{m}$, is between 8 and 11 grains.

To my parents, wife, children, brothers and sisters

Acknowledgements

First, I would like to convey my sincere thanks to my supervisor Dr. Stephanie Vialle for her guidance, comments, advice and outstanding supervision. I greatly benefited from her experience and scientific insights throughout my PhD.

I am indebted to the Federal government of Nigeria (PTDF) for the sponsorship for which without it this my dream would not have be possible.

I would like to thank my co-supervisors Prof. Boris Gurevich and Dr. Mahyah Madadi for their tireless effort in trying to make this my work possible.

I would like to extent my gratitude to my family for their patient during my studies, especially my wife (Zulai), mother (Hadiza) and my father (Ali). In addition, the same goes to my children.

I would also like to thank my colleagues for their support both moral and academics throughout my stay in the department.

Table of Contents

Abstract	iii
Acknowledgements	v
Chapter 1	1
Introduction.....	1
1.1 Motivation.....	1
1.2 Review of formation factor values obtained from laboratory and field measurements 1	
1.3 Review of formation factors obtained from digital images	2
1.4 Goal of the thesis	4
1.5 Thesis outline	4
1.6 Thesis work flow	5
Chapter 2	6
Theoretical background of the electrical properties of sand.....	6
2.1 Introduction.....	6
2.2 Porosity	6
2.2.1 Factors affecting porosity.....	7
2.2.1.1 Particle size distribution	8
2.2.1.2 Particle shape	9
2.2.1.3 Particle arrangement	12
2.3 Laboratory porosity measurements	13
2.3.1 Direct method	13
2.3.2 Density method.....	13
2.3.3 Optical method	13
2.3.4 Mercury injection method.....	14
2.3.5 Gas expansion method	14
2.4 Conductivity.....	14
2.5 Formation factor	17

2.6 Archie's law	18
2.7 Full saturation.....	19
2.8 Frequency dependence.....	22
2.9 Effect of surface conductivity	25
2.10 The case of clay sand.....	28
2.11 Representative Element Volume (REV).....	31
2.12 Conclusion	34
Chapter 3	35
Presentation of samples and laboratory experiments	35
3.1 Introduction.....	35
3.2 Sand sample locations and collections	35
3.3 Sand sample description	37
3.3.1 Composition of Scarborough and Cottesloe sand samples	37
3.3.2 Grain size distribution.....	37
3.4 Sample preparation.....	39
3.4.1 Cleaning	39
3.4.2 Drying	40
3.4.3 Packing.....	41
3.5 The case of clay sand mixtures	43
3.6 Injected solutions.....	46
3.7 Laboratory set-up	47
3.7.1 Cells	47
3.7.1.1 Flow cell.....	47
3.7.1.2 Static cell	48
3.8 L-C-R (Induction Capacitance Resistance) meter.....	49
3.9 Conductivity meter.....	50
3.10 Tanks.....	53

3.11 Connecting tubes	54
3.12 Valves	54
3.13 Wire and clips.....	54
3.14 Computation of formation factor.....	55
3.15 Conclusion	57
Chapter 4	57
Micro-CT scan images: acquisition, analysis and computation	58
4.1 Introduction.....	58
4.2 Clean sand.....	58
4.2.1 Image acquisition.....	58
4.2.2 Image loading	59
4.2.3 Image filtering	63
4.2.3.1 Median filter	64
4.2.3.2 Edge preserving filter	65
4.2.3.3 Non-Local filter	66
4.2.4 Histogram of material in the image	68
4.2.5 Image segmentation	70
4.2.6 Types of segmentation	71
4.2.6.1 Two-phase segmentation by global thresholding	71
4.2.6.2 Watershed segmentation	76
4.2.7 Image cropping.....	77
4.2.8 Pre-processing	80
4.3 Clay sand.....	82
4.3.1 Loading the image	82
4.4.2 Image filtering	83
4.3.2.1 Non-Local filter	84
4.3.3 Image segmentation.....	87

4.3.3.1 Multi-threshold	87
4.3.4 Watershed segmentation	88
4.3.5 Image cropping	91
4.3.6 Pre-processing the image files	93
4.4 Conclusion	95
Chapter 5	96
Results from laboratory and micro-CT scan images	96
5.1 Introduction	96
5.2 Laboratory (clean sand)	96
5.2.1 Flow cell	96
5.2.1.1 Two Rocks results	97
5.2.1.2 Scarborough results	100
5.2.1.3 Cottesloe results	105
5.2.2 Static cell	119
5.2.2.1 Two Rocks results	119
5.2.2.2 Scarborough results	122
5.2.2.3 Cottesloe results	126
5.3 Error and possible experimental defects	137
5.4 Micro CT-scan images	137
5.4.1 Porosity calculations from the images	138
5.4.2 Formation factor calculation from the images	138
5.4.2.1 Scarborough results	138
5.4.2.2 Cottesloe results	145
5.5 Electrical computations (clean sand)	150
5.6 Volume analysis of the components	158
5.7 Grain size analysis	160
5.7.1 Label diameter distribution	160

5.8 Cottesloe clay sand results	166
5.8.1 Introduction	166
5.8.2 Laboratory result of clay sand	166
5.8.3 Micro CT-scan image result of clay sample	168
5.8.3.1 Clay sand result.....	169
5.8.3.2 Grain size analysis	172
5.8.3.3 Plots of the electrical potential field after finite element code	175
5.9 Conclusion	179
Chapter 6	181
Synthesis and future directions	181
6.1 Introduction.....	181
6.2. Laboratory-measurement versus computed formation factor: the case of clean sand	181
6.3 Laboratory-measured versus computed formation factor: the case of clay sand	184
6.4 Summary of key findings and perspectives	185
6.5 Remaining questions	188

Table of figures

Figure 1.1: The thesis work flow.	5
Figure 2. 1: The fitting of particles that causes porosity (a) irregular shaped particles not fitting (b) regular shaped particles fitting.....	7
Figure 2.2: Parking in two size systems: (a) diameter ratio = 50.5 (b) diameter ratio = 6.3 after Westman and Hugill (1930).	9
Figure 2.3: Roundness and sphericity of grain particles after Powers (1953).....	10
Figure 2.4: Formation factor-porosity data of unconsolidated particle aggregates of various shapes after Wyllie and Gregory (1953).	11
Figure 2.5: Relation between porosity and particle diameter to assemblages of uniform grains as reported by Ogolo et al. After Leva et al. (1951)	11
Figure 2.6: Particle arrangement (a) Face-centred packing (b) Body-centred packing.	12
Figure 2.7: Predicted and measured bulk electrical conductivity σ_0 response to sand water saturation and temperature (T) (Liu and Moysey, 2012).	20
Figure 2.8: Normalized electrical resistivity of sand as a function of water saturation. The curve fit to Archie’s second law leads to $n = 1.3$	22
Figure 2.9: Frequency dependence of the real (σ') and imaginary part (σ'') of a pump-induced complex conductivity at room temperature after Shan et al. (2003).....	23
Figure 2.10: Scheme to drive pore and fluid properties from complex electrical data or frequency domain IP data using constant phase angle model after Börner et al., 1991.....	24
Figure 2.11: The electrical double layer (a) Gouy-Chapman model (b) Stern Model after Ruffet et al. (1995).....	26
Figure 2.12: Schematic representation of the electrical double layer situated at the mineral surface (Revil and Glover, 1997).....	27
Figure 2.13: 2D Schematic representation of structure and composition of Kaolinite clay minerals.	28
Figure 2.14: 3D Schematic representation of structure and composition of Kaolinite clay minerals.	28
Figure 2.15: Representative elemental volume (REV) I domain of microscopic effects, II domain of REV	33
Figure 2.16: 3D cubes of $(200)^3$, $(350)^3$, $(500)^3$, and $(700)^3$ from the Cottesloe clay sand approaching REV.....	34

Figure 3.1: Sampling points. (TRC, SCB and CTL as Two rocks, Scarborough and Cottesloe Beaches.....	36
Figure 3.2: Putting the sample in a clearly labelled polythene bag	37
Figure 3.3: washing the sand sample in the laboratory	40
Figure 3.4: Drying the sand in the sun	41
Figure 3.5: Packing the sand sample loosely in the cell to achieve high porosity.....	42
Figure 3.6: Sticks used for packing the sand.	42
Figure 3.7: Weighing balance taking a measurement of dry sand	43
Figure 3.8: Hygroscopic (adsorption) water after Saarenketo (1998)	44
Figure 3.9: The pure kaolinite clay and the drying of the pure kaolinite clay.....	45
Figure 3.10: Static cell showing sealed cover with weight on top to prevent evaporation	46
Figure 3.11: Measuring the volume of water and measuring 10 mg of table salt	47
Figure 3.12: Schematic drawing of the experimental set up and the picture of the cell	48
Figure 3.13: Schematic drawing of the experimental set up and the picture of the static cell	49
Figure 3.14: L-R-C (Inductance Resistance Capacitance) meter with the flow cell during experiment.	50
Figure 3.15: Conductivity meter notifying “due for calibration”	51
Figure 3.16: Encased Hanna probe measuring conductivity of water flowing out of the flow cell.....	52
Figure 3.17: Hanna probe measuring saline water drained from the static cell	52
Figure 3.18: Conductivity value after confirmation of calibration	53
Figure 3.19: Tanks used in the experiment to store the saline solutions.....	53
Figure 3.20: An example of the tubes used in the experiment	54
Figure 3.21: Valves used in the experiment to manually control the flow rate of solutions... ..	54
Figure 3.22: Wire and clips used in the experiment	55
Figure 3.23: Parameters set for the recording by the LCR meter.	55
Figure 3.24: Water drained from the static cell for conductivity measurement	56
Figure 4.1: (a) Microgram holder with the sand sample (b) XRM 500.....	59
Figure 4.2: Loaded Scarborough raw image before adjusting the colour map.....	60
Figure 4.3: Loaded Cottesloe raw image before adjusting the colour map.....	61
Figure 4.4: Loaded Scarborough raw image before adjusting the colour map.....	62
Figure 4.5: Loaded Cottesloe raw image before adjusting the colour map.....	63

Figure 4.6: (a) Scarborough raw and median filtered image (b) Cottesloe raw and median filtered image	65
Figure 4.7: Figure 4.6: (a) Scarborough raw and edge preserving filtered image (b) Cottesloe raw and edge preserving filtered image	66
Figure 4.8: Non-local filter: (a) Scarborough (b) Cottesloe images	68
Figure 4.9: Histogram (a) Scarborough (b) Cottesloe images showing the peaks of pore, quartz and carbonate with their mid points at the troughs.	69
Figure 4.10: Histogram (a) Scarborough (b) Cottesloe beach images.	70
Figure 4.11: Threshold image of (a) Scarborough and (b) Cottesloe images.	72
Figure 4.12: 2-Phase segmentation of (a) Scarborough and (b) Cottesloe samples	73
Figure 4.13: Segmentation of Scarborough beach sample (a) under-segmentation (b) correct segmentation and (c) over-segmentation. The areas shown by the red-circled are the examples of areas affected by under-segmentation and over-segmentation.....	75
Figure 4.14: Watershed images of slices at (a) 50, (b) 150 (c) 250, (d) 350, (e) 450 and (f) 550 slices of Scarborough beach.	77
Figure 4.15: Watershed images of slices at (a) 50, (b) 150 (c) 250, (d) 350, (e) 450 and (f) 550 slices of Cottesloe beach.	77
Figure 4.16: 2D sub-volume of $(700)^3$, $(500)^3$, $(350)^3$, and $(200)^3$ cubes for (a) Scarborough and (b) Cottesloe samples.	79
Figure 4.17: 3D sub-volume of $(700)^3$, $(500)^3$, $(350)^3$, and $(200)^3$ cubes for (a) Scarborough and (b) Cottesloe samples.	80
Figure 4.18: Binary image (a) 700, (b) 500, (c) 350, and (d) 200 cubes of Scarborough beach sample.....	81
Figure 4.19: Binary image (a) 700, (b) 500, (c) 350, and (d) 200 cubes of Cottesloe beach sample.....	81
Figure 4.20: Loaded Cottesloe clay sand raw image with 1.3739μ resolution before adjusting the colour map.	82
Figure 4.21: Adjusted raw loaded Cottesloe clay raw image after adjusting the colour map.	83
Figure 4.22: Different filters of Cottesloe shaly sand (a) Bilateral, (b) Curvature driven, (c) Anisotropic (d) Edge preserving filter.	84
Figure 4.23: Non-local filter (a) single filter with neighbourhood 21 and similarity 0.6 (b) double filter with neighbourhood 2 and similarity 0.3.....	86

Figure 4.24: Multi-segmentation showing 700 cube of the Cottesloe clay sand image with the quartz (deep blue colour) surrounding both the clay and carbonate with examples shown in black circles.	87
Figure 4.25: Region of watershed segmentation (a) pore (b) quartz (c) clay and (d) carbonate of Cottesloe beach sample.	89
Figure 4.26: Watershed segmented image of Cottesloe with 3% clay (a) 700 (b) 500 (c) 350 and (d) 200 cubes.	89
Figure 4.27: Histogram of Cottesloe mixed with 3% clay showing the best threshold for the pore, quartz, clay and carbonate.	90
Figure 4.28: Rendered volume of the whole sample of Cottesloe shaly sand.	90
Figure 4.29: Cropped 700-cube volume rendering of (a) pore (b) quartz (c) clay and (d) carbonate of Cottesloe shaly sand.	91
Figure 4.30: Cottesloe sand with 3% clay representative of 3D sub-volume (a) 700 (b) 500 (c) 350 and (d) 200 cubes.	92
Figure 4.31: Cottesloe shaly sand showing the pore (blue), quartz (light blue), clay (yellow) and Carbonate (maroon) (a) 700 (b) 500 (c) 350 and (d) 200 cubes.	94
Figure 4.32: Cottesloe with clay sand showing potential field variation of (a) 700 (b) 500 (c) 350 and (d) 200 cubes.	95
Figure 5.1.1: Graph of the electrical conductivity of the formation and the electrical conductivity of water and against time from flow cell measurements of Two Rocks samples.	99
Figure 5.1.2: Graph of the electrical conductivity of the formation and the electrical conductivity of water and against time from flow cell measurements of Scarborough sample 1.	101
Figure 5.1.3: Graph of the electrical conductivity of the formation and the electrical conductivity of water and against time from flow cell measurements of Scarborough sample 2.	104
Figure 5.1.4: Graph of the electrical conductivity of the formation and the electrical conductivity of water and against time from flow cell measurements of Cottesloe samples.	107
Figure 5.1.5 Graphs of the electrical conductivity of the formation against the electrical conductivity of water for flow cell measurements of Two Rocks Beach.	110
Figure 5.1.6: Graphs of the electrical conductivity of the formation against the electrical conductivity of water for flow cell measurements for Scarborough sample 1.	112

Figure 5.1.7: Graphs of the electrical conductivity of the formation against the electrical conductivity of water for flow cell measurements for Scarborough sample 2	115
Figure 5.1.8: Graphs of the electrical conductivity of the formation against the electrical conductivity of water for flow cell measurements for Cottesloe samples	118
Figure 5.2.1: Graph of the electrical conductivity of the formation and the electrical conductivity of water and against time from static cell measurements of Two Rocks samples.....	122
Figure 5.2.3: Graph of the electrical conductivity of the formation against time from static cell measurements of Cottesloe samples.....	128
Figure 5.2.4: Graphs of the electrical conductivity of the formation against the electrical conductivity of water for static cell measurements of Two Rocks samples.....	131
Figure 5.2.5: Graphs of the electrical conductivity of the formation against the electrical conductivity of water for static cell measurements of Scarborough sample 2.	134
Figure 5.2.6: Graphs of the electrical conductivity of the formation against the electrical conductivity of water for static cell measurements of the Cottesloe samples.	136
Figure 5.3.1: Electrical formation factor versus porosity for Scarborough micro CT-scan images.....	141
Figure 5.3.2: Scarborough Micro CT-scan images of cubes with measurements for the flow cell in pink and static in blue while green is for the cubes.....	142
Figure 5.3.3: (a) Porosity against cube sizes and (b) formation factor against cube sizes for Scarborough Beach sample.	144
Figure 5.3.4: Electrical formation factor versus porosity for Cottesloe micro CT-scan images	146
Figure 5.3.5: Cottesloe Micro CT-scan images of cubes with measurements for the flow cell in pink and static in blue while green is for the cubes.	148
Figure 5.3.6: (a) Porosity against cube sizes and (b) formation factor against cube sizes for Cottesloe Beach sample.....	149
Figure 5.4.1: Binary images of Scarborough Beach sample.....	151
Figure 5.4.2: Binary image of Cottesloe Beach sample.....	152
Figure 5.4.3: Potential field images of (a) $(700)^3$, (b) $(500)^3$, (c) $(350)^3$ and (d) $(200)^3$ cubes of Scarborough Beach sample.	154
Figure 5.4.4: Potential field images of (a) $(700)^3$, (b) $(500)^3$, (c) $(350)^3$ and (d) $(200)^3$ cubes of Cottesloe beach sample.	155
Figure 5.4.5: Conductivity images along x, y and z-axes.	155

Figure 5.4.6: Percentage volume of components in Scarborough clean sand sample.	159
Figure 5.4.7: Percentage volume of components in Cottesloe clean sand sample.	160
Figure 5.5.1: Graph of grain count and cumulative frequency of (a) pore (b) quartz and (c) carbonate from Scarborough Beach sample.	163
Figure 5.5.2: Graph of grain count and cumulative frequency of (a) pore (b) quartz and (c) carbonate from Scarborough beach sample.	165
Figure 5.5.3: Summary of measurements from laboratory and micro CT-scan images from Scarborough and Cottesloe Beaches.	166
Figure 5.6.1: Cottesloe with 3% clay (a) conductivity of formation against time (b) conductivity of formation against conductivity of water.	168
Figure 5.6.2: Formation factor against cube sizes of Cottesloe Beach samples with 3% clay (a) $(700)^3$ (b) $(500)^3$ (c) $(350)^3$ and (d) $(200)^3$ cubes.	170
Figure 5.6.3: Porosity against cube sizes of Cottesloe Beach sand with 3% clay.	171
Figure 5.6.4 Formation factor against cube sizes of Cottesloe Beach sand with 3% clay	171
Figure 5.6.5: Frequency distribution of components in the Cottesloe sand with 3% clay (a) pore (b) quartz (c) clay and (d) carbonate.	174
Figure 5.6.6: Cottesloe with 3% clay showing the components: deep blue (pore); sky blue (quartz); maroon (carbonate); and yellow (clay) of (a) $(700)^3$ (b) $(500)^3$ (c) $(350)^3$ and (d) $(200)^3$ cubes.	176
Figure 5.6.7: Cottesloe with 3% clay showing potential field variation of (a) $(700)^3$ (b) $(500)^3$ (c) $(350)^3$ and (d) $(200)^3$ cubes.	177
Figure 5.6.8: Summary of measurements from laboratory and micro CT-scan images from Cottesloe clay sand.	179
Figure: 6.1: Summary of laboratory and micro CT scan results with results from Research 182	
Figure: 6.2: Summary of laboratory and micro-CT scan image of Scarborough clean sand	183
Figure: 6.3: Summary of laboratory and micro-CT scan image of Cottesloe clean sand	184
Figure: 6. 4: Comparing the scale of time spent for micro-CT image, clean sand using flow cell, clean sand using static cell and clay sand using static cell.	187

List of tables

Table 2.1: The porosity of different apparent volume occupied by unit true volume of mixing coarse and fine grain studied by Westman and Hugill (1930).	9
Table 2.2: The effect of grain shape on porosity	10
Table 2.3: Effect of different particle arrangement on porosity after Ogolo et al. (2015)	13
Table 2.4: Specific electric resistivity ρ of minerals after Olhoeft (1981).....	16
Table 2.5: Table of Cation exchange capacity of various clays: Keller and Frischknecht (1966)	29
Table 2.6: Cation exchange capacity (CEC) and colloid content of five soils of different textures After: McNeill (1980)	30
Table 2.7: Specific surface area of different clay types after Corey (1994).....	31
Table 3.1: The of coordinates for the sands samples collected.....	35
Table 3.2: Summary of EqDiameter of materials of Scarborough and Cottesloe Beaches	38
Table 3.3: Summary of EqDiameter of materials from Cottesloe clay sand	39
Table 4.1: X, Y and Z cropping dimensions of $(700)^3$ cubes of Scarborough and Cottesloe beach samples	78
Table 4.2: X Y and Z cropping dimensions of $(500)^3$, $(350)^3$ and $(200)^3$ cubes of Scarborough and Cottesloe beaches.	78
Table 4.3: X Y and Z cropping dimensions of $(500)^3$, $(350)^3$ and $(200)^3$ cubes of Scarborough and Cottesloe beaches.	92
Table 5.1: Summary of laboratory and micro-CT scan image results from Scarborough Beach samples.....	157
Table 5.2: Summary of laboratory and micro-CT scan image results from Cottesloe Beach samples.	157
Table 5.3: Percentage volume of components in Scarborough and Cottesloe clean Beach sand samples.	158
Table 5.4: Summary of EqDiameter of materials	161
Table 5.5: Summary of EqDiameter of materials	175
Table 5.6: General table for the Cottesloe clay sand mixture	178

Nomenclature

Glossary of abbreviations

TRC Two Rocks sample

SCB Scarborough sample

CTL Cottesloe sample

CTWL Cottesloe with clay sample

FF Formation factor

XRCM X-ray micro-computed tomography

DRP Digital rock physics

GPU Graphical processing unit

NIST National Institute of Standards Technology

REV Representative elemental volume

CEC Cation exchange capacity

EDL Electrical diffuse layer

Min Minimum

Max Maximum

WA Western Australia

LCR Inductance capacitance resistance meter

phi Porosity

p Pore

q Quartz

cl Clay

c carbonate

Symbols

ϕ Porosity

σ Conductivity

σ_{eff} Effective conductivity

Chapter 1

Introduction

1.1 Motivation

Electrical properties of rocks and sediments are important parameters for well-log and reservoir interpretation. Laboratory measurements of such properties are often time-consuming and difficult, if not impossible in some cases, as for example in low permeability, high-clay-content formations, for which the equilibrium time between the minerals and the saturating fluid can reach several months. To get the formation factor from laboratory measurements, it typically takes a week for a high-permeability, clean sandstone, whereas it can take several months for a clay-rich sandstone.

In this work, I will focus on unconsolidated media, namely beach sand. Unconsolidated formations are commonly found in various industry and environmental applications: in the oil & gas industry, many oil reservoirs are unconsolidated, such as heavy oil sands; some groundwater aquifers are sand and gravel formations; coastal areas are of increasing interest with the necessity to monitor seawater intrusion and the potential of groundwater contamination. From an experimental viewpoint, sand is a particularly interesting medium: one can easily, and in a very well controlled way, vary many parameters such as grain size, grain sorting, porosity (by varying the degree of compaction), mineralogy, etc. and analyse how these parameters affect the electrical formation factor.

1.2 Review of formation factor values obtained from laboratory and field measurements

[Archie \(1942\)](#) defined the electrical formation factor (FF) as the ratio of the resistivity of porous medium completely saturated with electrolyte to the resistivity of the electrolyte itself; and is controlled by the pore geometry as conduction of electrical current is predominantly through [the pore fluid](#).

[Slawinski \(1926\)](#) discussed the relationship between porosity and formation factor for aggregates of spheres both in contact and dispersed, but his contribution has been neglected

because the mathematical approach he used is rather simple. Nevertheless, he presented enough experimental evidence to support his theoretical deductions. [Wyllie and Gregory \(1953\)](#) determined empirically the relationship between the formation factor and porosity of unconsolidated mixtures of particles of typical geometrical shapes, as well as the effect of cementation. They found that formation factor increases rapidly with a decrease in porosity. However, the accuracy of the results was limited due to the method of the synthetic cementing specimen. The studied aggregates were spheres within a porosity range of 0.12-0.56 and cubes, cylinders, discs and triangular prism within a porosity range of 0.3-0.45: the measured formation factors were 3.6-4.7, 3.6-6.5, 4.7-5.6, 3.5-4.6 and 3.8-4.6 for the spheres, cubes, cylinders, discs, and triangular prisms, respectively, and in the porosity ranges indicated above. [Wyllie et al. \(1956\)](#) and [Wyllie \(1957\)](#) calculated the formation factor from aggregates of spheres (porosity range of 0.12-0.56), triangular prisms, cubes and cylinder discs with the porosity range of (0.30-0.45) but did not include the cementation exponent. [Carothers and Porter \(1971\)](#) also published the results of 2295, formation factor values from wells of the offshore of California Pliocene and wells the Pliocene strata offshore California and Miocene sand strata offshore Texas Louisiana gives a formation factor range of 1.0-8.1. [Jackson et al. \(1978\)](#) analysed various grain shapes and sizes of artificial and natural samples from which they got a formation factor ranging from 1.5-5.5. [Kamel \(2001\)](#) estimated the sonic acquired porosity and formation factor borehole geophysical sonic logs in a formation with established lithology from the Gulf of Mexico. He uses sonic transient times of formation and sonic transient times of fluid both in μs per feet to calculate the formation factor using resistivity logs with the connate water resistivity R_w and formation resistivity R_f . Getting information from the core is often difficult and readily not available most times. Furthermore, sample recovery and preservation is a well-recognized problem, especially for unconsolidated formation in which the in-situ arrangement of grains is not preserved, hence making questionable the representativeness of the value obtained in the laboratory compared to that of the field. Therefore, to calculate the formation factor, two porosity logs must be available, but usually, the lack of these porosities makes the computation of the formation factor very difficult if not impossible.

1.3 Review of formation factors obtained from digital images

Because formation factor depends on mineralogy and microstructure (as discussed in the paragraphs above), an alternative to laboratory measurements has been the development of the

computation of electrical properties from rock digital images. In particular, X-ray micro-computed tomography (XRCM), has the capacity to provide excellent, detailed 3D images of the pore-scale. The difference in the x-ray absorption by different materials can help in distinguishing the material component of the sample under investigation (e.g., pore, quartz carbonate, and clay).

Digital Rock Physics (or DRP), the computation of rock properties (e.g. permeability, electrical conductivity, elastic moduli, etc.) from digital images of rocks, combines three key components that have grown rapidly over the last ten years due to technological developments. First is a high-resolution imaging technology, which allows the comprehensive study of the pore architecture of porous materials. Second is, the progressive numerical processes for simulating the complex physical phenomenon while the third is the rapid, massively parallel computation, adopting robust graphical processing units (GPU's) that were basically developed for computer gaming and animation (Walls and Sinclair, 2011). Despite the fact that there are various techniques for gaining a 3D image of sand microstructure, which is very important for understanding the characterization of the sand microstructure, as shown by Andrä et al. (2013), Saenger et al. (2014) grouped them into either the destructive method or the non-destructive method. Because of heterogeneities, petrophysical and multi-phase flow properties strongly depends on the scale of investigation Lopez et al. (2012).

Various models have been proposed for the computation of electrical properties from microstructural models over the past 50 years. These ranges from statically models used to reconstruct 3D porous materials (e.g. Adler et al., 1990; Adler et al., 1992; Joshi, 1974; Miller, 1969; Milton, 1982; Torquato, 1987; and Yeong and Torquato, 1998) to direct measurement of a 3D structure from synchrotron and X-ray computed microtomography (e.g. (Arns et al., 2001; Dunsmuir et al., 1991; Spanne et al., 1994; Arns et al., 2001; Øren and Bakke, 2002; and Spanne et al. 2000) or laser confocal microscopy (Fredrich et al., 1995). In most of the studies using XRCM images, the numerical prediction of electrical conduction conductivity underestimates the experimental results by 30 to 100%, which leads to an overestimation of the formation factor (Auzerais et al., 1996; Schwartz et al., 1994; and Spanne et al., 1994). Several explanations have been put forward to justify this discrepancy: percolation differences between the model and real material, mainly to a smaller volume sampling in the model (Adler et al., 1992; Bentz and Martys, 1994); the addition of a third phase to the traditional two-phase model (rock matrix being one phase and the saturating fluid being a second phase) that counts for the bound fluid at the grain fluid interface (Zhan and Tokoz, 2007); discretization errors and statistical fluctuations (Arns et al., 2001).

1.4 Goal of the thesis

The main goal of this research work is to provide a robust methodology to obtain the electrical formation factor from digital images, first from a simple porous medium (sand pack) and then for other porous media of increasing complexity.

In particular, I use here X-ray micro computed tomography images from three sets: clean sand of Scarborough beach (Western Australia), clean sand of Cottesloe beach (Western Australia), and a mixture made of Cottesloe beach sand and various amount of clay sand.

This work is not the first one providing electrical formation factor values from digital images; however, to my knowledge, none provides such a comprehensive and robust method. The key points are 1) a synthetic of the Representative Elemental Volume (REV) above which the computed parameters are stable, 2) a comparison of *trends* between two properties (e.g., formation factor and porosity), computationally derived and produced in the laboratory, and not a comparison of *single values*, as, because the two measurements are done at different scales and because rocks are heterogeneous at all scales, these two values do not have to much (Dvorkin et al., 2011) and 3) the use (and the modification in case of the presence of clays) of freely available codes from National Institute of Standards Technology (NIST).

1.5 Thesis outline

The thesis comprises six chapters.

Chapter 1 – Introduction: In this chapter, I have laid down the motivation for the research then a review of other workers on electrical formation factor from laboratory and digital images add this followed by the goal of the thesis and the thesis work flow.

Chapter 2 – Theoretical background of electrical properties of sand: This chapter explains the basics of the theoretical concepts that is use in this research work. It comprises an introduction to the chapter, porosity and factors affecting porosity, porosity measurement, conductivity, formation factor, Archie's law, saturation, frequency dependence, the effect of surface conductivity as well as case of clay sand.

Chapter 3 – Laboratory experiment: In this chapter, after introducing the sample collection, their description and preparation are outlined. The injected solutions used are presented in this chapter. How the electrical formation factor is computed is also described.

Chapter 4 – Micro-CT scan images: The focus of this chapter is the image acquisition, processing and pre-processing for electrical computations of both the clean sand and clay sand images.

Chapter 5 – Results: This chapter contains the; laboratory results of the flow cell and static cell, formation factor from images, grain size analysis, case of clay sand, electrical computations of both clean and clay sand as well as a conclusion.

Chapter 6 – Discussion and conclusion: In this chapter, the main outcomes of the research is summarize, the research is discussed within the context of other research works done by other researchers for both the clean and clay sand and finally a conclusion is presented.

1.6 Thesis work flow

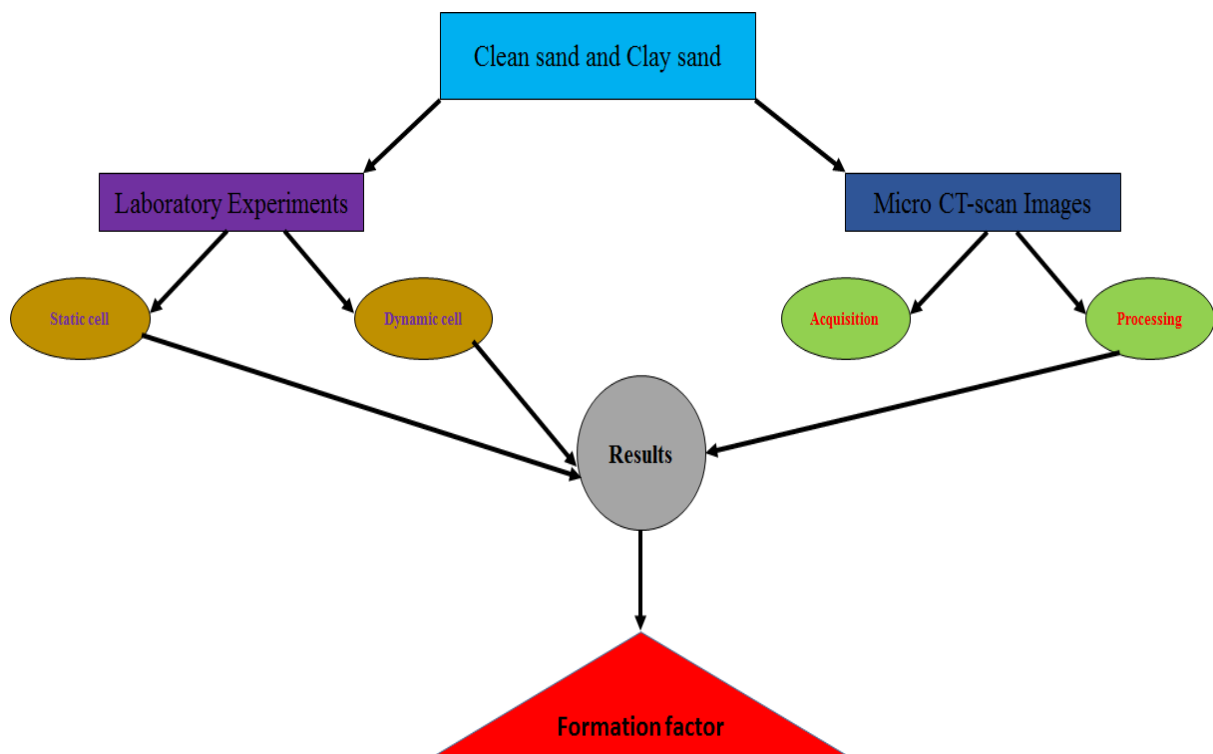


Figure 1.1: The thesis work flow.

Chapter 2

Theoretical background of the electrical properties of sand

2.1 Introduction

In this chapter, I will be presenting some basic general knowledge and the concept of the electrical properties of sand as well as the tools that I used in generating, analysing and interpreting my data from the laboratory experiments of the clean sand and shaly sand samples. The calculation of porosity is discussed here because the electrical property of sand is governed by the pore space (porosity) as well as the pore geometry. This will be followed by discussing the methodology I used to calculate the conductivity of the formation as well as the conductivity of the water saturating the clean sand/shaly sand, and ultimately to calculate the formation factor using the Archie law. Other parameters that had an influence on my laboratory experiments discussed here includes the dependency of the measurements on saturation, and the frequency under which the research was conducted on the porous sand media of the clean sands of Two Rocks, Scarborough and Cottesloe and the shaly sand of Cottesloe. In the case of the shaly sand, the effect of surface conductivity is discussed here, and finally, the Representative Elemental Volume (REV) is presented (that is the cube that can be selected at random and the variation or change in physical properties as porosity and formation factor is very small). At the end of this chapter, I will have equipped myself ready for the laboratory experiment that is coming in the next chapter (chapter 3).

2.2 Porosity

Sand samples packed in the cell for the experiment have spaces between them called pores; these pores are the result of the irregular-shaped particles not fitting together. Imagine a round grain fitting to a hexagonal area; the edges will not fit thereby leaving some pore spaces, as in Figure 2.1a. Similarly, imagine a hexagonal grain fitting another hexagonal space of the same size, there will be no space left to create the pore spaces, as in Figure 2.1b. The phenomenon described in figure 2.1a is characteristic of all natural sands. However, the shape, size, and

arrangement of the particles in Figure 2.1 a determine the amount and nature of the pore spaces created i.e. the porosity of the sample.

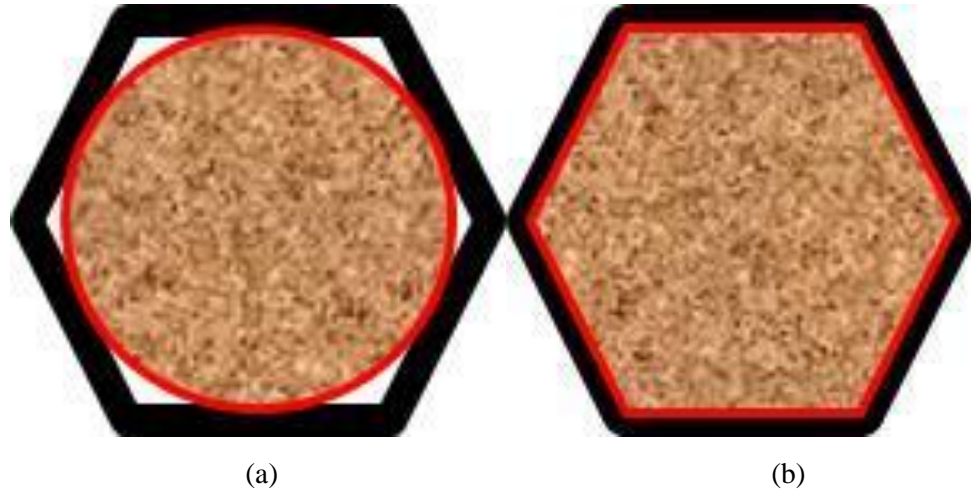


Figure 2. 1: The fitting of particles that causes porosity (a) irregular shaped particles not fitting (b) regular shaped particles fitting.

Therefore, porosity, or void fraction, is a measure of the void spaces in a material and is a fraction of the total volume. The porosity of any given porous media varies from close to zero in igneous crystalline to almost one for fibrous materials, with most sedimentary rocks falling in-between this range. Below is the equation for calculating the porosity.

$$\phi = \frac{V_p}{V} = \frac{V - V_g}{V} \quad 2.1$$

where V_p is the volume of the pore, V_g is the volume of the grain and V is the total volume

There is an intergranular porosity, that is, the porosity due to the pore volume between the sand grains and intragranular porosity which is the porosity due to the voids within the grains e.g. in the carbonates within the sand samples.

2.2.1 Factors affecting porosity

Five factors affect porosity:

- 1 Particle size distribution
- 2 Particle shape: porosity increases as particle uniformity decreases
- 3 Particle arrangement: porosity decreases as compaction increases
- 4 Cementation and

For unconsolidated media, such as sand, which is the object of this thesis, only factors 1 to 3 are in place.

2.2.1.1 Particle size distribution

All the natural sands found in our coastal beaches consists of different grain sizes and these sizes range from very coarse to very fine grains, these natural beaches contain all the sizes in this range. My study samples are made of grains of various sizes (though I did not do a grain size analysis). The size of the grain has a direct relationship on the porosity of the sample, the coarser the particles, the greater the porosity. Therefore, porosity decreases as the grain sizes reduce because smaller grains tend to occupy the void spaces, thereby reducing the porosity.

[Jackson \(1975\)](#) carried out an experiment on eight (8) samples of natural and artificial sand whose grains varied widely in size. Four of the samples were mixtures of different mean sizes, but similar range of size giving an almost identical formation factor. Four (4) of the samples were of similar size range, but with gradually increasing spread sizes, giving a formation factor that exhibited gradual movement leaning to low porosity with high porosity as the spread of sizes increase, the porosity decreases as the range of particle size increases. Similarly, [Rogers and Head \(1961\)](#) experimented with synthetic sands and they showed that porosity is dependent on grain size for well-sorted sands. But [Pryor \(1973\)](#) also analysed 950 different grains of sand and showed that porosity decreased with an increase in grain size. [Bell \(2013\)](#) also gave porosity ranges of 0.44-0.49, 0.41-0.48 and 0.39-0.41 for coarse, medium and fine grain sands respectively.

[Westman and Hugill \(1930\)](#) studied a mixture of sand made of mixtures of round particles. These particles had two distinct sizes of coarse and fine grains and the mixtures was made up of real volumes with densities of 2.69 and 2.75 for the coarse and fine grains respectively. The result of their experiment was the porosity variation shown in Table 2.1. They noted that if the diameter ratio is unity, there would be no particle size effect on mixing and the apparent volume would follow the straight lines GF and GM Figure 2.2. Whenever the diameter ratio is very large, the finer materials will fill the matrix without any change in volume despite the fraction of the finer materials increasing.

Table 2.1 gives the apparent volume occupied by the unit true volume of mixing coarse and fine grain. This is used in plotting the graphs in Figure 2.2 starting with completely coarse grain with no fine grain and by gradually adding fine grain by reducing an equal volume of the

coarse e.g., 90% coarse grain mixed with 10% fine grain, and this continuing this until a mixture of completely fine grain with no coarse grain is achieved.

Table 2.1: The porosity of different apparent volume occupied by unit true volume of mixing coarse and fine grain studied by [Westman and Hugill \(1930\)](#).

Coarse (% by true vol.)	Fine (% by true vol.)	Porosity (% by true vol.)
100	0	37.7
90	10	31.5
80	20	25.1
70	30	18.5
60	40	23.6
50	50	27.9
40	60	31.6
20	80	37.8
0	100	42.5

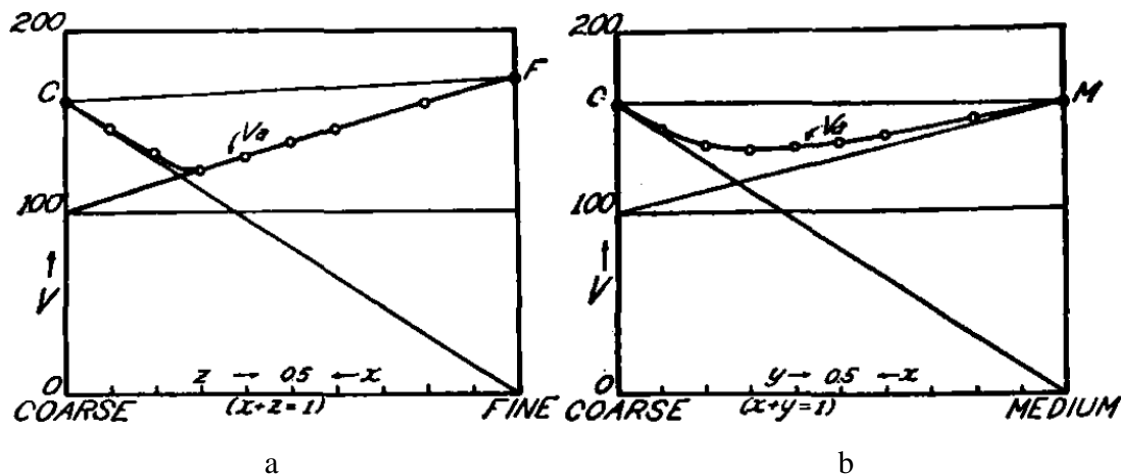


Figure 2.2: Packing in two size systems: (a) diameter ratio = 50.5 (b) diameter ratio = 6.3 after [Westman and Hugill \(1930\)](#).

2.2.1.2 Particle shape

Natural sands are made of grains of different shapes or even grains that are shapeless; therefore, the three sand samples I have worked on in the laboratory are not exceptional. The sand samples are made of various particle shapes. However, angular particles tend to show higher porosity compared to more rounded particles, and, similarly, the porosity increases as particle uniformity decreases. Elongated particles can pile on top of each other more than sub-rounded and well-rounded particles; the piling of these particles tend to close the pore spaces thereby reducing the porosity. Since it is difficult for the sub-rounded particles to pile on top of each other, they will have more pore spaces and therefore will ultimately have higher porosity. When talking

about the shape of sand we are looking at two properties, roundness and sphericity. Roundness describes whether the grain has sharp or smooth edges on its surface, while sphericity describes how closely the grain assumes the form of a sphere. The shape of a grain influences porosity because of its effects on how individual particles can lock together. Table 2.2 shows the variations of porosity by different shapes of grains.

Table 2.2: The effect of grain shape on porosity

Grain shape	Maximum porosity
Cube	0.425
Cylinder	0.429
Disc	0.553
Sphere	0.399

Jackson (1975) studied the effect of the particle shape on porosity using a suite of different samples with the same size but with different grain shapes: glass spheres, a rounded commercial sand, a shaly beach sand, and shell fragments. Porosity rises from 0.32 to 0.62 from the glass beads through to the shell fragments.

The shape (roundness and sphericity) is caused by the effects of transport, the journey made by the sand during its life history in which grains collide with each other and thereby break the edges of the particle. Therefore, how spherical and well-rounded a grain may be is determined by how far it moves from its source: the further away from the source the more rounded.

Powers (1953) developed a visual comparison chart of reference particles of known sphericity and roundness (Figure 2.3). From this figure, the porosity is highest at the left side (very angular) of the figure and the porosity decreases towards the right, with, finally, the least porosity obtained at the extreme right of the figure (well-rounded).

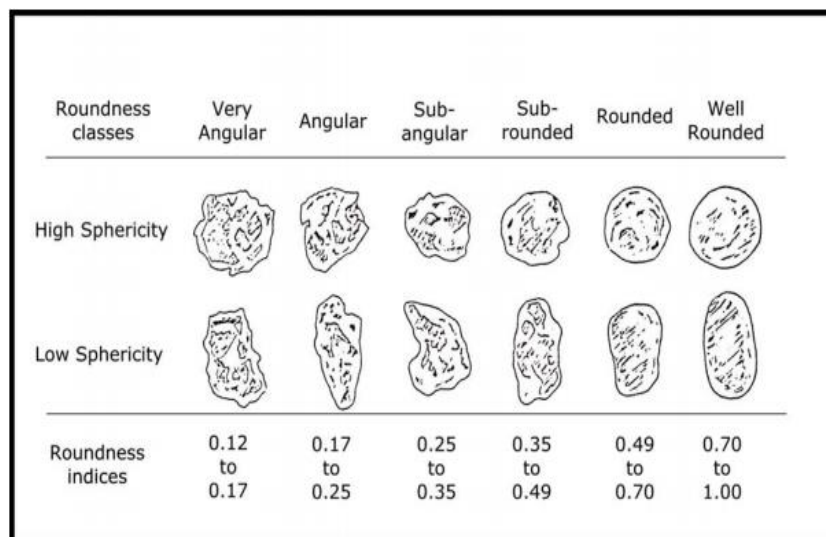


Figure 2.3: Roundness and sphericity of grain particles after Powers (1953).

Wyllie and Gregory (1953) investigated the effect of particle shape on porosity, and found the highest porosity was from triangular-shaped aggregates followed by cubes, discs, and spheres while cylinders had the least porosity (figure 2.4).

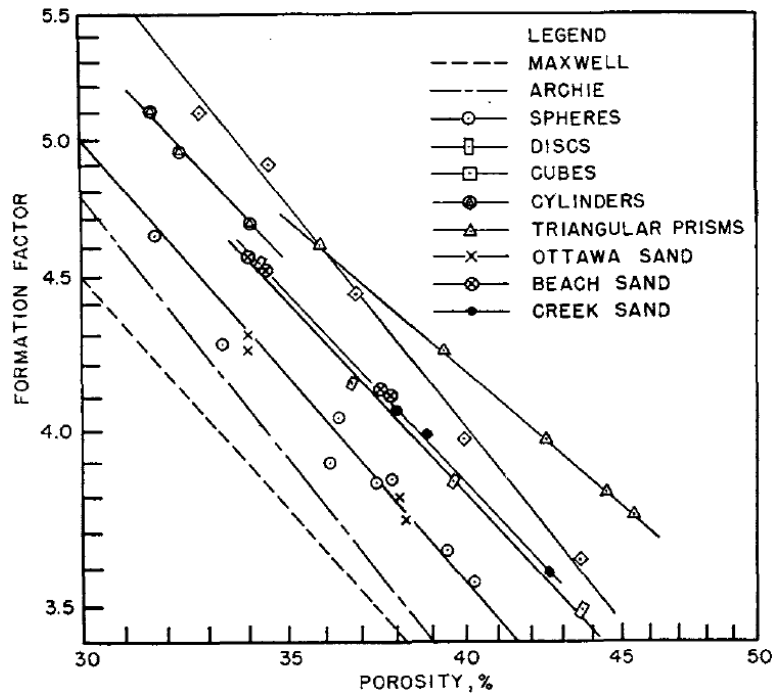


Figure 2.4: Formation factor-positivity data of unconsolidated particle aggregates of various shapes after Wyllie and Gregory (1953).

Ogolo et al. (2015) also reviewed the work of Leva et al. (1951) on the relation between porosity and particle diameter for assemblages of uniform grains in which they show angular grains tend to have higher porosity than rounded grains (Figure 2.5)

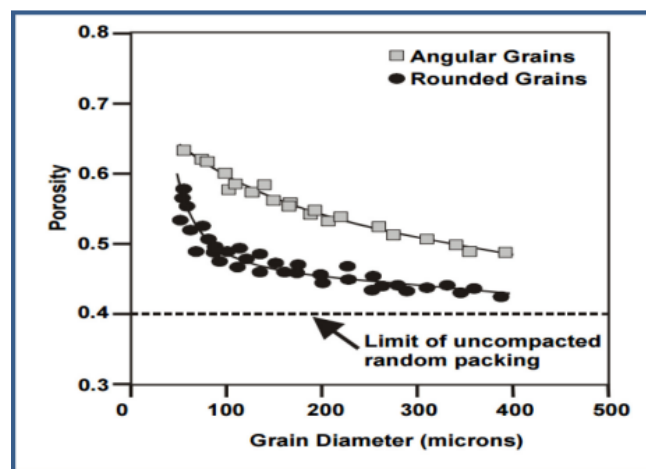


Figure 2.5: Relation between porosity and particle diameter to assemblages of uniform grains as reported by Ogolo et al. After Leva et al. (1951)

2.2.1.3 Particle arrangement

The particles' arrangement in their natural setting is determined by the energy of the transporting medium (e.g. wind or water). When the energy is high the medium becomes turbulent hence no gradation; likewise, compaction of the grains caused by lithostatic pressure that is the weight of the due to burial (i.e. overburden) decreases the porosity. In laboratory experiment of this research, the particle arrangement was achieved by gently shaking the cell to make the grains come closer to each other, thereby reducing the pore spaces.

To understand the values of porosity experienced, imagine round balls of the same size stacked on top of each other in columns. Calculation shows that the porosity of spherical of four spherical balls laced on top of each other will be 47.6% (Figure 2.6a). But when the same balls are packed in the closest possible arrangement, in which the upper balls sit in the valley between the lower balls, the porosity is reduced to 25.9% Figure 2.6b. Changing the size of the balls will not change the porosity. Fang (2013) stated that, generally, packing density decreases with a decreases with grain size while Zhang et al. (2006) also studied the X-ray microtomography of fixed beds of equilateral cylinders of diameter 1.8mm, and found porosities of 0.406, 0.343 and 0.285 for cubic, tetragonal and triclinic packing arrangements respectively.

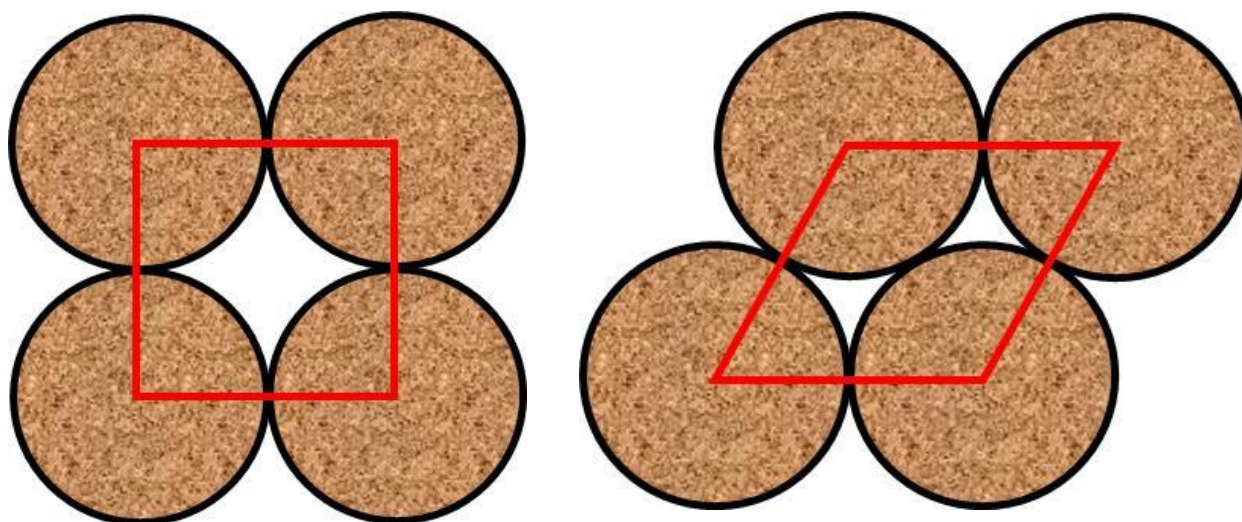


Figure 2.6: Particle arrangement (a) Face-centred packing (b) Body-centred packing.

Table 2.3 below shows the effect of particle arrangement on porosity.

Table 2.3: Effect of different particle arrangement on porosity after [Ogolo et al. \(2015\)](#)

Particle arrangement	Porosity
Cubic	47.6
Rhombohedral	26.0
Orthorhombic	39.5
Tetragonal	30.2
Tetrahedral	26.0
Pyramidal	26.0
Hexagonal	39.5
Triclinic	26.0
Cubic	47.6

2.3 Laboratory porosity measurements

There are several methods of measuring porosity, including:

- 1 Direct method
- 2 Density method
- 3 Optical method
- 4 Mercury injection method
- 5 Gas expansion method and

2.3.1 Direct method

The total volumes and volumes of the grains are determined directly as in equation 2.1. Then

$\phi = 1 - \left(\frac{V_s}{V} \right)$ gives the average porosity of the rock. Because the direct method determines the

pore volume from the difference $V - V_s$, it will include all of the pore space even when the pore is not connected to the outside of the rock by a continuous pore network.

2.3.2 Density method

Measuring bulk density ρ of the sand and the average density ρ_s of the solid constituents

allows the determination of the total porosity $\phi = 1 - \left(\frac{\rho}{\rho_s} \right)$.

2.3.3 Optical method

For cases where porosity microstructure is isotropic, porosity can be determined from a two-

dimensional section as $\phi = \frac{A_p}{A}$ where A is the area of the total image and A_p is the area

intersected by the pores. Usually, it is necessary to impregnate the pores with a material such as wood's metal or plastic to enhance the contrast between mineral pores.

2.3.4 Mercury injection method

After evacuating a sand of pore fluids, the bulk volume was determined by immersing the sand in a mercury bath. At atmospheric pressure conditions, the mercury will not enter the pore space. The mercury pressure is raised until it begins to get into the pore space. If the pressure is increased sufficiently, the mercury will enter most of the pores, thus determining the pore volume.

2.3.5 Gas expansion method

This method is similar to the mercury injection method except that the medium used is highly compressible (ideal gas) which requires almost no pressure differential to enter the pore space. The bulk volume V of the sand is determined through an independent measurement. Then the sand is enclosed in a container of known volume V_1 , having initial a gas pressure P_1 , and connected to an evacuated container of known volume V_2 . When the valve between these two containers is opened slowly, isothermally, the gas expands into the evacuated container, and the gas pressure decreases to P_2 . The volume P_2 can then be determined using the ideal gas law.

2.4 Conductivity

Conductivity is the ability of a solution to pass an electric current. The group quartz, which is the main interest in this research work, falls into a group of solid material called the dielectric; other groups are conductors and semiconductors based on their magnitude and mechanism of electrical conduction. All materials have some degree of conductivity, in the saturated sand; the level of ionic strength has a broad spectrum, which varies from low conductivity (deionized water) to high conductivity of concentrated solutions (brine) as found in this research work.

There is a great difference in the effective conductivity of sand ranging ($10^{-14} - 10^{-10} \text{ Sm}^{-1}$) to the conductivity of the saline water filling the pore spaces (ranging from $10^{-2} - 1 \text{ Sm}^{-1}$). This wide difference in conductivity between the pore and grains will allow current to flow entirely within the saline pore water so that the particle shapes and their arrangement influence the path of the electric current that follows Ohm's law.

$$\vec{J}(r) = \sigma(r)\vec{E}(r) = -\sigma(r)\vec{\nabla}V(r) \quad 2.2$$

where J is the current density, σ is the conductivity of the fluid ∇V potential difference

Because of fluctuations in conductivity at a pore scale $\sigma(r)$, the potential $V(r)$ will depend on the microgeometry. By applying a potential difference ∇V between two parallel planes located at $z = 0$ and L , the effective conductivity of the homogeneous and isotropic sand sample, the current density $\langle J \rangle$ parallel to the field is

$$\langle \vec{J} \rangle \equiv \frac{1}{A} \iint_s (\vec{J} \cdot \hat{z}) dS \equiv \sigma_{eff} \left(\frac{\Delta V}{L} \right) \quad 2.3$$

where A is cross-sectional area perpendicular \hat{z}

The effective conductivity depends on the volume fraction of the sand, and its specific conductivities, as well as the sand microstructure. The charge conservation becomes

$$\vec{\nabla} \cdot \vec{J}(r) = -\vec{\nabla} \cdot (\sigma(r)\vec{\nabla}V(r)) = 0 \quad 2.4$$

If the distribution of the conductivity $\sigma(r)$ is known, the effective conductivity is

$$\sigma_{eff} \equiv \left(\frac{L}{\Delta V} \right) \frac{1}{A} \iint_s \sigma(r) (-\hat{z} \cdot \vec{\nabla}V) dS \quad 2.5$$

Because the sand sample does not contain any clay, and the injected solutions have a much larger conductivity of 10^{-2} to $5.0 \cdot 10^{+1}$ S/m than that of quartz or carbonate with a surface conductivity of $5.4 \cdot 10^{-3}$ S/m (Miller, 1969) and $1.4 \cdot 10^{-3}$ S/m (Vialle, 2008) respectively. Therefore, the surface and matrix electrical conductivities can be neglected (Johnson and Sen, 1988, Garrouch and Sharma, 1994). The wide range of difference between the resistivity of various minerals together with fresh and saline water are given in Table 2.4 after Olhoeft, 1981. The conductivity in the medium comes from dissolved ions as conductors. The major positively charged ions are sodium (Na^+) calcium (Ca^+) potassium (K^+) and magnesium (Mg^+), while the major negatively charged ions are chloride (Cl^-), sulphate (SO_4^{-2}), carbonate (CO_3^{-2}), and bicarbonate (HCO_3^-). In my research work, only sodium and chloride are of concern because I used table salt. The salt dissolves in water and breaks into positively and negatively charged ions. Conductivity is directly related to salinity that is the total concentration of all dissolved salts in water the higher the number of dissolved salts the higher the conductivity. As for the grains, the sand samples I used in the experiments have grain boundaries, which either reduce or enhance electrical conduction. This is because grain boundaries may act as barriers for an electric current when electronic conduction dominates while grain boundaries may increase

conduction when ionic conduction plays a great role. [Schock et al. \(1989\)](#) show that the grain-boundary effect is negligible for grain-size larger than 0.1 mm. It was also established that tortuosity and constriction effect the conduction of porous media ([Berg, 2012](#)).

The conductivity of a porous medium depends on both the specific properties of the grains and their ratio and distribution. Most minerals are insulators; however, numerous minerals are semi-conductors. In solutions, the current is carried by cations and anions; the conduct of the electric current depends on factors such as

- (a) Concentration
- (b) Mobility of ions
- (c) Valence of ions

Electrolytes include acids, bases, and salts, and can be either strong or weak. In my research work I have used dissolved table salt as an electrolyte to make five (5) different saline solutions. A network might represent a simplification of the pore microstructure of a porous medium, where pore bodies corresponds to the nodes of the network and pore throats to resistors. Electric conductance depends on the length of the electric field lines and changes in drift velocity, in addition to the porosity and conductance of the electrolyte [Berg \(2012\)](#).

The following factors influence the accuracy of conductivity measurements

- (a) Polarization (solved by applying and alternating current)
- (b) Contamination (solved by cleaning the surface of the electrodes before and after every experiment)
- (c) Geometry (was not taken care of in my research work, but can be solved by using a 4 electrode conductivity cell)
- (d) Cable resistance (correction is made only for readings below 50 Ω)
- (e) Cable capacitance (applied on four pole cell)
- (f) Frequency change (using low-frequency 1-10Hz for low conductivities and high frequency >100Hz for high conductivities) and
- (g) Temperature (Solved by conducting experiments at room temperature).

I will be discussing the details of these factors in chapter 3.

Table 2.4: Specific electric resistivity ρ of minerals after [Olhoeft \(1981\)](#).

Material	Electrical resistivity ρ (Ωm)
Quartz	2.0×10^{14}
Calcite	9.0×10^{13}
Dolomite	4.3×10^{13}
Biotite	8.3×10^{10}
Orthoclase	1.4×10^{12}
Aragonite	8.3×10^9
Kaolinite	3.2×10^7
Freshwater	$10^1 - 10^2$
Saline water	$2.3 \times 10^2 - 2.0 \times 10^1$

2.5 Formation factor

Electrical formation factor (FF) refers to the ratio of the electrical resistivity of a saturated medium (sediment or rock) to that of the saturating fluid (Guéguen and Palciauskas, 1994).

The formation resistivity factor is an intrinsic property of a porous insulating medium, related to the degree of efficiency and inefficiency of electrolyte-filled paths to conduct electrical current through the medium and is independent of the electrical conductivity of the electrolyte in its pores.

There is a difference between the conductivity of the sand matrix and the fluid saturating the sand. The model of a fluid-saturated sand is a two-component medium: the solid grains (volume fraction $1 - \Phi$ and conductivity σ_s), and saline water (volume fraction ϕ and conductivity σ_w ,

with a ration being $\frac{\sigma_s}{\sigma_w} \approx 10^{-10}$

The effective conductivity of sand saturated with fluid will be proportional to the conductivity of the fluid σ_w .

$$\sigma_{eff} = \frac{\sigma_w}{F} \quad 2.6$$

The formation factor F depends on the sand microstructure and the ratio $\frac{\sigma_s}{\sigma_w}$ and is essentially

zero for clean sand; therefore, the formation factor is only a function of porosity.

Formation factor is an important parameter in exploration geophysics, which is contrary to the electrical resistivity of reservoirs which is dependent on the resistivity of the saturating fluid. Hence, the same type of reservoir can exhibit high or low resistivities (Mitsuhata et al., 2006; Constable and Srnka, 2007; and Jinguuji et al., 2007). The formation factor is independent of fluid salinity.

$$F = \frac{R_s}{R_w} \quad 2.7$$

and

$$R_s = r_s \frac{A}{L} \tag{2.8}$$

where F is the formation factor, R_s is the resistivity of the sand sample saturated with water, R_w is the resistivity of the water, r_s the measured resistance of the sand sample saturated with water, A the surface area of the electrode, L the length of the cell.

To obtain the formation factor, the sample's resistivity, once it has stabilized, is plotted against the saline water's resistivity, and the formation factor is obtained from the inverse of the slope.

2.6 Archie's law

The conductivity of a rock or sand is related to its porosity, such a relationship was proposed by Archie (1942). He worked in the laboratory on sands formations saturated with 0.34 to 1.74M NaCl and showed that F is related to porosity in the following manner

$$F = \phi^{-m} \tag{2.9}$$

and

$$\frac{R_f}{R_w} = \phi^{-m} \tag{2.10}$$

where F is the formation factor, ϕ is the porosity, R_f is the resistivity of the formation, R_w is the resistivity of water and m is the cementation factor. Archie initially proposed that $m = 2.0$; later it was found that the values varied with the type of formation

Equation 2.10 is only valid in fully saturated media.

Although equation 2.9 has a great and theoretically, better pedigree, equation 2.10 is the version that is commonly applied because it fits experimental data.

Porosity controls the resistivity factor, and the type of formation does not have a significant effect. Authors like [Jones and Buford \(1951\)](#), [Lynch \(1962\)](#), [Diment et al. \(1959\)](#), [Keller and Frischknecht \(1966\)](#) and [Keller \(1971\)](#) modified Archie's Law for use in porous media which were saturated with water.

[Keller \(1971\)](#) precisely recognized that the modified Archie's Law expressions apply only when the sand is fully saturated with water.

The interpretation of logging data is based on Archie's law, (equation 2.11) which is an empirical correlation of the electrical resistivity index and its brine saturation. Archie's law

indicates that the resistivity index is only a function of the conductivity phase saturating the formation.

[Sweeney and Jennings \(1960\)](#) also conducted laboratory experiments and show that although Archie's law is widely used, it is not always valid this is because clay content affects the resistivity of the porous media.

The saturation of sand can be partial when the whole pore spaces are completely filled up with water and air. Archie investigated the work of other researchers on partially saturated sands and he found that bulk resistivity of a sand R_t partially saturated with aqueous the fluid, the of resistivity R_w is directly proportional to the resistivity of the rock when fully saturated with the same fluid.

$$R_t = IR_0 \quad 2.11$$

The constant of proportionality I is the resistivity index that describes the effect of partial saturation of the sand. If the sand is fully saturated, $I = 1$ and if the sand is not fully saturated with conductive fluid, $I = \infty$. The resistivity index, therefore, varies between one and infinity depending upon the degree of saturation of the sand.

Archie observed that the following relationship exists empirically

$$I = S_w^{-n} \quad 2.12$$

where: S_w is fractional water saturation of the sand, I is the resistivity index, and n is the saturation exponent. Combining the equations 2.11 and 2.12

$$R_t = R_0 S_w^{-n} \quad 2.13$$

2.7 Full saturation

The sand samples in the laboratory experiment were assumed to be fully saturated; however, this was not so especially at the beginning of each sample experiment when the sand was loose. Air bubbles are trapped in the sand sample during packing; however, the air bubbles are gradually removed, becoming fewer or none at all, mostly at the end of the experiment with each sample achieving lower porosity. Fluid saturation is defined as the ratio of the volume of fluid in a given sand sample to the volume of the sand sample ([Torsæter and Abtahi, 2000](#)). Saturation is full when all the pore spaces are fill with a fluid (water) without air, given as:

$$S_w = \frac{V_w}{V_p} \quad 2.14$$

where S_w = fluid saturation, V_w = Volume of the fluid, and V_p = Volume of the pore.

The accepted formation that relates water saturations and true resistivity is that of Archie given as

$$S_w = \sqrt[n]{\left(\frac{R_w}{R_t} \frac{a}{\phi^m}\right)} \quad 2.15$$

where S_w is fluid saturation, R_w is the resistivity of water, R_t is the true resistivity, a is a unique property and n is the saturation exponent.

The saturation exponent is an empirical constant that related to the connectivity of the electrically conductive phase, that is, water that saturates the sand samples.

Although Archie's Law is generally used to determine fluid saturation from resistivity measurements, it is not always correct because the saturation-resistivity relationship depends on the saturation history, wettability, salinity of the brine phase, the content of clay minerals well as the distribution of water in the sand (Liu and Moysey, 2012).

Schwartz et al. (2009) predicted σ_0 response to the saturation ratio and temperature assessed by fitting an empirical equation to measured electrical conductivity data Figure 2.7. They show experimentally that there was low, medium and high electrical conductivity of samples with 8°C, 22°C, and 40°C respectively.

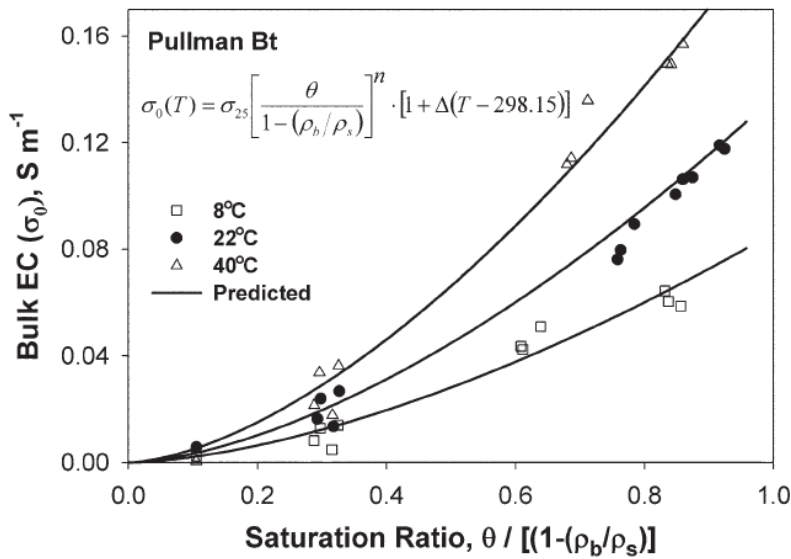


Figure 2.7: Predicted and measured bulk electrical conductivity σ_0 response to sand water saturation and temperature (T) (Liu and Moysey, 2012).

The Young- Laplace equation implies that conductance distribution is effectively truncated at the largest water-filled pore.

$$W_p(g/x, \theta) \propto \frac{1}{b} Ei \left[a \left(\frac{x}{L} \right)^b \left(\frac{\beta - \phi + \theta - \theta_t}{\beta - \theta_t} \right)^b \right] \quad 2.16$$

where θ_t critical volume fraction (expressed moisture content) percolation, x is the system length path through an interconnected cluster of conductance with arbitrary minimum value, L is quantity related to correlation length, b is $2/\nu$ and ν is the discrepancy of correlation length in percolation theory of [Aharony and Stauffer \(2003\)](#), g is controlling conductance, and p is fractional water content. The additional saturation-dependent factor in the disagreement of the exponential integral is provided by scaling the argument that makes the factor equal to 1 at saturation and allows for the divergence of correlation length when $\beta = \phi$ and moisture content takes on its critical value. Note that $W_p(g/x; \theta)$ is defined by equation (2.19) only between bounds g_{\max} and g_{\min} . In keeping with a notation that expresses all quantities in terms of critical conductance, these values are:

$$g_{\max} = g_c \left[\frac{\beta - \theta + \theta}{\beta - \phi + \theta - \theta_t} \right]^{3/(3-D)} \quad 2.17$$

$$g_{\min} = g_c \left[\frac{\beta - \theta}{\beta - \phi + \theta - \theta_t} \right]^{3/(3-D)} \quad 2.18$$

Results for the saturated case is obtained by substituting $\theta = \phi$. In the limit of zero moisture content, $g_{\max} = g_{\min}$, even though equations 2.20 and 2.21 really apply only for θ and θ_t .

The saturation exponent normally has a range of values from 1.8 to 2.0, however much lower and much higher values have been found by [Guichet et al. \(2003\)](#) who found a value of 1.3 for water saturation of sand Figure 2.8.

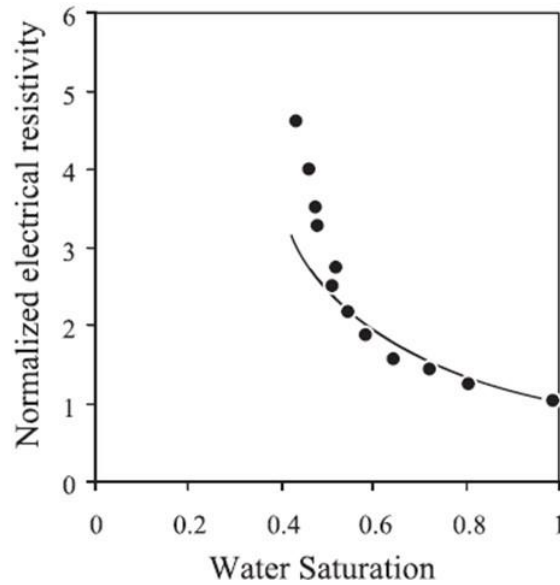


Figure 2.8: Normalized electrical resistivity of sand as a function of water saturation. The curve fit to Archie's second law leads to $n = 1.3$.

My experimental study on the dependence of saturation and apparent resistivity is hinged on the assumption that the fluid distribution within the sample was homogeneous.

2.8 Frequency dependence

The following complex conductivity measurements offer an advanced method for the separation of electrical volume and interface effects:

A Vinegar and Waxman (1984) and Börner et al. (1991) for low-frequency range ($f < 10\text{kHz}$) following Induced Polarization (IP),

B Kulenkampff and Schopper (1988) for frequencies above 1Khz.

Frequency-dependency of sand conductivity

$$\sigma^* = \sigma'^* + i\sigma''^* = \sigma + i\omega\varepsilon \tag{2.19}$$

Can be approximated by a power law for the frequency range between 10^3 and 10^4 Hz (Börner et al., 1991, Börner, 1992).

$$\sigma^*(\omega) = \sigma'^*(\omega) + i\sigma''^*(\omega) = \sigma_n \cdot (i\omega_n)^{1-p} \tag{2.20}$$

where

$\sigma^*(\omega)$ frequency-dependent conductivity,

σ^* Conductivity amplitude at frequency $\omega = 1\text{Hz}$; real and imaginary component:

σ_n Real component of conductivity at frequency $\omega = 1\text{Hz}$, volume (electrolytic) conductivity combined with real component of interface conductivity at frequency $\omega = 1\text{Hz}$

σ_n "Imaginary component of conductivity at frequency $\omega = 1\text{Hz}$; imaginary component of interface conductivity at frequency $\omega = 1\text{Hz}$

$$\omega_n = \frac{\omega}{\omega} = 1\text{Hz} \quad 2.21$$

(1-p frequency exponent [Börner et al., 1991](#). between 0.95 and 1)

This power law (equation 2.20) is identical to the frequency-independent phase angle typical for water absorbing systems ([Dissado and Hill, 1984](#)).

An investigation of [Börner et al., 1991](#) on sandstones in the frequency range between 10^3 - 10^4 Hz confirms the strong correlation between the imaginary part of complex conductivity and the specific surface area: in this range, the only source of internal capacity of the porous medium interface region. The double layer mechanism acts as the capacitor.

- Real conductivity is influenced by volume (electrolytic) and interface properties.
- Imaginary conductivity is part influenced by interface effects alone [Figure 2.9](#).

A determination of the porosity and specific surface area of reservoir rocks comes directly from complex measurements done.

$$\sigma_n' = \sigma_n \cdot \cos \left[\left(\frac{\pi}{2} \right) 1 - p \right] \text{ (Real part)} \quad 2.22$$

$$\sigma_n'' = \sigma_n \cdot \sin \left[\left(\frac{\pi}{2} \right) 1 - p \right] \text{ (Imaginary part)} \quad 2.23$$

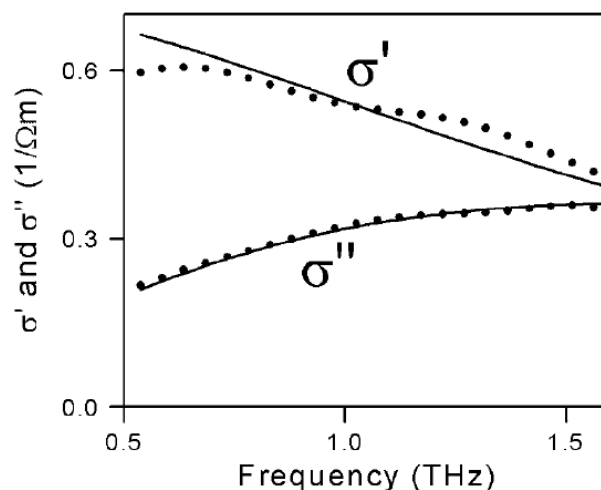


Figure 2.9: Frequency dependence of the real (σ') and imaginary part (σ'') of a pump-induced complex conductivity at room temperature after [Shan et al. \(2003\)](#).

The steps to derive fluid properties from a complex data frequency domain are presented in [Figure 2.10](#) after [Börner et al., 1991](#).

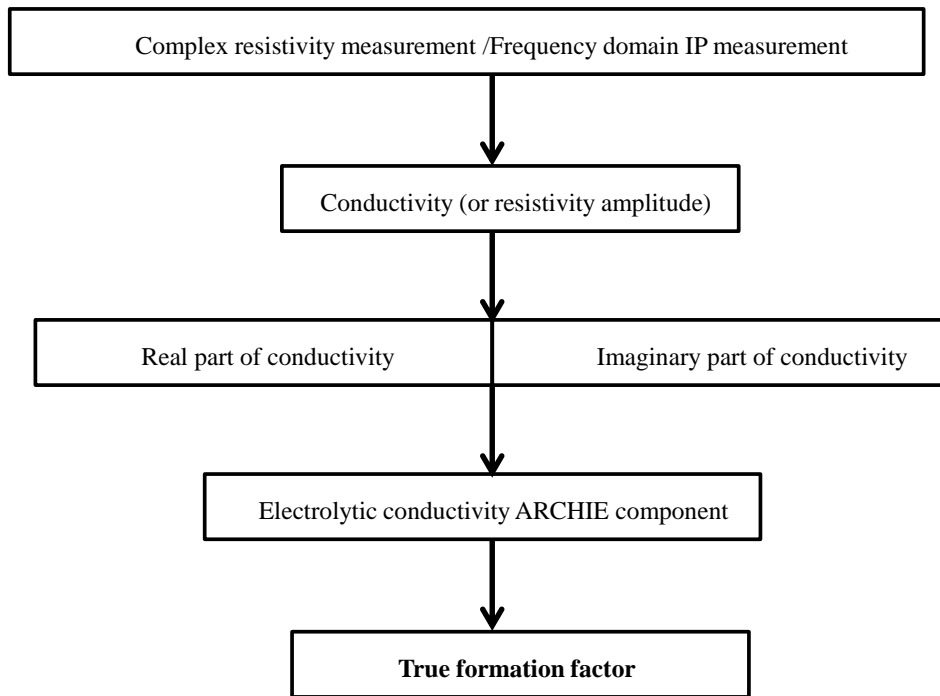


Figure 2.10: Scheme to drive pore and fluid properties from complex electrical data or frequency domain IP data using constant phase angle model after [Börner et al., 1991](#).

Based on complex resistivity spectrum for measurement between 10^{-3} - 10^6 Hz [Olhoeft \(1985\)](#) found a significant indication of different electrochemical reactions, in particular, clay-organic reaction. The low frequency, complex electrical conductivity was influenced by changes of the interface properties; as a result, there was contamination. Similarly, [Börner et al. \(1993\)](#) studied the influence of various contaminants on complex electrical conductivity, and found the interface is very sensitive to changes in the pore fluid. They show the influence of contaminants with respect to the level of conductivity components and the shape of the frequency dependence. The sensitivity of the electrical properties particularly at lower frequencies is the physical basis for the detection of contamination for induced polarization measurements.

The low-frequency power law of conductivity (equation 2.20) changes for frequencies above 10Hz, to another power law with an exponent $1 - \alpha$ which is higher than $1-p$. Low-frequency dependence of the conductivity is controlled by “large structures” of the pore space (conductivity, tortuosity) and thus, permeability. The high-frequency dependence of the conductivity is controlled by “small structures” of the pore space (pore wall morphology and clay particles).

2.9 Effect of surface conductivity

The electrical properties of sand depend on its composition, microstructure and interfacial effects; this includes the bulk properties of the sand and the geometry of the constituents of the sand. The electrical conductivity of saturated sand results from the conduction through the bulk solution occupying the pores as well as the conduction occurring at the fluid grain interface. The three separate phases found in a porous medium are the grains, the fluid-filled pores and the interfacial region that is in most cases not considered. The fluid-mineral interaction is an interfacial effect which is particularly important for electrical properties of clayey samples (Olhoeft et al., 1987). Surface electrical conductivity in rocks is an important parameter commonly used in characterizing hydrocarbon reservoirs Waxman and Smits (1968). The effect of the specific surface conduction can be from contributions of (a) conduction within the diffuse electrical layer, which is so small and can be neglected in the total specific surface conductance; (b) conduction in the Stern layer, which has been shown to vary significantly with the salinity of the pore fluid at low salinities; (c) a system operating directly on the mineral surface, independent of salinity. The macroscopic conductivity of a saturated porous medium with insulating grains results from two mechanisms: (i) bulk conduction, which corresponds to electron migration of the ions in the interconnected pore space, and (ii) surface conduction, which corresponds to electrical conduction near the fluid-grain interface e.g. (Pride, 1994; Revil and Glover, 1997). The surface of a grain, when it is in contact with an electrolyte, is typically charged with specific conductance of quartz (8.9×10^{-9} S) while the conductivity of clay is (2.5×10^{-9} S). The effect of surface conductivity was studied by researchers like Archie (1942); Waxman and Smits (1968); Johnson and Sen (1988) and Knight and Nur (1987). The existence of a rough interface can produce a local reduction of the strength of the electric field in the vicinity of the mineral surface which modifies the contribution of the interfaces to the total electrical conductivity (Schwartz et al., 1989).

When an electrolyte is exposed to a solid mineral surface, either there will be an electrochemical reaction where a double-layer is formed. When the mineral grain has an unbalanced structural charge, a layer of excess ions develops in response to the local potential (clay particles for instance) that are negatively charged, hence, in solution, they attract an excess of cations. This creates what is refer to as the “double layer”, composed of the fixed negative charge on the clay particle and the mobile positive charge in a thin solution layer adjacent to the interface (Figure 2.11). Far away from the surface, the densities of both positive and negative ions are equal.

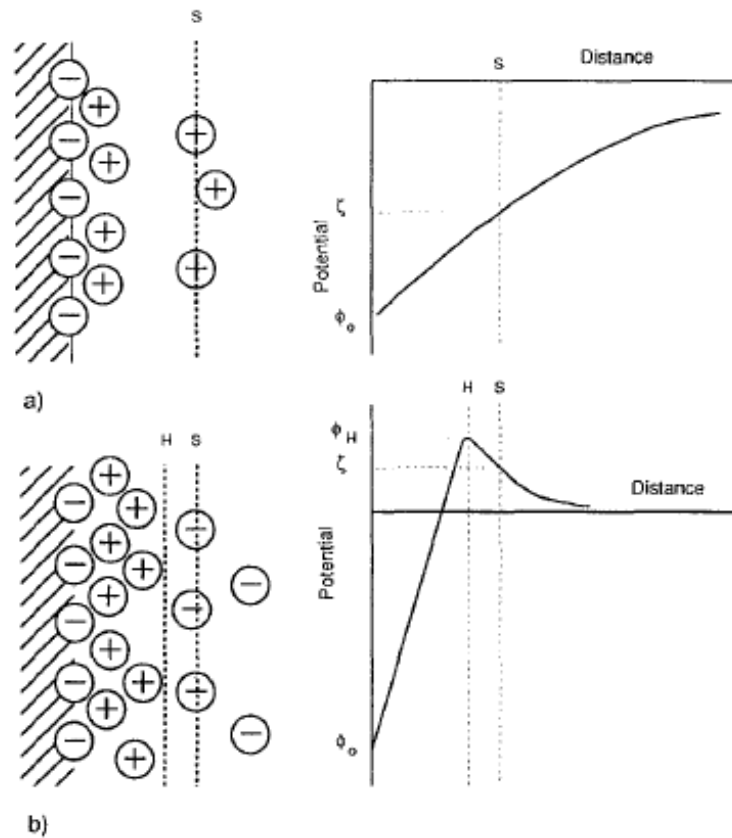


Figure 2.11: The electrical double layer (a) Gouy-Chapman model (b) Stern Model after [Ruffet et al. \(1995\)](#).

Conductivity will depend on frequency when there is diffusion, or when the diffusion occurs through a double layer, and the dependency will have an effect only at very high frequencies since the time constant to establish the double layer is very short unless the surface is rough.

The second conductive component was first detected and described for sandy clay by [Patnode and Wyllie \(1950\)](#). They found that Archie's relationships did not apply to sandy clay; it was apparent that the current was carried through a medium other than the saturating solution. They called this additional conduction "conductive solids" which include wet clay components in the form of disseminated particles. Clay and grain surface phenomena create a "double layer or interface conductivity" and electrical double-layer (Stern model). The two components are combined into a parallel conductor system Figure 2.12.

$$\sigma_{shalyrock} = \sigma_{electrolytic} + \sigma_{clay} = \frac{\sigma_{water}}{F} + \sigma_{clay} \quad 2.24$$

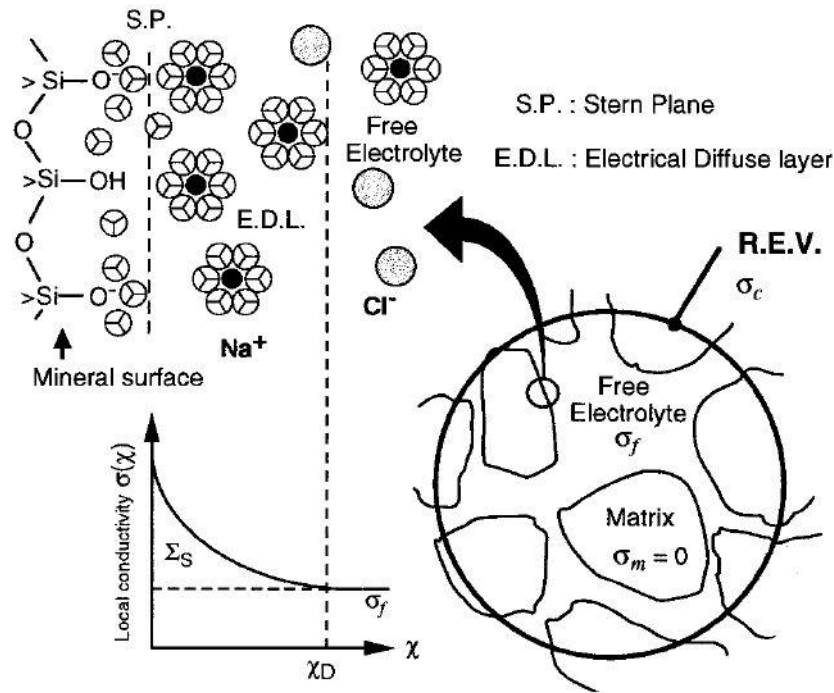


Figure 2.12: Schematic representation of the electrical double layer situated at the mineral surface (Revil and Glover, 1997).

When thermodynamic conditions are different from the electrical diffuse layer (EDL) condition, the mineral surface S gets an excess of charge through ionization reactions. This excess charge is balance by mobile ions in an electrical diffuse layer. The parameter σ_c is the effective electrical conductivity of a representative elementary volume (R.E.V.), whereas σ_f and σ_m are the free electrolyte and matrix conductivities respectively. The counterion of the electrical diffuse layer are maintained at some distance from the mineral surface by the water adsorbed on the surface forming the “Stern layer”, and a hydration shell around each the cation. The Stern layer and the diffuse layer comprise the so-called “double layer”. (Figure 2.12). This double layer formation is due to the presence of clay - e.g. Kaolinite in this research work - and is dependent on the cation exchange capacity (CEC), the cation exchange capacity (CEC) is the total capacity of a porous media to hold exchangeable cations. CEC is an inherent porous media characteristic and is difficult to alter significantly and sands with higher clay fraction tend to have a higher CEC.

2.10 The case of clay sand

The preceding discussion pertains to the case of clean sand, but in the case of shaly sand there, is an additional charge carrier in the fluid phase. The presence of conducting minerals example kaolinite changes the pore surface conduction, producing a second conducting component and therefore, Archie's equation must be modified. (Equation 2.23) (e.g. Kaolinite in **Error! Reference source not found.** and **Error! Reference source not found.**).

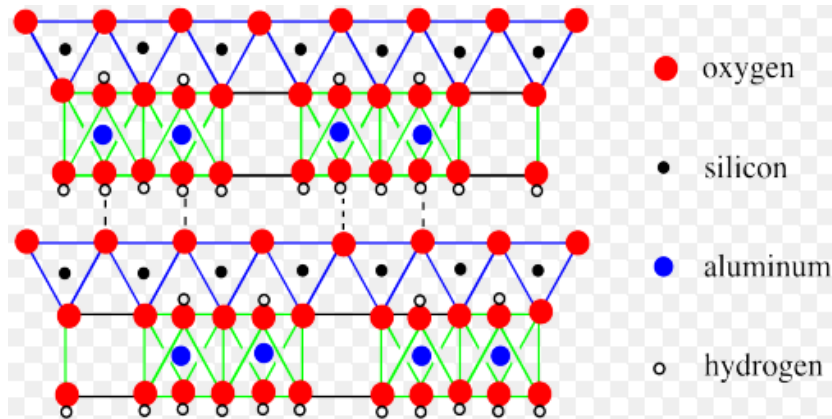


Figure 2.13: 2D Schematic representation of structure and composition of Kaolinite clay minerals.

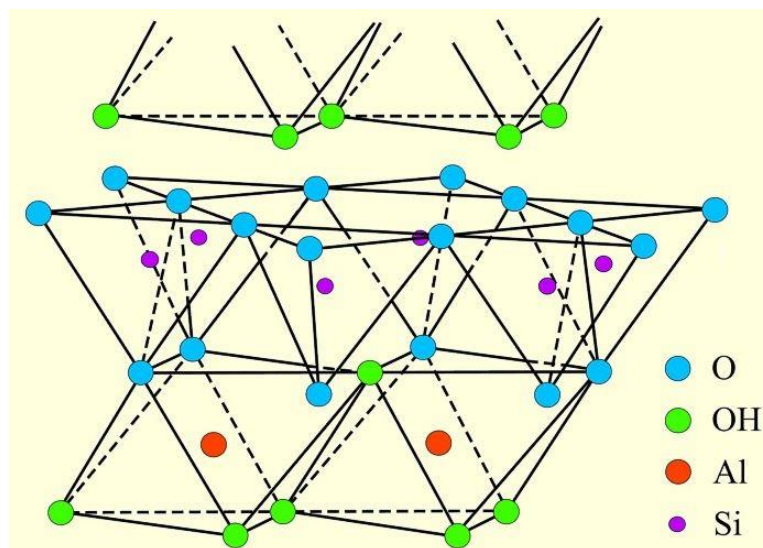


Figure 2.14: 3D Schematic representation of structure and composition of Kaolinite clay minerals.

Clay minerals have negatively charged sites on their surfaces that absorb and hold positively charged ions (cations) by electrostatic force. When an atom or molecule loses or gains one or more electrons, then it turns into either a positive (cation) or negative (anion) electric charge respectively. The common cations found in solutions are hydrogen (H^+) and sodium (Na^+) as

in the case of my research work, but other ones include potassium (K⁺), calcium (Ca²⁺), magnesium (Mg²⁺), ammonium (NH₄⁺) and aluminium (Al³⁺).

There are many models of the physical explanation of clay conductivity based on the double layer proposed by researchers like [Winsauer and McCardell \(1953\)](#), [Guyed and Wichmann \(1971\)](#), and [De Witte \(1955\)](#). But the two most popular models are the ones proposed by [Waxman and Smits \(1968\)](#) and [Bulling and Breyer \(1989\)](#).

[Waxman and Smits \(1968\)](#) published their theory and model for sandy clay. In this model, the “electrical current associated with clays travels along the same tortuous paths as current attributed to ions in pore water”. This results in relationship with unique formation factor F

$$\sigma_0 = \frac{1}{F} \cdot (\sigma_w + B \cdot Q_v) \quad 2.25$$

Or in terms of resistivities

$$\rho_0 = F \cdot \rho_w \cdot (1 + B \cdot Q_v \cdot \rho_w)^{-1} \quad 2.26$$

The empirical parameter (counterion mobility) after [Waxman and Thomas \(1974\)](#) describes slight interface conductivity dependence on salinity.

$$B = 3.83 * \left[1 - 0.83 * \exp\left(\frac{-0.5}{\rho_w}\right) \right] \quad 2.27$$

Clay parameter Q_v , is related to the cation exchange capacity (CEC) by

$$Q_v = \frac{1 - \phi}{\phi} \cdot \frac{d_s}{100} \cdot CEC \quad 2.28$$

where d_s is the solid grain density (in g/cm³) and ϕ porosity; cation exchange capacity CEC is in milliequivalents per 100g of sand and measured in the laboratory. The cation exchange capacity is the ability of sands to hold positively charged ions or the total capacity of the sands to hold exchangeable cations; different materials have different cation exchange capacities. Table 2.5 gives the cation exchange capacity of different clays after [Keller and Frischknecht \(1966\)](#) while table 2.6 gives the cation exchange capacity of various soils after [Olhoeft \(1981\)](#). Table 2.5 and Table 2.6 show the cation exchange capacity of kaolinite and quartz (the concern of this research work) below.

Table 2.5: Table of Cation exchange capacity of various clays: [Keller and Frischknecht \(1966\)](#)

Clay type	Kaolinite	Mica	Chlorite	Montmorillonite	Vermiculite
Cation exchange capacity (meq/100g)	3-15	10-40	10-40	80-150	100-260

Table 2.6: Cation exchange capacity (CEC) and colloid content of five soils of different textures After: McNeill (1980)

Soil type	Organic matter in %	Clay in % by weight	CEC in meq/100g
Sand	1.7	7.0	6.3
Sandy loam	3.2	13.2	13.7
Loam	4.9	16.8	20.2
Silt loam	5.4	18.4	24.0
Clay loam	5.5	31.2	27.2

Bulling and Breyer (1989) showed that in dispersed clay, electric current flowed through a mixture of pore water and dispersed clay in pores as:

$$F_{im} = \frac{a}{\phi_{im}^m} \quad 2.29$$

and the specific resistivity of a water clay mixture parallel model (weighted arithmetic mean for conductivity) is applied:

$$\rho_{slurry} = S_{sim} \cdot \left(\frac{S_{sim} - q}{\rho_w} \right) + \left(\frac{q}{\rho_{clay}} \right)^{-1} \quad 2.30$$

where ρ_w is formation water resistivity and ρ_{clay} resistivity of the dispersed clay.

ϕ_{im} = intermatrix porosity, which includes the space, occupied by fluids and dispersed clay.

S_{im} = the fraction of the intermatrix porosity occupied by the formation-water, dispersed clay mixture.

q = the fraction of intermatrix porosity occupied by the dispersed clay.

Then the conductivity of the dispersed clay results is

$$\sigma_{dis} = \rho_{dis}^{-1} = (\rho_{slurry} \cdot F_{im})^{-1} = \frac{\phi_{im}^m}{a \cdot S_{im}} \cdot \left(\frac{S_{im} - q}{\rho_w} + \frac{q}{\rho_{clay}} \right) \quad 2.31$$

Cation exchange capacity is a typical property of clays and relates to the clay mineral structure. Because of the geometric nature of these fundamental structural units, structures are sheetlike, one type consists of octahedral units of oxygen or hydroxyl around a central atom (usually aluminium), and the other type is tetrahedral unit composed of a central silicon atom surrounded by oxygen (Figures 2.13 and 2.14). The fluid-mineral interaction is an interfacial effect which is principally significant for the electrical properties of clayey sand samples Olhoeft et al. (1987).

The two phenomena that relate to the physical properties of clay are:

- 1 The presence of water trapped between “plates” with its influence on conductivity and porosity measurement are not part of effective porosity.
- 2 The presence of a strong negative surface charge with the ability to absorb ions (e.g. radioactive ions) creates a double layer of pore fluid.

The capacity of the clay minerals to form an electric double layer is the basis for cation exchange phenomena. During the mixing of saline water and clay, positive charges (cations) are absorbed on the clay’s surface. Cations (Ca, Mg, H, K, and Na) are loosely held on the surface and can subsequently be exchanged for other cations or essentially go into solution should the clay mix with water. For this reason, they are called “exchangeable ions” and the cation exchange capacity is a measure of the number of cations that are required to neutralize the clay particle as a whole; that is, the weight of ions in milliequivalent absorbed per 100 grams of clay.

When evaluating adsorption, the specific surface area of sand grains is usually not of much interest compared to that of clays contained in the sand. Table 2.7 gives the range of specific areas expected from clays by [Corey \(1994\)](#).

The effect of the surface area is, therefore, negligible in my research work because I used kaolinite that has the least surface area effect as can be seen from 2.7

Table 2.7: Specific surface area of different clay types after [Corey \(1994\)](#).

Clay type	Area m ² /gram
Kaolinite	45
Illite	175
Montmorillonite	800

2.11 Representative Element Volume (REV)

There are many scales of interest in different fields, and virtually all materials are heterogeneous when the scale of observation is small enough. Discrepancies manifest when the physical properties (e.g. porosity and formation factor) are of multiple levels when considered, thereby the smaller scale and larger scale denoted by microscale and macroscale respectively. Of particular interest in this research work are the variables that are associated with representative elemental volume. There is a linear relationship between grain size and representative elemental volume (REV); in the coarse grain sample under investigation (Scarborough), the REV is large, while the fine grain sample (Cottesloe) has small REV.

Although many researchers try to define the representative elemental volume, prominent among them are:

[Drugan and Willis \(1996\)](#); [Freudenthal \(1950\)](#); [Hashin \(1983\)](#); [Ostoja-Starzewski \(2002\)](#)

- An imaginary unit that represents or define an arbitrary probability of the heterogeneity of the actual material. In the presence of n independent geometrical parameters (e.g. porosity), there will be n values for the representative cells since each geometrical parameter has a separate scale homogeneity ([Freudenthal, 1950](#)).
- The model of material used to determine the corresponding effective properties for the homogenized macroscopic model. It should be large enough to contain sufficient information about the microstructure. However, it should be much smaller than the macroscopic volume ([Hashin, 1983](#)).
- The smallest material volume element of the composite for which the usual spatially constant property representative is a sufficiently accurate model to represent a mean constitutive response ([Drugan and Willis, 1996](#)).
- Define the representative elemental volume in two situations: (i) unit in a periodic microstructure, and (ii) volume containing the large (mathematically infinite) set of microscale elements possessing statistically homogeneous properties ([Ostoja-Starzewski, 2002](#))

To measure the density of the collection of a granular sand sample at a point a at a time t on one dimension is achieved by using a sampling length x centred at a and measuring the mass m of the sand sample in this interval. The density can be computed by equation 2.32 after Roberts (1994).

$$(L; a, t) = \frac{m(L; a, t)}{L} \tag{2.32}$$

The density computed will be a function of not only portion but also the sampling L as shown qualitatively in Figure 2.15. This graph has three distinct regions: the microscopic region (I) is characterized by fluctuations of readings and region II (the representative elemental volume region) is essentially constant. The representative elemental volume (REV) is assumed to be sufficiently large so that fluctuations are smooth but sufficiently small so that macroscopic changes do not affect the result ([Bear, 1972](#)). In this research, I determine the representative elemental volume (REV) by evaluating both the formation factor and porosity as a function of cube sizes. The starting formation factor and porosity value vary a lot (due to the heterogeneity of the selected cube sample). However, it is convergent upon the growth of the sample volume

until the formation factor and porosity become uniform (homogeneous). The homogeneity is achieved at different values depending on the grain size, and coarser grains tend to have larger values compared to fine grains.

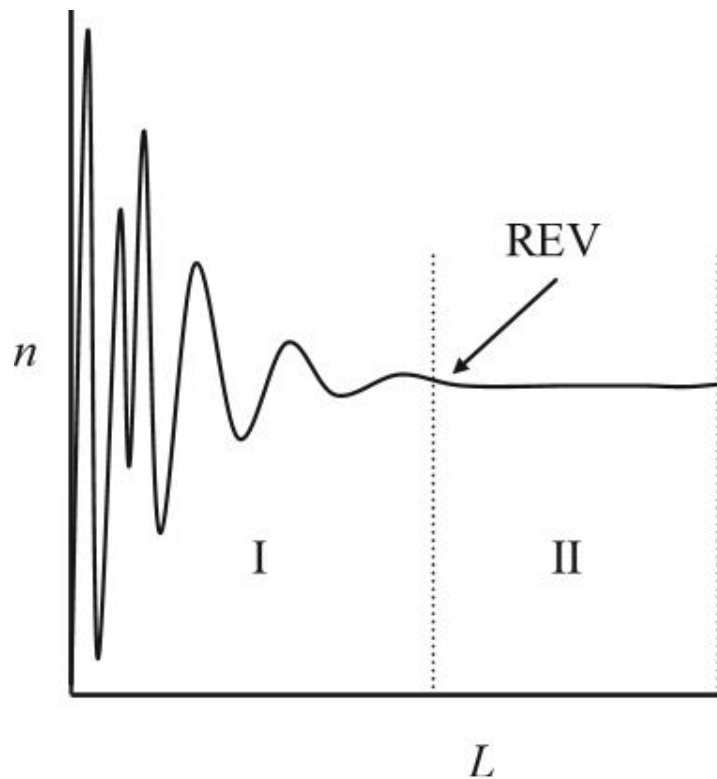


Figure 2.15: Representative elemental volume (REV) I domain of microscopic effects, II domain of REV

Figure 2.15 shows the fluctuations and tapering of a physical component like porosity and formation factor before and after reaching the Representative Elemental Volume (REV). The vertical dash lines give the minimum and maximum values of the Representative Elemental Volume of a media. n gives the physical property under consideration e.g. porosity and L gives the size of a cube picked at random. It is an important parameter for pore-scale numerical and statistical analysis. The microscopic porous medium may be defined by smooth porosity variation as a function of sample volume (cube size) (Dullien, 2012). Since there is no universally accepted measure for the size of REV, however, it is necessary to determine whether the data collected and analysed in this research satisfy the REV requirements. Although in the case of an increase in the size of the cube far beyond the REV, the uniformity or heterogeneity will be maintained, but it is essential to achieving the REV that is very important for getting an average properties of a homogeneous media. An example of cubes approaching the Representative Elemental Volume (REV) for three cubes cropped from a Cottesloe micro-CT scan image is shown in Figure 2.16, the REV is achieved from $(500)^3$.

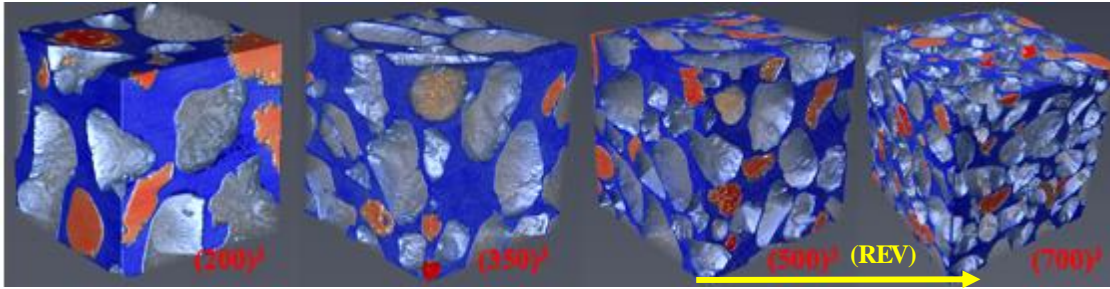


Figure 2.16: 3D cubes of $(200)^3$, $(350)^3$, $(500)^3$, and $(700)^3$ from the Cottesloe clay sand approaching REV.

Note that in the laboratory experiments, I use samples on the cm-scale for the determination of the formation factor and compare the formation factor with the formation factor from the micro CT-scan images generated from the three sets of images (one clean sand sample from Scarborough and Cottesloe and a clay sand sample from Cottesloe) on a μm scale. Therefore, because of the known heterogeneous nature of the samples, there is always a risk that the selected scanned area is not representative compared to the full sample size used in the laboratory measurements. Although there are three different lengths of scales that are made of pore scale (microscopic), local scale (macroscopic or lab) and field scales, but, one usually associates macroscopic variables with a representative elemental volume that is at a micro scale (Bear, 1972). What is the actual size of REV? Does the size of REV vary spatially even in a “homogeneous” medium? Are the REVs similar or significantly different for different quantities at a given location? In addition, how do macroscopic coefficients like porosity vary with scale?

2.12 Conclusion

I have presented the basic understanding and the concept of the properties of sand. The elements discussed includes the porosity of sand, the formation factor, Archie’s law (the underlying principle of my research), the dependence of these measurements on frequency and saturation, and the effect of clay on the sand. Clay sand and cation exchange capacity are discussed because both the laboratory and micro CT-scan measurements of clean and clay sand are considered. The other parameter discussed here is the representative elemental volume, which forms the main unit of upscaling the microscopic (micro CT-images) measurements to the macroscopic (laboratory) measurements. The essential tools so far discussed will clear the way for the research work to the next chapter that is generating a reliable data from the laboratory measurements.

Chapter 3

Presentation of samples and laboratory experiments

3.1 Introduction

In this chapter, I will be presenting the locations and collection of the three different sand samples of Two Rocks (five subsamples), Scarborough (two subsamples) and Cottesloe (one subsample) beaches. After presenting the sample collection, then I will present the two different sand sample preparations that involved the cleaning, drying, mixing and packing of the clean and clay sand samples into the cells. I will be presenting the grain size distribution of the sand samples as well as the preparation of the different solutions used in the experiments. The preparation of the shaly sand sample that included the drying and mixing of the sample is discussed here. Also presented here are the two different laboratory experimental setups called “flow cell” and “static cell” that I used in this research work, then the description of the instruments used in the laboratory experiment is also presented here.

3.2 Sand sample locations and collections

Eight sand samples were collected from the coastal margin of the Perth basin, Western Australia at 3 different beaches Figure 3.1. Five samples were collected from Two Rocks Beach, two samples from Scarborough Beach and one sample from Cottesloe Beach and their coordinates are presented in Table 3.1 below.

Table 3.1: The of coordinates for the sands samples collected

Beach	Northings	Eastings
Two Rocks	31°31'07.58"S	115°36'08.82"E
	31°30'54.54"S	115°35'57.66"E
	31°30'41.31"S	115°35'45.82"E
	31°30'26.79"S	115°35'31.25"E
	31°30'09.00"S	115°35'04.98"E
Scarborough	31°53'51.58"S	115°45'17.51"E
	31°53'51.87"S	115°45'17.99"E

Cottesloe 31°59'37.54"S 115°45'03.10"S

The sand samples collected were labelled clearly in a polythene bag and the sample was taken to the laboratory for keeping and preparation for laboratory experiments as in Figure 3.2

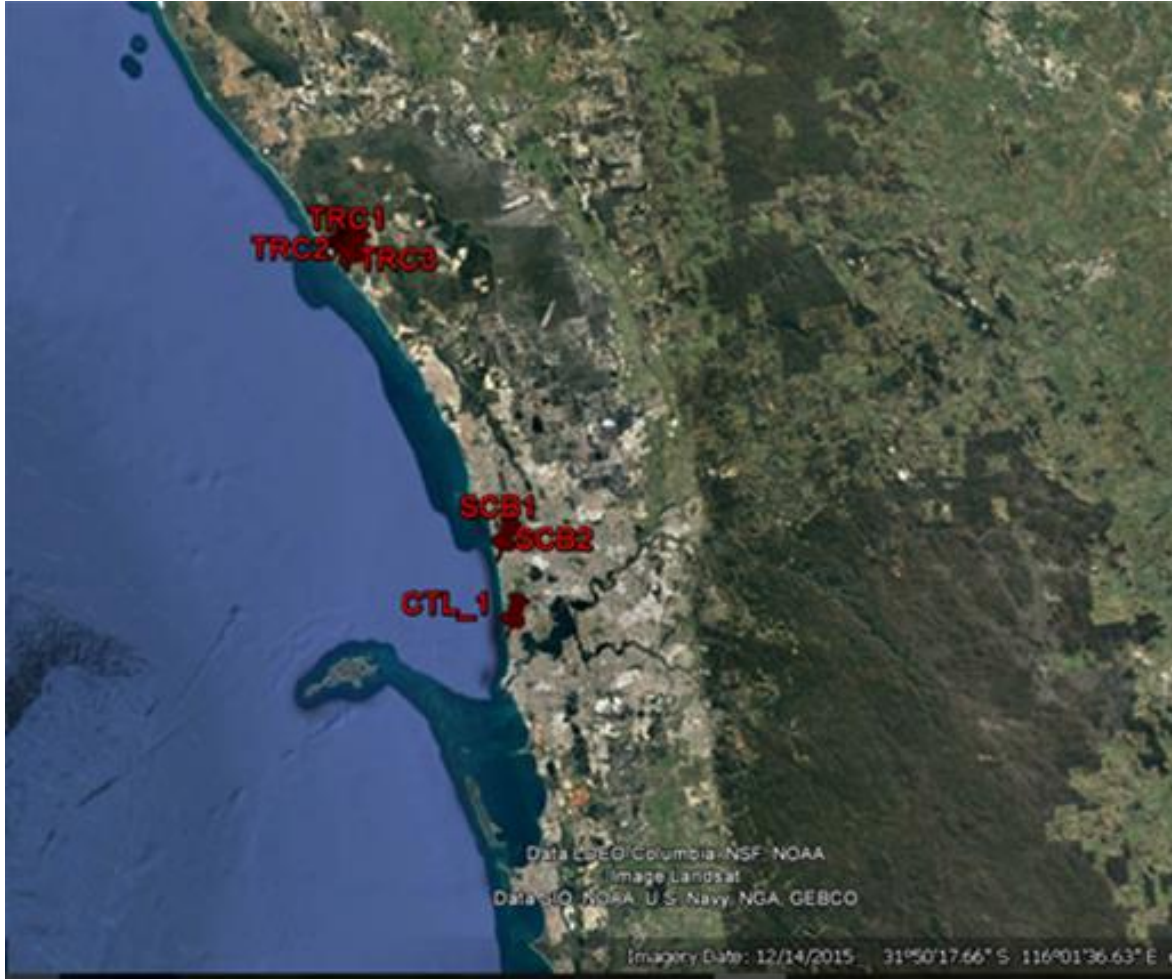


Figure 3.1: Sampling points. (TRC, SCB and CTL as Two rocks, Scarborough and Cottesloe Beaches



Figure 3.2: Putting the sample in a clearly labelled polythene bag

3.3 Sand sample description

3.3.1 Composition of Scarborough and Cottesloe sand samples

The clean sand samples of Scarborough and Cottesloe Beaches were composed of two solid materials (quartz and carbonate) with pore spaces while the clay sand sample of Cottesloe consists of materials (quartz, clay, and carbonate) in different proportions. The percentage distribution of the materials in the clean sand samples based on image segmentation is 67.3% and 16.3% for quartz and carbonate respectively in the Scarborough Beach clean sand sample, while the remaining 16.4% makes the pore; while the Cottesloe Beach clean sand sample has 66.7% and 17.1% of quartz and carbonate and the remaining 16.2% is the pore. The percentage distribution of materials for the Cottesloe clay sand is quartz 65.4%, carbonate 16.2%, and clay has 3.0% while pore occupies 15.4%. The details of the composition of the sand samples used in the research are discussed in chapter four.

3.3.2 Grain size distribution

To do the grain size analysis, I used Avizo Fire software. The diameter of the solid materials that make up the sand samples are: the clean sand of Scarborough has quartz with 16.1 μm , 794.0 μm and 120.0 μm minimum, maximum and average diameters respectively, and carbonate with 18.57 μm , 446.0 μm , and 168.3 μm diameters for minimum, maximum and average diameters respectively. The clean sand of Cottesloe has quartz with 15.26 μm , 606.4 μm and

159.2 μm minimum, maximum and average diameters respectively, and carbonate with 15.26 μm , 415.5 μm , and 172.8 μm diameters for minimum, maximum and average diameters respectively. The clay sand of Cottesloe has quartz with 14.2 μm , 740.2 μm and 196.3 μm minimum, maximum and average diameters respectively, clay with 15.6 μm , 375.2 μm , and 68.1 μm diameters for minimum, maximum and average diameters respectively, and carbonate with 14.5 μm , 519.3 μm and 172.9 μm minimum, maximum and average diameters respectively. A summary of the grain size analysis presented for the clean sands of Scarborough and Cottesloe Beach sand samples is presented in (Table 3.2 and Table 3.3), however, the details of the analysis are presented in chapter four.

Table 3.2: Summary of EqDiameter of materials of Scarborough and Cottesloe Beaches

Beach	Material	Range (μm)	Average (μm)	Grain size distribution range	
Scarborough	Pore	Min	18.57	0-100 (58)	
				101-200 (42)	
		Max	693.9	199.4	201-300 (48)
				301-400 (34)	
				401-500 (9)	
				>500 (3)	
	Quartz	Min	16.11	0-100 (267)	
				101-200 (42)	
		Max	794.0	120.0	201-300 (48)
				301-400 (27)	
				401-500 (14)	
				>500 (10)	
Carbonate	Min	18.57	0-100 (30)		
			101-200 (25)		
	Max	446.0	168.3	201-300 (20)	
			301-400 (11)		
			401-500 (4)		
			>500 (0)		
Cottesloe	Pore	Min	15.26	0-100 (87)	
				101-200 (123)	
		Max	415.5	172.8	201-300 (131)
				301-400 (28)	
				401-500 (2)	
				>500 (0)	
	Quartz	Min	15.26	0-100 (209)	
				101-200 (117)	
		Max	606.4	159.2	201-300 (113)
				301-400 (63)	
				401-500 (9)	
				>500 (1)	
Carbonate	Min	15.26	0-100 (65)		
			101-200 (54)		
	Max	415.5	172.8	201-300 (32)	
			301-400 (6)		
			401-500 (0)		

Table 3.3: Summary of EqDiameter of materials from Cottesloe clay sand

Beach	Material	Range (μm)	Average (μm)	Grain size distribution range		
Scarborough	Pore	Min	18.57	199.4	0-100 (58) 101-200 (42) 201-300 (48) 301-400 (34)	
		Max	693.9		401-500 (9) >500 (3)	
	Quartz	Min	16.11	120.0	0-100 (267) 101-200 (42) 201-300 (48) 301-400 (27)	
		Max	794.0		401-500 (14) >500 (10)	
	Carbonate	Min	18.57	168.3	0-100 (30) 101-200 (25) 201-300 (20) 301-400 (11)	
		Max	446.0		401-500 (4) >500 (0)	
	Cottesloe	Pore	Min	15.26	172.8	0-100 (87) 101-200 (123) 201-300 (131) 301-400 (28)
			Max	415.5		401-500 (2) >500 (0)
Quartz		Min	15.26	159.2	0-100 (209) 101-200 (117) 201-300 (113) 301-400 (63)	
		Max	606.4		401-500 (9) >500 (1)	
Carbonate		Min	15.26	172.8	0-100 (65) 101-200 (54) 201-300 (32) 301-400 (6)	
		Max	415.5		401-500 (0)	

3.4 Sample preparation

In this research work. I studied two types of unconsolidated porous media: clean beach sands from Two Rocks, Scarborough, and Cottesloe Beaches of the Perth basin (WA) and clean sand from Cottesloe beach mixed with 10% and 3% by weight of pure clay (kaolinite).

3.4.1 Cleaning

The sand samples collected from the field were washed clean to remove plant and grass particles as well as the salt from the sea (Figure 3.3). I started my experiment with very low

salinity of either fresh water as in the case of the clean sand and deionized water as in the case of the clay sand. Failure to clean the sand very well with tap water results in a decrease in the resistance of the sand instead of an increase (note: this decrease in resistance during some of the experiments are shown in chapter four during presentation of results).



Figure 3.3: washing the sand sample in the laboratory

3.4.2 Drying

The sand sample collected was washed with tap water and is allowed to dry in the sun for two days. As the sand was drying in the sun, I mixed the sand by hand regularly to dry it fast. However, during rainy days it takes more than two days to dry. Figure 3.4 shows the picture of drying the sand in the sun.



Figure 3.4: Drying the sand in the sun

3.4.3 Packing

The dry sand sample was moistened to allow good packing into the cell. At the beginning of the experiment, I made a loose packing to have high porosity so that I could decrease the porosity after each experiment as shown in Figure 3.5. The packing was possible with the help of sticks manually tied together (Figure 3.5). The decrease in porosity was achieved by gently shaking the cell to reposition the sand grains, and then I added measured dry sand to fill up the space made because of the shaking. The shaking, measuring the dry sand, and refilling the cell by adding the measured dry sand was done as many as four to six times depending on the sand sample; this allowed me to get measurements at different porosities up to six times.

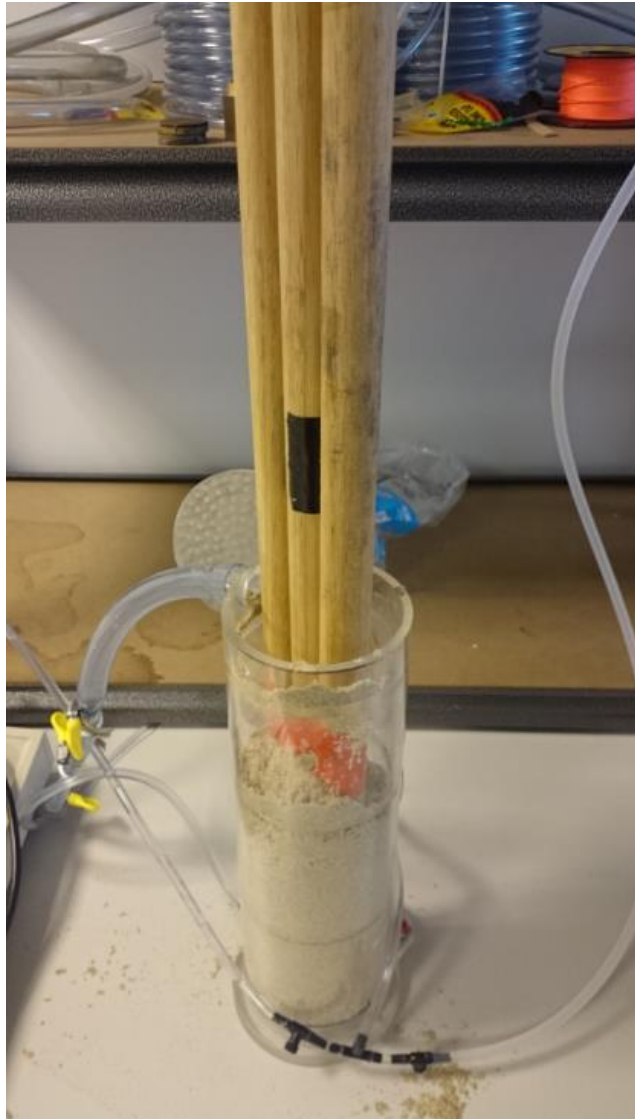


Figure 3.5: Packing the sand sample loosely in the cell to achieve high porosity.



Figure 3.6: Sticks used for packing the sand.

At the beginning of each experiment, the weight of the dried sand sample was measured using the electric balance. To change the porosity (reduce the porosity) as described in Figure 3.5, the weight of all the dry sand added during each porosity change was recorded. At the end of

each experiment of each sample, the sand sample compacted in the cell was carefully taken out of the cell, dried in the sun and the weight of the sand was measured again using the electric balance as in Figure 3.7 (this serves as a check for the weight of the measured sand added).

The porosity is calculated using

$$\phi = \frac{V - \frac{m}{\rho}}{V} \quad 3.1$$

where ϕ is the porosity, V is the volume of the cell used (cm^3), ρ is the density of the sand ($2.7\text{g}/\text{cm}^3$) and m is the mass of the dry sand (g).

From above, both the volume and the density of the sand sample remains the same in the two different cells used except the mass of the dry sand that keeps changing as the porosity is reduced (as earlier mentioned by gently shaking the sand).



Figure 3.7: Weighing balance taking a measurement of dry sand

3.5 The case of clay sand mixtures

The clay (kaolinite) with sand sample for the experiment was prepared in three steps

- Washing the sand
- Drying the sand and clay
- Mixing the sand with clay

The sand sample collected from the Cottesloe beach was cleaned with tap water to remove dirt, leaves and sea salt from the sand just like the way I cleaned the sand during the clean sand preparation as shown in Figure 3.3.

At first 10g of clay by weight of the sand was prepared but after performing the experiment for about 65 days, the result was bad, especially at higher salinities of 25mg/l and 35mg/l. This

might have been due to there being too much clay, or the problem might have been from the frequency selected during the experiment (100Hz). Another sample of 3% of clay by weight of the sand was prepared with the Cottesloe sand and this experiment was at a frequency of (1 KHz). The Kaolinite used in the experiment was dried for 72 hours in an oven at a temperature of 106°C as shown in Figure 3.9. Subjecting the Kaolinite clay to 72 hours' drying in an electric oven at a temperature of 106°C was to remove all the hygroscopic water in the clay. The hygroscopic water attached to the Kaolinite clay is shown in Figure 3.8 after Saarenketo (1998). The weighted kaolinite clay was mixed manually with the washed dried clean sand by hand for about 1 hour.

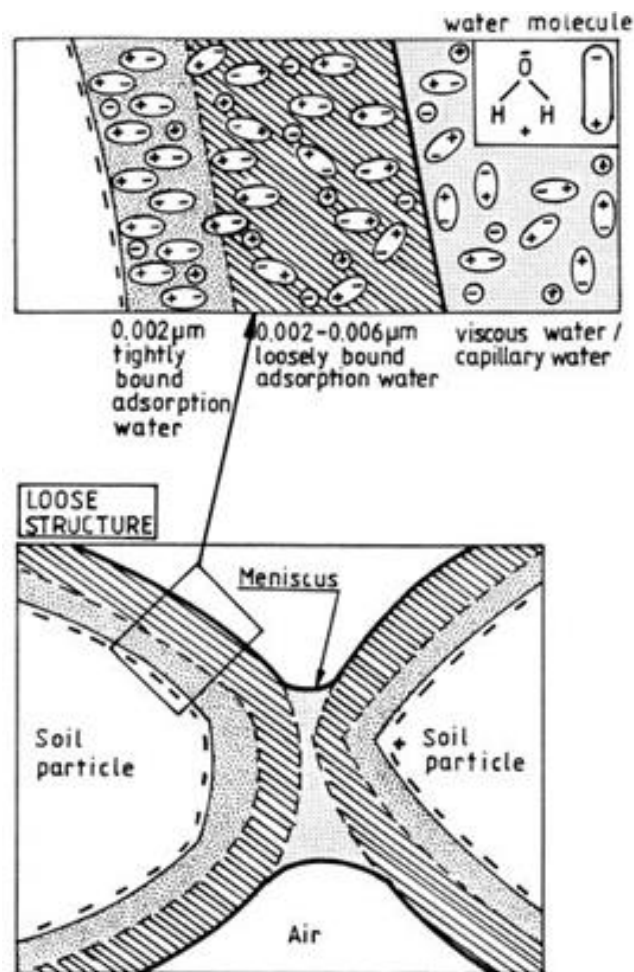


Figure 3.8: Hygroscopic (adsorption) water after Saarenketo (1998)



Figure 3.9: The pure kaolinite clay and the drying of the pure kaolinite clay

I used the static cell for the experimental set up of the clay sand. Although the same saline water was used for the clean sand, for the clay sand experiment, I used deionized water first, before replacing it with freshwater, this is because I wanted to recognize the effect of the clay on the conductivity of the sand, which can be observed only at a very low salinity. However, in the clay sand experiment, part of the clay is washed out of the cell during the draining of the saline water from the static cell for conductivity measurement of the water.

The edges of the static cell and its cover must be sealed completely with Sellotape and a weight placed on top of the cell to prevent the drying of the sample, because it takes a longer time (70 days) for the experiment to be completed (Figure 3.10).



Figure 3.10: Static cell showing sealed cover with weight on top to prevent evaporation

The description of correction in the clay sand mixture was discussed in chapter 2 under the heading “The case of clay sand”.

3.6 Injected solutions

I used deionized water and table salt (NaCl) for the preparation of the different saline solutions used in this research work. Deionized water, fresh water, 5.0mg/L, 15.0mg/L, 25.0mg/L and 35.0mg/L saline water were used to saturate the sand samples for the experiment. To get the respective saline water for the experiment, an amount of weight in grams of table salt was measured and the salt was mixed with an equal amount of tap water to produce the required salinity. As an example from the laboratory, I added 10.0g of salt to 2 litres of tap water to get 5.0mg/L of saline water (Figure 3.11).



Figure 3.11: Measuring the volume of water and measuring 10 mg of table salt

3.7 Laboratory set-up

3.7.1 Cells

I used two different types of cells in the experimental set-ups to monitor the electrical conductivities of the sand samples with a two-pole technique, as a function of the salinity of the saturating pore water. These two experimental set-ups are schemed in figure 3.12 and figure 3.13. Both cells were made of Perspex (acrylic) and had an outlet and an inlet connected by tubing to a tank that served as a reservoir for the various solutions injected into the sand samples.

3.7.1.1 Flow cell

For the flow cell measurements, the sand sample electrical resistance is measured simultaneously as the saline solutions of increasing salinities were flowing through the sand samples. The cell was of cylindrical shape, 27cm in length and 5cm in radius (total volume of $2,120.6 \text{ cm}^3$). The cell was equipped with two electrodes made of zinc wire gauze with surface area of 78.55 m^2 . The electrodes were glued to the bottom and the lid cover of the cylindrical flow cell Figure 3.12..

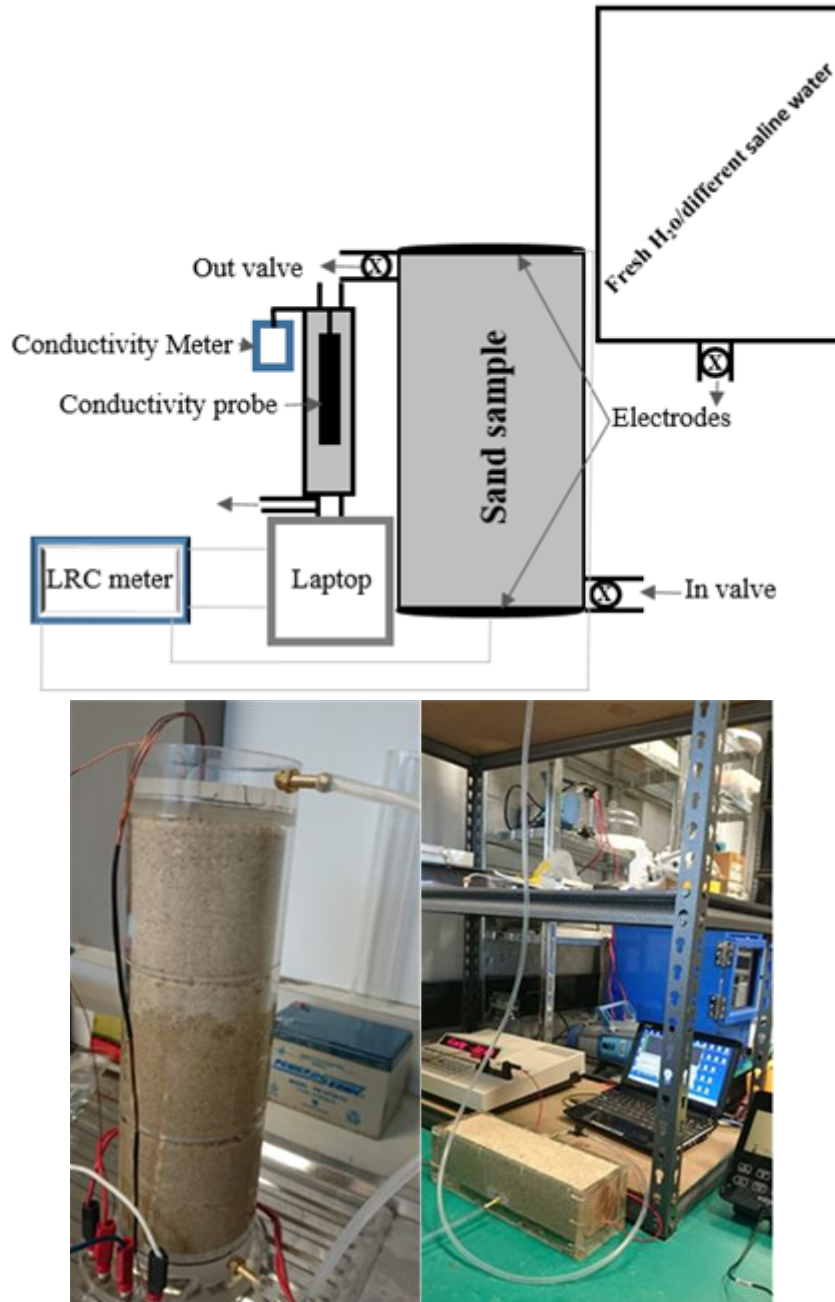


Figure 3.12: Schematic drawing of the experimental set up and the picture of the cell

3.7.1.2 Static cell

For the static cell measurement, the sand samples were saturated one after the other with saline solutions of increasing salinities and allowed to equilibrate with no fluid flow until stability of the sand sample electrical resistance reading was achieved. When the resistance reading became stable, the water was drained out of the cell before the sand sample was saturated the with the next saline solution. The static cell was rectangular in shape, 29.8cm in length, 8.7cm

in width and 6.2cm of height (total volume 1,607.41cm³). The static cell electrode was made of a zinc plate with a surface area of 53.94 cm². The electrodes for the static cell were fixed on both sides of the rectangular cell Figure 3.13..

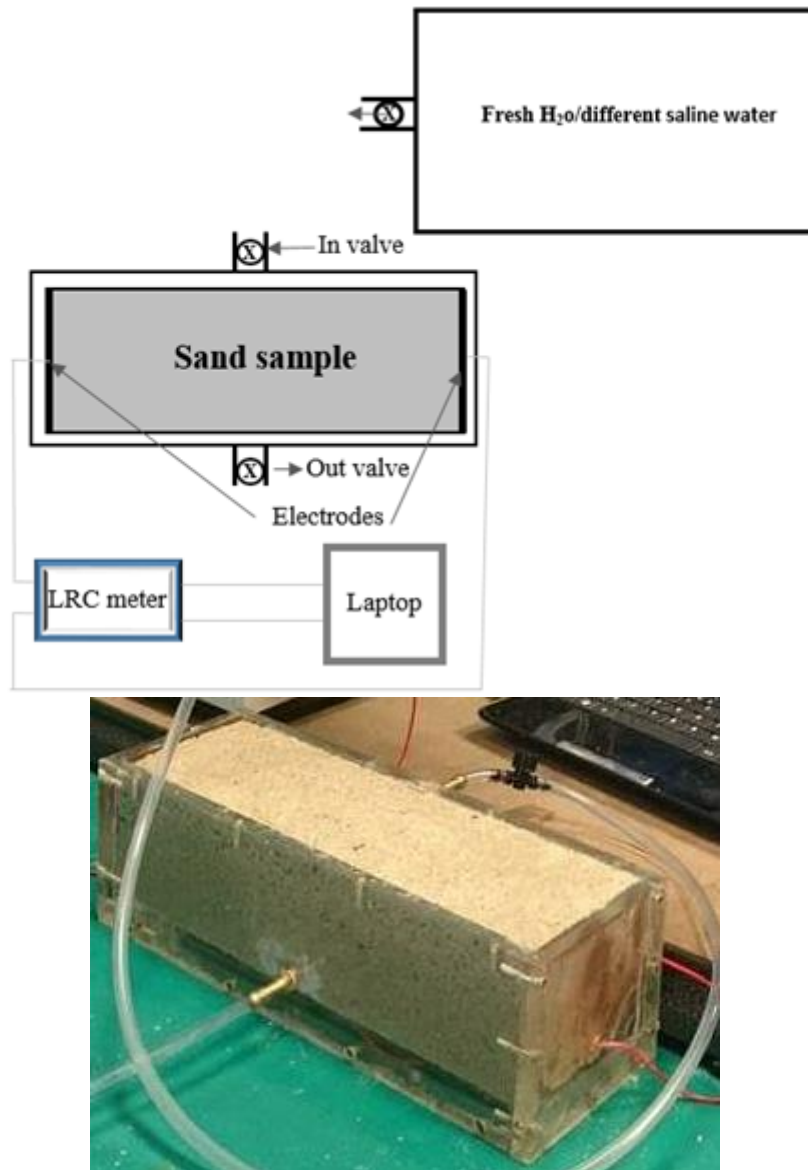


Figure 3.13: Schematic drawing of the experimental set up and the picture of the static cell

angle between voltage and current (i.e. electrode polarization): the monitored Q factor did not exceed 0.095, indicating the system was nearly purely resistive.

3.8 L-C-R (Induction Capacitance Resistance) meter

An LCR meter (Stanford Research System) was connected to the cell via the two electrodes on the top and bottom of the cell (flow cell) and at the two sides of the cell (static cell). The meter was connected the laptop via a crocodile wire clip to monitor the electrical resistance of

the sand sample as shown in Figure 3.14; the recording time interval for the flow cell laboratory measurements was taken at 1 minute intervals while the recording time interval for the static cell laboratory measurement was taken at 10 minutes intervals. A drive voltage of one (1) Vrms was applied and a frequency of 1 KHz was chosen to minimize the phase angle between voltage and current (i.e. electrode polarization): the monitored Q factor did not exceed 0.095, indicating the system was nearly purely resistive (Figure 3.14 3.14).

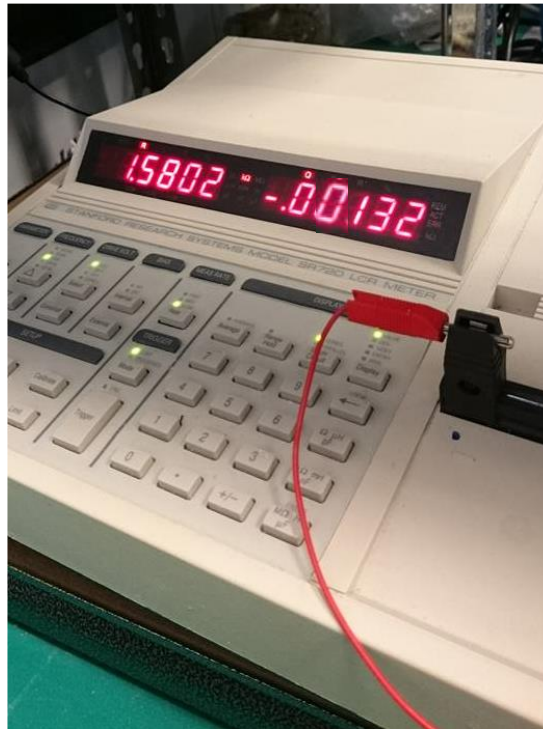


Figure 3.14: L-R-C (Inductance Resistance Capacitance) meter with the flow cell during experiment.

3.9 Conductivity meter

The conductivity meter used for the laboratory experiment was a Hanna *edge* (Figure 3.16 3.16). I calibrated the meter before using it. This calibration is performed whenever it is due (which is every week) with solutions that came with it from the manufacturer. Whenever calibration is due, the meter gives a blinking notice on the screen that reads “calibration due” as shown in (Figure 3.15). Some of the rules followed during the experimental measurements include:

- Frequent calibration of the probe, a blinking notice shown on the screen as “Calibration due” and the calibration done using the solution supplied by the supplier.
- Temperature of measurement, maintained under room temperature at all times.
- Making sure that the probe marker level is dipped below the meniscus of the solution before taking measurement (Figure 3.15)

- Probe must be positioned at the centre of the measuring container containing the solution to measure (Figure 3.17)
- Cleaning the probe with deionized water before and after every measurement and
- Wiping the inside and outside of the probe by using soft tissue paper and allowing it to dry before taking measurement. The first two rules applied for both flow and static cell experiments while the other rules were followed during the flow cell measurements only. These rules were observed so that accurate values of conductivity of the water were measured.



Figure 3.15: Conductivity meter notifying “due for calibration”

During calibration, a notification of confirmation is displayed on the screen and must be saved after confirmation. The conductivity as given by the manufacturer was 12.88 mS/cm while the measured conductivity given after measuring the solution was 12.87mS/cm so as part of the correction, a value of 0.01 mS/cm was corrected (added) to all the readings made with this calibration as shown in (Figure 5.18).



Figure 3.16: Encased Hanna probe measuring conductivity of water flowing out of the flow cell



Figure 3.17: Hanna probe measuring saline water drained from the static cell



Figure 3.18: Conductivity value after confirmation of calibration

3.10 Tanks

The different solutions use in the experiments were stored in an open tank; the tanks were placed on a rack much higher than cell to allow free flow of the fluid due to gravity; the flow rates ranged from 0.52 to 2.75 ml/s (Figure 3.19). To change the saline solution whenever a stable reading was achieved, the tank was replaced by the next saline solution to be used.



Figure 3.19: Tanks used in the experiment to store the saline solutions

3.11 Connecting tubes

White transparent tubes of various sizes (5mm, 12mm and 15mm) were use in the experiment (figure 3.20). This is because the diameter of the hole on the tank is big compared to the diameter of the inlet and outlet of the cells used (Figure 3.19)



Figure 3.20: An example of the tubes used in the experiment

3.12 Valves

The valves used in the experiment to control the flow of solutions from the tanks into the cells as well as the flow of the fluid in and out of the cells are shown in (Figure 3.21). The valves used were also of different sizes due to the different sizes in the tubes used.



Figure 3.21: Valves used in the experiment to manually control the flow rate of solutions

3.13 Wire and clips

Wires and clips were used to connect the LCR meter to the (cell Figure 3.22). The clips have to be gripped firmly by the LCR meter to get a good recording of the resistance as shown in Figure 3.14.

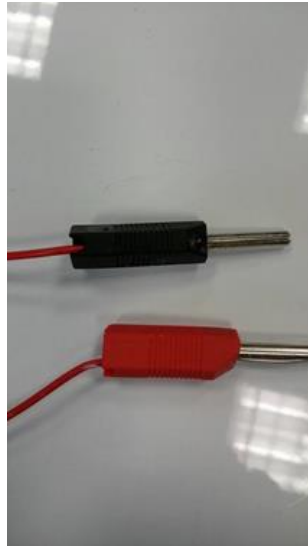


Figure 3.22: Wire and clips used in the experiment

3.14 Computation of formation factor

A Realterm program is the interface I use to record the data as a text document. The parameters set in the Realterm programs include port, capture and send as shown in (Figure 3.23 3.23)

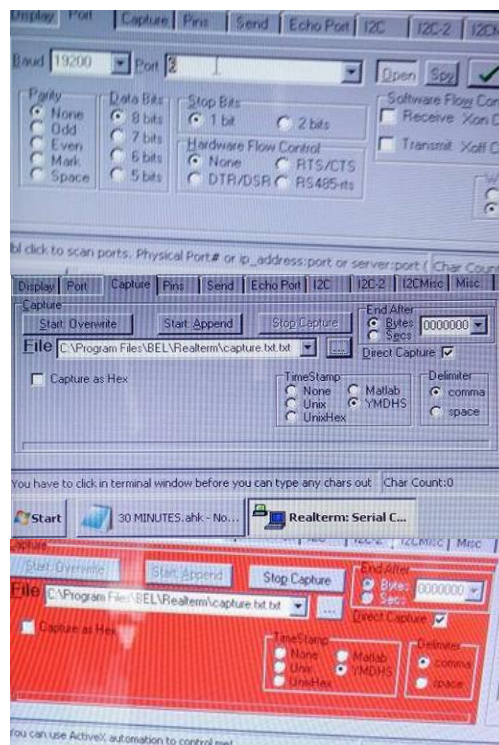


Figure 3.23: Parameters set for the recording by the LCR meter.

The Realterm serial capture program is automated using an Auto Hotkey program to record and store the resistance of the sand measured by the LCR meter at pre-determined times. The times set for recording of the data for the clean sand was 5 minutes for the flow cell measurements and every 10 minutes for the static cell measurements. While for the Cottesloe clay sand, measurement was recorded every 30 minutes.

For the flow cell experiment, the conductivity meter measured and stored the conductivity and temperature readings at a pre-determined time set at 5-minute intervals synchronous with recording the resistance by the LCR meter. Readings were automatically stored and were retrieve at the end of each experiment for analysis of the results. However, in the case of the static cell, the LCR meter recorded the same way as the flow cell but this time, the saturating water is left in the cell and is allowed to stabilize. After stabilizing, the water was drain in to a washed plastic bottle as shown in Figure 3.24 and the conductivity was measured separately.



Figure 3.24: Water drained from the static cell for conductivity measurement

Therefore, to obtain electrical formation factor F it is

$$F = \frac{R_s}{R_w} \quad 3.2$$

with

$$R_s = r_s \frac{A}{L} \quad 3.3$$

where F is the formation factor, R_s is the resistivity of the sand sample saturated with water, R_w is the resistivity of the water, r_s the measured resistance of the sand sample saturated with water, A the surface area of the electrode, L the length of the cell and C_w the measured conductivity of water.

To obtain the formation factor, the sample's inverse resistivity (conductivity), once it had stabilized, was plotted against the saline water's conductivity; the inverse of the slope gives the formation factor. Refer to (Figures 5.15, 5.16, 5.17, and 5.18) for clean sand samples and (Figures 5.24, 5.25 and 5.26) for clay sand samples all in chapter 5.

Because the sand samples do not contain any clay (in the case of the clean sand), and because the injected solutions have a conductivity was (10^{-2} to $5.0 \cdot 10^{+1}$ S/m) much larger than that of quartz or carbonate, the surface conductivity $5.4 \cdot 10^{-3}$ S/m (Miller, 1969), and $1.4 \cdot 10^{-3}$ S/m (Vialle, 2008) respectively. The surface and matrix electrical conductivities can be neglected e.g. (Johnson and Sen, 1988; Saarenketo, 1998). However, considering the surface conductivity is very important in the case of the Cottesloe shaly sand.

3.15 Conclusion

In this chapter, I have discussed the sample location, preparation and composition. Following this is the grain size distribution, preparation of the solutions used in the experiment as well as the preparation of the Cottesloe shaly sand.

The description of the two cells as well as the laboratory set up were also discussed here followed by the description of the instruments used in the experiments as well as the rules followed in order to acquire correct data. Having described this, in the next chapter I will be presenting the laboratory results obtained from the methods described in this chapter.

Chapter 4

Micro-CT scan images: acquisition, analysis and computation

4.1 Introduction

In this chapter, I will start by presenting the clean sand, where I will be describing the generation of the image data; followed by loading the data and then image processing. In the image processing, I will discuss the filtering and segmentation methods that I used in processing the clean sand. Filtering is an important phenomenon for preparing data before image segmentation; this helps smooth noisy images, which is sometimes-called “denoising” filters. Denoising effectively reduces noise, and require careful use in other not to alter the material content in image, especially for analysis purposes. By applying the intensity range adjustment it makes the visualization clear for ideal quality images with respect to features of interest that used for qualitative analysis. For accurate identification of different materials, in particular with noisy, inhomogeneous background or artefacts, image filtering is necessary. I have applied four different types of a filter before making a choice of selecting the best option. The best suit filter is the Local mean filter because it gives approximately the same porosity (with an average difference of 3%) between the values computed from the laboratory and micro CT scan measurement but also gives the best image quality too. After filtering the image, then follows segmentation. I applied two different segmentation techniques; these are the global threshold and watershed segmentation methods. I applied the global threshold to allow me to segment the image into pores and grains (the two grains merged together) for calculation of porosity and then I applied the watershed segmentation algorithm to separate the different materials for grain size analysis. Also in this chapter, the image cropping of volumes is presented i.e. $(700)^3$ $(500)^3$ $(350)^3$ and $(200)^3$ sub-volumes for statistical analysis and at the end of this chapter I will present the pre-processing of the micro CT scan images of the cubes for electrical computations.

4.2 Clean sand

4.2.1 Image acquisition

Two samples were prepared for imaging with micro-CT, one of the Scarborough beach and one for Cottesloe beach. Loose moist sand is prepared in a cylindrical Pyrex glass tube of 6 mm in diameter and 6 cm in height, and inserted in a core holder. The sand samples is scanned with 3D X-ray Microscope Versa XRM 500 see Figure 4.1(b) using X-ray energy of 60keV, a

current of 70.66 μA and energy of 5 MWatts. A total number of 1021 of 2D images for Scarborough beach sample and 991 of 2D images for Cottesloe beach sample were acquired with exposure times of 10.38s for Scarborough beach sample and of 9.52s for Cottesloe beach sample, with a total scanning time of 2hrs 55minutes and 2hrs 42 minutes for Scarborough and Cottesloe beaches respectively. Nominal voxel sizes of $(2.5761\mu\text{m})^3$ and $(2.5516\mu\text{m})^3$ 8bit is achieved with source-to-sample and detector-to-sample distances of 11mm, for both Scarborough and Cottesloe beach samples. Initial cone-beam 3D image reconstruction is accomplished using initial software XM Reconstruction (XRadia).

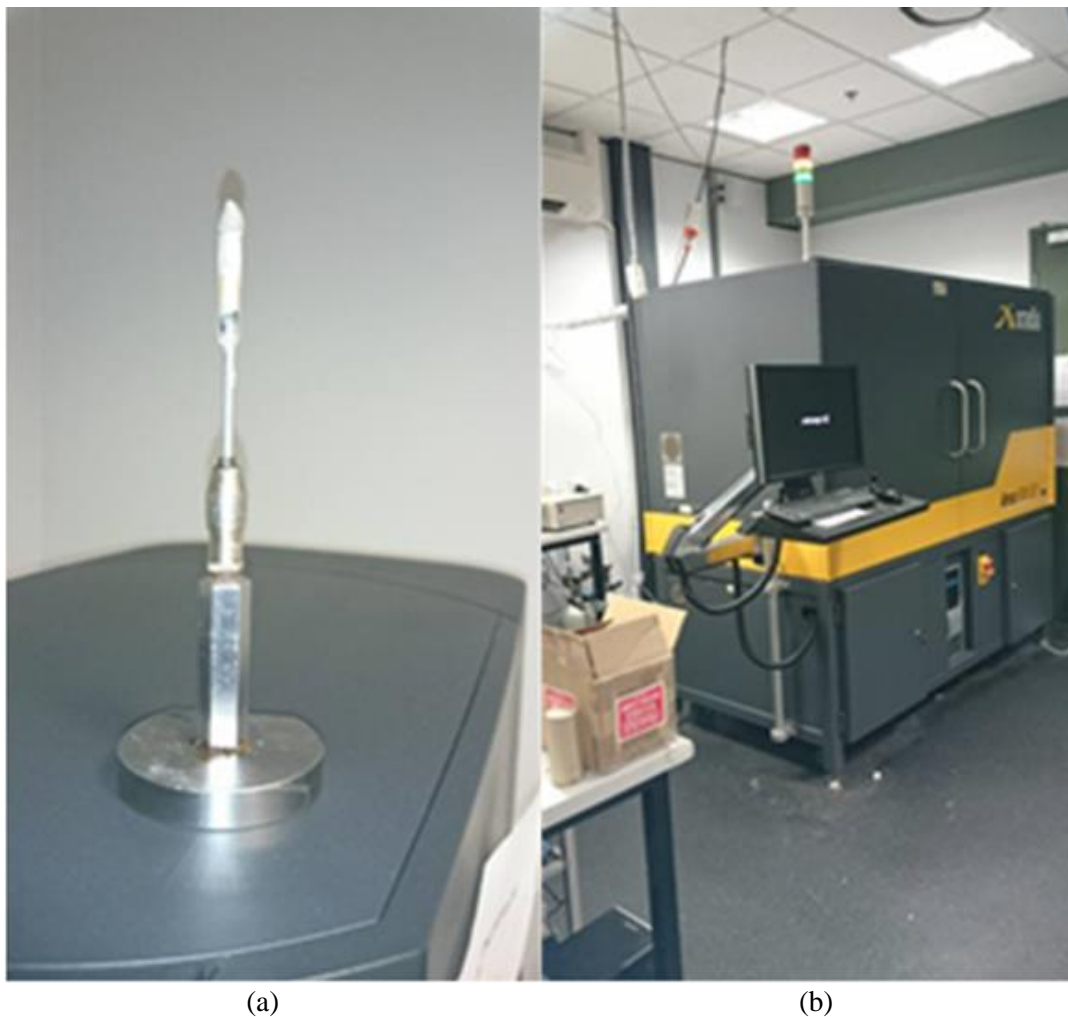


Figure 4.1: (a) Microgram holder with the sand sample (b) XRM 500

4.2.2 Image loading

After loading the image into Avizo software with the voxel intensity of 65535 and 62700 8 bits for Scarborough and Cottesloe images the image appears dark and not clear because of the voxel intensity of the image not adjusted to the actual area of interest of the image. After loading the raw image into Avizo software, (with a default colour map) the voxel intensity

range of 0 to 65535 and 0 to 62700 for Scarborough and Cottesloe beach respectively see Figures 4.2 and 4.3

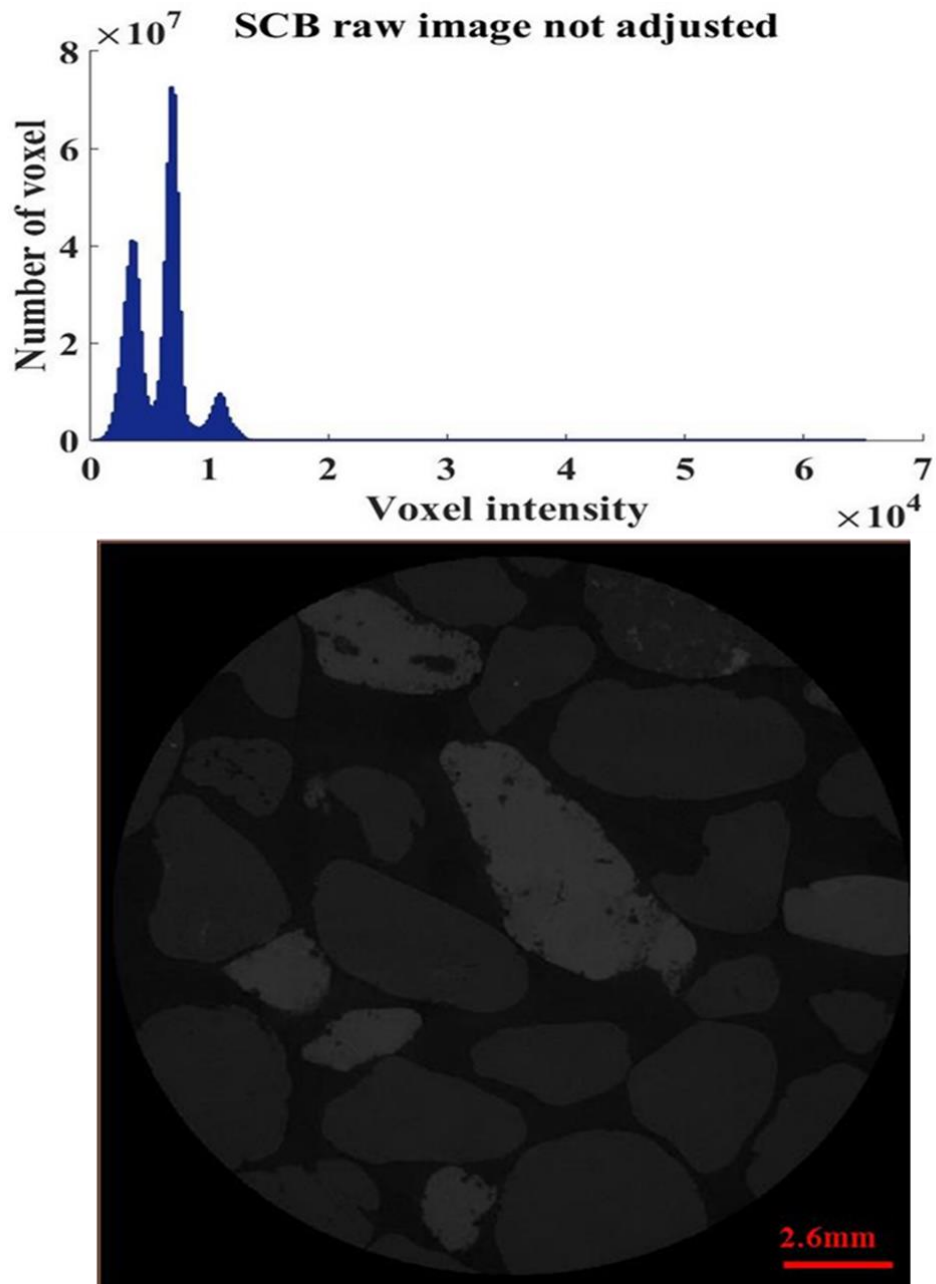


Figure 4.2: Loaded Scarborough raw image before adjusting the colour map.

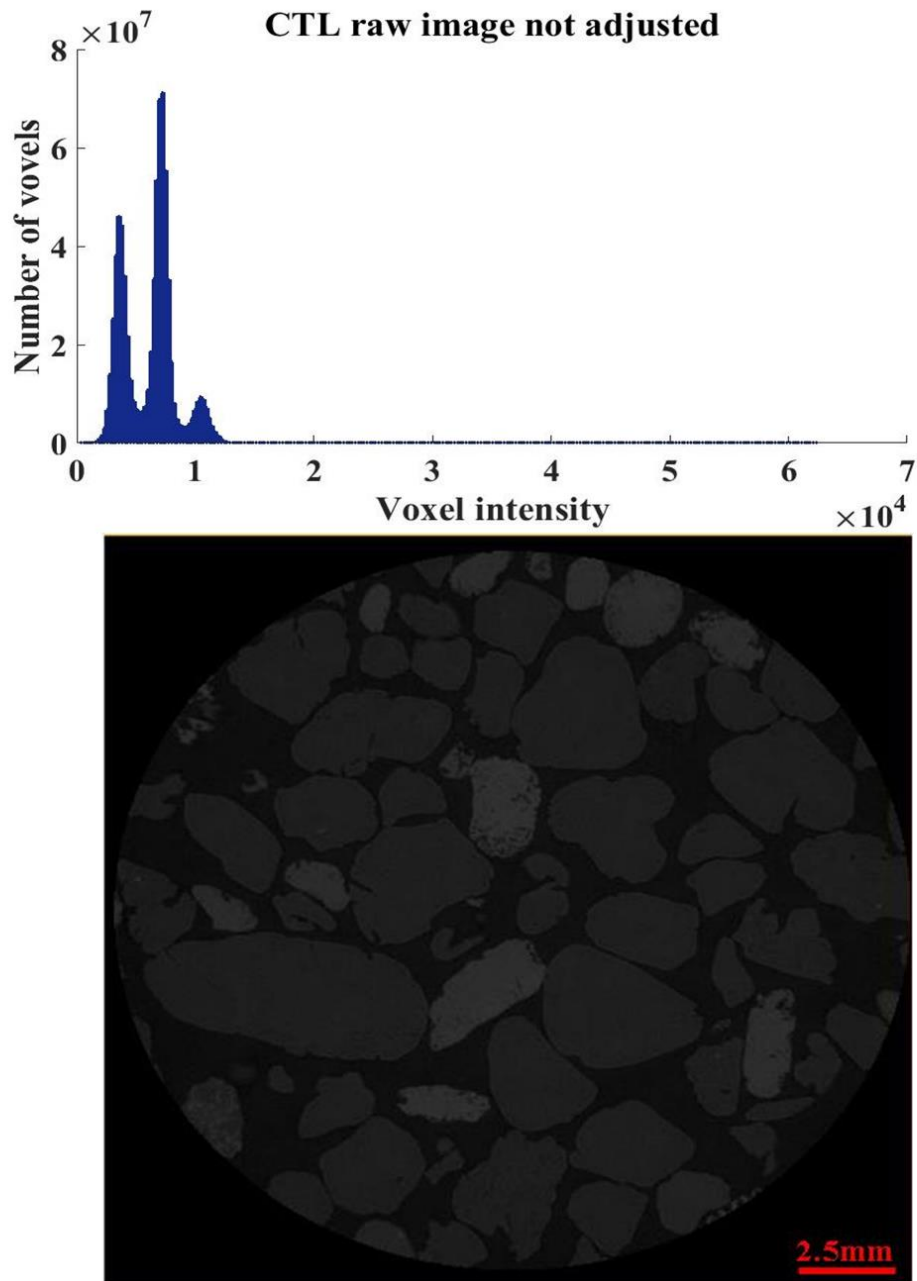


Figure 4.3: Loaded Cottesloe raw image before adjusting the colour map.

Adjusting the image intensity after loading the image is necessary to view the image clearly; this adjustment accomplished by adjusting the colour map to the actual area of interest of the image view, this is achieved by adjusting the slide bar. The Scarborough image has colour map voxel intensity range of 1348 - 13215 while Cottesloe has a range of 2034 - 13218 as shown in Figure 4.4 and Figure 4.5 respectively for Scarborough and Cottesloe beaches.

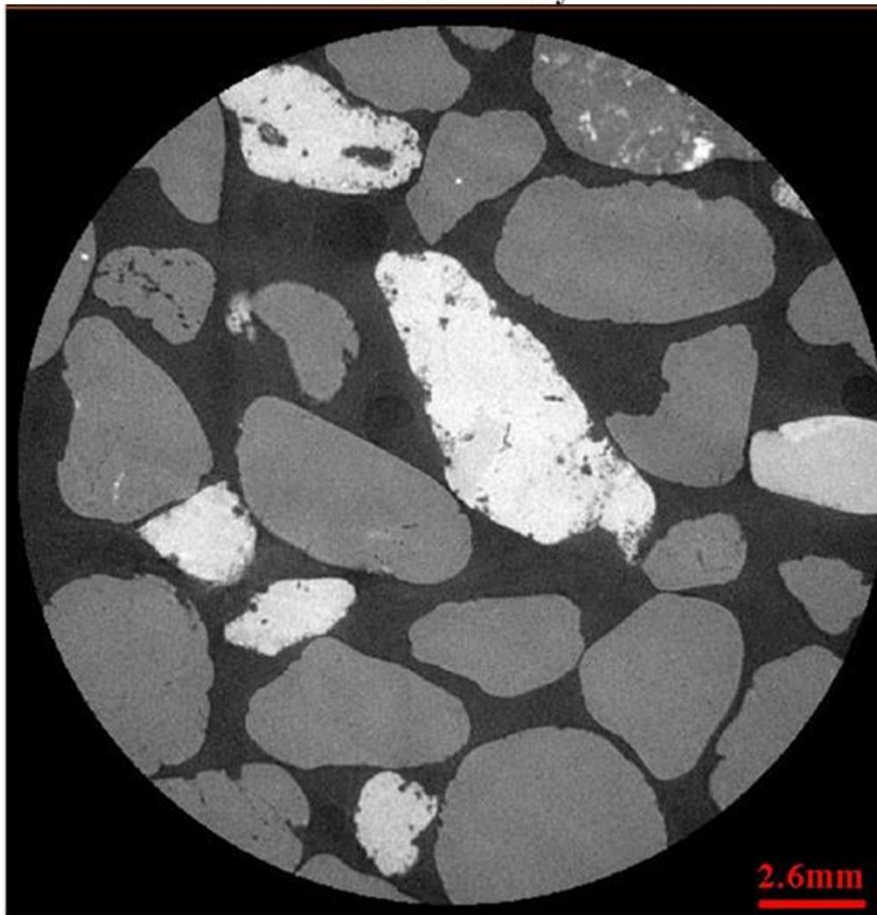
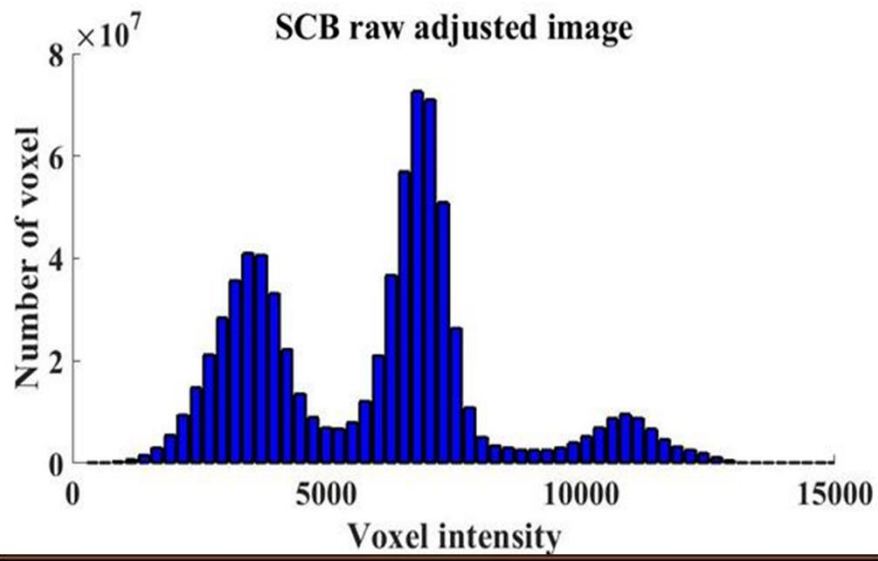


Figure 4.4: Loaded Scarborough raw image before adjusting the colour map.

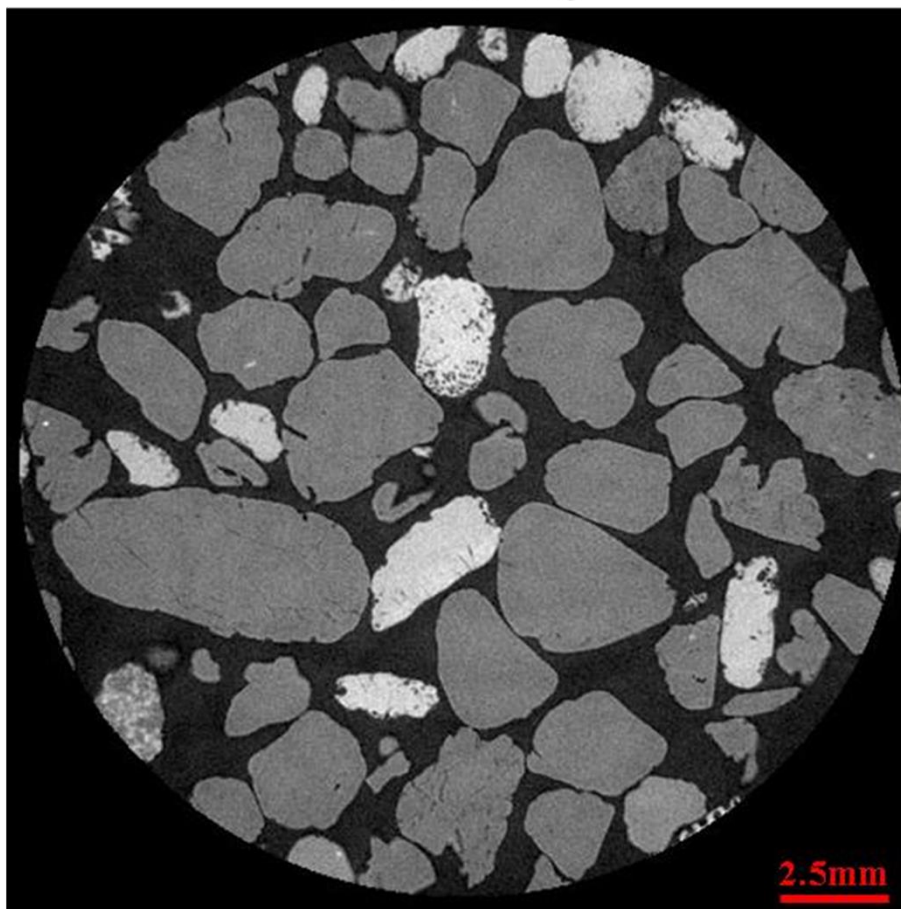
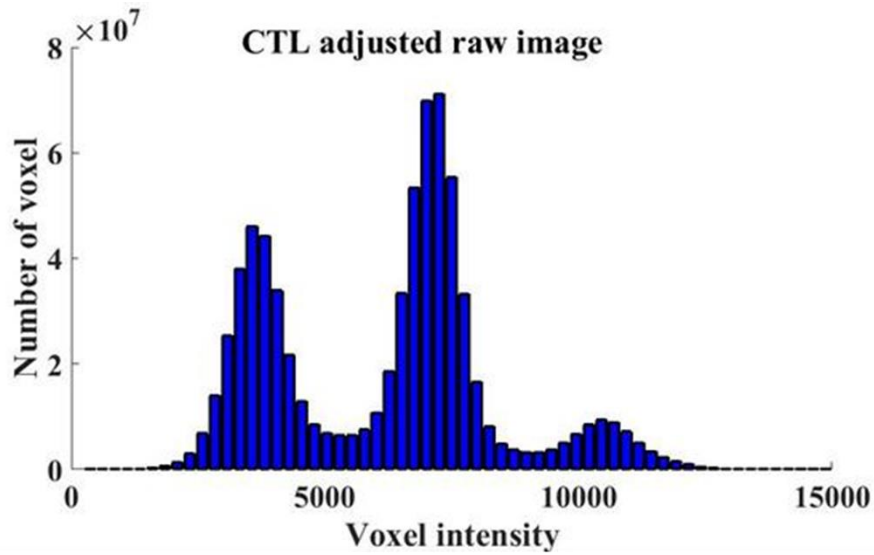


Figure 4.5: Loaded Cottesloe raw image before adjusting the colour map.

4.2.3 Image filtering

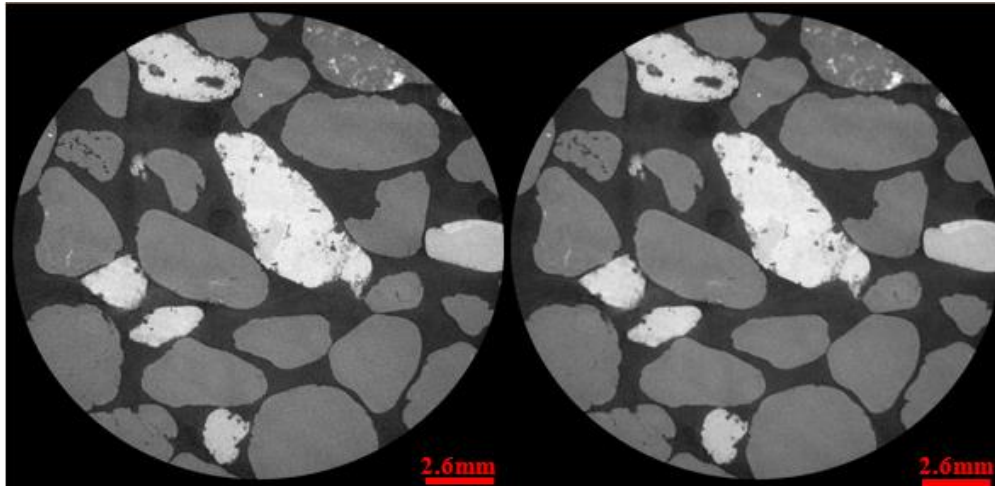
Filtering is an important process for preparing image data before segmentation; this helps smooth noisy images, which is a sometimes-called “denoising” filter. Denoising effectively

reduces noise and requires careful use in other not to alter the material content in the image, especially for analysis purposes. It is necessary to reduce the image noise or artefacts and enhance features of interest before segmentation (Chaouachi et al., 2015). I used software package Avizofire 9 (FEI Visualization Sciences Group) for image enhancement and segmentation. It is essential to deploy same enhancement steps and parameters for the digitally sampled whole image of (987 X 1011 X 1007) and (988 X 1012 X 991) for both Scarborough and Cottesloe beaches. Avizo offers several functions such as extract the sub volume (Extract Sub volume function), splitting the volume (Split Volume function), and the cropping of region of interest (Interest cropping tool). I use four different digital image filter types available for enhancing the image quality features and performances, depending on the image (imputed) and the controlling parameters, the best selection is made.

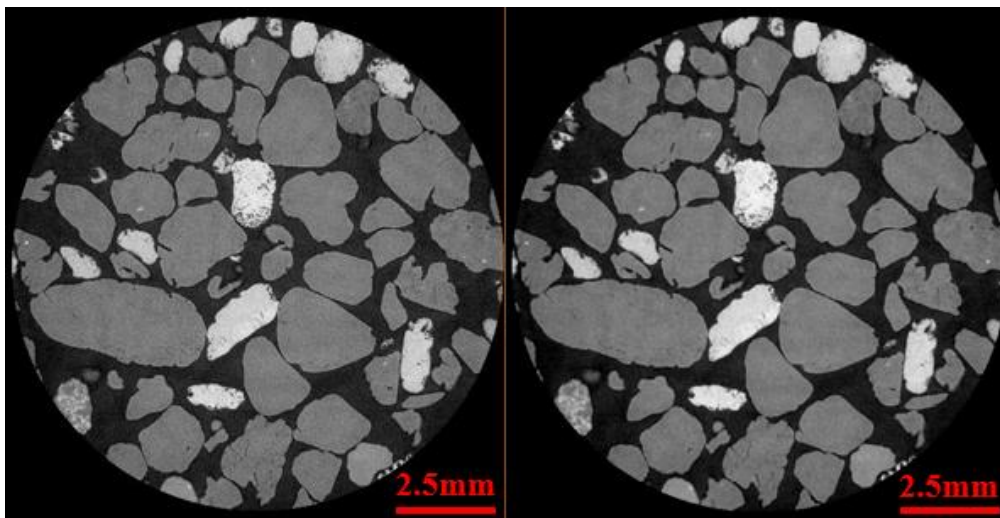
The type of filters I apply are outline below.

4.2.3.1 Median filter

This is a basic filter preserving edges of the image. It is very effective on salt-and-pepper noise (scatter dots). Figure 4.6 below shows the median filtered image of Scarborough and Cottesloe Beach samples.



(a)



(b)

Figure 4.6: (a) Scarborough raw and median filtered image (b) Cottesloe raw and median filtered image

4.2.3.2 Edge preserving filter

This filter enhances the image by maintaining the boundary of different materials or phases. There are two categories of edge detection; these are the gradient magnitude of greyscale images (Sobel Filter), which is quick basic edge detection and Image gradient a comprehensive module supporting quick approximation of noise reducing gradient. Edge detection is well-developed image processing technique. Edges resolved by Edge detection filter are disconnected and therefore, to segment the objects in the image one needs similar region boundaries. Another edge detection filter developed by [Lindeberg \(1998\)](#) was a combined method that segments edge into straight and curved edge segments for parts-based object recognition, based on a minimum description length (MDL). A criterion that enhances the

image by a split-and-merge-like method and breakpoints is gain from integral intersection having more likely points at which to consider partitions into different segments. Presented in Figure 4.7 is the edge preserving filter of (a) Scarborough and (b) Cottesloe samples.

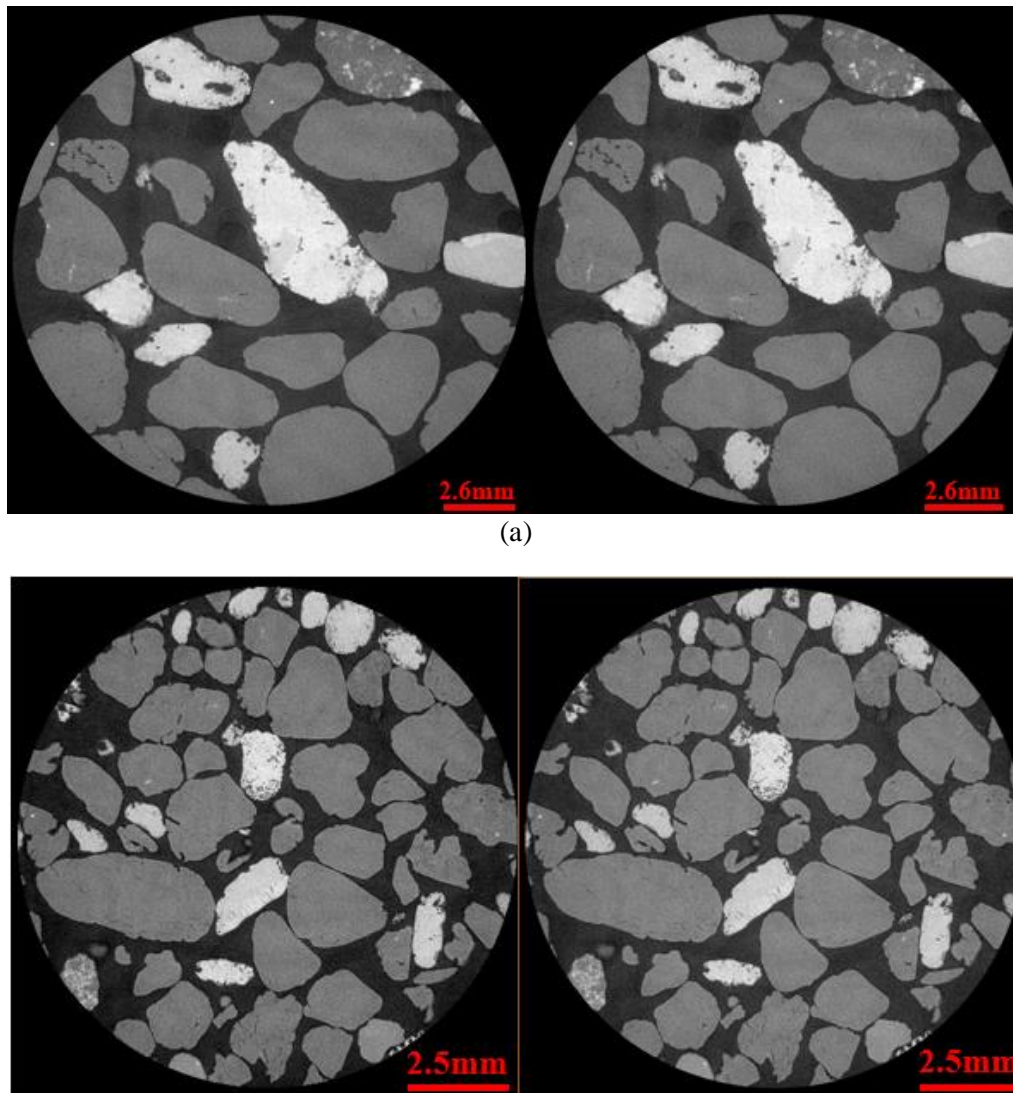


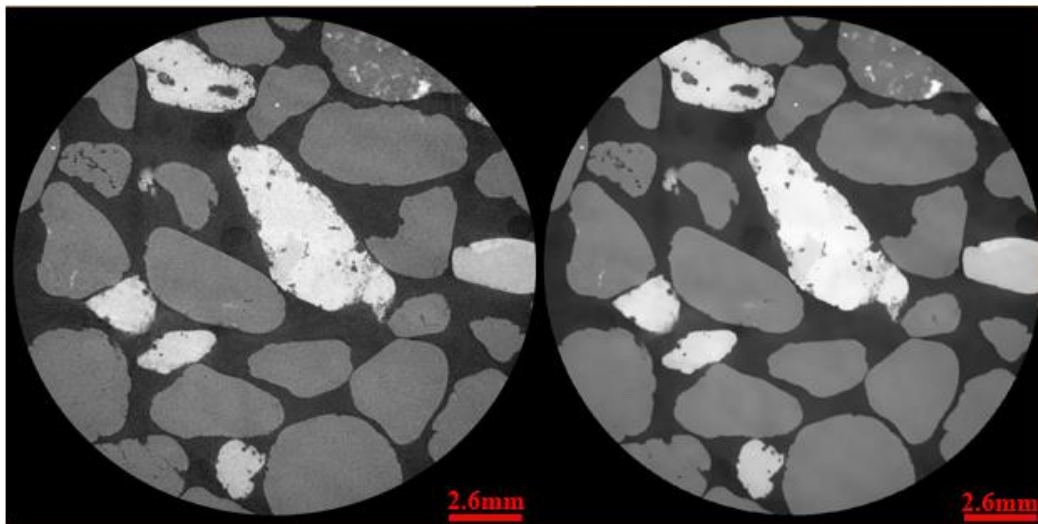
Figure 4.7: Figure 4.8: (a) Scarborough raw and edge preserving filtered image (b) Cottesloe raw and edge preserving filtered image

The intensity value of each pixel in an image is replaced by the weighted average of intensity values from nearby pixels. The weight depends on the distance in colour space from the pixel in question. The preserved sharp edges by systematically excluding pixels across discontinuities from consideration.

4.2.3.3 Non-Local filter

The approach of a Non-local filter introduced by [Buades et al. \(2005\)](#) based on non-local averaging of all pixels in the image. Non-Local Means filter method works by denoising the image attacked by white Gaussian noise with zero mean variance. The computed pixel is based

on the pixel intensity from the data gained on the entire image and it stops repetition caused due to the presence of closeness in patterns and features in the image. In this method, the replaced grey value of each pixel achieved by the entire average of the grey values of all pixels in the image. The value given is corresponding to the similarity between the local neighbourhood of the pixel under consideration and the neighbourhood corresponding to other pixels in the image. Non-local filter algorithm implements denoising scalar volume data by comparing each voxel with another voxel in the stack. Preliminary study on the effect of various image filters on the images result makes it necessary to determine the best option of filters aiming at high quality-images to gain volume rendered images for Scarborough and Cottesloe beach samples. Non-Local filter applied on the raw image in XY plane with the local neighbourhood of six and adaptive (true) for Scarborough and Cottesloe beaches respectively. Grey-scale images of the 2D image processed using the non-local filter with the range in intensity of 1348 – 13215 and 2034 - 13218 for raw images of Scarborough and Cottesloe beaches is shown on Figure 4.6 with aim of removing concentric shadows in images and properly enhancing interfaces between pores and grains as well as removing noise. We can easily notice that the quality of the image have increased by comparing images Figure 4.4 with Figure 4.6(a) and Figure 4.5 with Figure 4.6(b) images for Scarborough and Cottesloe images. The white grains are carbonate; grey grains are quartz, while black corresponds to void space (pores) as shown in figure 4.8.



(a)

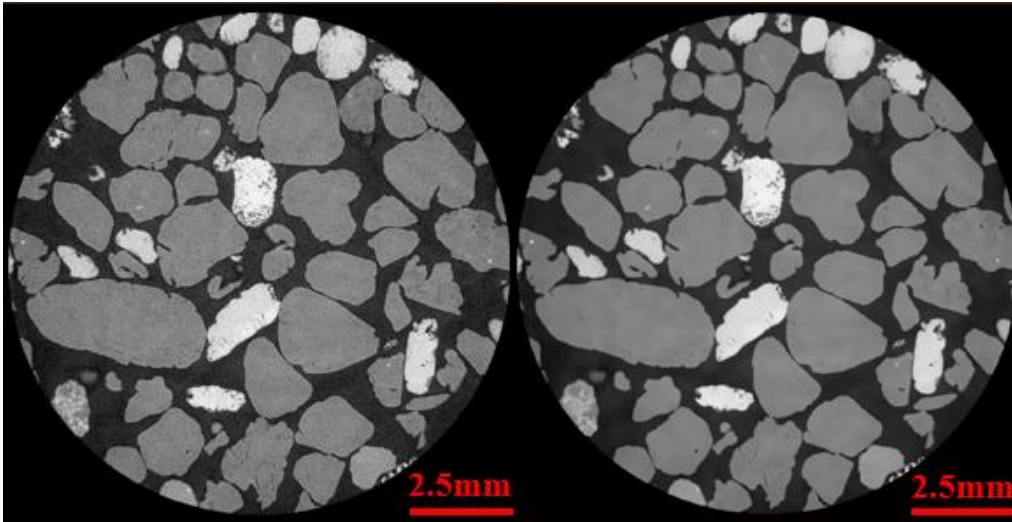
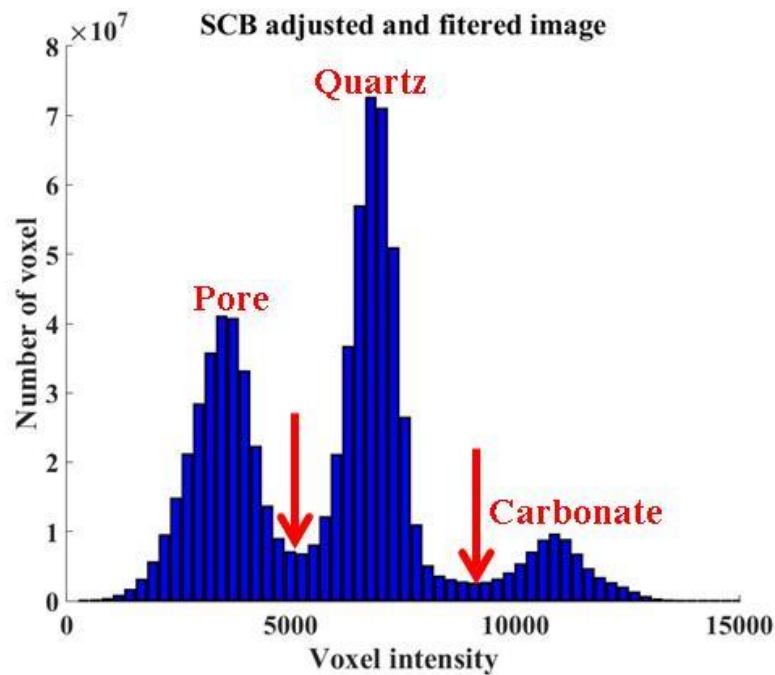


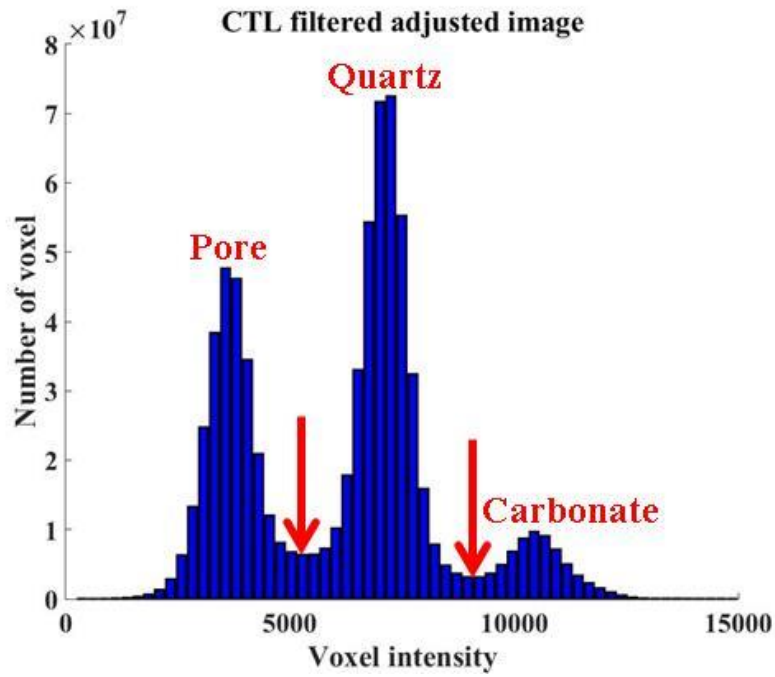
Figure 4.9: Non-local filter: (a) Scarborough (b) Cottesloe images

4.2.4 Histogram of material in the image

Micro CT-scan image analysis offers the possibility to analyse size and shape of individual particles present in a sample. Various image analyses are available. In this method, I use histogram computed from pixels in image, with the peaks and valleys in histogram used to locate cluster in image colour or the intensity as a measure Figure 4.10 4.9.



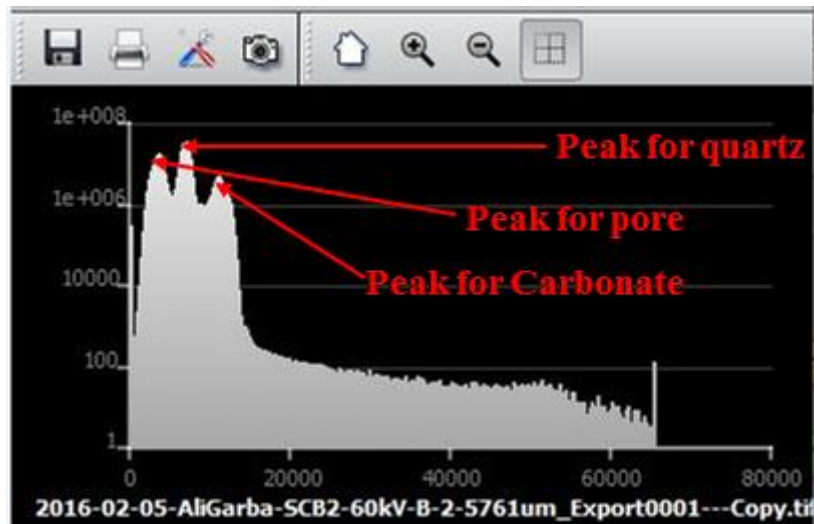
(a)



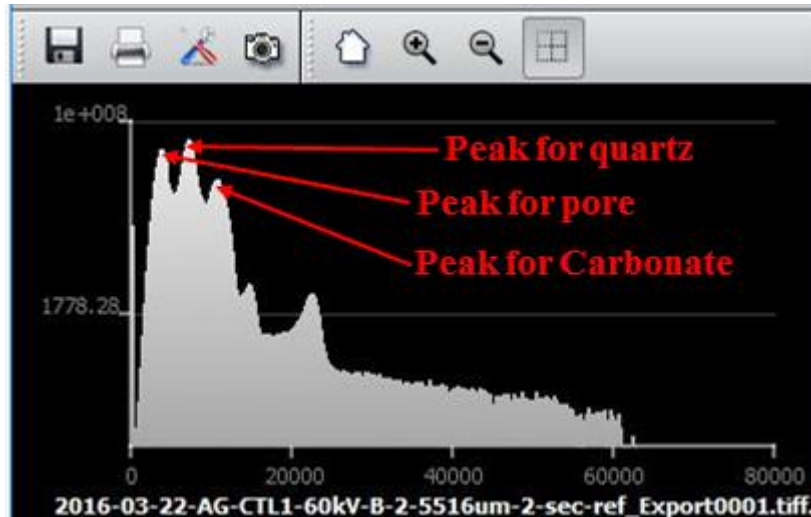
(b)

Figure 4.10: Histogram (a) Scarborough (b) Cottesloe images showing the peaks of pore, quartz and carbonate with their mid points at the throughs.

Presented in Figure 4.10 is the histogram of the equivalent diameter distribution of Scarborough and Cottesloe.



(a)



(b)

Figure 4.11: Histogram (a) Scarborough (b) Cottesloe beach images.

4.2.5 Image segmentation

The objective of image segmentation is to reduce image into meaningful phase. Segmentation algorithm assigns a pixel to an image label that describes a material or a region to which it belongs, for example, the pixel of image will belong to either material one or material two. The segmentation process is a prerequisite for surface model generation, and used in accurate quantification like volume measurement, and is stored as a separate data object called the *label field*. (Details is presented at appendixes A 4.4 and A 4.5)

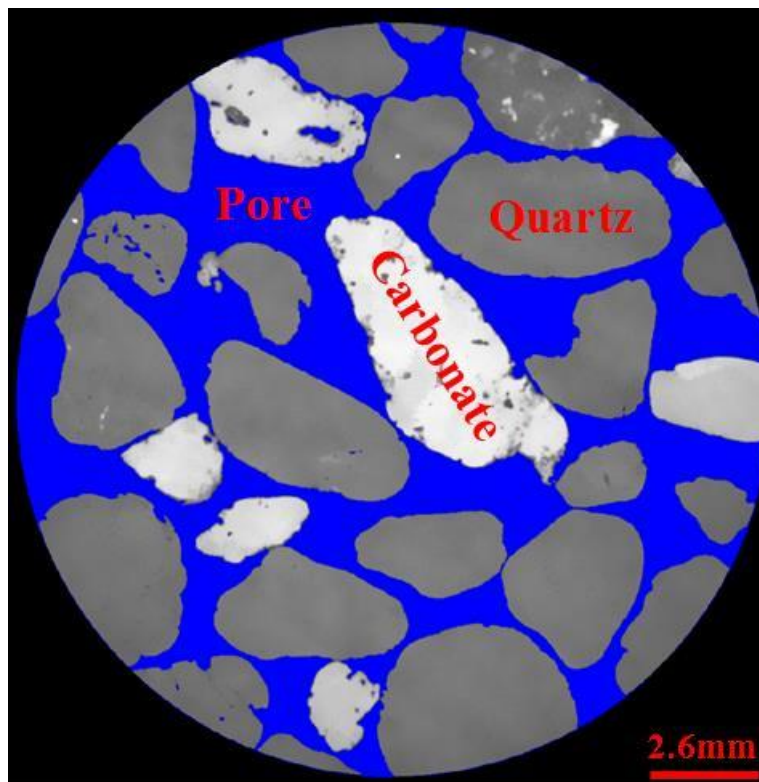
Image segmentation mainly used to establish objects and boundaries (lines, curves etc.) in images. More precisely, image segmentation is the process of assigning a label to each pixel in the image such that pixels with the same label share certain characteristics.

Each of the pixels in a region is identical with respect to some attribute or computed property such as colour, intensity or texture. Bordering parts are significantly different with respect to the same characteristics. The filtered images were segmented using two types of thresholding algorithms: the first one resulted in a 2-phase segmentation that was further use for calculating porosity as well as computing samples' electrical computations; the second one is the watershed algorithm that resulted in a 3-phase (pore, quartz and carbonate) segmentation used for grain analysis. Note that filtering and segmentation workflows were applied on the full 3D dataset.

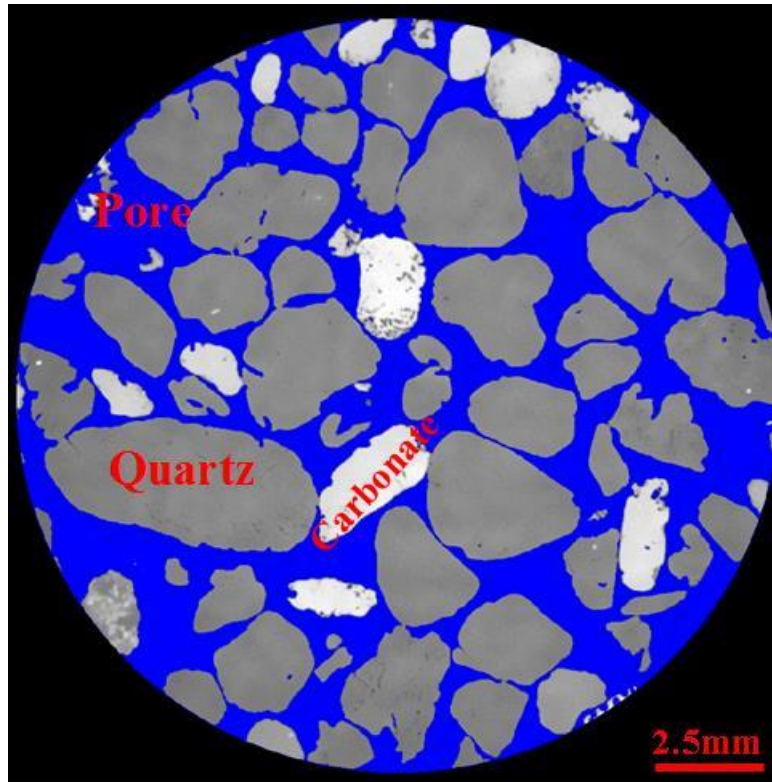
4.2.6 Types of segmentation

4.2.6.1 Two-phase segmentation by global thresholding

The threshold segmentation requires less manual interaction and it typically requires the high-quality image. During global thresholding, each voxel that has a value lower than the threshold is assigned to the exterior and each voxel value greater than or equal to the threshold is assigned inside. The voxel labels that are not part of the object have voxel values above the threshold, and it is suppressed by setting a remove couch option, which assures that only the largest coherent area labelled as the foreground (inside) and other voxels assigned to the background (exterior). I use the global threshold segmentation algorithm to separate pores from grains: the set intensity value separating pores from grains (both quartz and carbonate grains having higher intensity values than that of pores) kept the same for 2D slices. Parameters such as contrast thresholds for 2-phase segmentation are set according to the data range. Scarborough beach images has a range 1234 – 13107 Figure 4.9(a) and Cottesloe has a range 1823 – 12483 Figure 4.9(b) and the threshold images of the Scarborough and Cottesloe are presented in Figure 4.11 showing clearly the pore, quartz and carbonate grains.



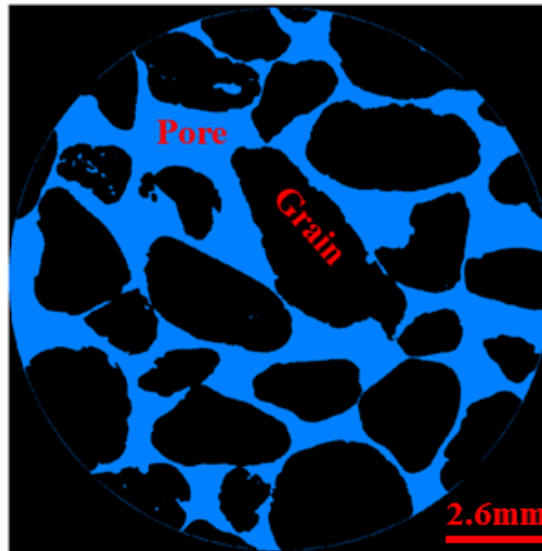
(a)



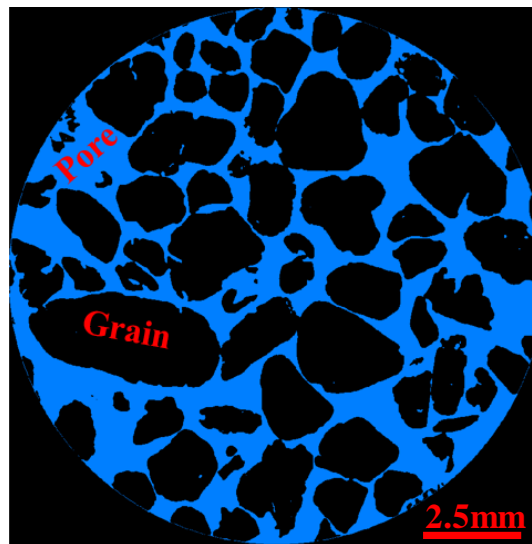
(b)

Figure 4.12: Threshold image of (a) Scarborough and (b) Cottesloe images.

Global threshold is available for semi-automatically drawing edges, whereby rough lines are smoothed and bordered to enlarge some principle of a match with the image, by preference, edge finding can be fully automatic (I applied this type). In this research work, the filter output has been thresholded at a value of five; voxels from zero to five are displayed as blue and all pixels greater than 5 are labelled as edge voxels and displayed as black. The algorithm runs on a raster scan, visiting each voxel in turn, starting at the top-left corner of the image and scanning along each row, finishing at the bottom-right corner and the output of the 2-phase image segmentation of pores and grains is the result of the segmentation and is presented in Figure 4.12 ready for porosity calculation.



(a)



(b)

Figure 4.13: 2-Phase segmentation of (a) Scarborough and (b) Cottesloe samples

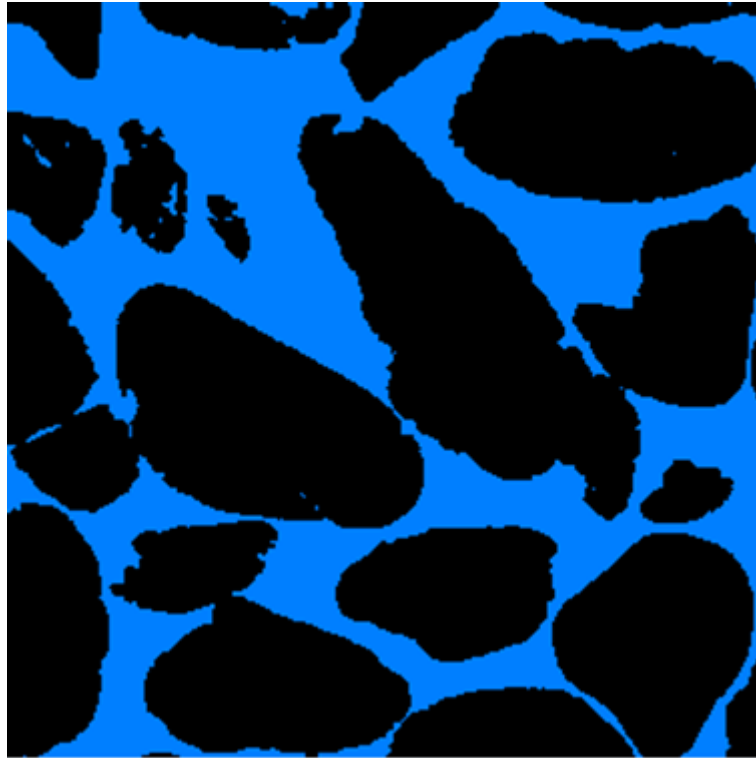
Poor segmentation leads to inaccurate porosity computation. Using Avizo 9 fire to compute the porosity of Scarborough beach sample as shown in Figure 4.14, under-segmentation of the image leads to enhancing the grains and suppressing the pores as seen in Figure 4.13(a) compared to Figure 4.13(b), which leads to an under-estimation of porosity. The result of the computed porosity is 0.342 instead of porosity 0.361. However, over-segmentation of image leads to suppressing the grains thereby enhancing the pore that leads to overestimation of porosity of 0.418 instead of porosity 0.361 Figure 4.13(c) compared to Figure 4.13(b).

To check the quality of segmentation, I compare the porosity calculated from volume fraction and the “measure and analyse” tool of Avizo (micro-CT scan images) as 0.361 to porosity measured in laboratory from Scarborough beach sand as 0.359. The porosity from CT-scan

image of Scarborough beach sample shows just a porosity 0.003 lower than the calculated from the laboratory measurements, which shows excellent agreement between calculated porosity and the measured porosity in the laboratory. Figure 4.13(b) shows the correct segmentation while Figure 4.13a and Figure 4.13c are under-segmentation and over-segmentation respectively; the effect is visible from the red circles on the images.



(a)



(b)



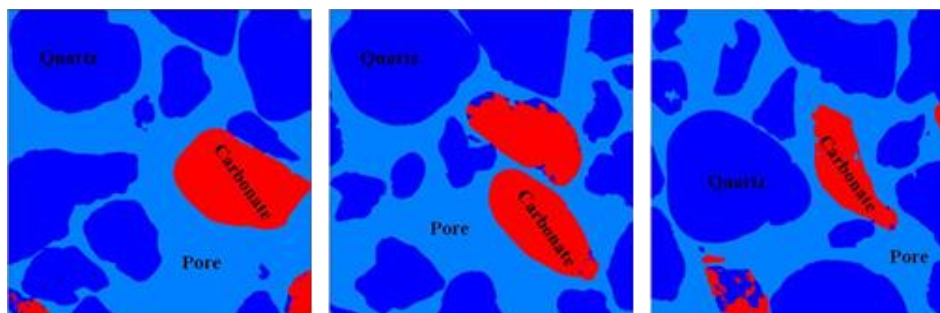
(c)

Figure 4.14: Segmentation of Scarborough beach sample (a) under-segmentation (b) correct segmentation and (c) over-segmentation. The areas shown by the red-circled are the examples of areas affected by under-segmentation and over-segmentation.

4.2.6.2 Watershed segmentation

In this section, I describe necessary steps of watershed segmentation. For grain size analysis and numerical modelling of images be performed, watershed segmentation must be applied. This process results in the transformation of pixels of a certain grey scale range. The watershed algorithm use a semi-automatically segmented tomographic data, treating grey values of gradient image as the topographic map where each grey value stands for the specific altitude. After placement of seeds or marker regions in catchment basins, representing minima are homogeneous areas with low gradient image virtually immersed. As soon as “water” from different basins meet the so-called watershed, boundary placed in between Vincent and Soille (1991) and Wang (1997). The algorithm performs well-placing watersheds on sharp intensity edges showing steep gradients and producing maxima in gradient images (Buades et al., 2005; Iassonov et al., 2009). With this approach, it is possible to extract pore and quartz and carbonate separately and accurately.

Variations in brightness or energy across image cause different threshold in different regions. Watershed technique provides an effective solution for these differences especially with the clay sand sample of Cottesloe beach sample. Module Marker-based Watershed performs fast determination of watershed lines from specified markers in a label image. It determines crest lines separating markers, crest lines are output in the binary image. I use marker-based watershed segmentation algorithm from Avizo Fire 9. I define three marker ranges of grey scale intensity for pore, quartz grains, and carbonate grains, respectively. I then performed watershed flooding for each of these three phases. The output image result of the three-phase watershed segmentation allows computation of pore volume, grain size distribution, as well as the volume fraction of different minerals Figure 4.14 and Figure 4.15 show the result of image output of watershed segmentation of slices at 50, 150, 250, 350, 450, and 550 for Scarborough and Cottesloe images.



(a)

(b)

(c)

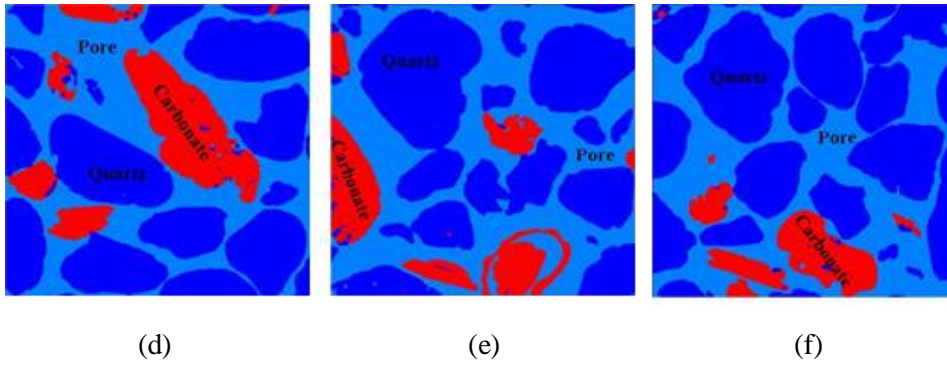


Figure 4.15: Watershed images of slices at (a) 50, (b) 150 (c) 250, (d) 350, (e) 450 and (f) 550 slices of Scarborough beach.

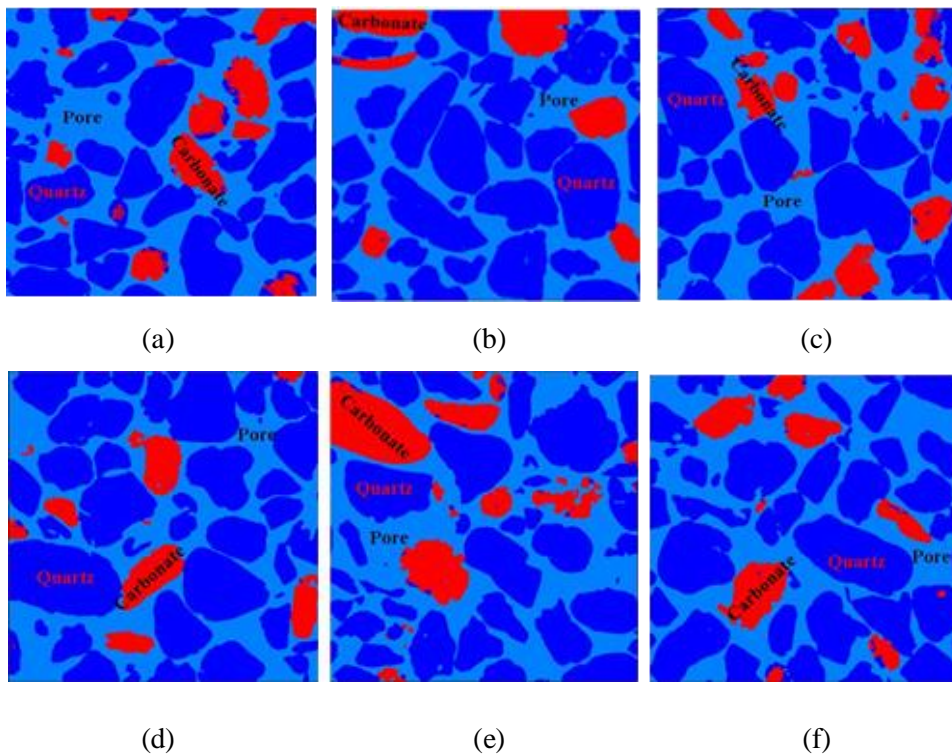


Figure 4.16: Watershed images of slices at (a) 50, (b) 150 (c) 250, (d) 350, (e) 450 and (f) 550 slices of Cottesloe beach.

4.2.7 Image cropping

Four (4) statistically representative volumes were crop from the main (987 X 1011 X 1007) voxels from Scarborough sand sample and (988 X 1012 X 991) voxels Cottesloe sand sample cubes. 3D filtered and segmented volumes of Scarborough and Cottesloe sand samples is subdivided into overlapping sub- cubes of four different sizes. Three (3) sub-cubes of size of $(700)^3$, 8 sub cubes of size of $(500)^3$, 13 sub cubes of size of $(350)^3$, and 20 sub cubes of size of $(200)^3$ (Figures 4.16(a) and 17 (a)) were cropped from the Scarborough sand images. Five

(5) sub cubes of $(700)^3$, 10 sub of size $(500)^3$, 13 sub of size $(350)^3$, and 24 sub cubes of $(200)^3$ (Figure 4.16s 4.16(b) and 17(b)) were also cropped from Cottesloe sand images. Table 4.1 gives the x, y, and z dimensions of the main $(700)^3$ cubes cropped for both Scarborough and Cottesloe images from which the sub cubes of $(500)^3$ $(350)^3$ $(200)^3$ were cropped at random and their dimensions are given on Table 4.2

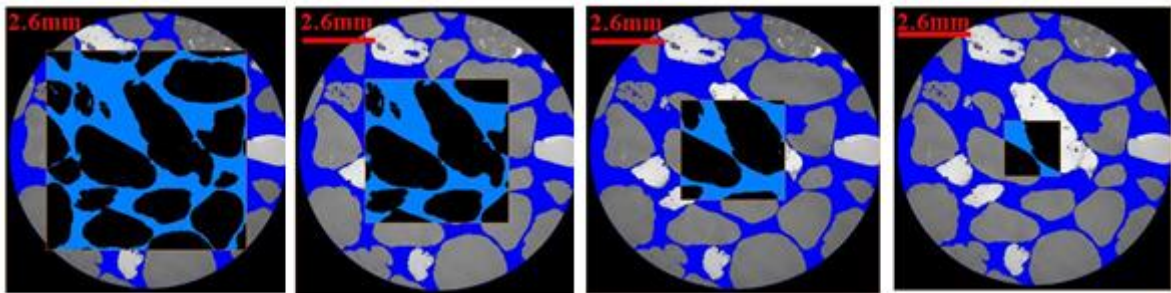
Table 4.1: X, Y and Z cropping dimensions of $(700)^3$ cubes of Scarborough and Cottesloe beach samples

$(700)^3$ dimensions									
Cube no	1			2			3		
Axis	X	Y	Z	X	Y	Z	X	Y	Z
Maximum	144	156	145	116	112	145	144	112	145
Minimum	843	855	844	815	811	844	843	811	843

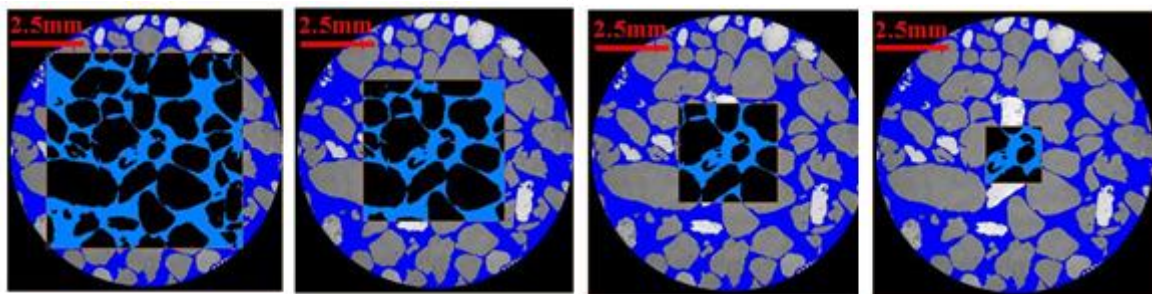
Table 4.2: X Y and Z cropping dimensions of $(500)^3$, $(350)^3$ and $(200)^3$ cubes of Scarborough and Cottesloe beaches.

$(500)^3$ dimensions															
Cube no	1			2			3			4			5		
Axis	X	Y	Z	X	Y	Z	X	Y	Z	X	Y	Z	X	Y	Z
Min	200	200	0	100	200	0	200	100	0	200	200	100	200	200	200
Max	700	700	500	600	700	500	700	600	500	700	700	600	700	700	700
Cube no	6			7			8								
Axis	X	Y	Z	X	Y	Z	X	Y	Z						
Min	100	100	200	0	200	200	0	100	200						
Max	600	600	700	500	700	700	500	600	700						
$(350)^3$ dimensions															
Cube no	1			2			3			4			5		
Axis	X	Y	Z	X	Y	Z	X	Y	Z	X	Y	Z	X	Y	Z
Min	300	300	0	200	350	0	350	350	0	200	200	0	300	300	350
Max	650	650	350	550	700	350	700	700	350	550	550	350	650	650	700
Cube no	6			7			8			9			10		
Axis	X	Y	Z	X	Y	Z	X	Y	Z	X	Y	Z	X	Y	Z
Min	0	300	0	350	0	0	0	100	200	0	0	0	0	350	0
Max	350	650	350	700	350	350	350	450	550	350	350	350	350	700	350
Cube no	11			12			13								
Axis	X	Y	Z	X	Y	Z	X	Y	Z						
Min	200	200	200	200	200	350	300	300	300						
Max	550	550	550	550	550	700	650	650	650						
$(200)^3$ dimensions															
Cube no	1			2			3			4			5		
Axis	X	Y	Z	X	Y	X	Y	Z	X	Y	X	Y	Z	X	Y
Min	500	500	0	300	400	500	500	0	300	400	500	500	0	300	400
Max	700	700	200	500	600	700	700	200	500	600	700	700	200	500	600

Cube no	6			7			8			9			10		
Axis	X	Y	Z	X	Y	Z	X	Y	Z	X	Y	Z	X	Y	Z
Min	200	100	100	500	400	400	200	200	200	0	500	500	500	500	0
Max	400	300	300	700	600	600	400	400	400	200	700	700	700	700	200
Cube no	11			12			13			14			15		
Axis	X	Y	Z	X	Y	Z	X	Y	Z	X	Y	Z	X	Y	Z
Min	300	0	0	300	0	100	500	0	100	300	400	400	400	400	0
Max	500	200	200	500	200	300	700	200	300	500	600	600	600	600	200
Cube no	16			17			18			19			20		
Axis	X	Y	Z	X	Y	Z	X	Y	Z	X	Y	Z	X	Y	Z
Min	250	0	200	250	250	250	400	400	400	300	300	300	200	200	200
Max	450	200	450	450	450	450	600	600	600	500	500	500	400	400	400

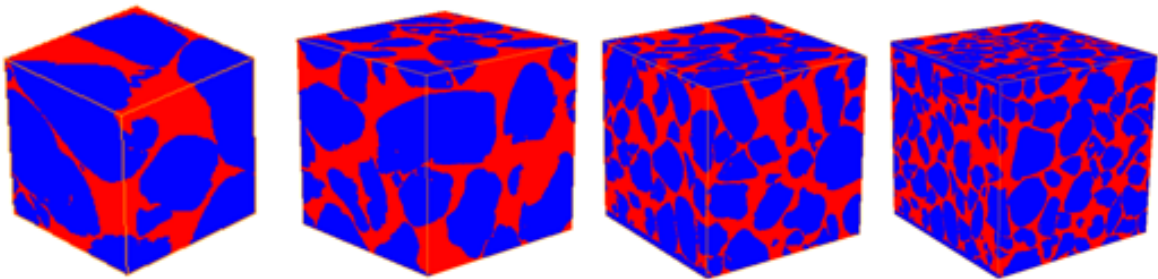


(a)

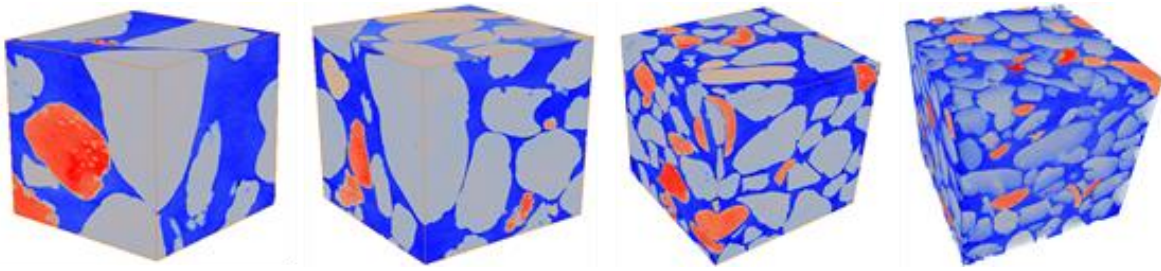


(b)

Figure 4.17: 2D sub-volume of $(700)^3$, $(500)^3$, $(350)^3$, and $(200)^3$ cubes for (a) Scarborough and (b) Cottesloe samples.



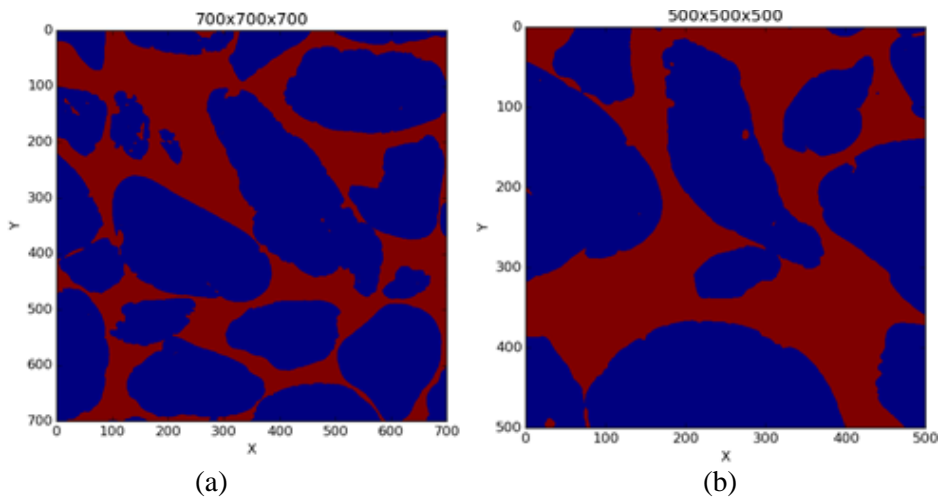
(a)



(b)
Figure 4.18: 3D sub-volume of $(700)^3$, $(500)^3$, $(350)^3$, and $(200)^3$ cubes for (a) Scarborough and (b) Cottesloe samples.

4.2.8 Pre-processing

The 96 cube images from Scarborough and Cottesloe were pre-processed using the Pawsey super-computing. I use my account to assess the super computer. The conductivity saved file are accessed and processed using a command and the result of the pre-processing produces the binary image of the CT scan images. An example of the binary images from Scarborough and Cottesloe CT-scan image sample from $(700)^3$, $(500)^3$, $(350)^3$, and $(200)^3$ are shown in Figure 4.18 and Figure 4.19. These binary images show the grains in blue colour while the red shows the pore and the results of these binary image cubes saved for processing the conductivity of each cube.



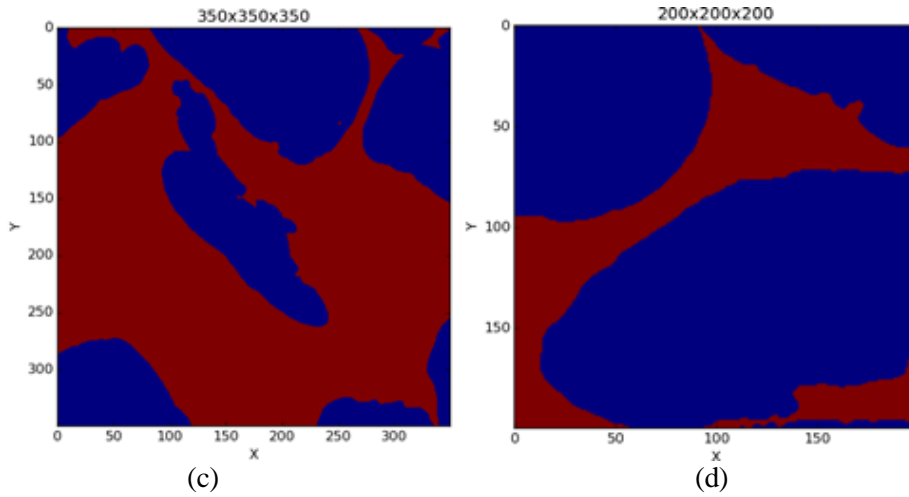


Figure 4.19: Binary image (a) 700, (b) 500, (c) 350, and (d) 200 cubes of Scarborough beach sample

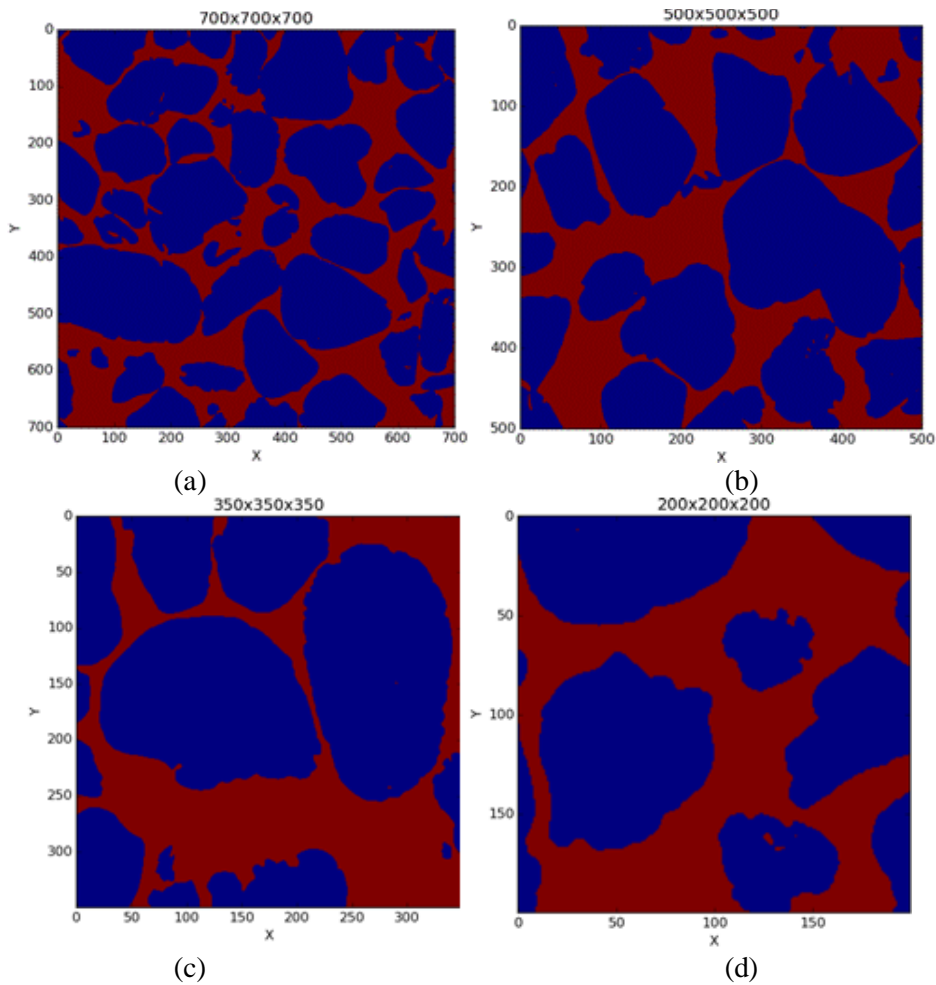


Figure 4.20: Binary image (a) 700, (b) 500, (c) 350, and (d) 200 cubes of Cottesloe beach sample

Details of binary images of all the cubes is presented at appendixes (Figures A 2.1, 2.2, 2.3, 2.4, 2.5, 2.6 and 2.7 for Scarborough and Cottesloe clean sand images)

4.3 Clay sand

4.3.1 Loading the image

Reconstructed images are limited to spatial resolution and affected by image artefacts; but already I was able to distinguish between pore, quartz, clay, and carbonate. Image artefacts that occurred mostly in samples were inhomogeneity in grey values, streaks resulting from bad rotation alignment and edge enhancement. Figure 4.20 shows the loaded raw image, with colour map ranging from zero to 65535.

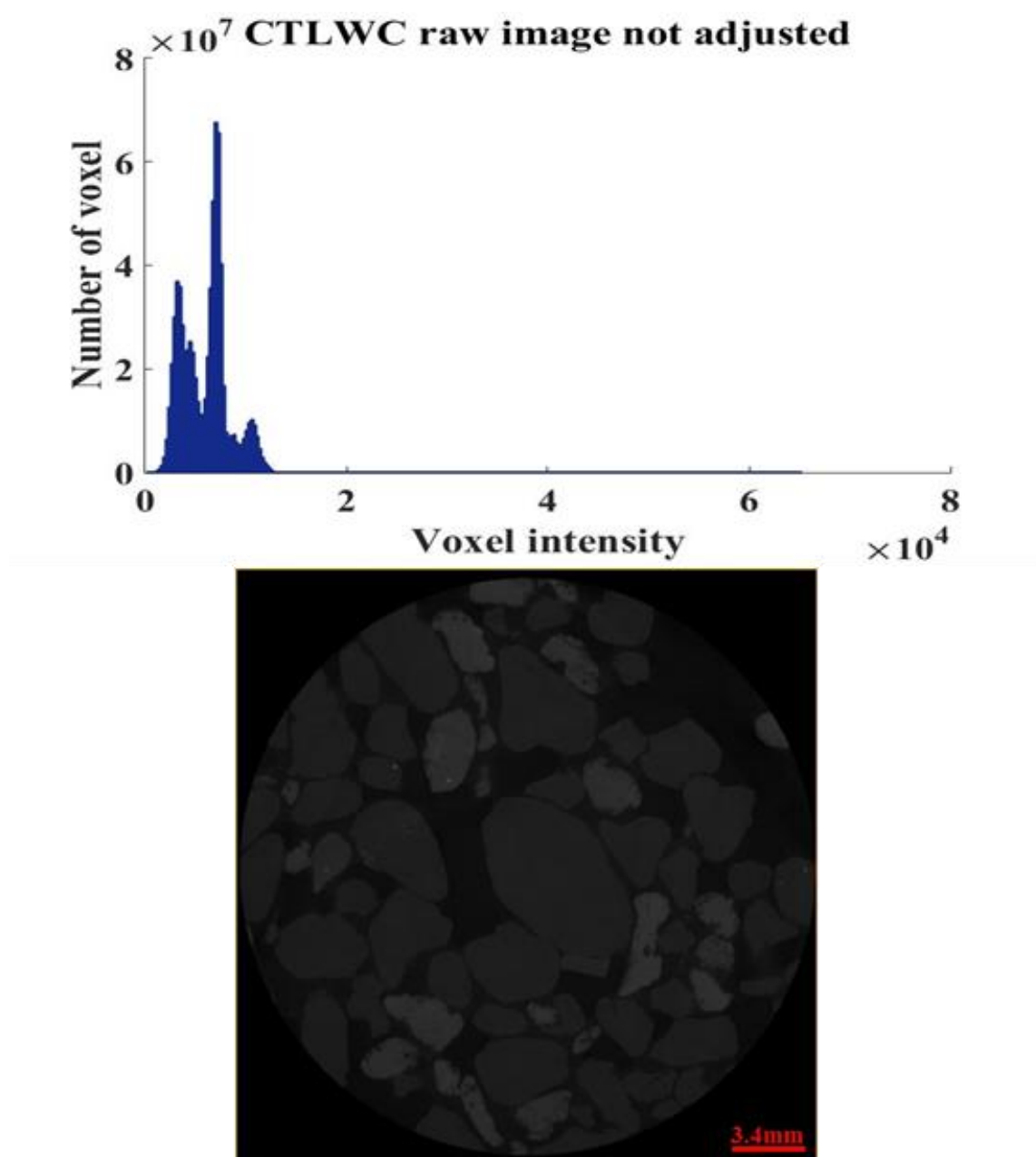


Figure 4.21: Loaded Cottesloe clay sand raw image with 1.3739μ resolution before adjusting the colour map.

Raw image loaded must be adjusted to view the image clearly; this is achieved by adjusting the colour map to the actual image view by adjusting the slide bar. The Cottesloe clay image has colour map range of 1365 – 12970 (Figure 4.21).

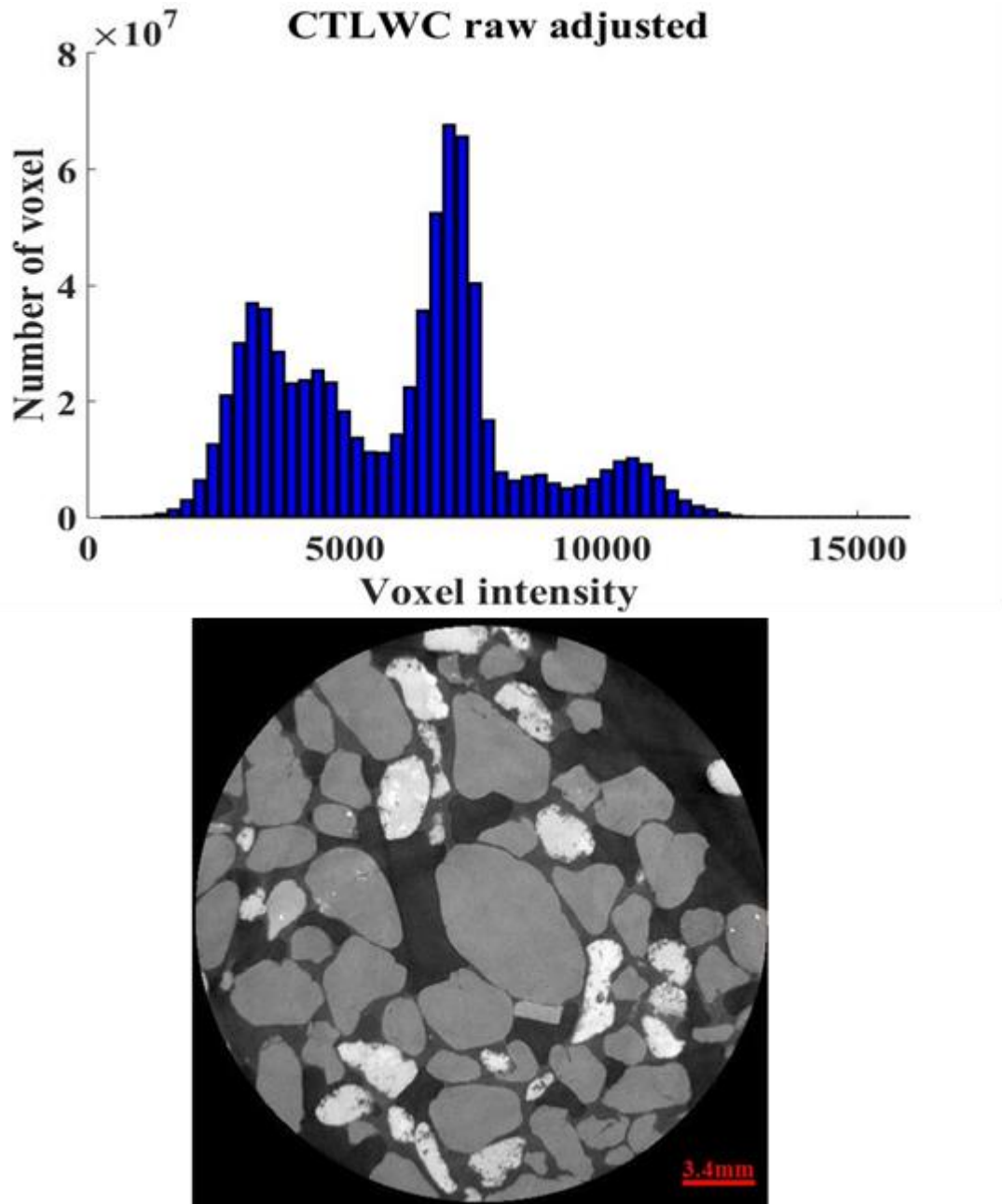


Figure 4.22: Adjusted raw loaded Cottesloe clay raw image after adjusting the colour map.

4.4.2 Image filtering

I used software package Avizo fire 9 (FEI Visualization Sciences Group) for image enhancement and segmentation. It is essential to deploy same enhancement steps and

parameters for each digitally sampled sub-volume. I tried four different filters, amongst the digital image filter tools that are available for enhancing the image quality (based on features and sophisticated algorithm. These filters have effects on the results depending on the image (imputed) and the controlling parameters. Figure 4.22 shows the images of bilateral, curvature driven, anisotropic and edge preserving filtered images with their calculated porosities

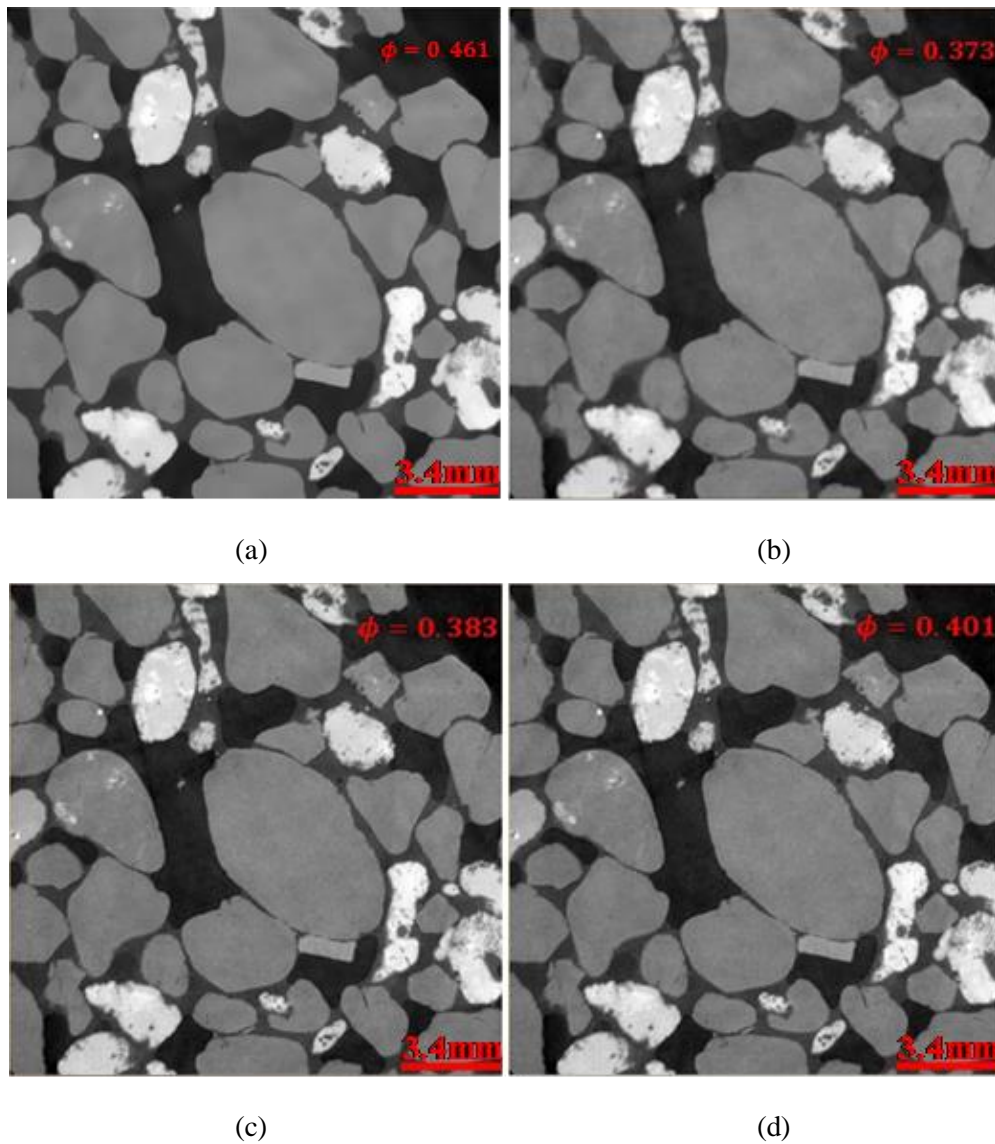
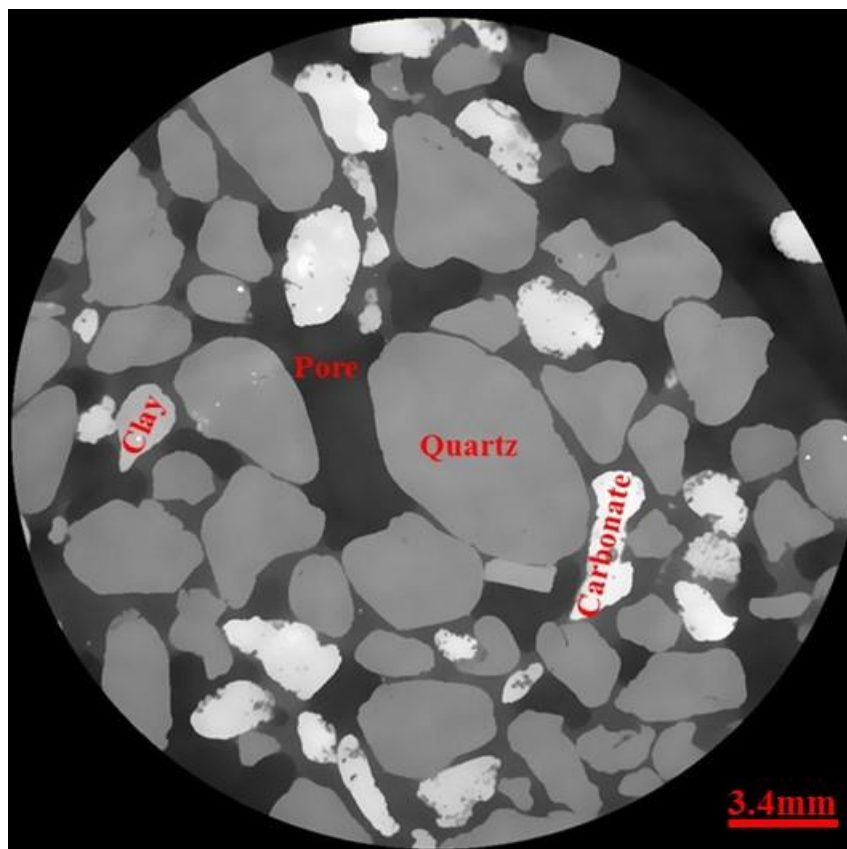


Figure 4.23: Different filters of Cottesloe shaly sand (a) Bilateral, (b) Curvature driven, (c) Anisotropic (d) Edge preserving filter.

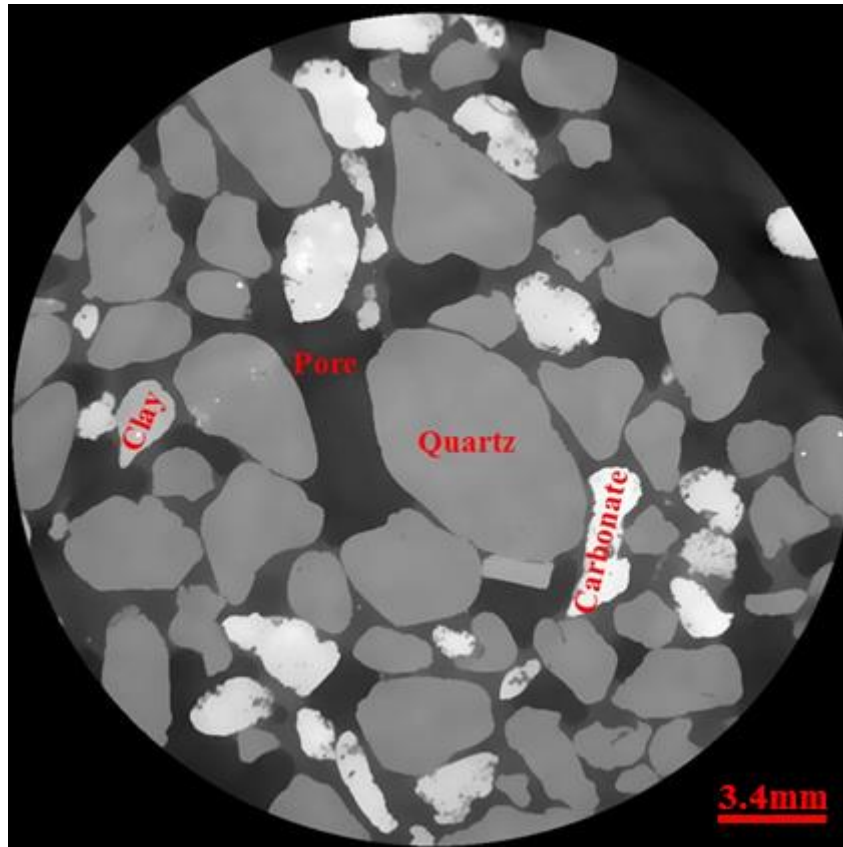
4.3.2.1 Non-Local filter

Grey-scale images of 2D were image processed using the non-local filter in intensity with the range of 1365–12970 for the raw image of Cottesloe clay-sand. Non-Local filter applied on raw images with aim of removing concentric shadows in images and properly enhancing

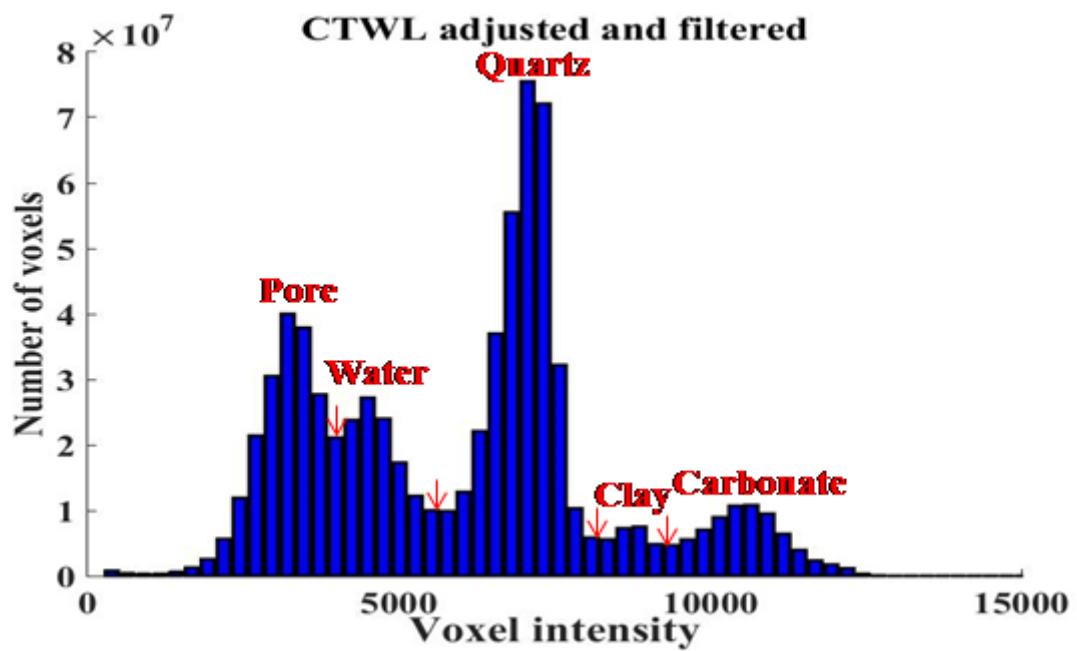
interface between pores and grains as well as removing noise. Preliminary study on the effect of various image filters on the images result makes it necessary to determine the best option of filter with the aim of getting a high quality-image (Avizo 8 user's guide). High quality images will result into getting good rendered volumes as well as obtaining accurate computations from the images. Due to complex nature of the Cottesloe clay sand image, a double Non-Local filter applied on the raw image in XY plane with the local neighbourhood of five, similarity of 0.3 and an adaptive true gave a good quality image Figure 4.23(a). However, another Non-Local filter applied on the first filtered image with a neighbourhood of two (2), similarity of 0.01 and an adaptive true gave an excellent quality image Figure 4.23(b). Shown in Figure 4.23(c) is the histogram of materials from the Cottesloe clay sand after adjusting.



(a)



(b)



(c)

Figure 4.24: Non-local filter (a) single filter with neighbourhood 21 and similarity 0.6 (b) double filter with neighbourhood 2 and similarity 0.3.

4.3.3 Image segmentation

Applying image segmentation on filtered images is to establish objects and boundaries (lines, curves etc.) on images. More precisely, image segmentation is the process of assigning a label to each voxel in the image such that voxels with the same label share certain characteristics. Due to the complexity of the shaly sand of Cottesloe sample, I employed the use of multi-threshold segmentation on the image.

4.3.3.1 Multi-threshold

Due to the complex nature of the clay sand image, I employed the multi-segmentation algorithm but the segmentation did not yield good result because there is outgrowth of quartz around the clay and carbonate. I tried changing the boundaries between the quartz and clay that can separate the two materials. However, all effort proves abortive, Figure 4.24 is the best image result of the multi-segmentation of the clay sand from Cottesloe sample. The light blue shows the pore, the deep blue shows the quartz, the red shows the clay while green show the carbonate.

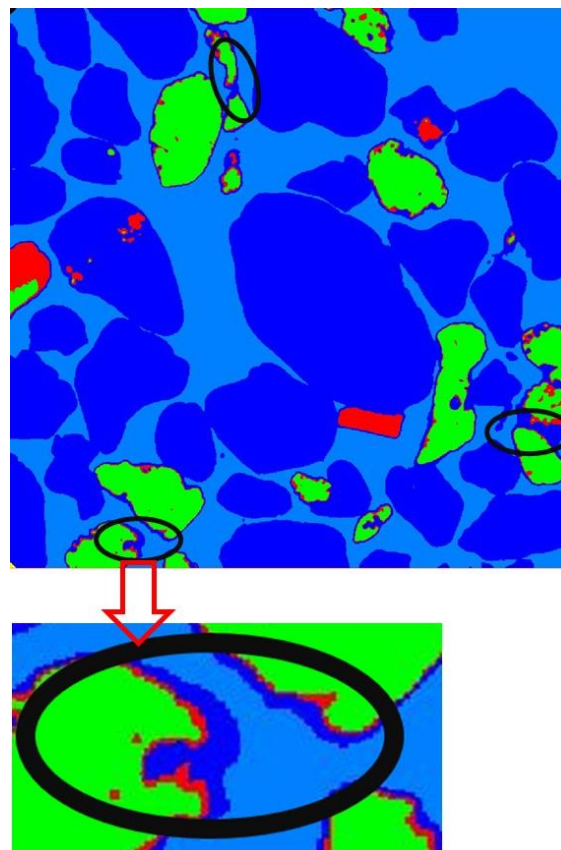


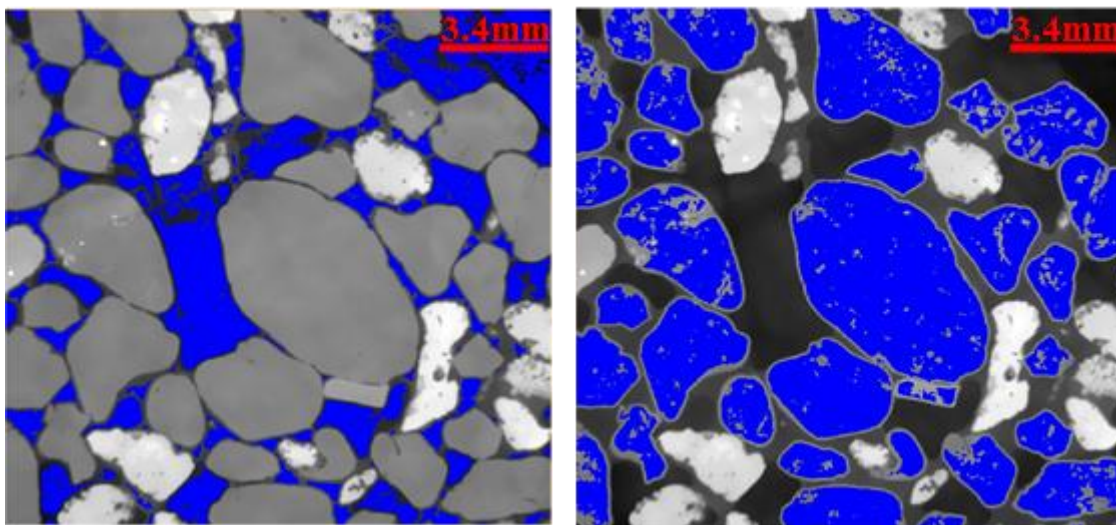
Figure 4.25: Multi-segmentation showing 700 cube of the Cottesloe clay sand image with the quartz (deep blue colour) surrounding both the clay and carbonate with examples shown in black circles.

4.3.4 Watershed segmentation

I applied watershed segmentation for the Cottesloe clay sand sample. Instead of calculating the porosity of the micro CT scan images from global threshold segmentation, I calculated the porosity after watershed segmentation. Since there are four components (pore, quartz, clay and carbonate), the number of phases is set to four for the water segmentation and is run one after the other, I start by applying the water segmentation with the range of the pore from 255 to 5875 (Figure 4.26 4.25(a)).

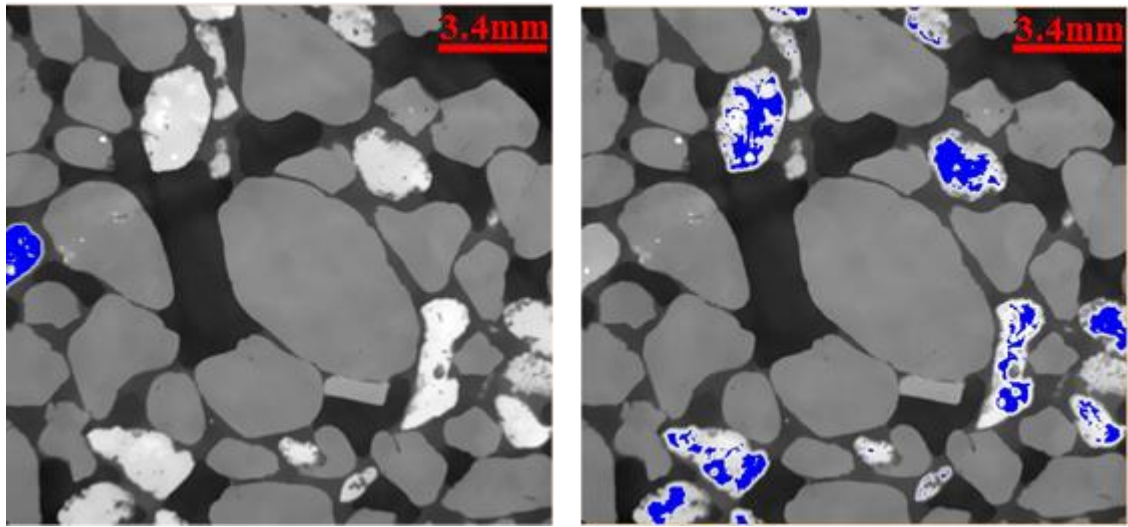
After processing the pore, the quartz is also process with the watershed with a range of 5895 to 8769 the watershed segmentation processes the quartz and which turns blue as shown in Figure 4.25(b).

Clay watershed segmentation done with a range of 8769 to 9975 and after processing; the clay turns blue as shown in Figure 4.25(c) and finally the carbonate is processed by the watershed segmentation and it turns blue Figure 4.25(d).



(a)

(b)

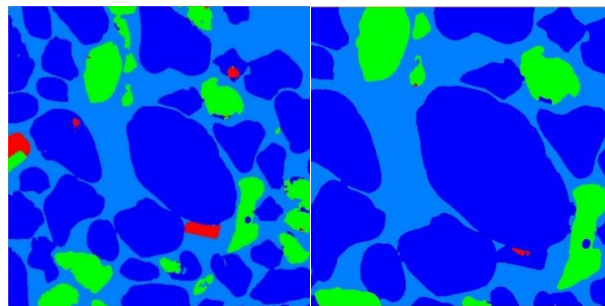


(c)

(d)

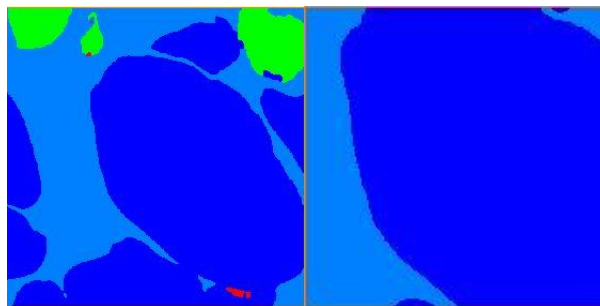
Figure 4.26: Region of watershed segmentation (a) pore (b) quartz (c) clay and (d) carbonate of Cottesloe beach sample.

The result of watershed segmentation is the basin which is a label image in which each component is assigned a label field and the output of the image is presented in Figure 4.26 for $(700)^3$, $(500)^3$, $(350)^3$, and $(200)^3$



(a)

(b)



(c)

(d)

Figure 4.27: Watershed segmented image of Cottesloe with 3% clay (a) 700 (b) 500 (c) 350 and (d) 200 cubes

Presented in Figure 4.27 is the histogram that show the voxel intensity of pore, quartz, clay and carbonate the legend on the right top corner p, q, cl, and c represent pore, quartz, clay and

carbonate respectively. After being satisfied with watershed segmentation, volume rendering of the image is applied Figure 4.28.

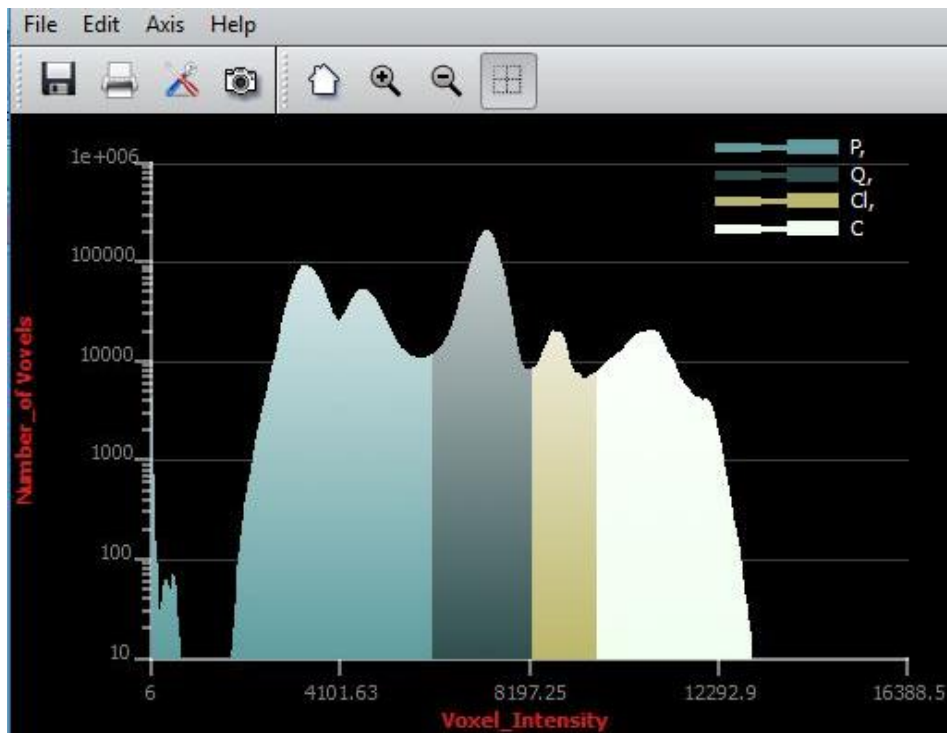


Figure 4.28: Histogram of Cottesloe mixed with 3% clay showing the best threshold for the pore, quartz, clay and carbonate.

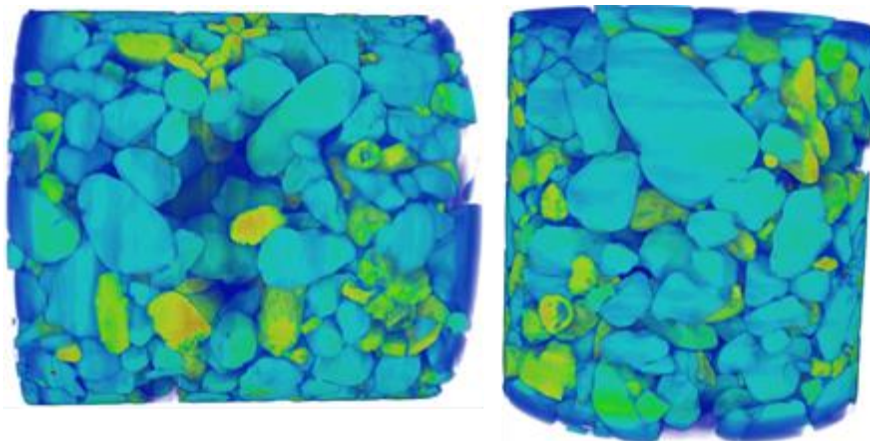


Figure 4.29: Rendered volume of the whole sample of Cottesloe shaly sand

After watershed segmentation, individual material volume rendering is applied and the outputs saved for grain size analysis. Presented in Figure 4.29 are the 3-D images of the pore, quartz, clay, carbonate and all the materials from the basins label fields of Cottesloe shaly sand (detail in Appendix A1.1, 1.2, 1.3, 1.4 and 1.5).

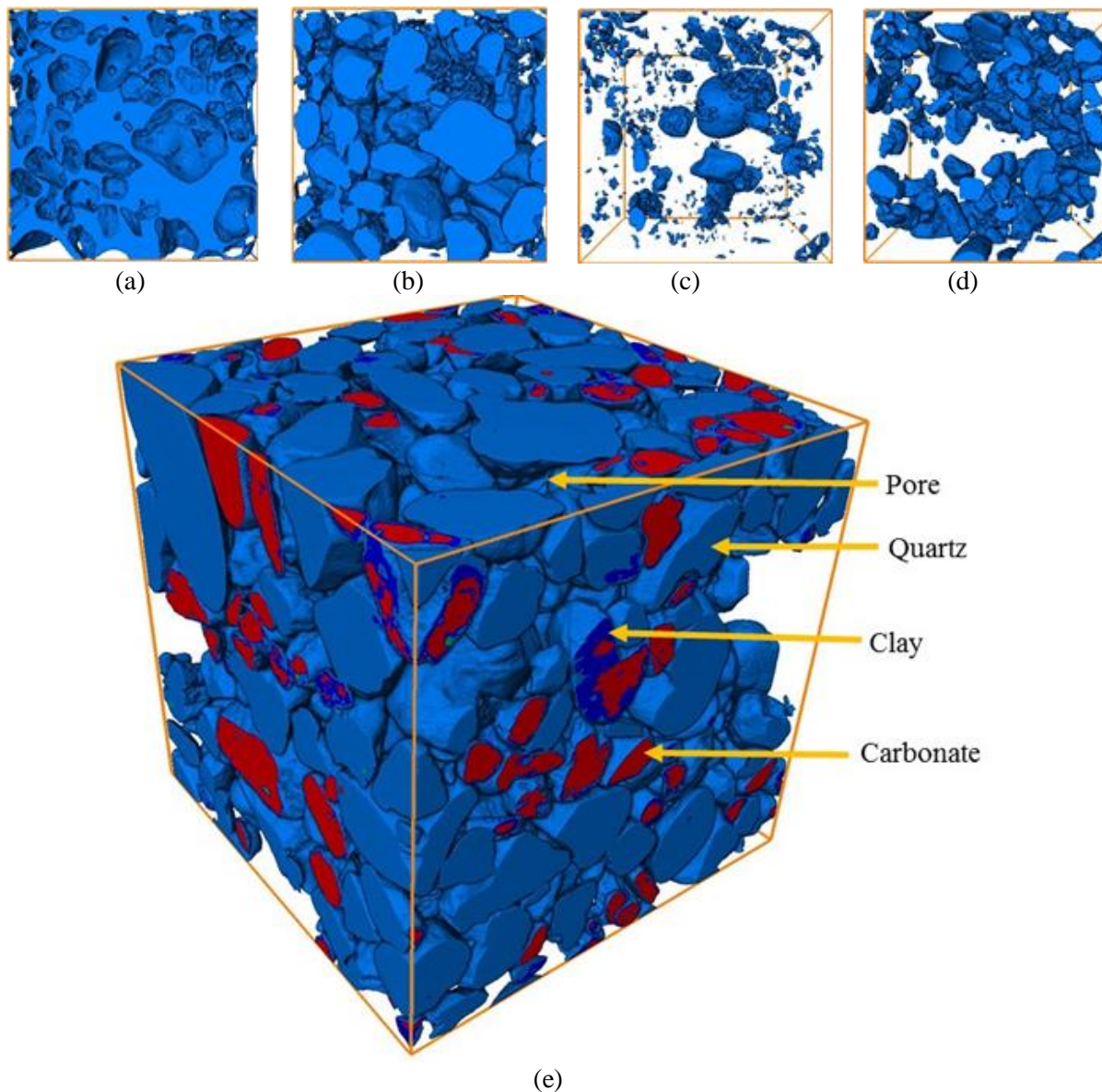


Figure 4.30: Cropped 700-cube volume rendering of (a) pore (b) quartz (c) clay and (d) carbonate of Cottesloe shaly sand.

4.3.5 Image cropping

In order to do the statistical computations of electrical properties of the clay sand sample, the main cube Figure 4.29€ is crop at random into seventy-eight (78) cubes. The cubes are made of four different sizes of cubes. These cubes are ten (10) cubes of $(700)^3$, fifteen (15) cubes of $(500)^3$, twenty-three (23) cubes of $(350)^3$ and thirty (30) cubes of $(200)^3$ an example is shown in Figure 4.30 and the cropping dimensions is shown on table 4.3.

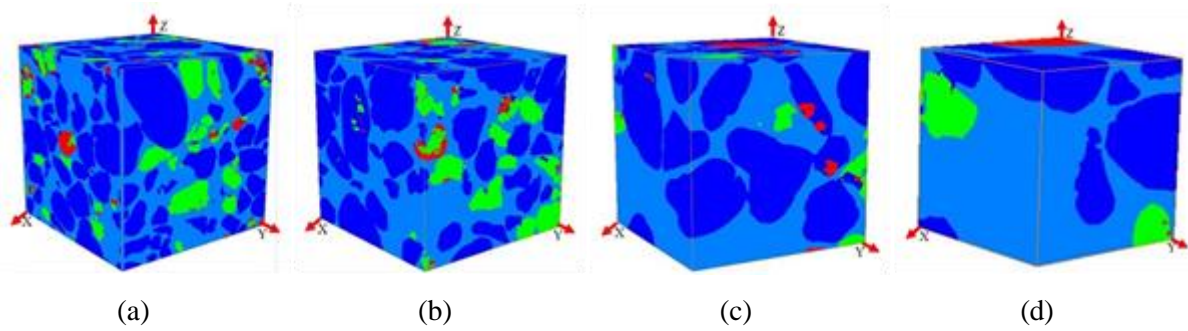


Figure 4.31: Cottesloe sand with 3% clay representative of 3D sub-volume (a) 700 (b) 500 (c) 350 and (d) 200 cubes.

Table 4.3: X Y and Z cropping dimensions of $(500)^3$, $(350)^3$ and $(200)^3$ cubes of Scarborough and Cottesloe beaches.

$(700)^3$ dimensions															
S/No	1			2			3			4			5		
Axis	X	Y	Z	X	Y	Z	X	Y	Z	X	Y	Z	X	Y	Z
Min	144	156	165	144	156	185	144	156	205	149	156	146	144	151	146
Max	843	855	864	843	855	884	843	855	904	848	855	845	843	850	845
S/No	6			7			8			9			10		
Axis	X	Y	Z	X	Y	Z	X	Y	Z	X	Y	Z	X	Y	Z
Min	149	151	175	140	156	165	144	156	165	149	151	165	144	146	175
Max	848	850	874	839	855	864	843	855	864	848	850	864	843	845	874
$(500)^3$ dimensions															
S/No	1			2			3			4			5		
Axis	X	Y	Z	X	Y	Z	X	Y	Z	X	Y	Z	X	Y	Z
Min	100	100	200	100	200	100	200	100	100	200	100	100	200	100	200
Max	599	599	699	599	699	599	699	599	599	699	599	699	699	599	699
S/No	6			7			8			9			10		
Axis	X	Y	Z	X	Y	Z	X	Y	Z	X	Y	Z	X	Y	Z
Min	150	150	150	100	200	150	200	150	100	150	100	200	0	0	0
Max	649	649	649	599	699	649	699	649	599	649	599	699	499	499	499
S/No	11			12			13			14			15		
Axis	X	Y	Z	X	Y	Z	X	Y	Z	X	Y	Z	X	Y	Z
Min	0	0	50	0	50	0	50	0	0	50	50	50	75	75	75
Max	499	499	549	499	549	499	549	499	499	549	549	549	574	574	574
$(350)^3$ dimensions															
S/No	1			2			3			4			5		
Axis	X	Y	Z	X	Y	Z	X	Y	Z	X	Y	Z	X	Y	Z
Min	100	300	300	50	300	200	0	100	200	200	100	300	350	0	0
Max	449	649	649	399	649	549	349	449	549	549	449	649	599	649	649
S/No	6			7			8			9			10		
Axis	X	Y	Z	X	Y	Z	X	Y	Z	X	Y	Z	X	Y	Z
Min	300	300	350	350	350	0	0	0	150	50	100	25	300	300	0
Max	649	649	699	699	699	349	349	349	499	399	449	374	649	649	349
S/No	11			12			13			14			15		
Axis	X	Y	Z	X	Y	Z	X	Y	Z	X	Y	Z	X	Y	Z
Min	350	250	350	25	25	25	75	75	75	50	50	25	75	25	75
Max	699	599	699	374	374	374	424	424	424	399	399	374	424	374	424
S/No	16			17			18			19			20		

Axis	X	Y	Z	X	Y	Z	X	Y	Z	X	Y	Z	X	Y	Z
Min	150	25	25	100	25	50	100	25	25	100	100	50	75	75	25
Max	499	374	374	449	374	399	449	374	374	499	499	399	549	449	649
S/No		21			22			23							
Axis	X	Y	Z	X	Y	Z	X	Y	Z						
Min	50	200	50	0	300	0	50	300	50						
Max	399	549	399	349	649	349	399	649	399						
(200)³ dimensions															
S/No		1			2			3			4			5	
Axis	X	Y	Z	X	Y	Z	X	Y	Z	X	Y	Z	X	Y	Z
Min	150	350	350	200	400	350	150	250	300	100	300	300	100	150	300
Max	349	549	549	399	599	549	349	449	499	299	499	499	299	349	499
S/No		6			7			8			9			10	
Axis	X	Y	Z	X	Y	Z	X	Y	Z	X	Y	Z	X	Y	Z
Min	250	350	350	150	250	300	150	150	250	200	100	250	400	350	100
Max	449	549	549	349	449	499	349	349	449	399	299	449	599	549	299
S/No		11			12			13			14			15	
Axis	X	Y	Z	X	Y	Z	X	Y	Z	X	Y	Z	X	Y	Z
Min	150	100	200	100	400	250	350	350	350	250	150	300	200	100	100
Max	349	299	399	299	599	449	549	549	549	449	349	499	299	299	399
S/No		16			17			18			19			20	
Axis	X	Y	Z	X	Y	Z	X	Y	Z	X	Y	Z	X	Y	Z
Min	100	100	200	350	300	350	400	350	250	400	400	400	200	150	100
Max	299	299	399	549	499	549	599	549	449	599	599	599	399	349	299
S/No		21			22			23			24			25	
Axis	X	Y	Z	X	Y	Z	X	Y	Z	X	Y	Z	X	Y	Z
Min	350	400	200	250	250	250	300	150	400	250	200	400	200	250	100
Max	549	599	399	449	449	449	499	349	599	349	449	399	399	449	299
S/No		26			27			28			29			30	
Axis	X	Y	Z	X	Y	Z	X	Y	Z	X	Y	Z	X	Y	Z
Min	150	150	150	250	150	300	150	250	100	100	150	100	400	100	200
Max	349	349	349	449	349	499	349	449	299	299	349	299	599	299	399

4.3.6 Pre-processing the image files

The 78 cube images shaly sand from Cottesloe was pre-processed using the Pawsey super-computing to produce the images in Figure 4.31 as well as the results of conductivity. Using the image and the conductivity result, the potential field variation is plotted as in Figure 4.32

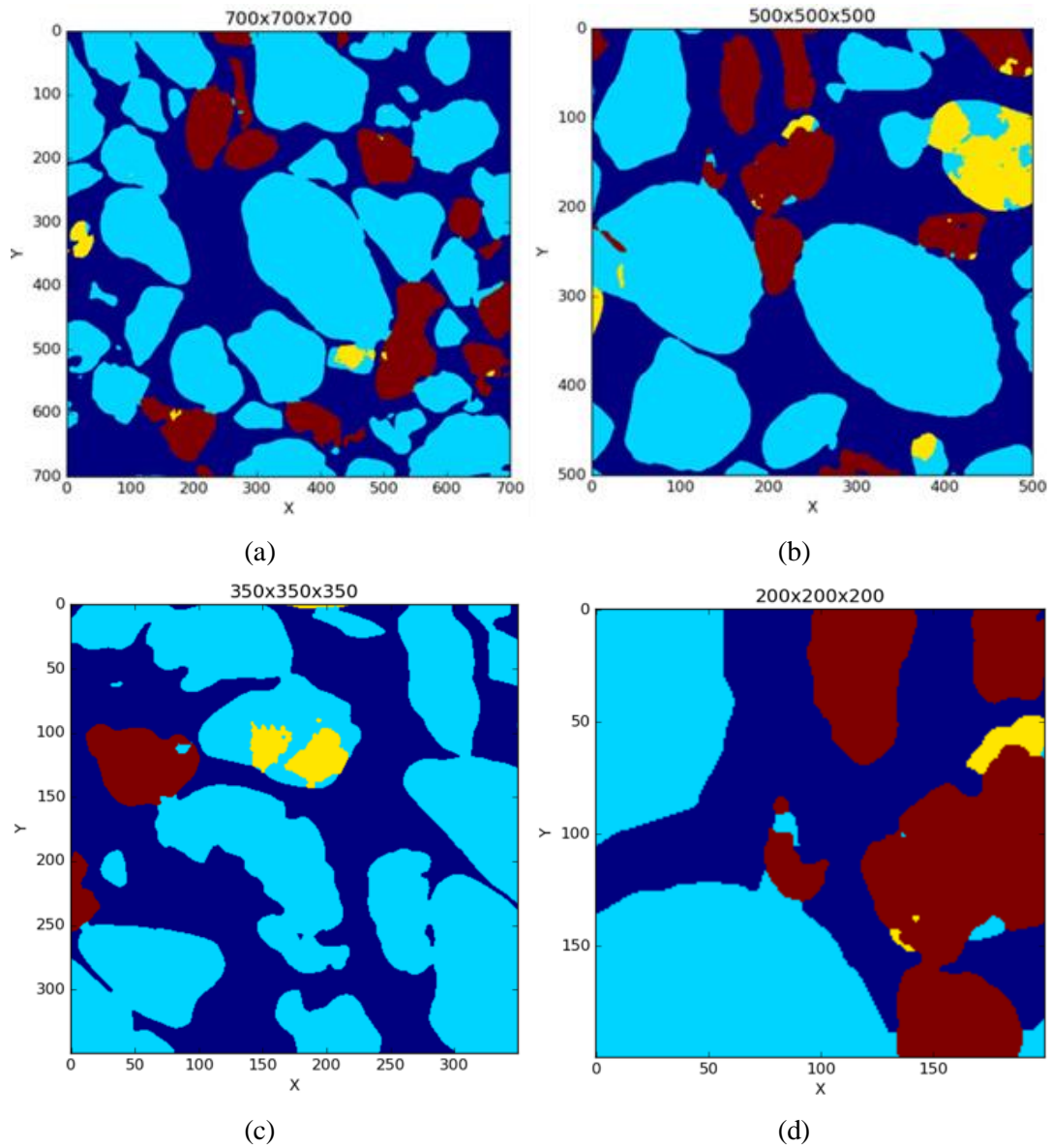
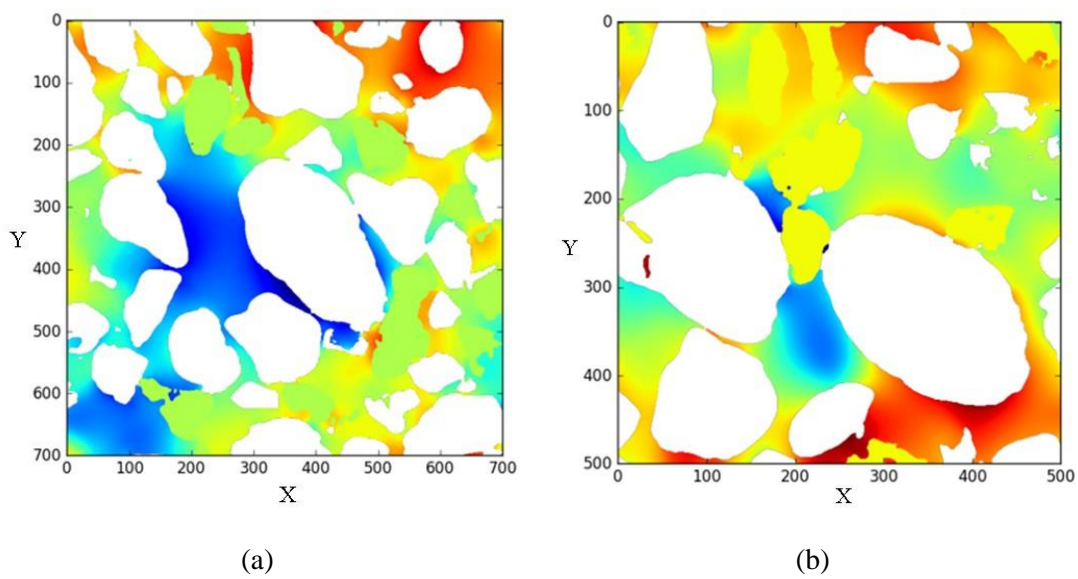
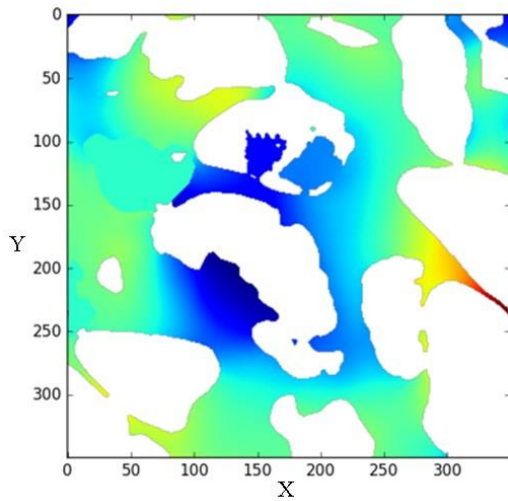
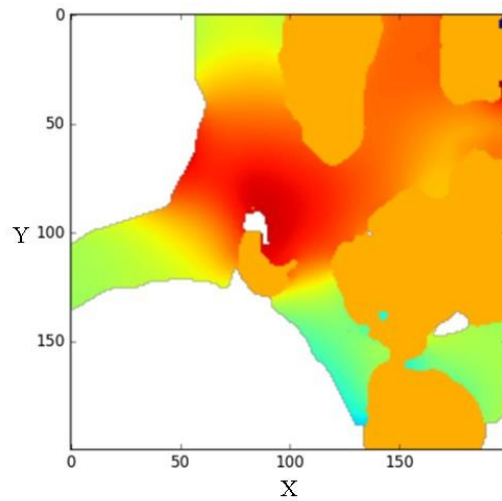


Figure 4.32: Cottesloe shaly sand showing the pore (blue), quartz (light blue), clay (yellow) and Carbonate (maroon) (a) 700 (b) 500 (c) 350 and (d) 200 cubes.





(c)



(d)

Figure 4.33: Cottesloe with clay sand showing potential field variation of (a) 700 (b) 500 (c) 350 and (d) 200 cubes.

4.4 Conclusion

In this chapter, I have discussed broadly two aspects: the images of the clean sand (from Scarborough and Cottesloe) and the images of the clay sand (from Cottesloe) images. Both the clean and clay sand took the same format of presentation in which I discussed the processes involved from the image acquisition then followed by the different filtering methods I used to filter the images before selecting the best filtering technique. Following the filtering image is the segmentation of the image; this involves separating the different materials in the image by assigning different label to each material. Watershed segmentation is the best option of segmentation that works very well on the clay sand image. After segmentation, the image is crop into a total of 174 cubes of 96 cubes from the clean sand of Scarborough and Cottesloe images while 78 cubes is from Cottesloe clay sand images. These cubes are the statistical representatives of the images ready for analysing the effective electrical conductivity. Finally, in this chapter a brief presentation of the image pre-processing is presented. In the next chapter, I will be presenting the laboratory and micro CT scan computation and results of the research works.

Chapter 5

Results from laboratory and micro-CT scan images

5.1 Introduction

In this chapter, I will present my results from the laboratory (flow and static cells) from Tow Rocks, Scarborough and Cottesloe Beaches and the micro CT-scan images of 96 cubes of four different sizes of 200^3 , 350^3 , 500^3 and 700^3 followed by the grain size analysis. Also presented here are the electrical computations (or electrical formation factor), which are the objective of this work. The slope of the electrical conductivity of water against the electrical conductivity of the formation gives the formation factor.

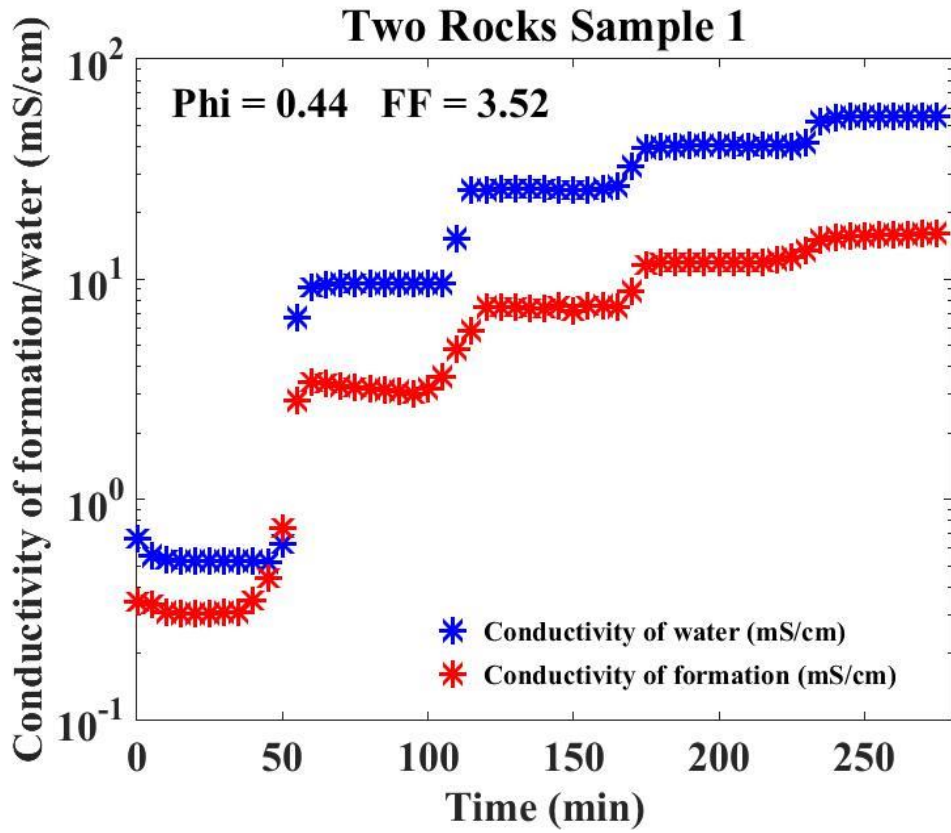
Results of micro CT-scan images of 96 cubes from the Scarborough and Cottesloe samples are analysed and presented in this chapter with 44 cubes of micro CT-scan images from Scarborough and 52 from Cottesloe. The resistivity of sand depends on porosity, texture, mineralogy and the pore fluid. This study shows that although pore geometry affects the formation factor, porosity is the primary factor affecting the formation factor. Archie was the first to demonstrate that the ratio of conductivity of pore fluid to bulk conductivity of fully saturated clean sands gives the formation factor. Digital rock physics combines modern microscopic imaging with advanced numerical simulations to analyse the physical properties of sands. Micro CT-scan images at the micro level (μm) and laboratory electrical methods at the macro level (cm) can contribute in different ways to characterizing sand samples.

5.2 Laboratory (clean sand)

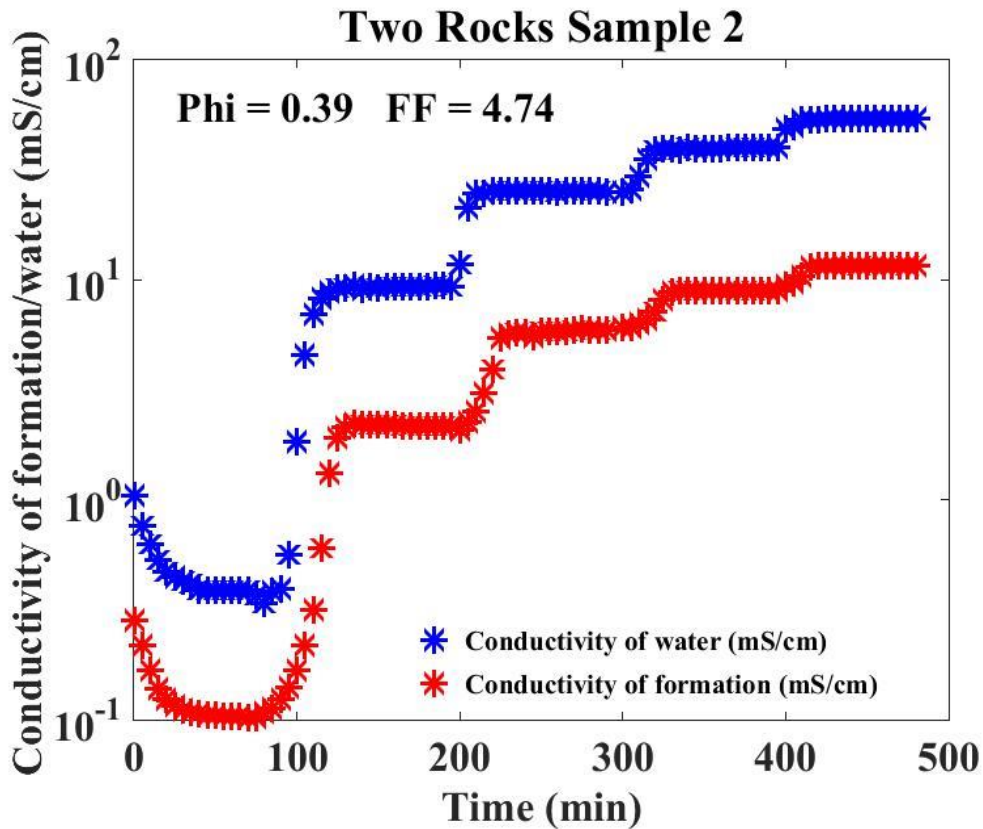
5.2.1 Flow cell

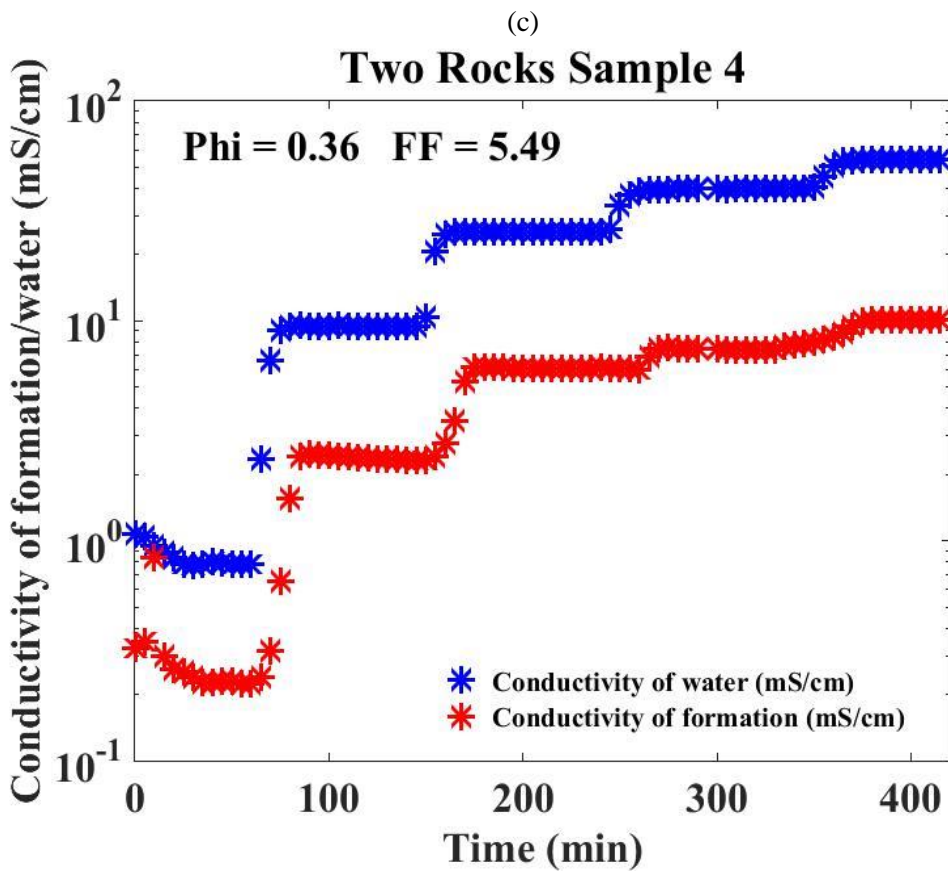
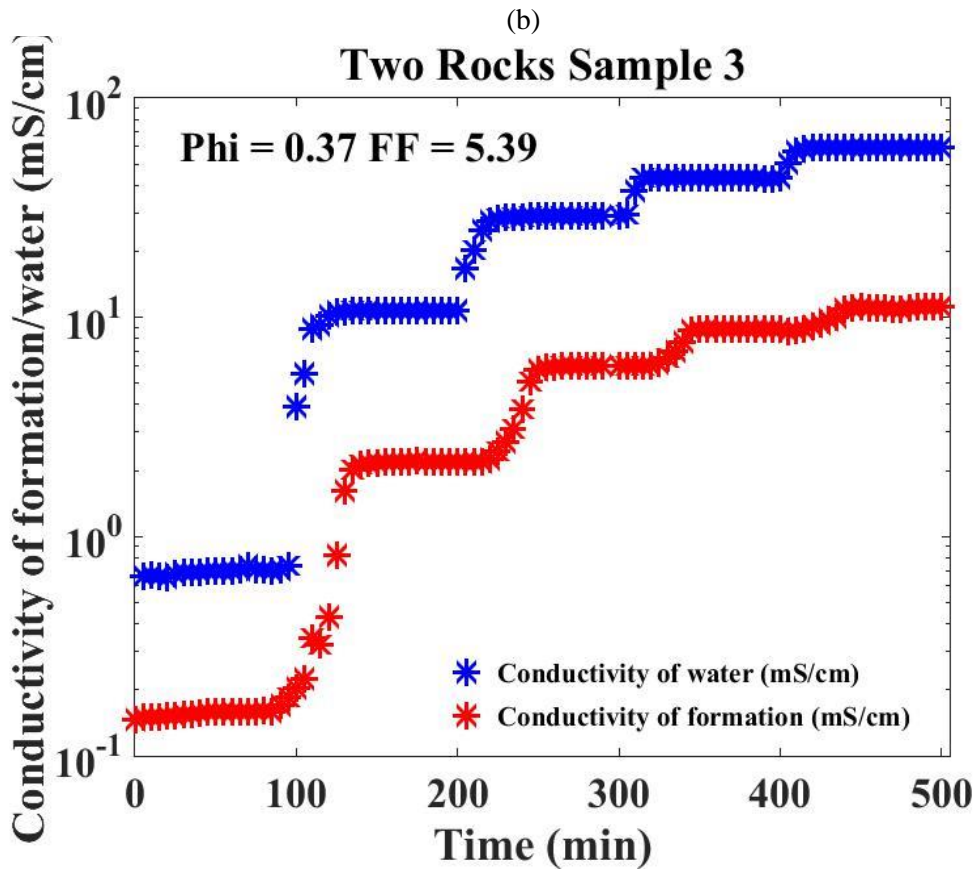
The plots of the electrical conductivity of the formation and the electrical conductivity of water against time for five samples of the Two Rocks Beach sample, two samples from Scarborough Beach and one sample from Cottesloe Beach are shown in Figures 5.1.1 and 5.1.2, 5.1.3 and 5.1.4 respectively. When both the electrical conductivity of the formation and the electrical conductivity of the water stabilizes, the average reading of five values taken as the electrical conductivity of the formation and the electrical conductivity of water for each salinity.

5.2.1.1 Two Rocks results

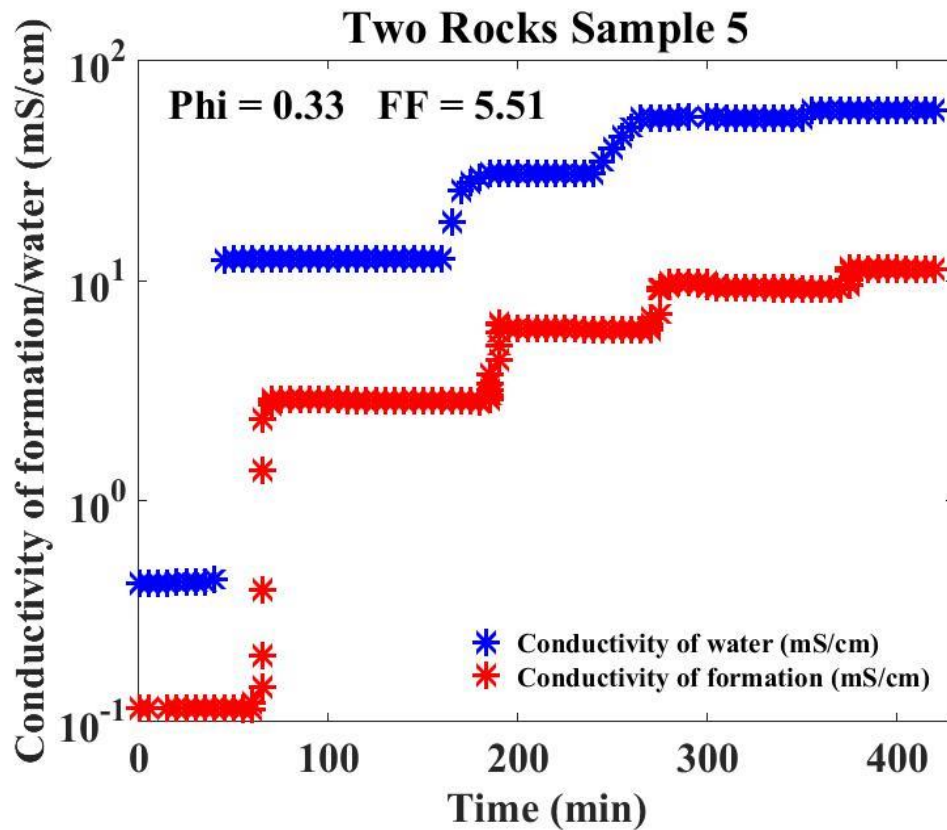


(a)





(d)

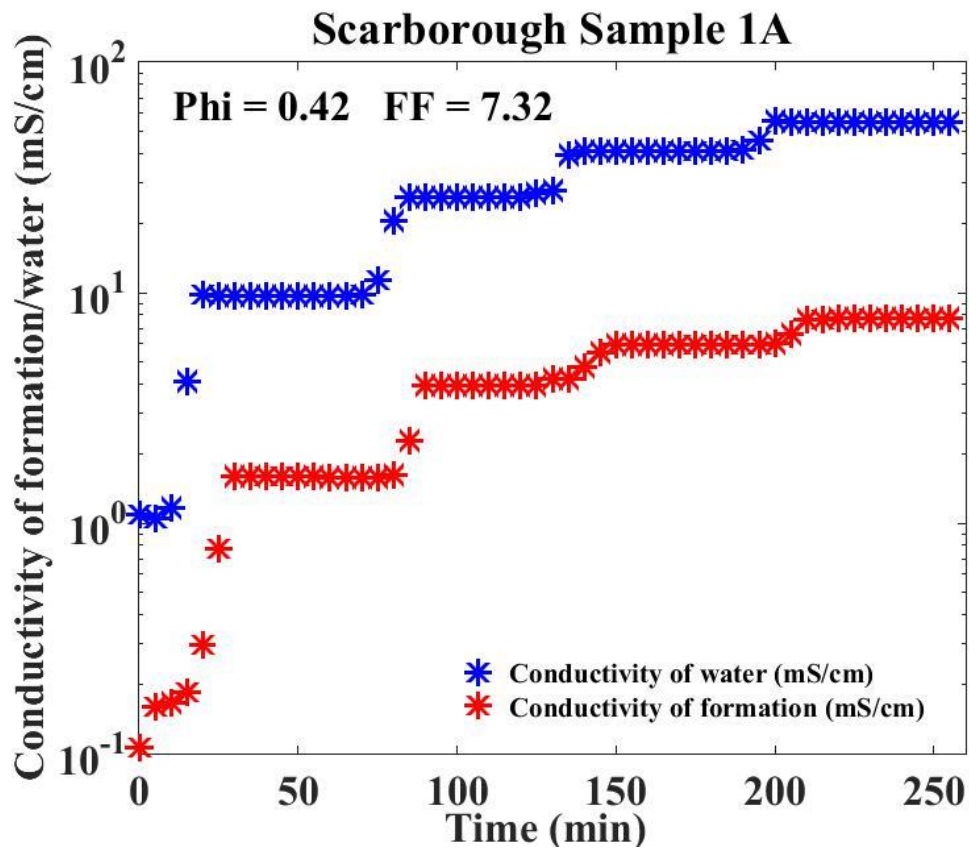


(e)

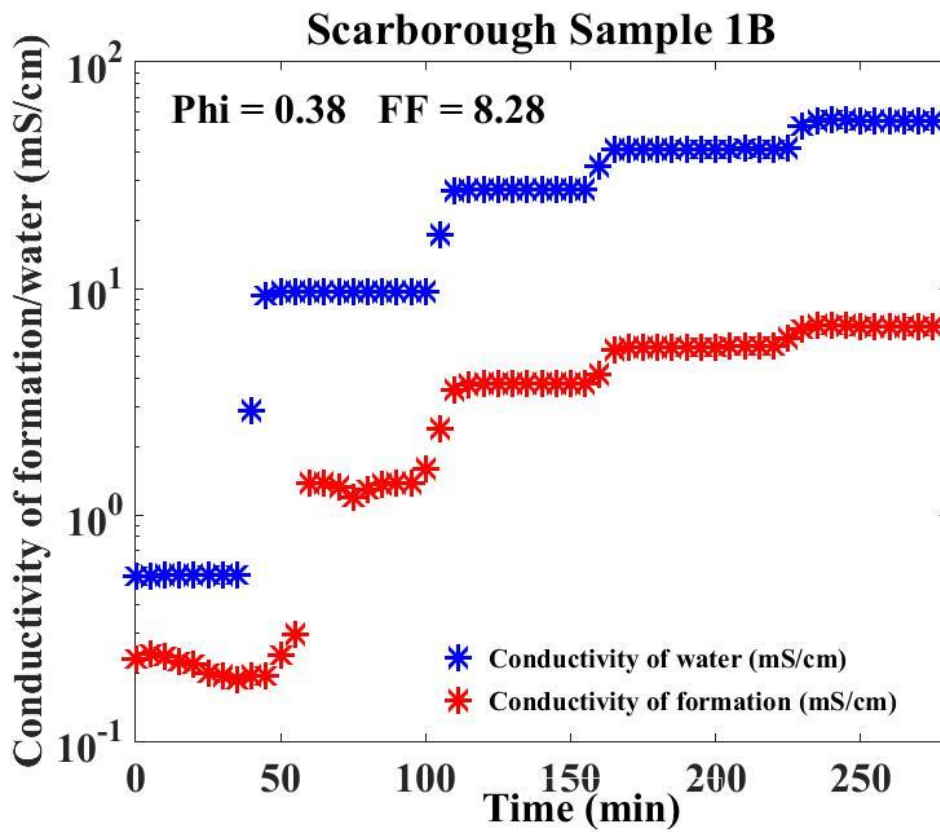
Figure 5.1.1: Graph of the electrical conductivity of the formation and the electrical conductivity of water and against time from flow cell measurements of Two Rocks samples.

In figure 5.1.1b and 5.1.1d, the experiment shows a decrease in electrical conductivity at the beginning of the experiment instead of an increase (Two Rocks samples 2 and 4). This is because the sample collected from the beach was not completely cleaned with fresh water to get rid of the saline water in the sand sample before I started taking measurements; the conductivity began to stabilize after about 30 minutes.

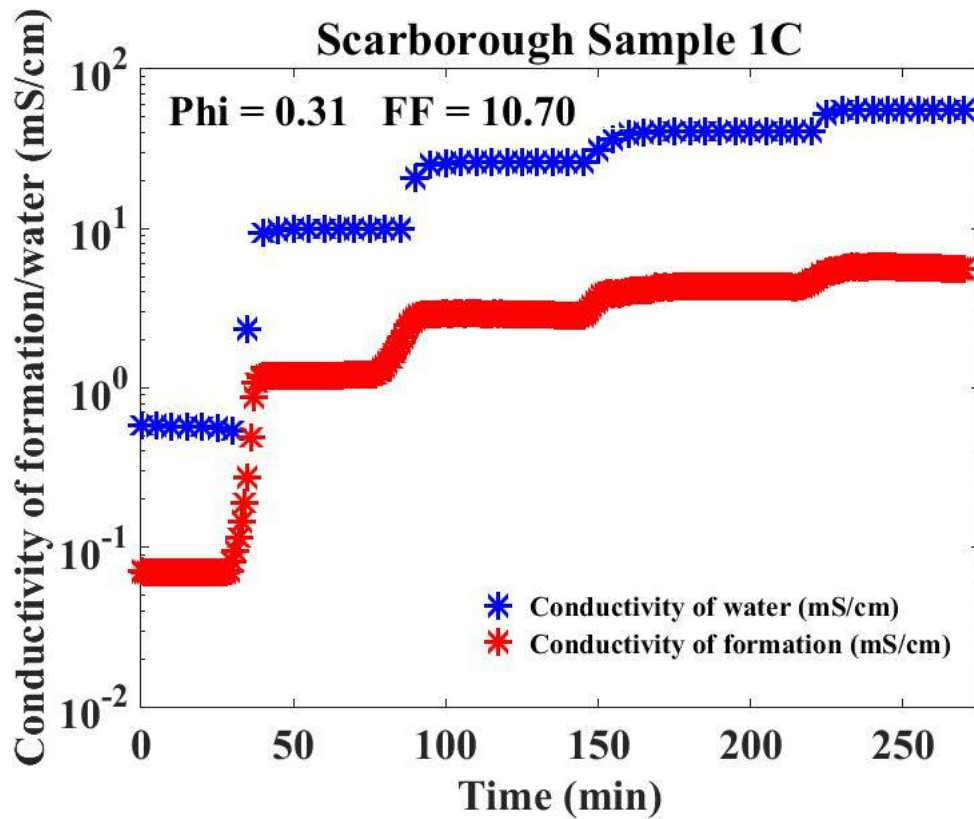
5.2.1.2 Scarborough results



(a)



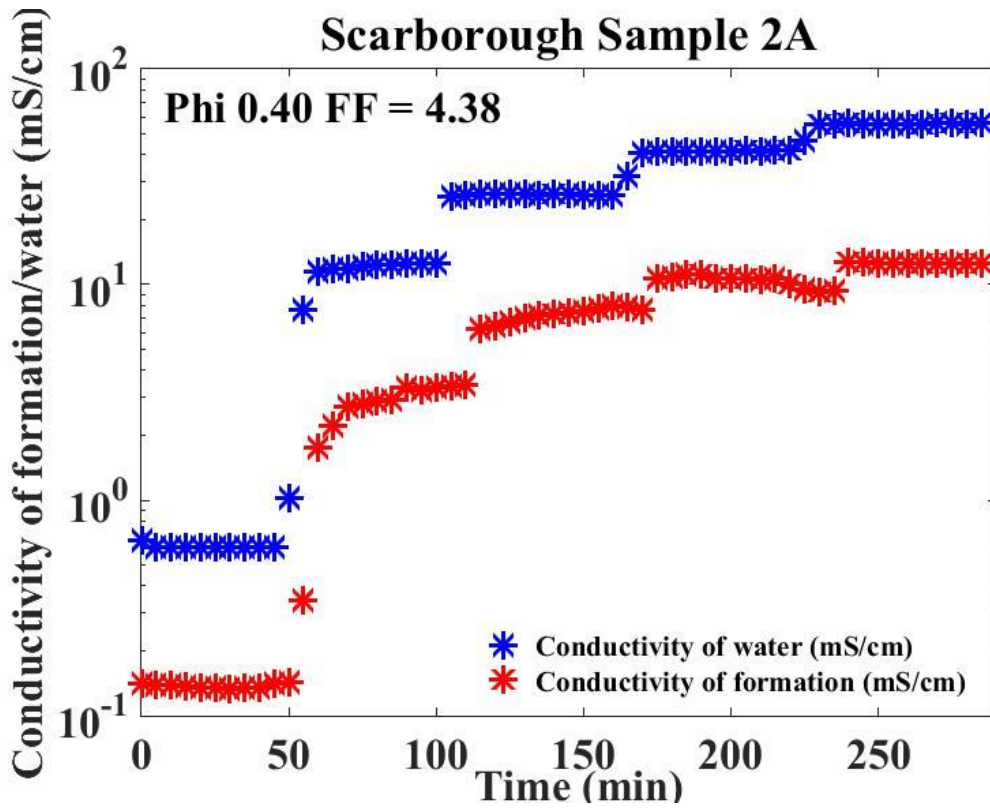
(b)



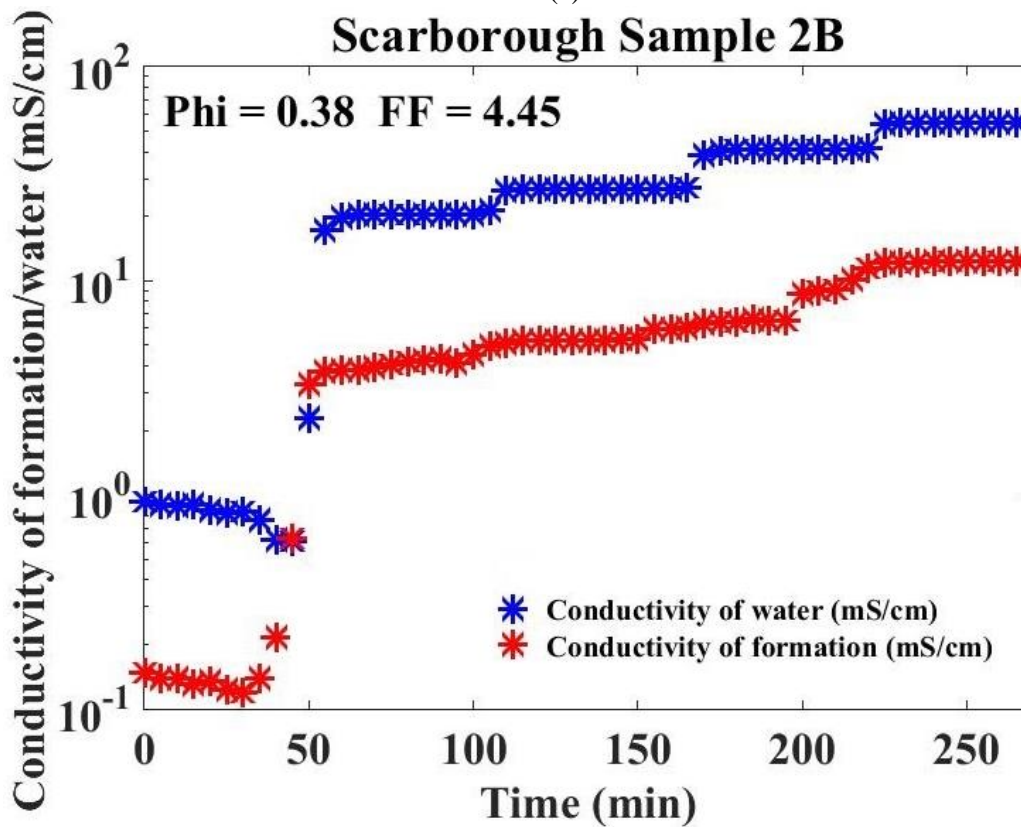
(c)

Figure 5.1.2: Graph of the electrical conductivity of the formation and the electrical conductivity of water and against time from flow cell measurements of Scarborough sample 1.

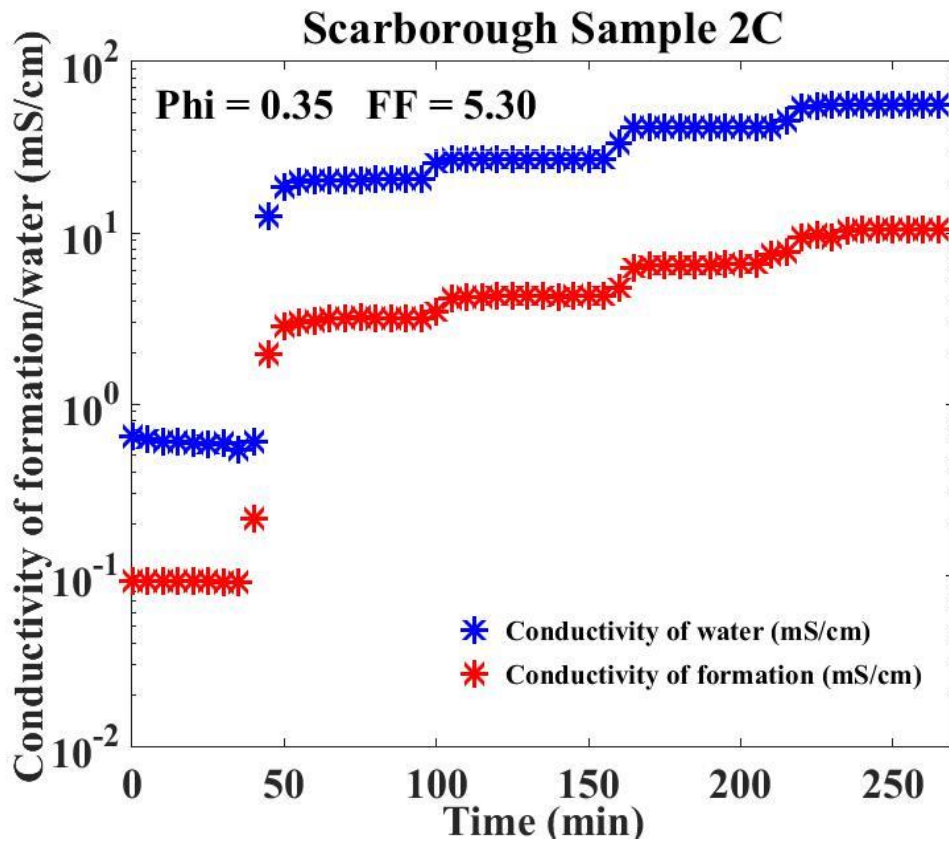
As the experiment conducted on Scarborough sample 1b (Figure 5.1.2(b)) shows, a slow decrease in formation conductivity was experienced during freshwater flow in the sample.



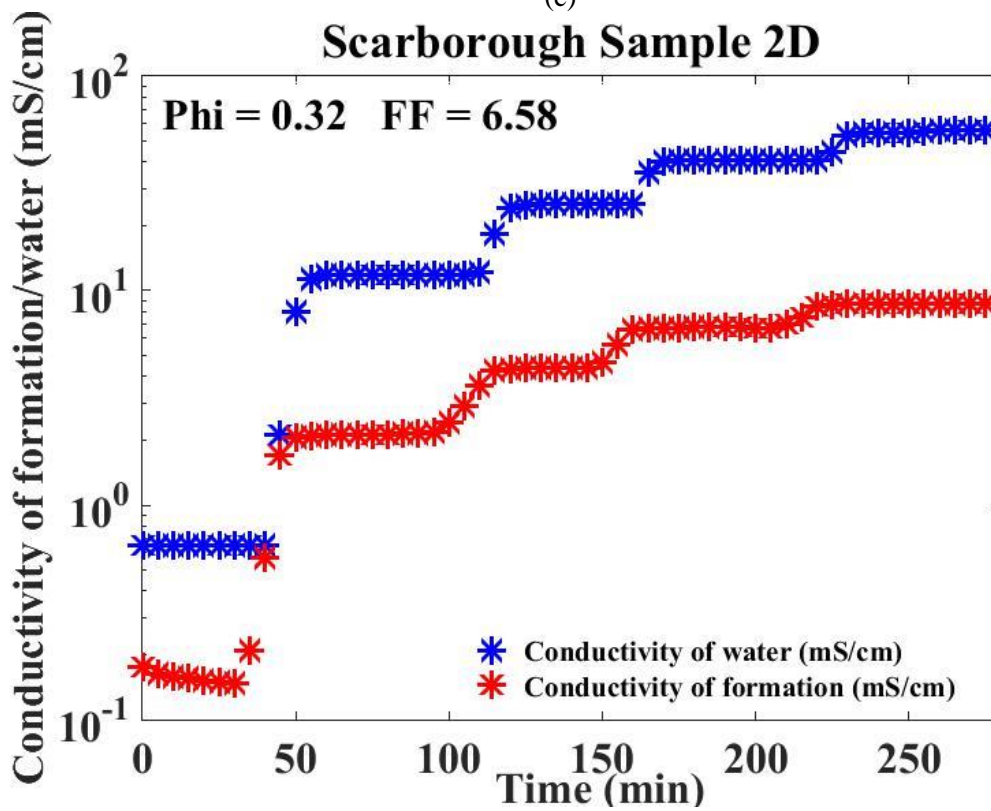
(a)



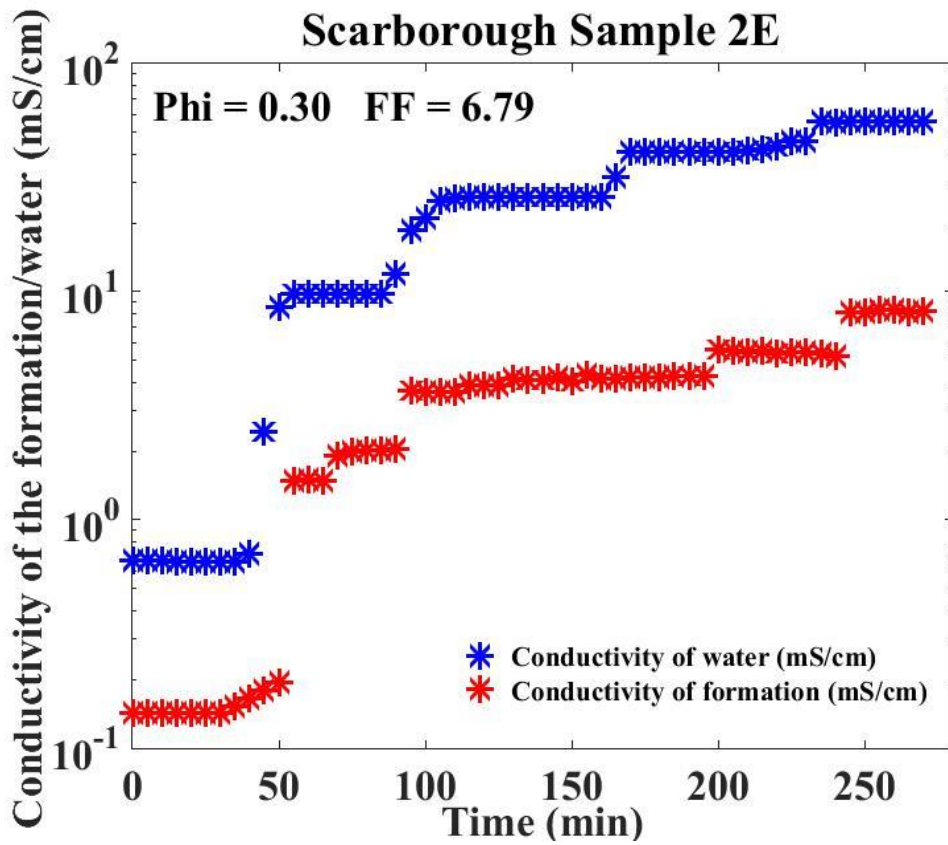
(b)



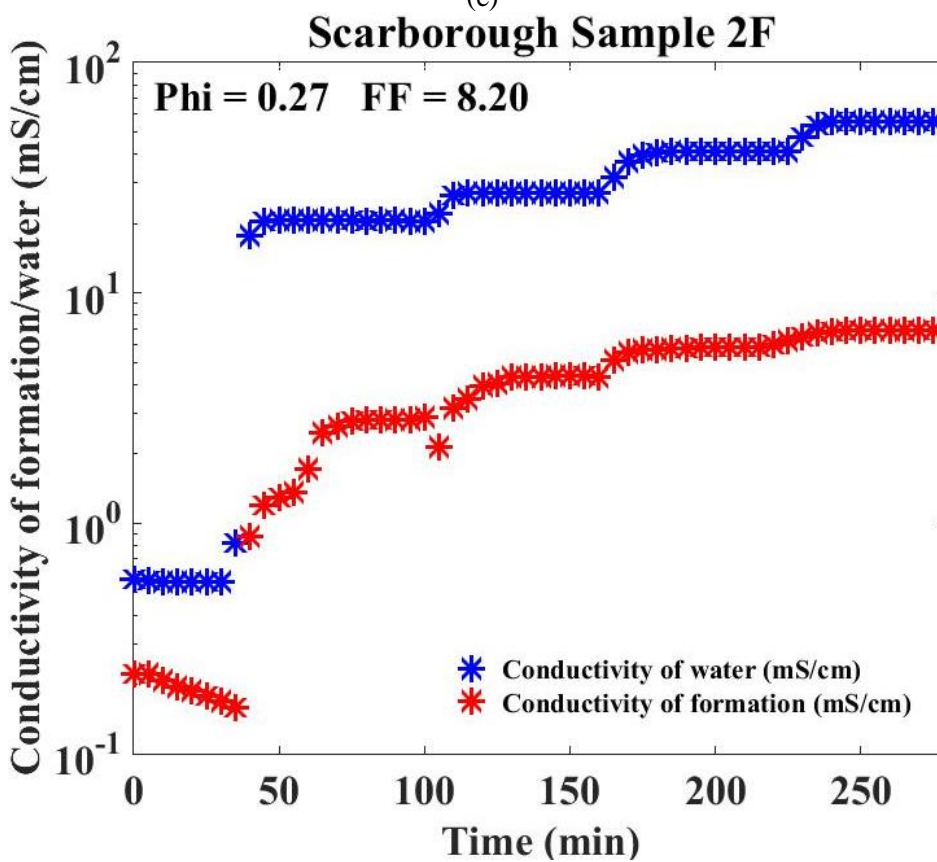
(c)



(d)



(e)

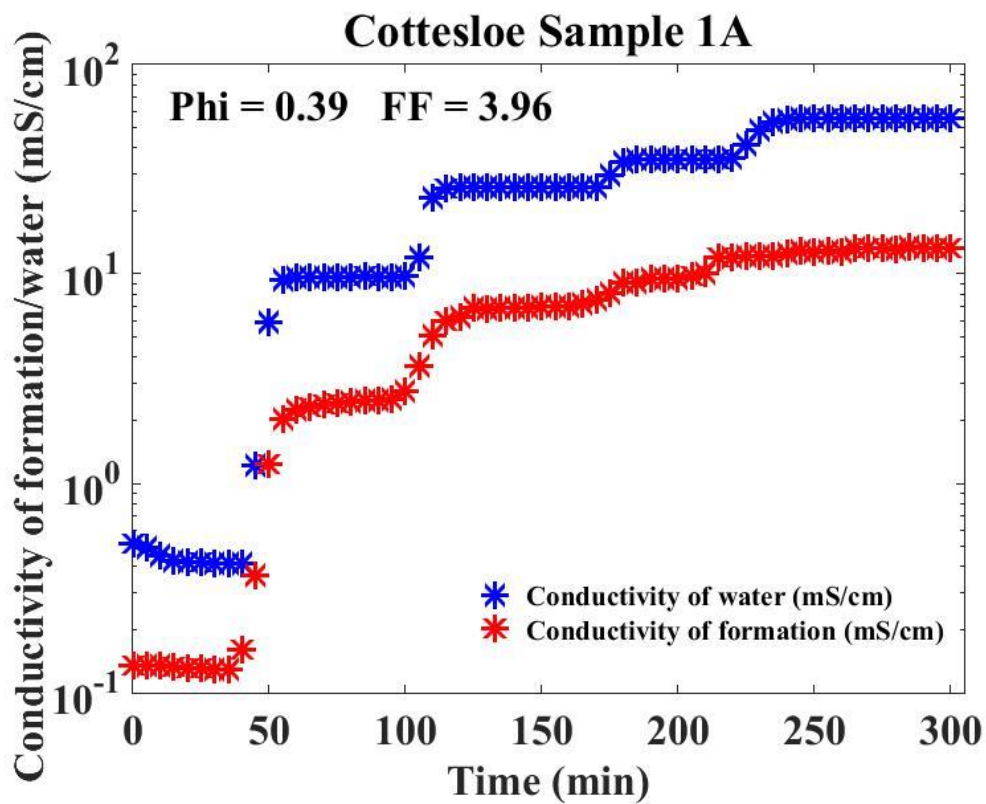


(f)

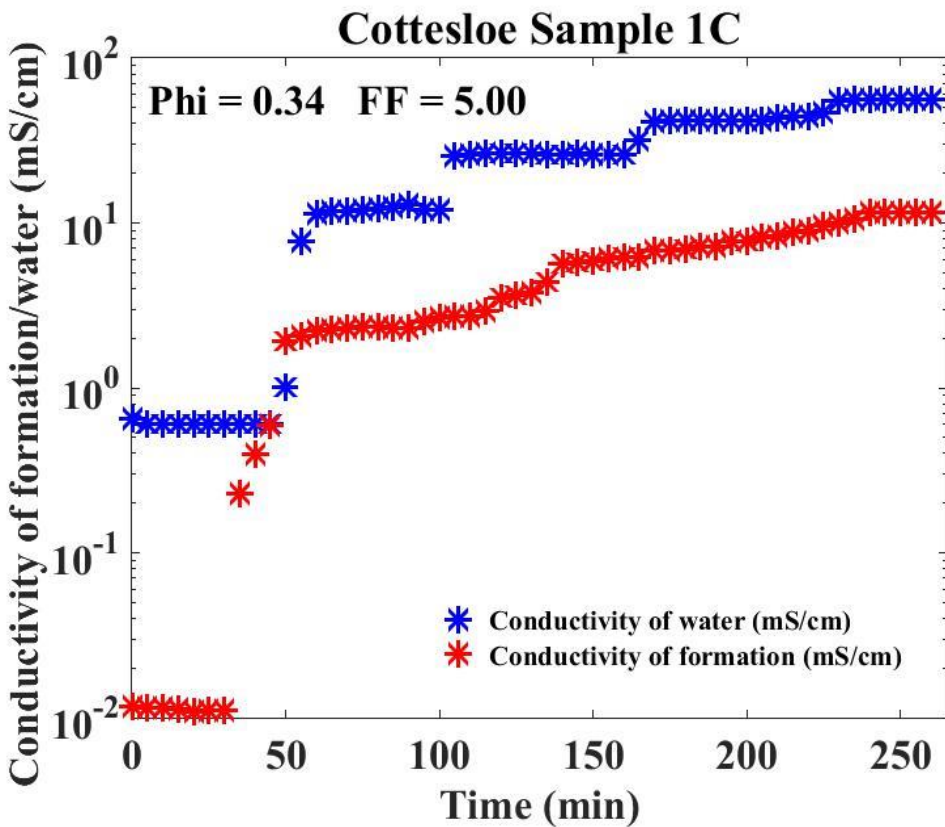
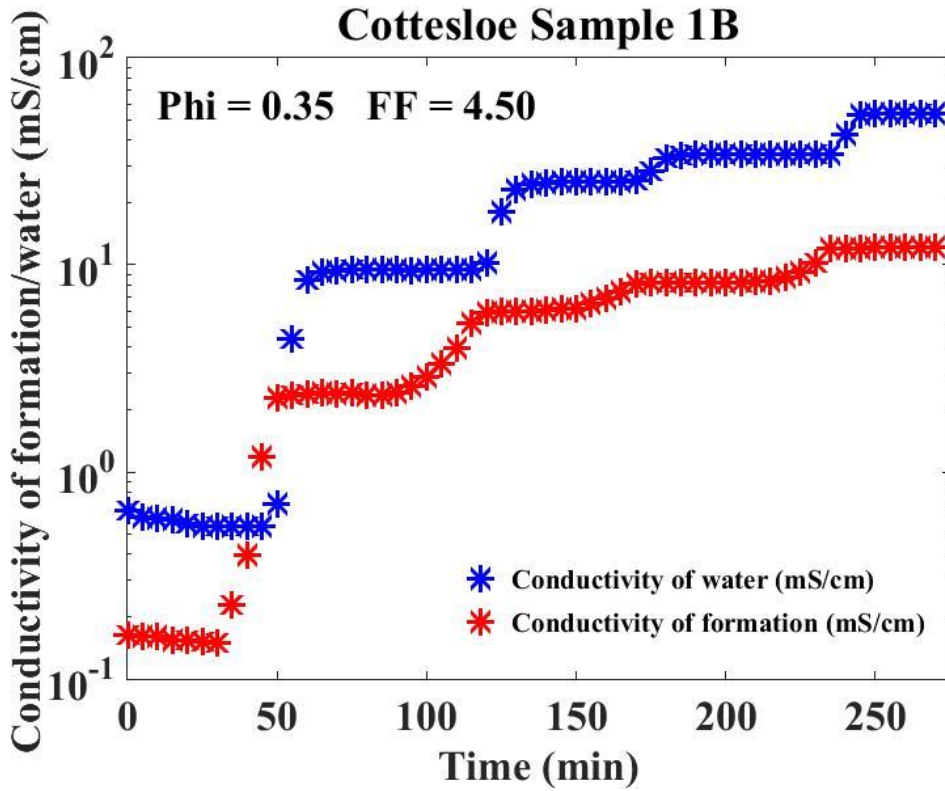
Figure 5.1.3: Graph of the electrical conductivity of the formation and the electrical conductivity of water and against time from flow cell measurements of Scarborough sample 2.

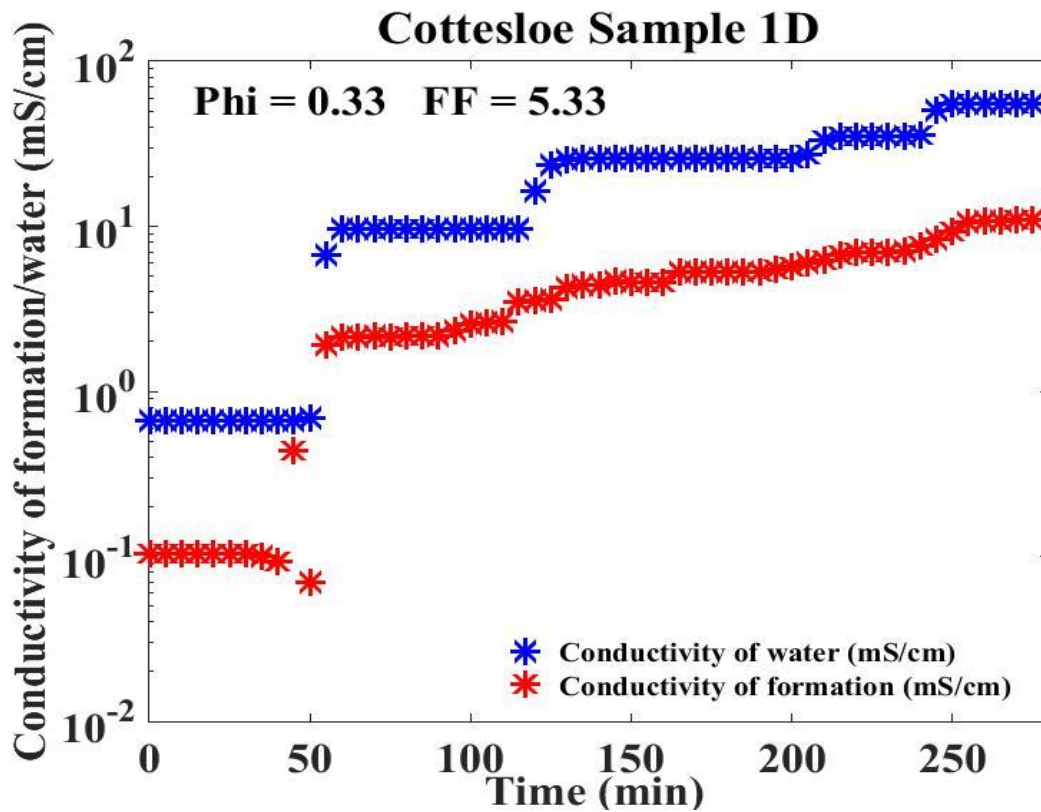
In the experiments conducted on Scarborough samples 2b, 2d, and 2f (results shown at Figure 5.1.3) at porosities of 0.38, 0.32 and 0.27 respectively, the conductivities of both the water and formation were almost the same when the freshwater was replaced by 0.5mg/l of saline water. During the Scarborough sample 2F experiment, after decreasing the porosity of the sample by shaking the cell, flushing out the 25mg/l saline water becomes very difficult and takes a longer time.

5.2.1.3 Cottesloe results

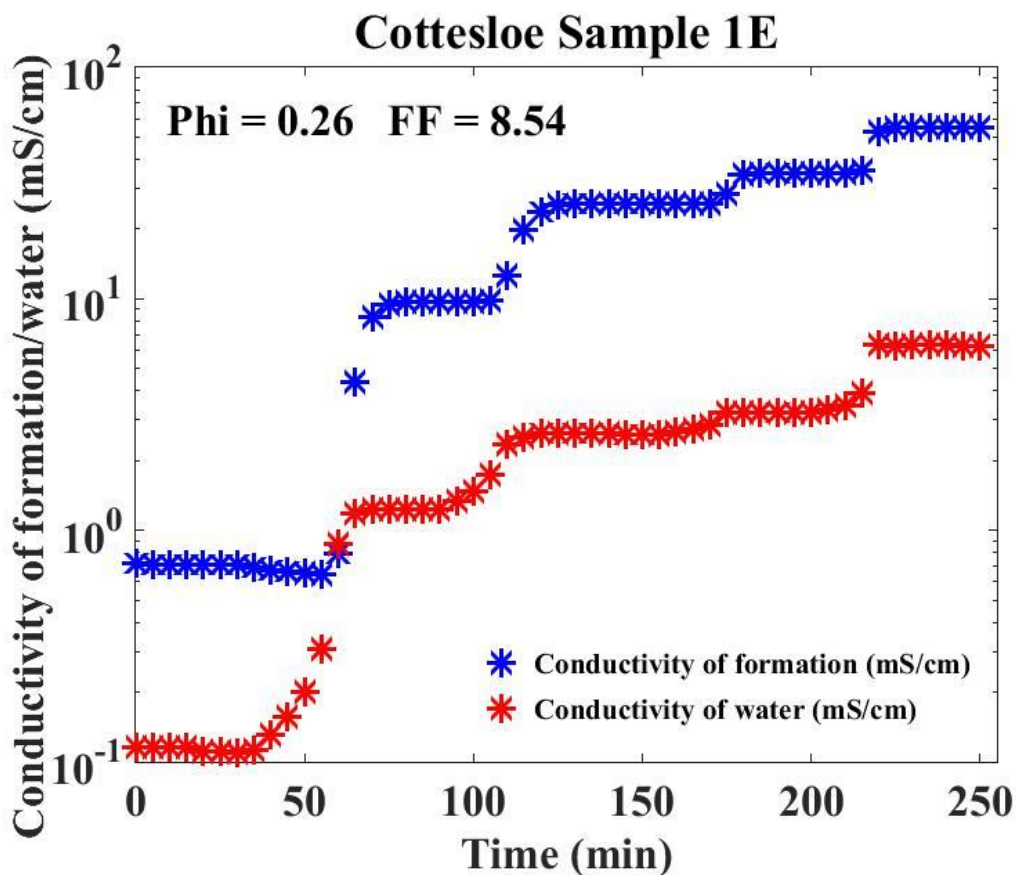


(a)





(d)

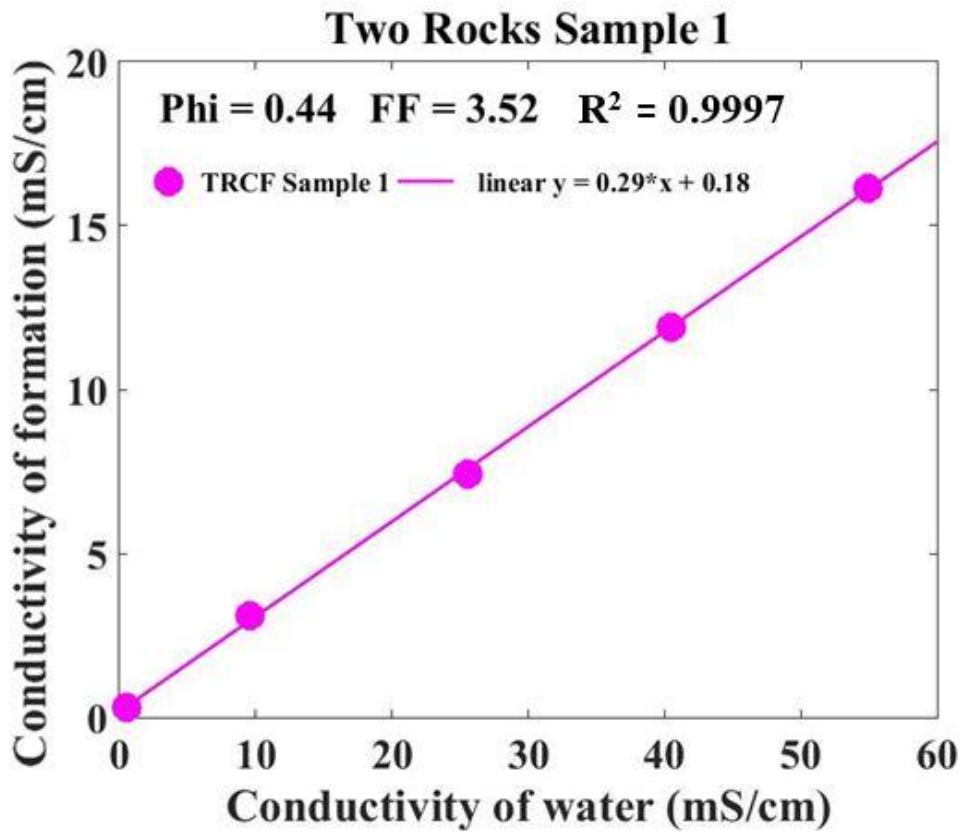


(e)

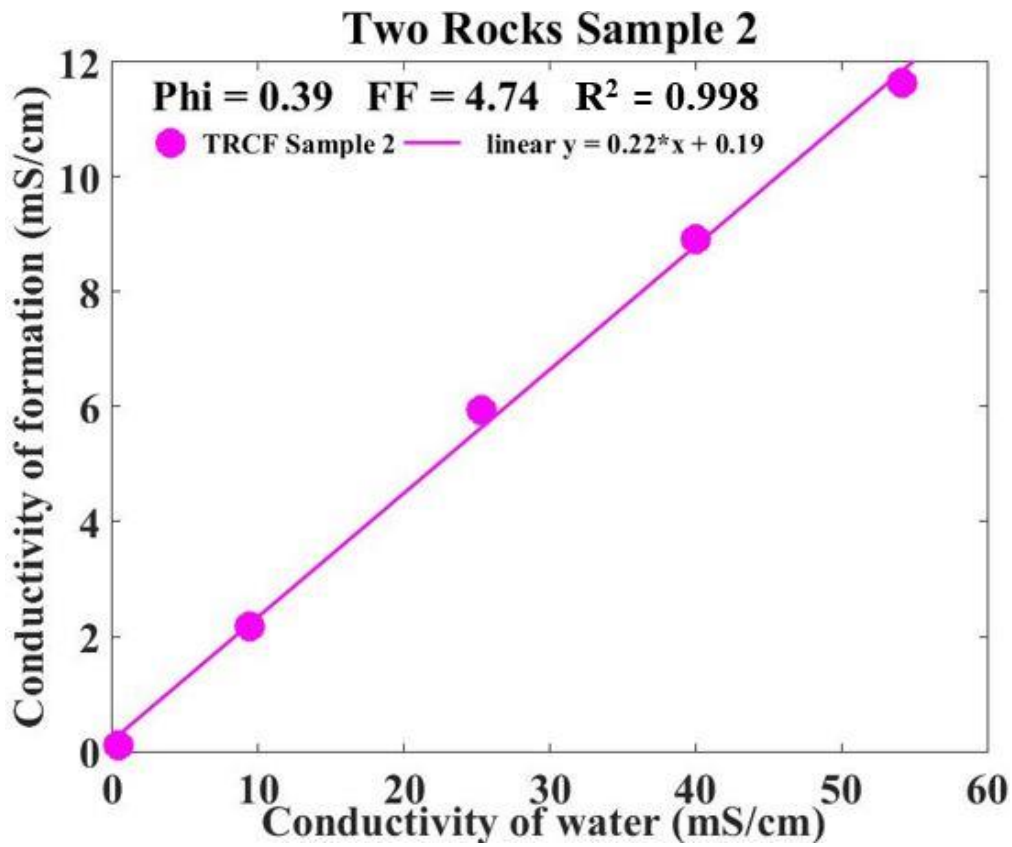
Figure 5.1.4: Graph of the electrical conductivity of the formation and the electrical conductivity of water and against time from flow cell measurements of Cottesloe samples.

During the Cottesloe laboratory experiments for the conductivity of formation in the case of the Cottesloe sample 1A there was not much-observed conductivity difference when flushing 25mg/l by 35mg/l saline water (Figure 5.1.4a). Similarly, I observed that during the Cottesloe sample C experiment, the conductivity of the formation during the flushing of 15mg/l by 25mg/l did not stabilize (Figure 5.1.4c).

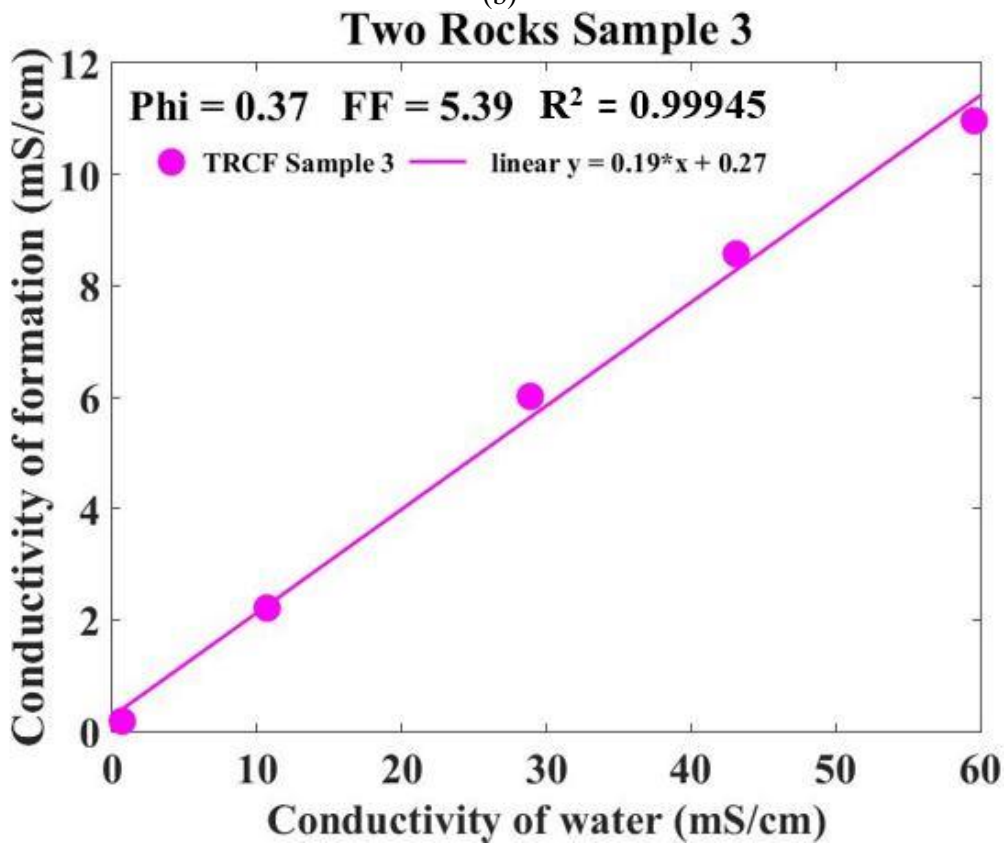
When a reading stabilizes in the experiments discussed in figure 5.1.1, the average of five (5) stable readings of the salinities fresh water, 0.5g/l, 15g/l, 25g/l and 35g/l was taken as the conductivity of the formation of that salinity as presented in equation 3.2 (Chapter 3). By plotting the electrical conductivity of the formation against the electrical conductivity of water, I obtained the formation factor linear function of the conductivity of water. The slope of the graph gives the formation factor as seen in figures 5.1.5, 5.1.6, 5.1.7, and 5.1.8 for the flow cell.



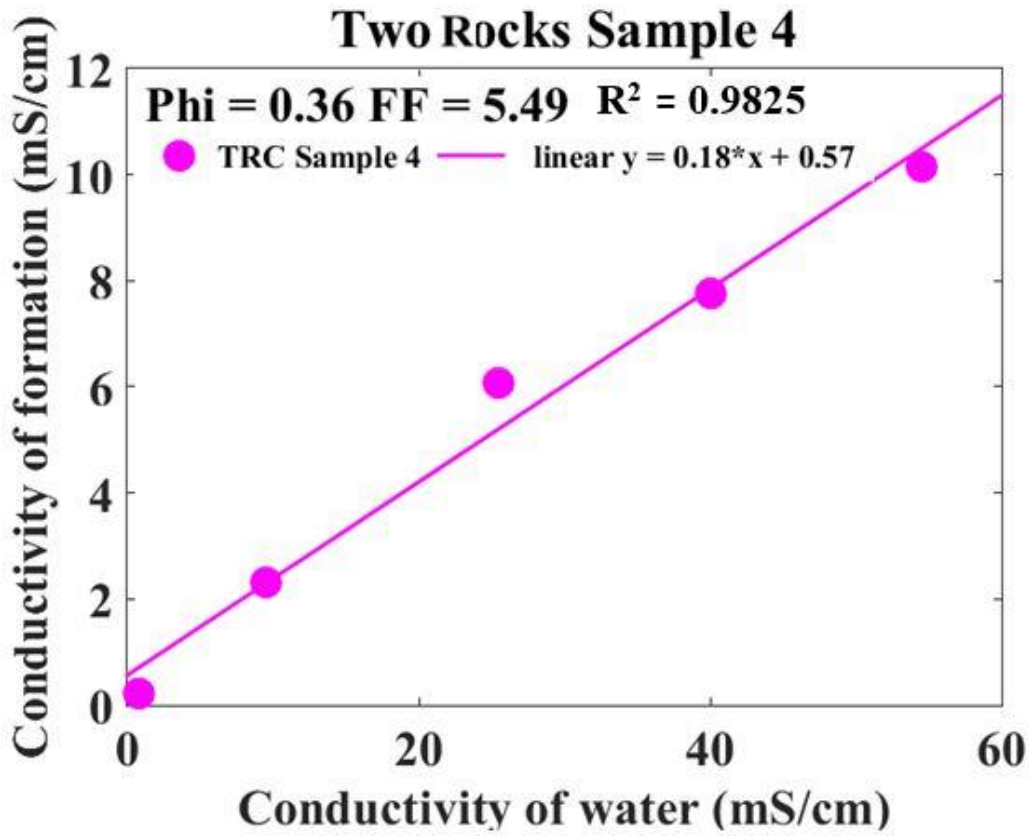
(a)



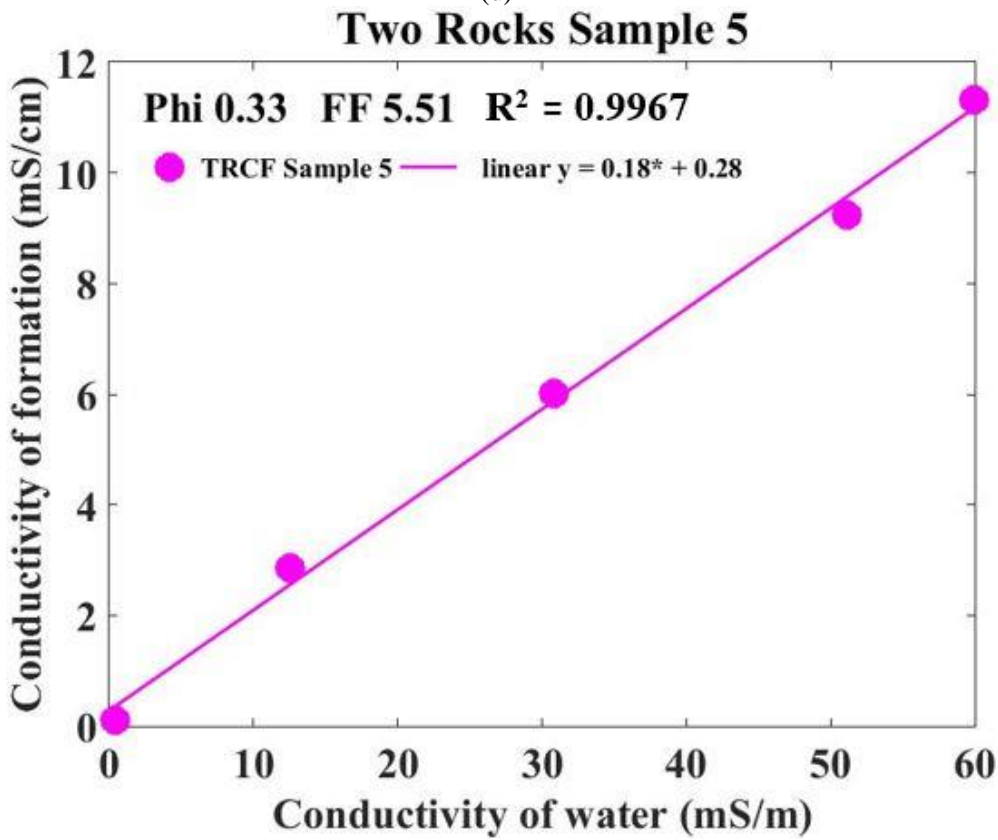
(b)



(d)



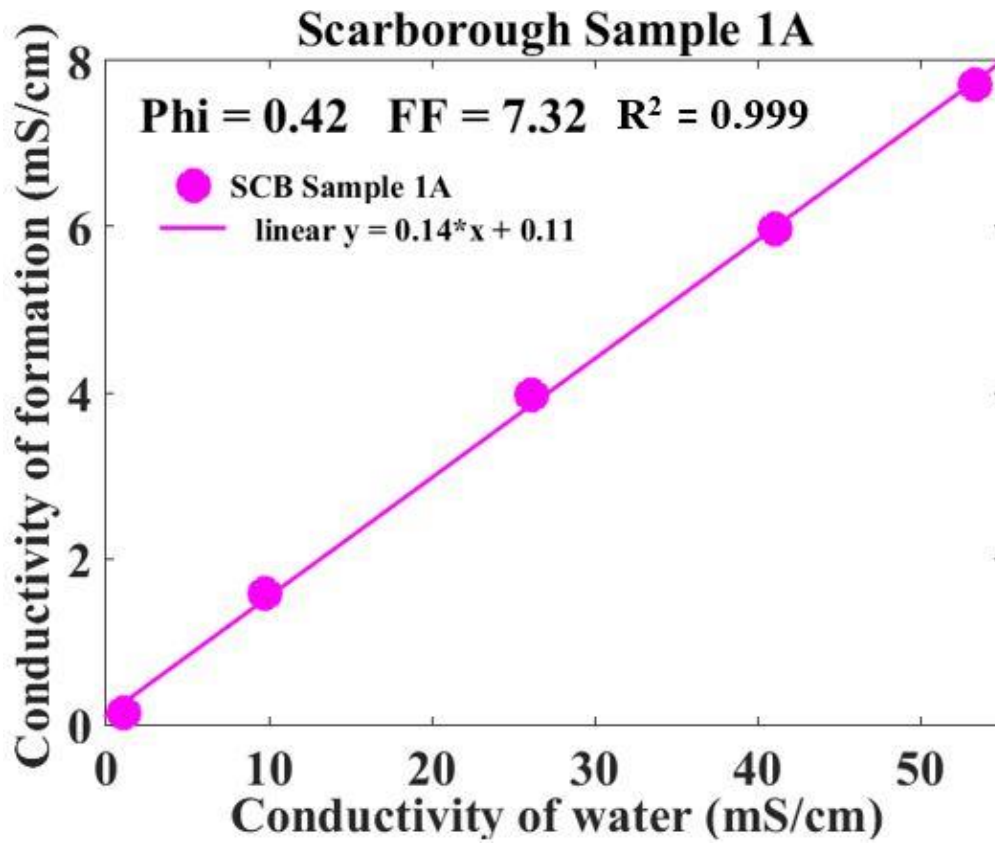
(d)



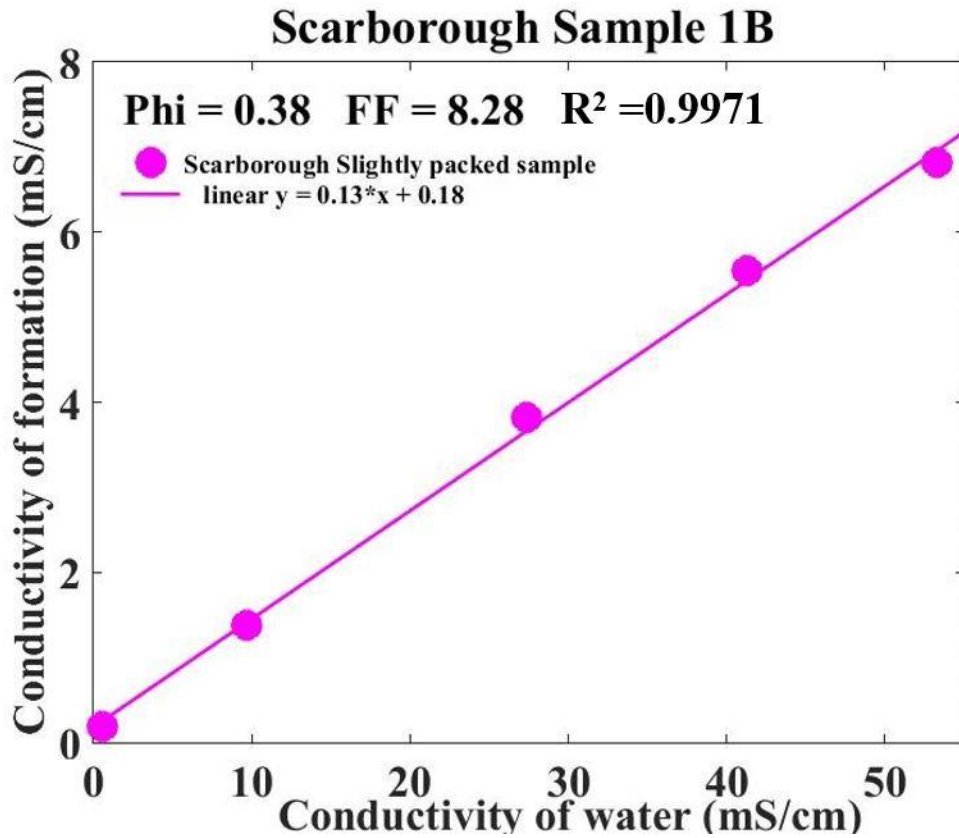
(e)

Figure 5.1.5 Graphs of the electrical conductivity of the formation against the electrical conductivity of water for flow cell measurements of Two Rocks Beach

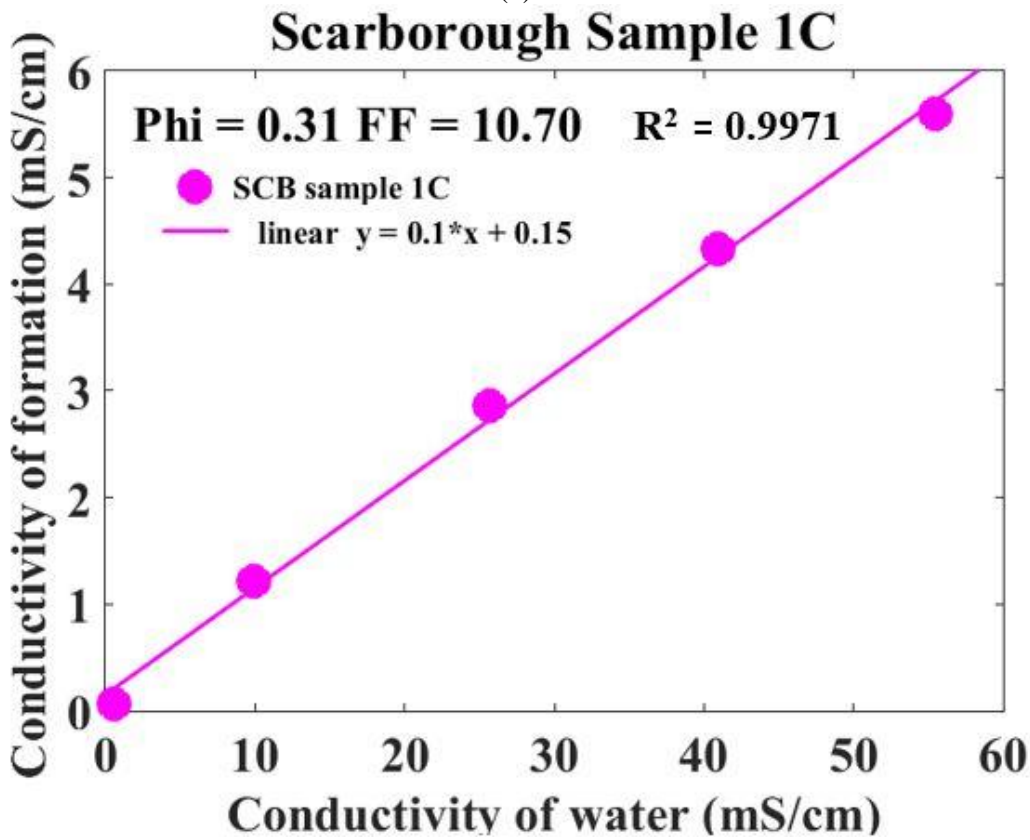
The graph of the electrical conductivity of the formation against the electrical conductivity of water of Two Rocks sample 4 for the flow cell experiment (Figure 5.1.5d) shows a data point at (15mg/l) is not out of point with the rest of the data.



(a)

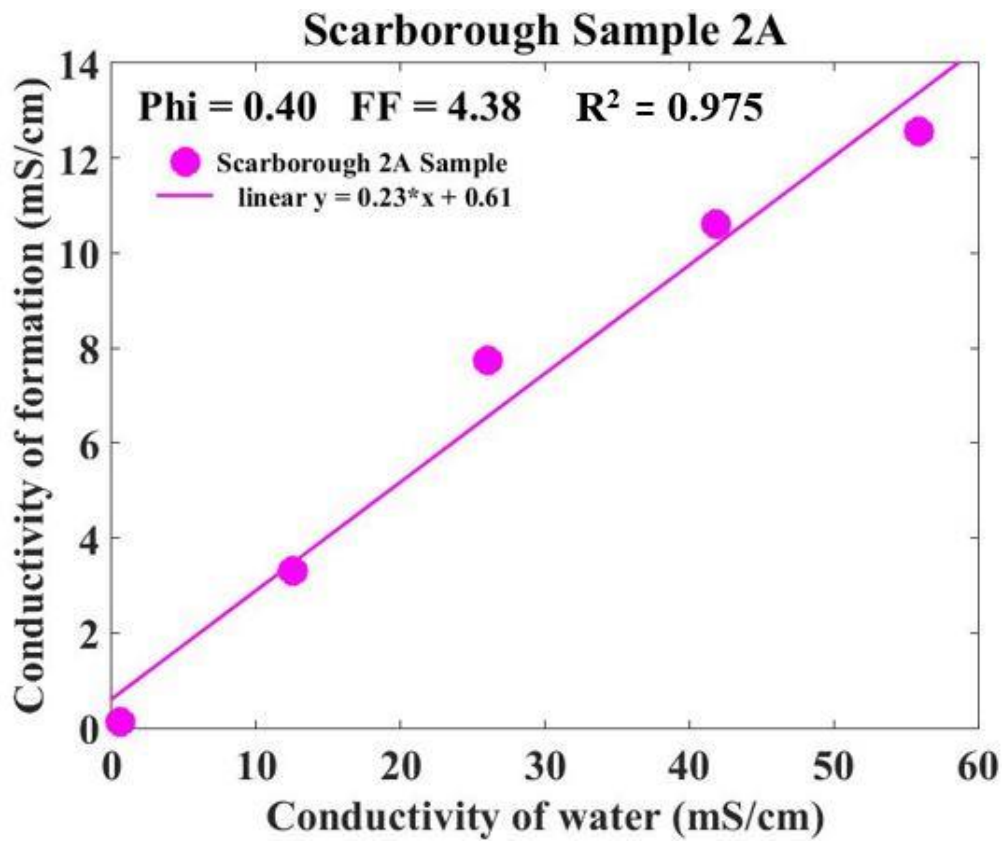


(b)

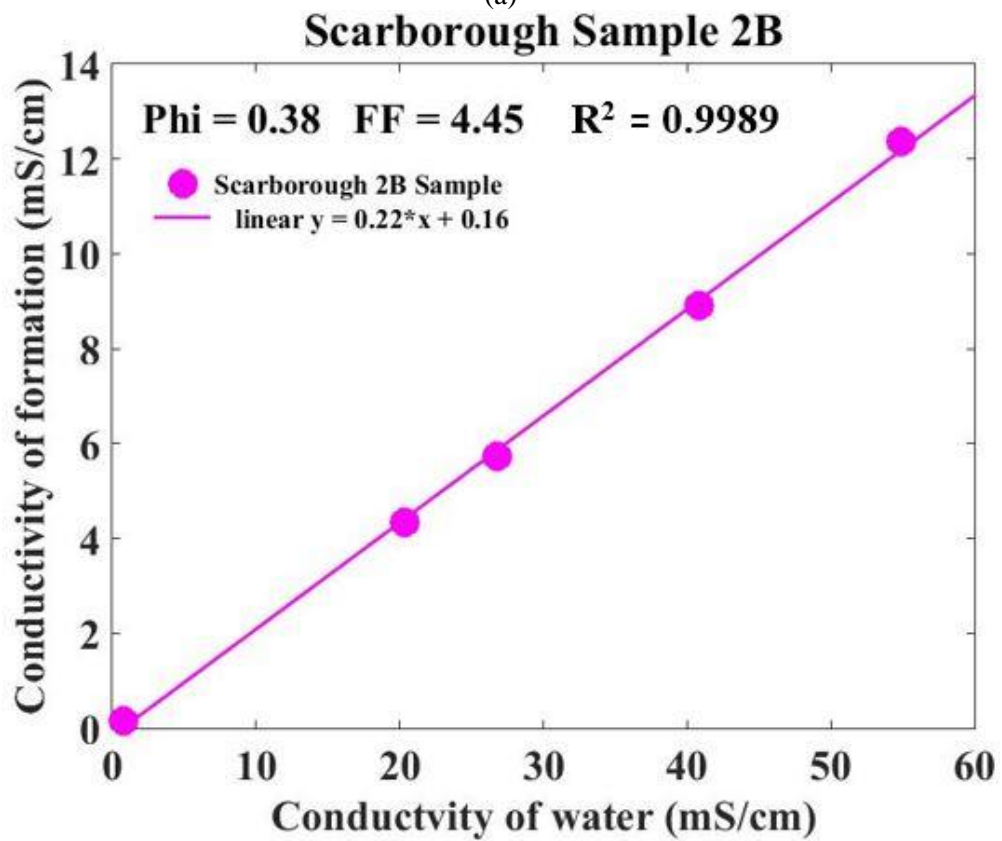


(c)

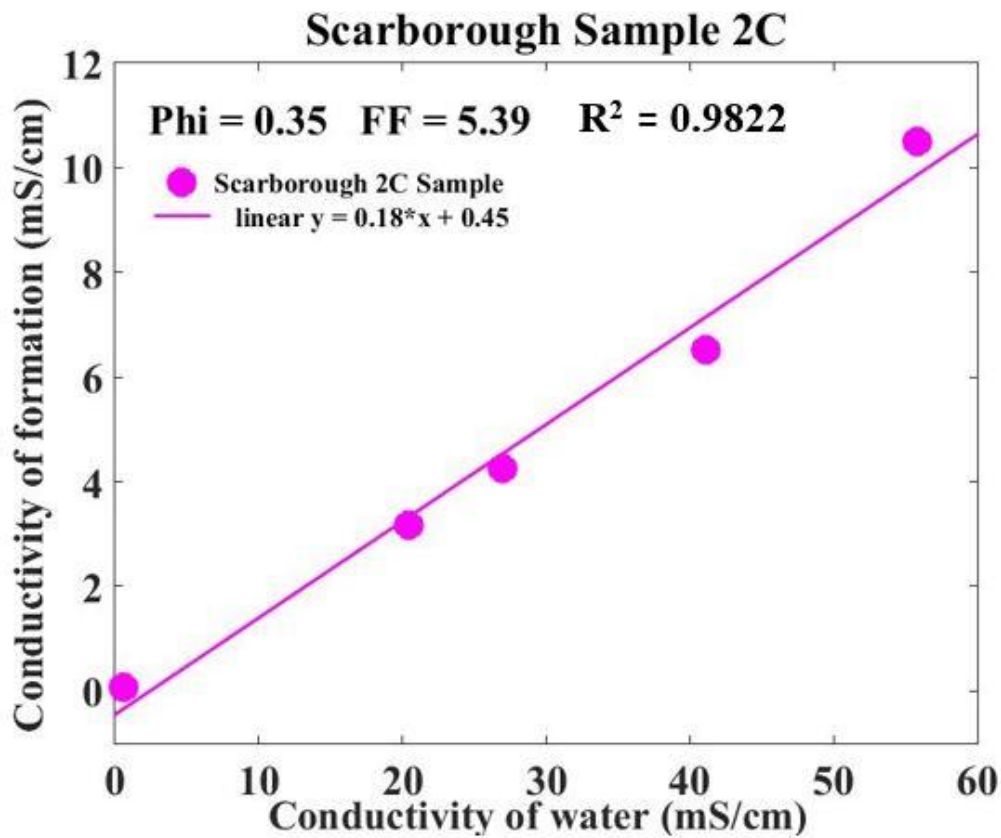
Figure 5.1.6: Graphs of the electrical conductivity of the formation against the electrical conductivity of water for flow cell measurements for Scarborough sample 1.



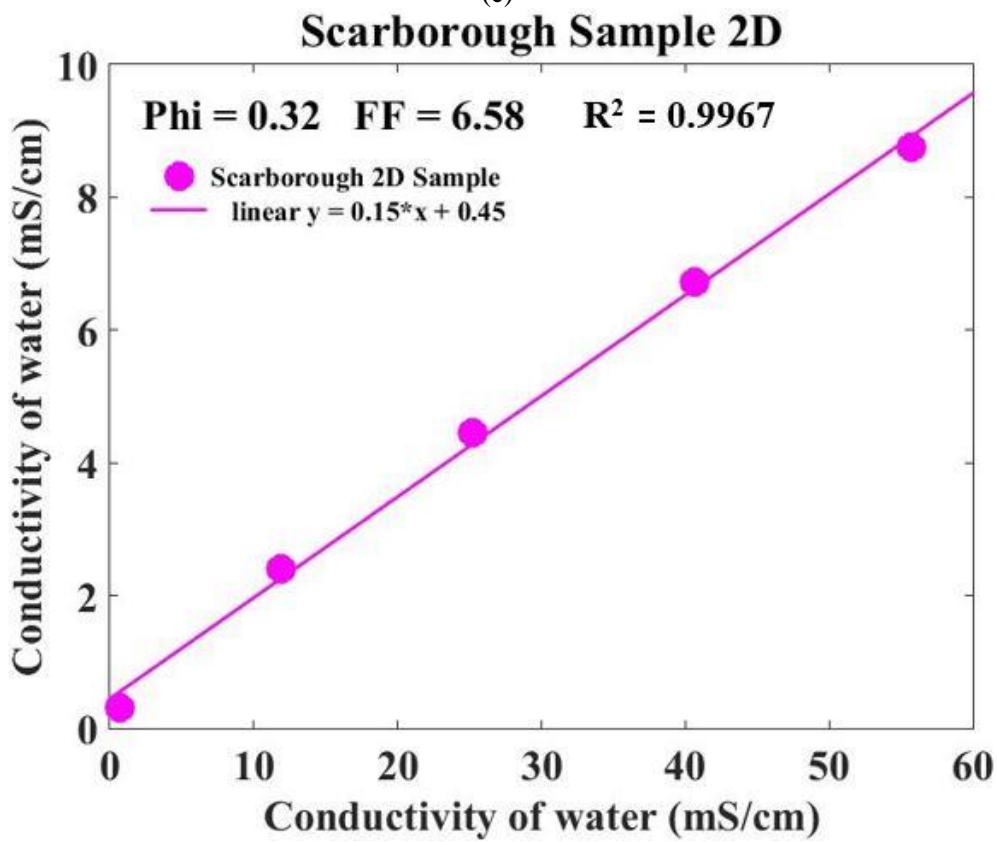
(a)



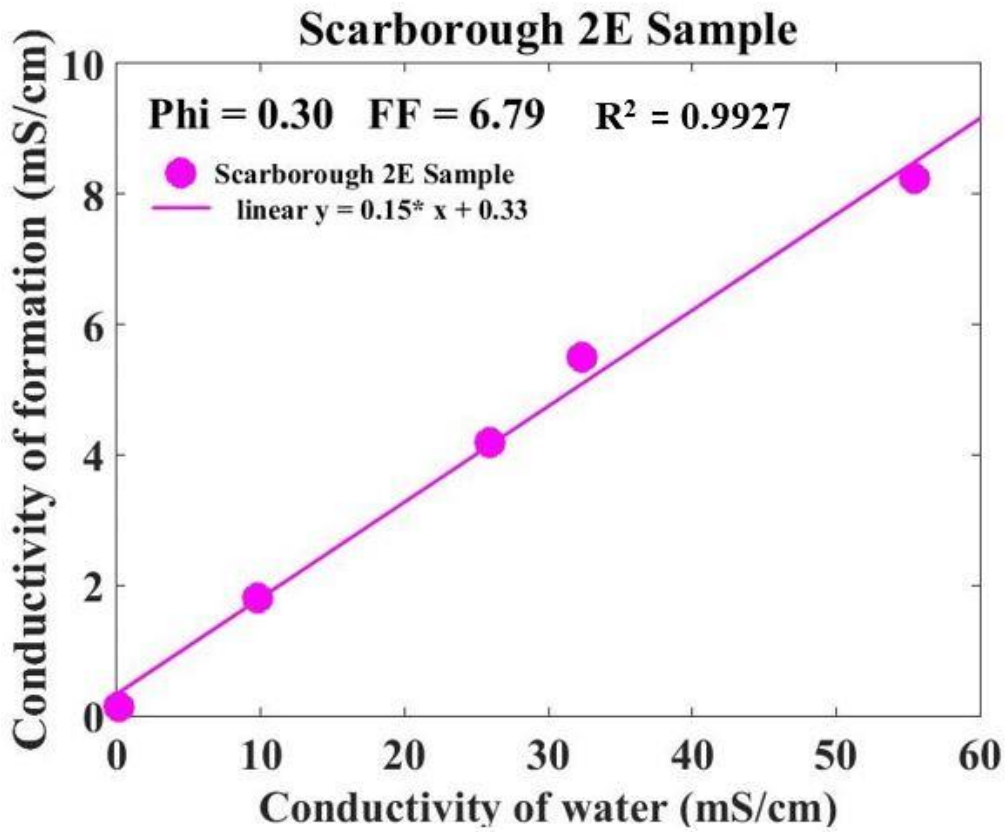
(b)



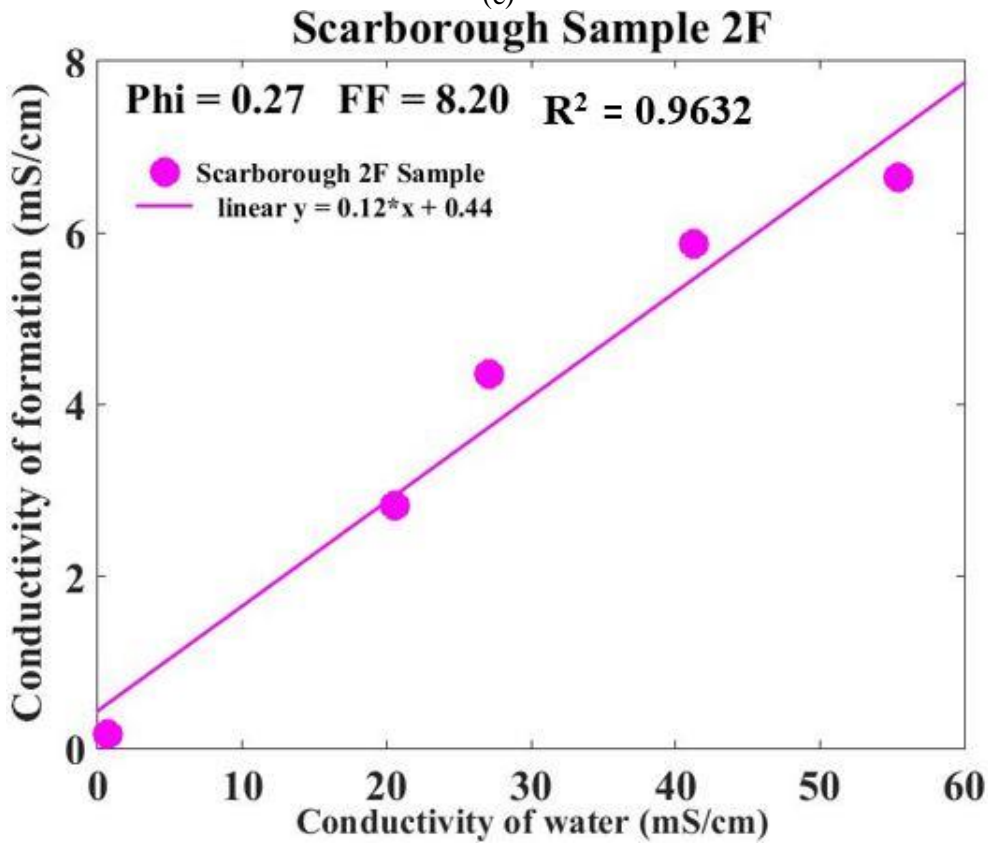
(c)



(d)



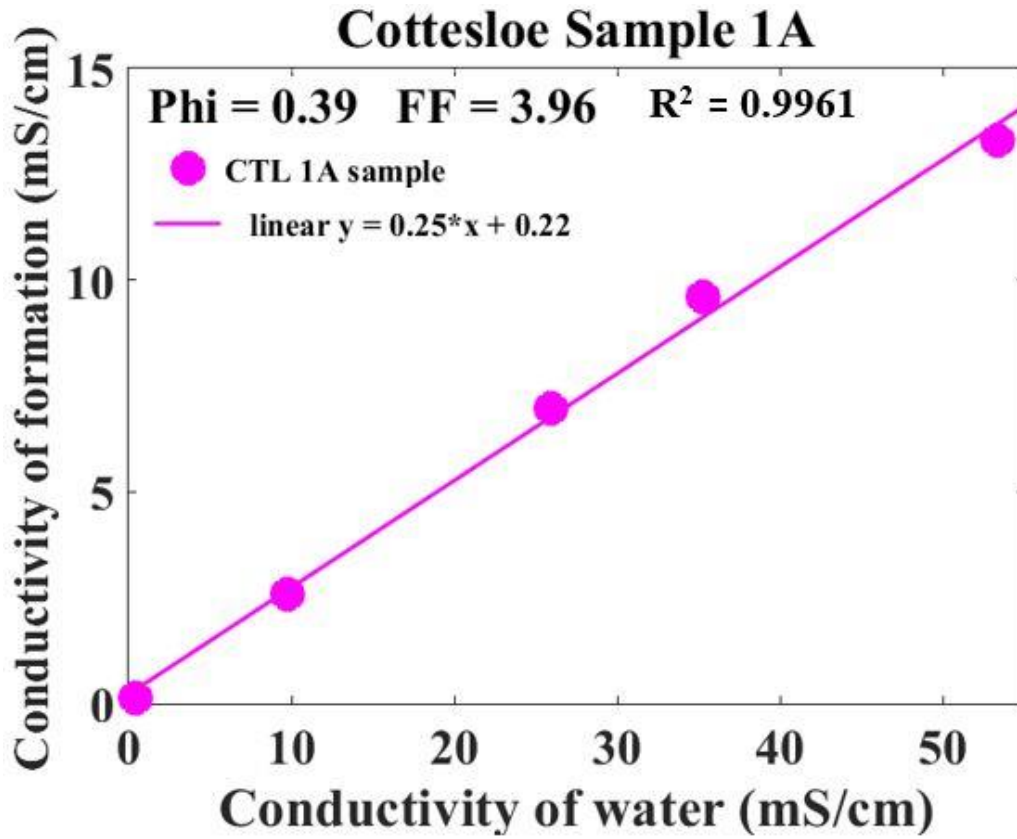
(e)



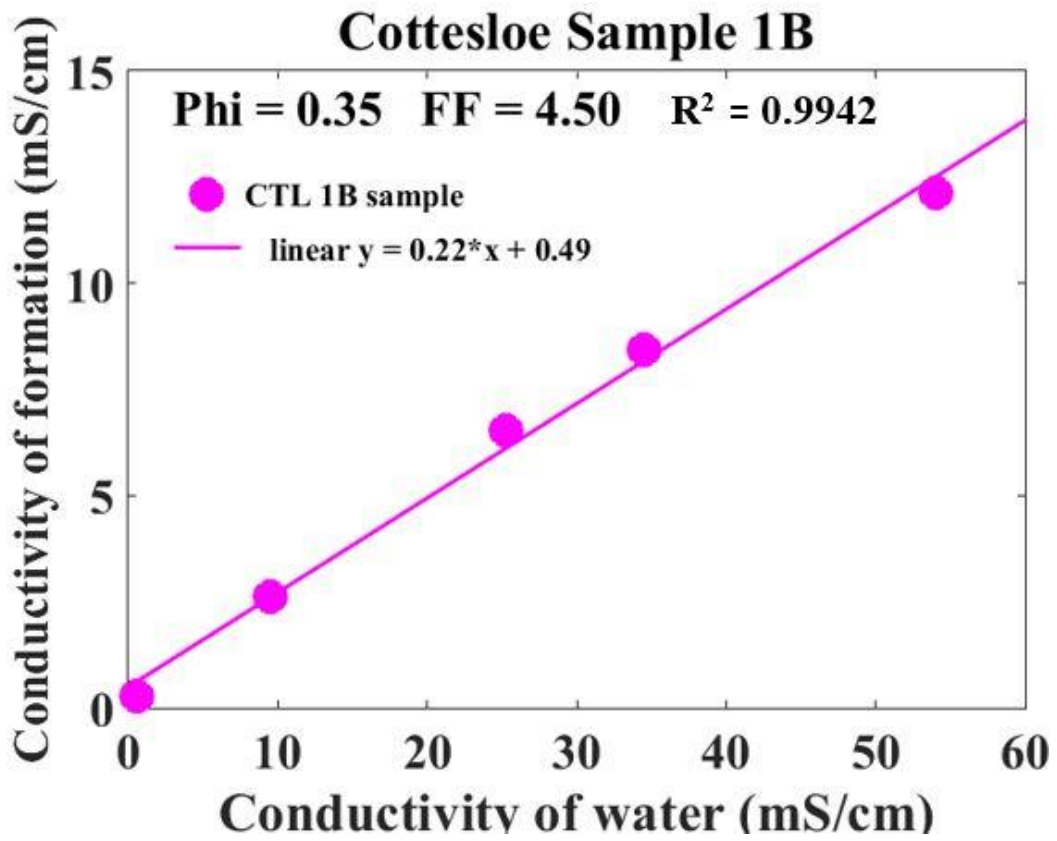
(f)

Figure 5.1.7: Graphs of the electrical conductivity of the formation against the electrical conductivity of water for flow cell measurements for Scarborough sample 2

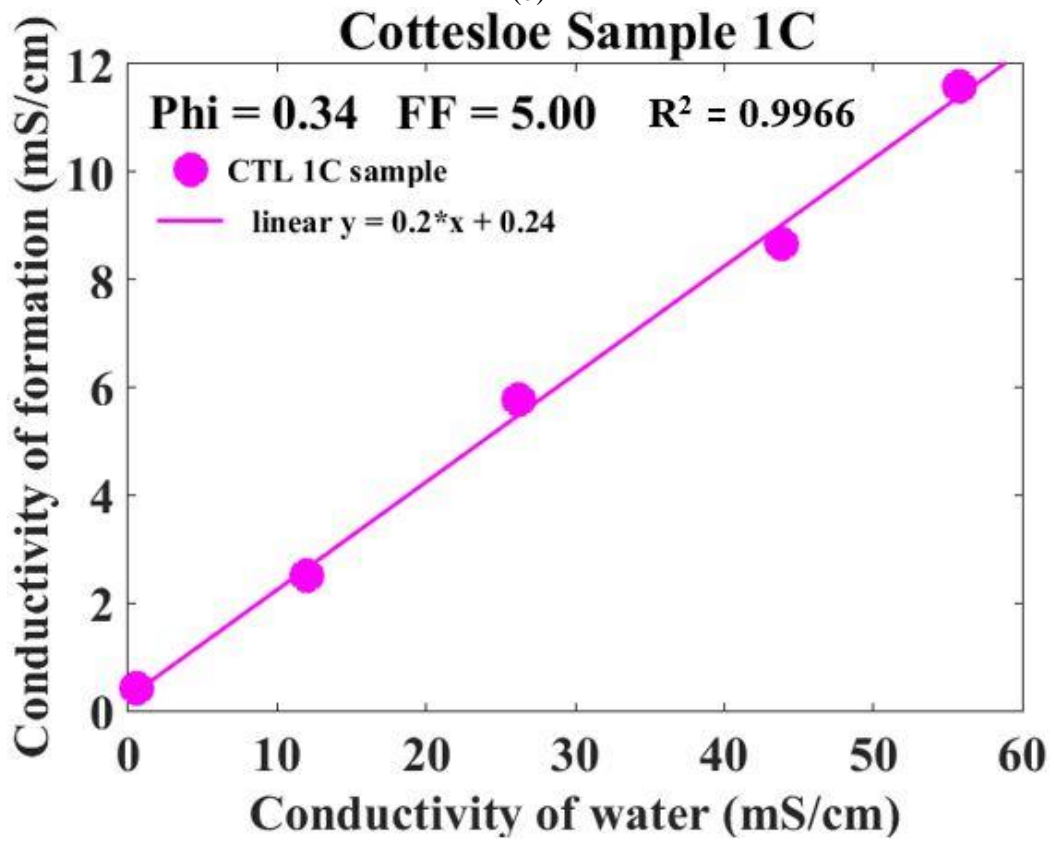
The graph of the conductivity of the formation against the conductivity of water for Scarborough Sample 2F (Figure 5.1.7(f)) shows scattered points; this is because the laboratory experiment (Figure 5.1.3f) showed unstable readings during the experiment that were associated with bad contact between the crocodile clip and the electrode.



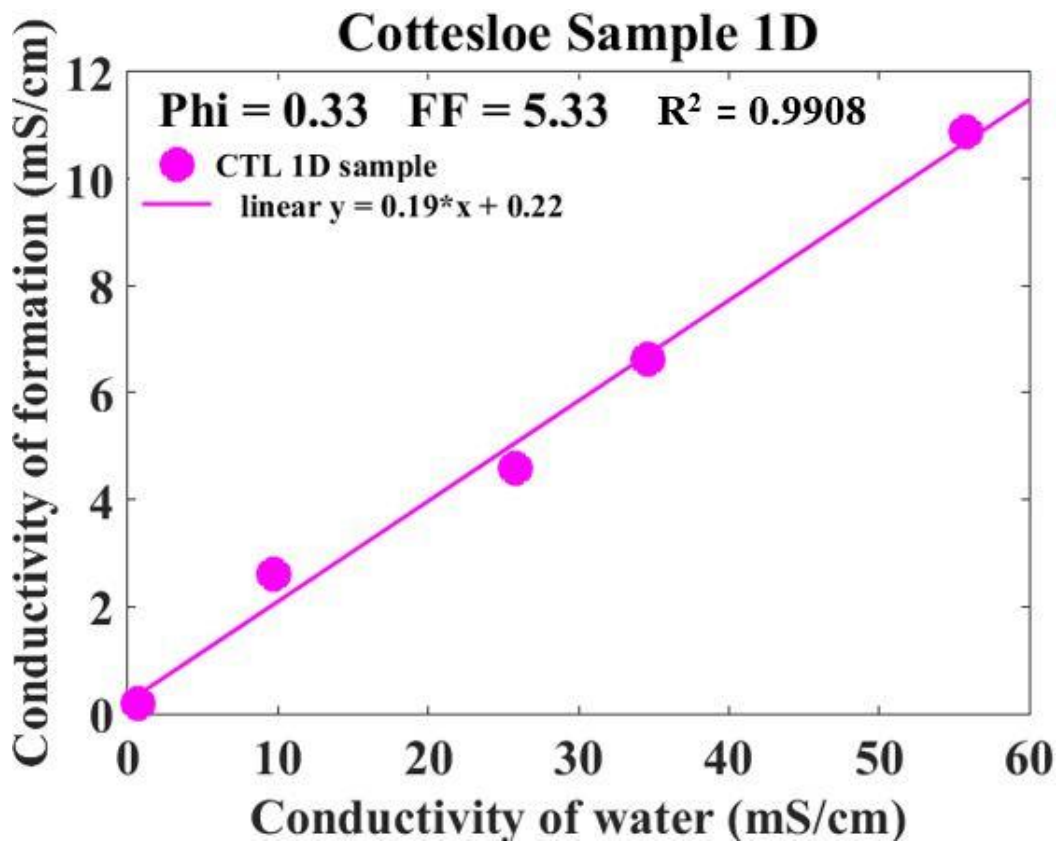
(a)



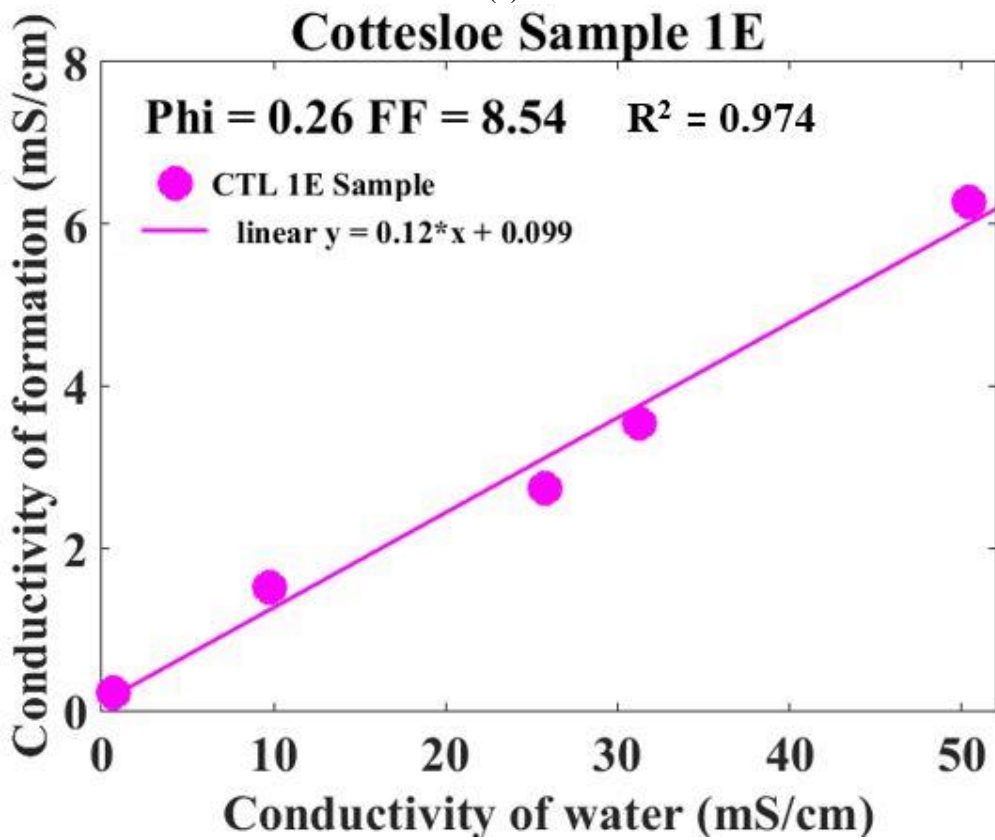
(b)



(c)



(d)



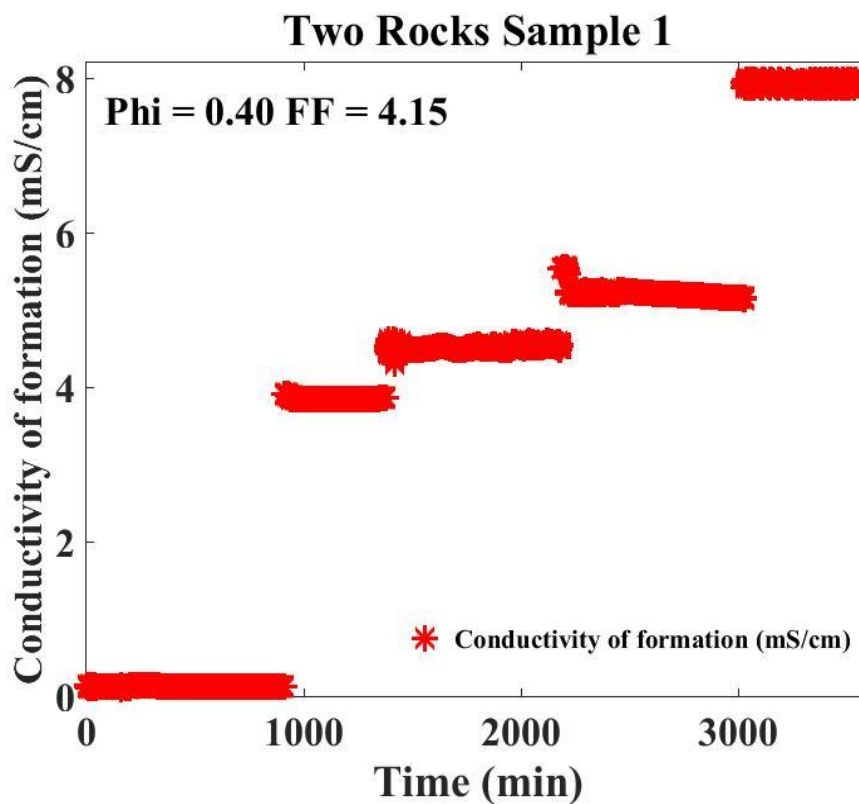
(e)

Figure 5.1.8: Graphs of the electrical conductivity of the formation against the electrical conductivity of water for flow cell measurements for Cottesloe samples

5.2.2 Static cell

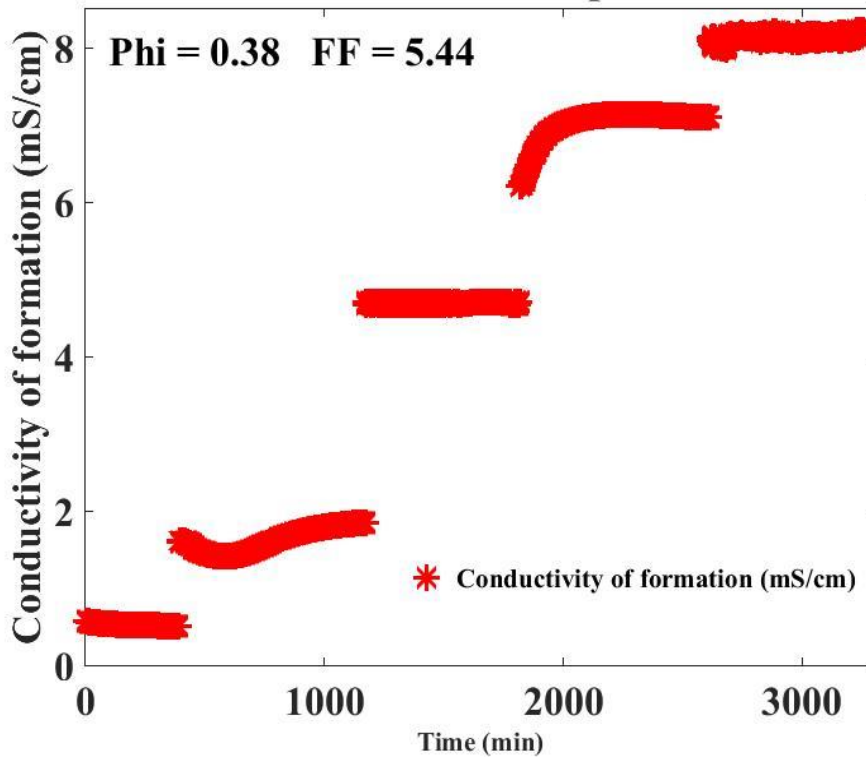
The electrical conductivity of the formation against time was plotted for the laboratory static cell measurements (Figures 5.1.9, 5.1.10 and 5.1.11) while the conductivity of the water was measured separately. An average conductivity takes from five readings (when reading stabilizes) was plotted against the conductivity of water (Figures 5.1.12, 5.1.13, and 5.1.14). Static measurement experiments were performed on Two Rocks, Scarborough and Cottesloe Beaches. In this experiment, measuring the resistance of the formation was achieved using a rectangular 2-electrode static cell (Perspex) see Figure 3.13. When readings of the resistance stabilized, I stopped the recording and I drained the water from the cell, and then measured the conductivity of the water using a conductivity meter (Hanna probe). I resumed the recording after replacing the water with the next-highest saline water.

5.2.2.1 Two Rocks results



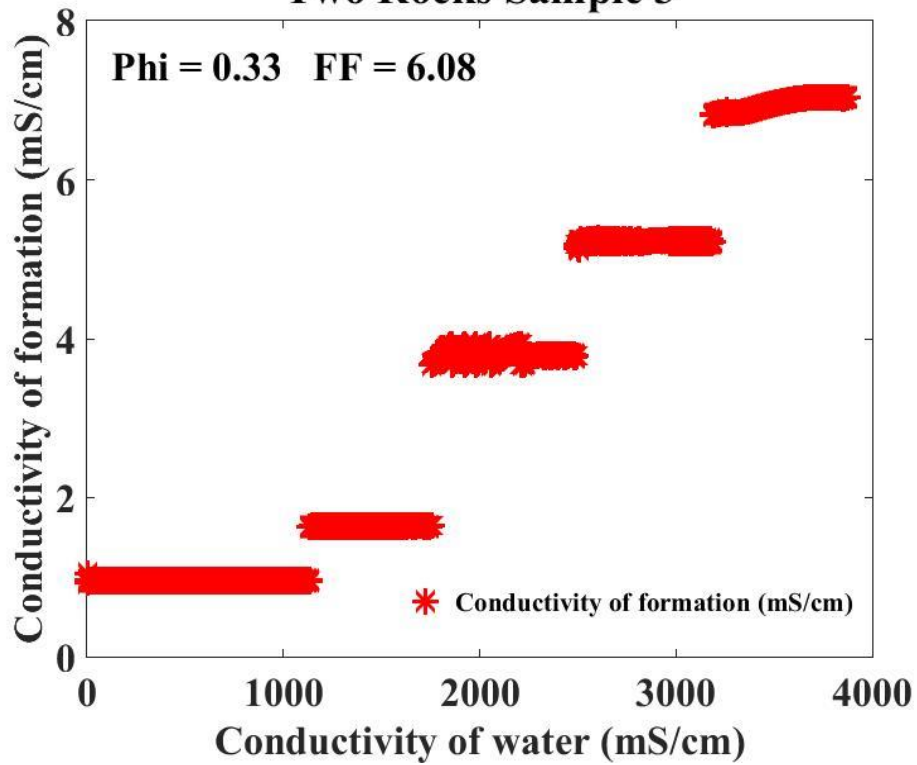
(a)

Two Rocks Sample 2

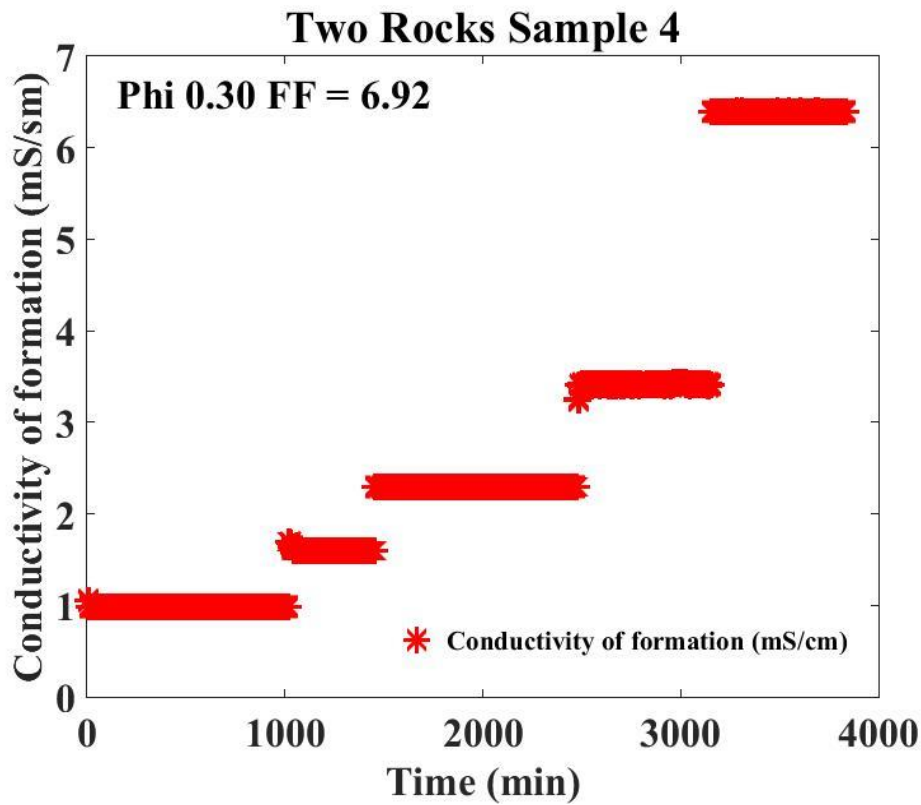


(b)

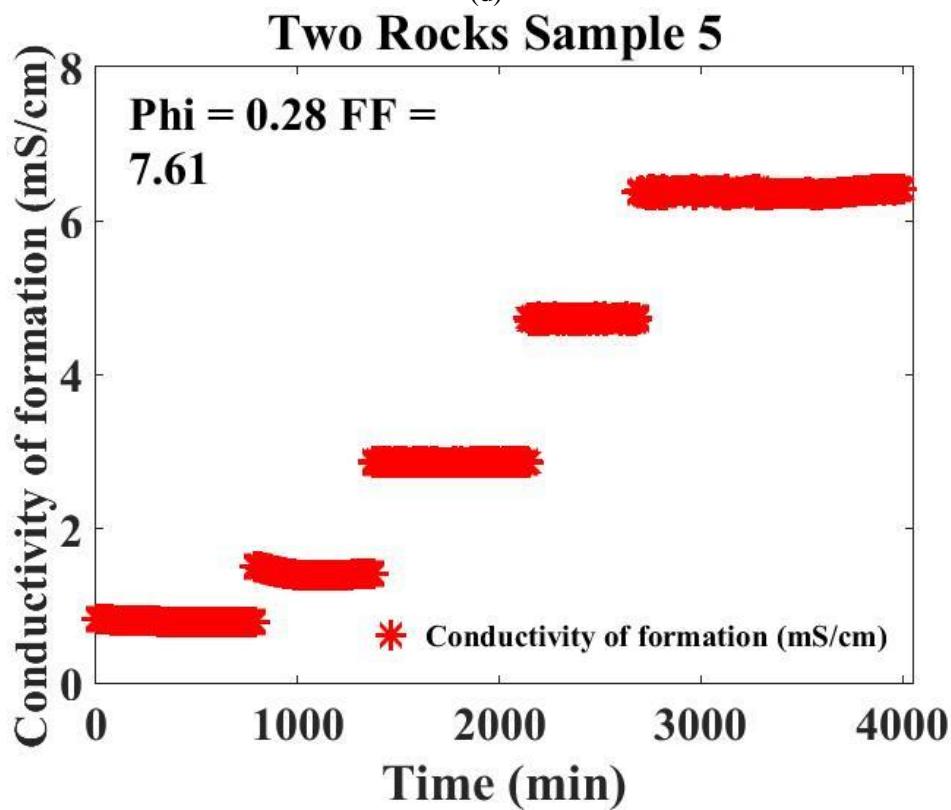
Two Rocks Sample 3



(c)



(d)

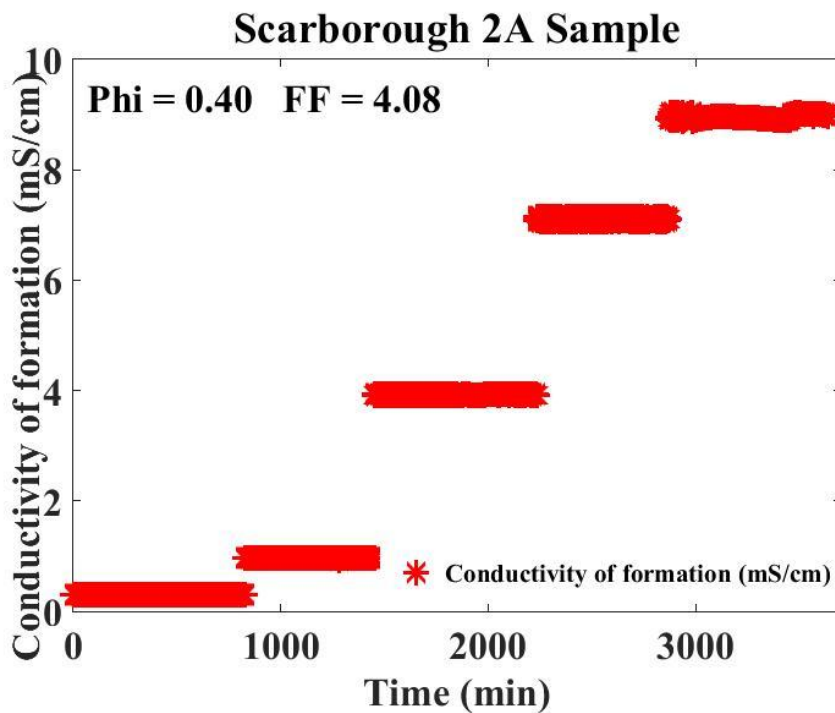


(e)

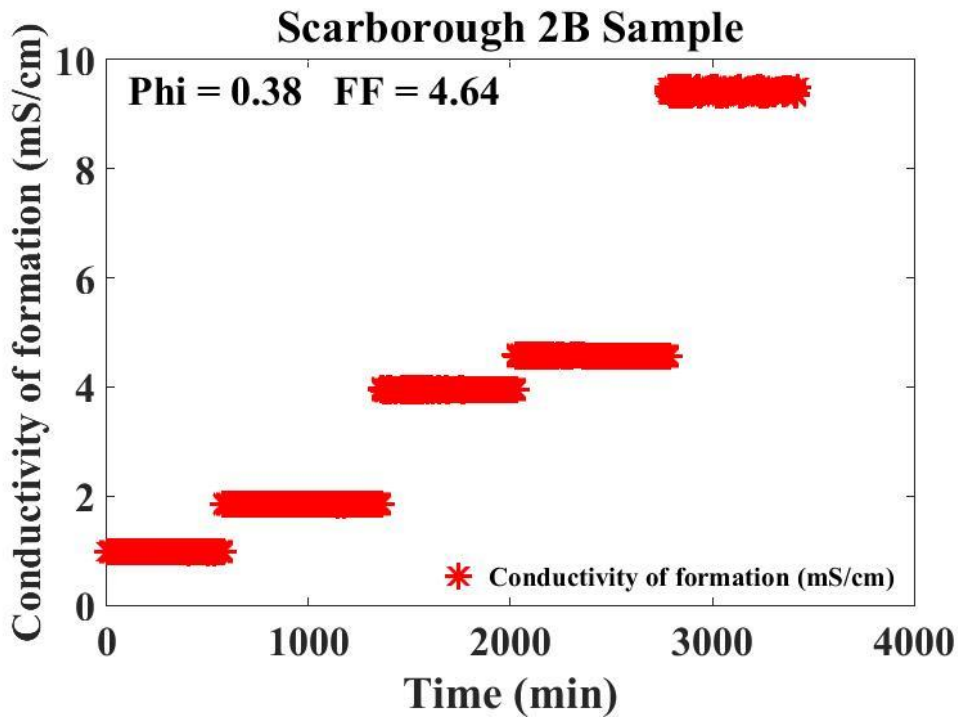
Figure 5.2.1: Graph of the electrical conductivity of the formation and the electrical conductivity of water and against time from static cell measurements of Two Rocks samples.

During the Two Rocks laboratory static experiments, there was an unstable reading recorded during sample 3 when flushing out the 5mg/l saline water Figure 5.2.1(c). Further, there was a great delay for the conductivity to stabilize during the injection of 35mg/l saline water for Two Rocks sample 5 static laboratory measurement that led to a time of about 4000 minutes Figure 5.2.1(e).

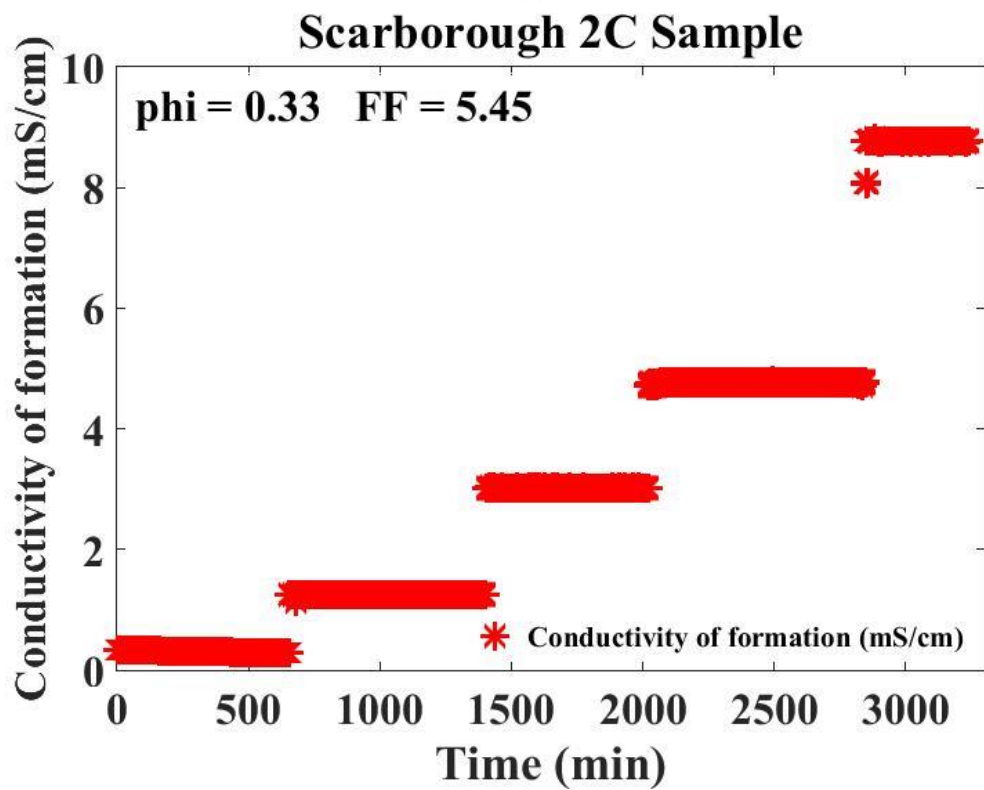
5.2.2.2 Scarborough results



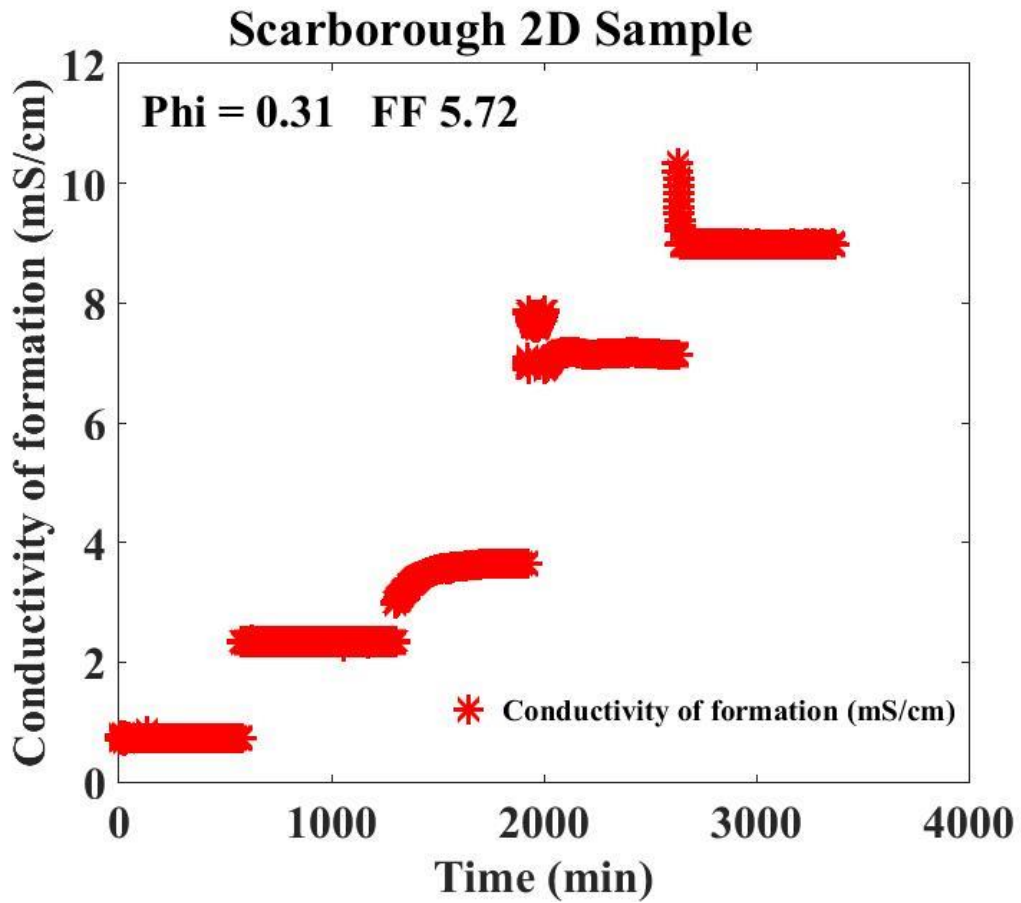
(a)



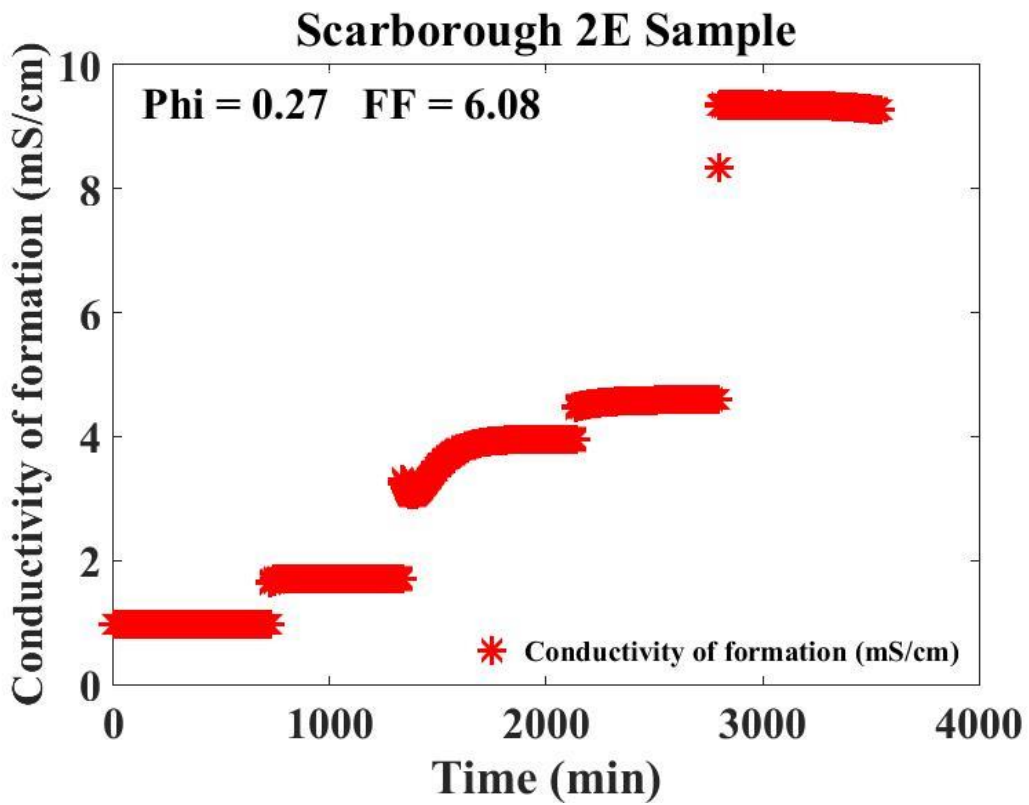
(b)



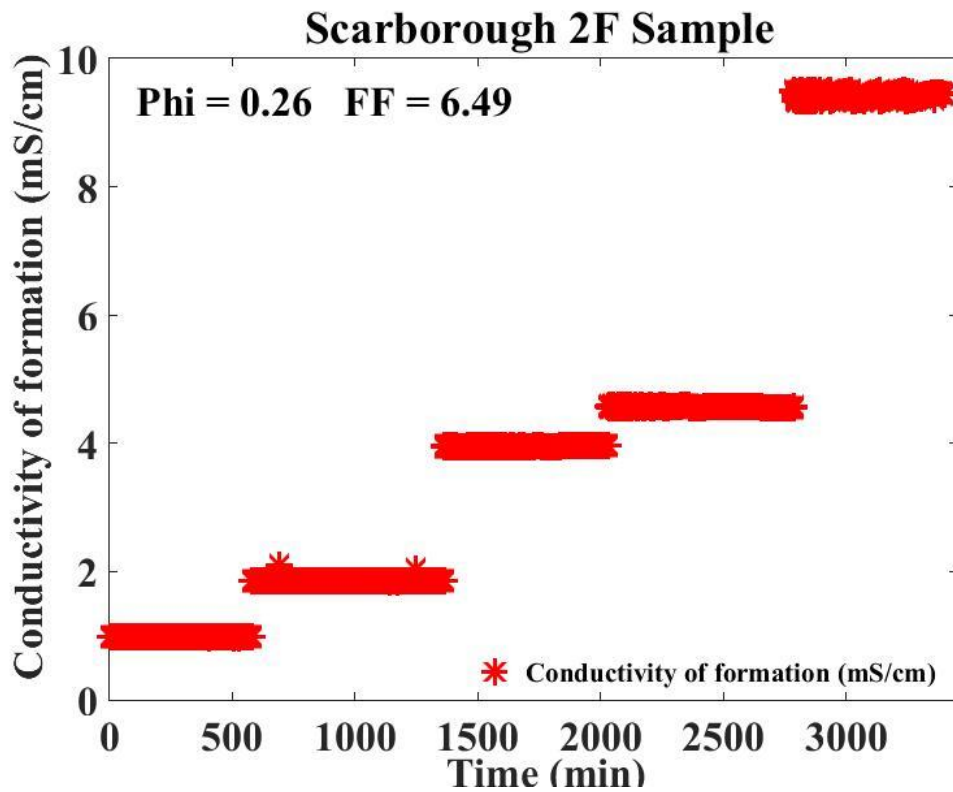
(c)



(d)



(e)



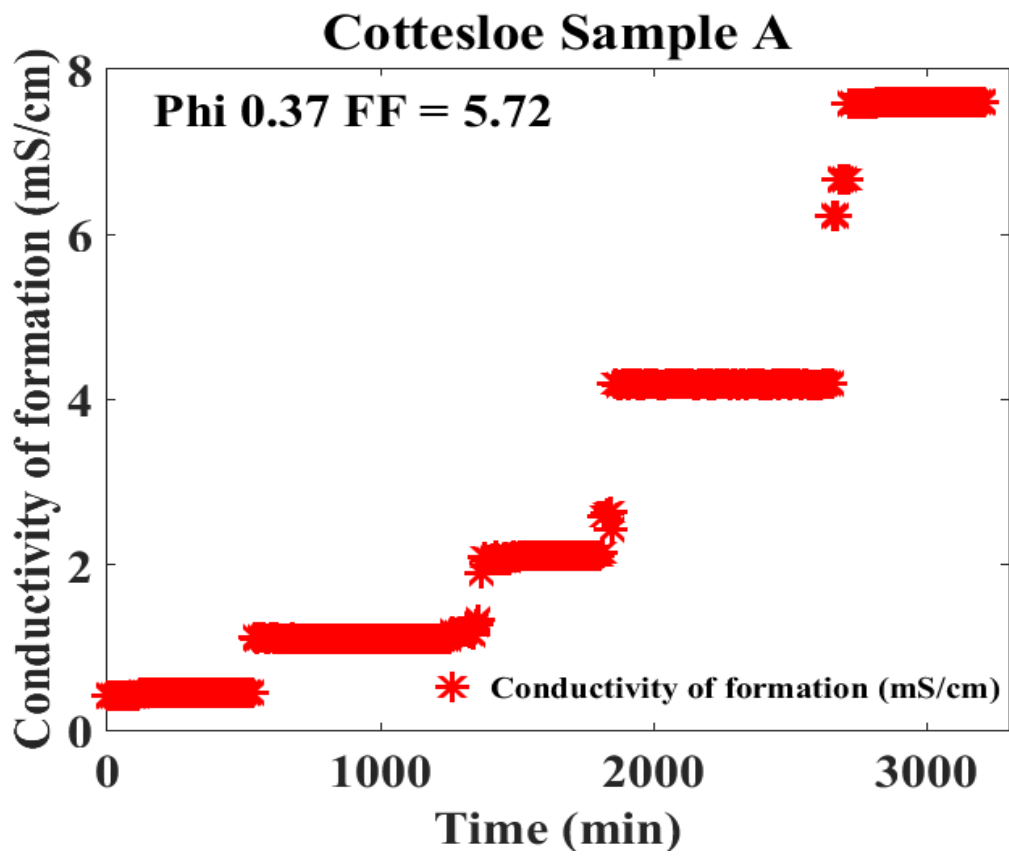
(f)

Figure 5.2.2: Graph of the electrical conductivity of the formation against time from static cell measurements of Scarborough sample 2.

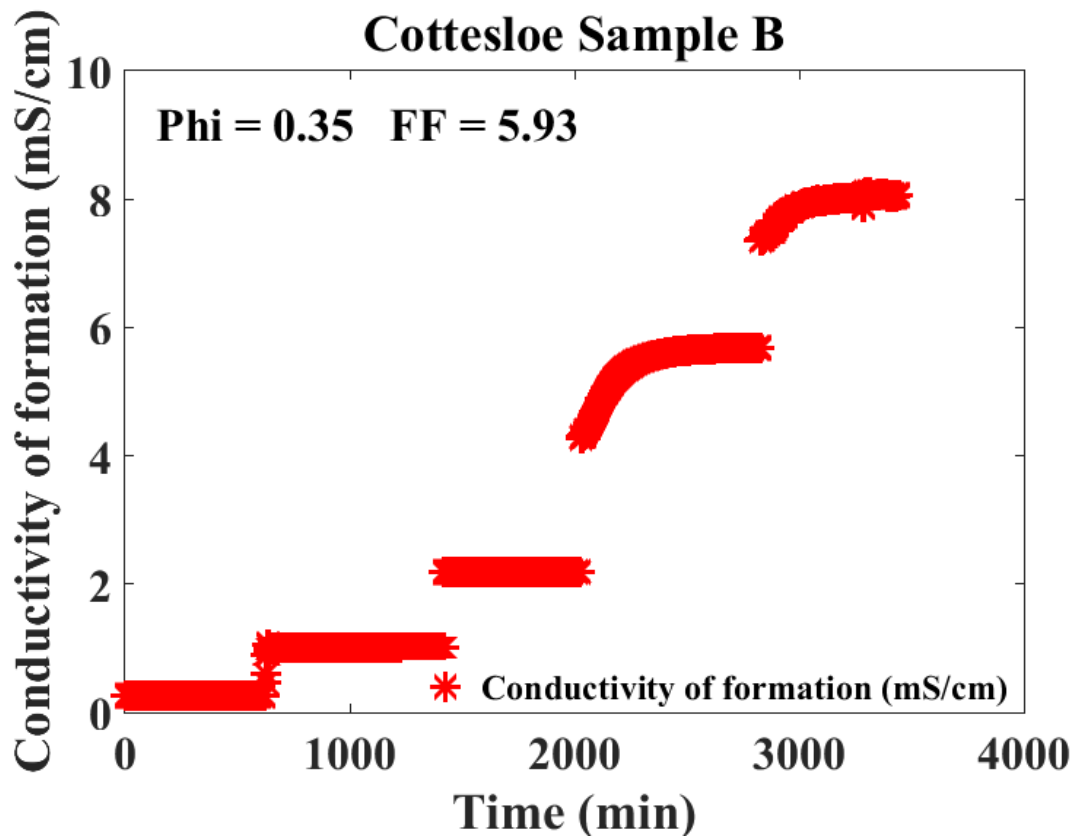
During the static laboratory, experiment of Scarborough Beach samples a, b and f (Figure 5.2.2 (a), (b) and (f)) during the flushing of 35mg/l the readings become unstable due to either electrochemical effects, physical variations of environmental errors. While during experiment (d) (Figure 5.2.2(d)), there was a sharp drop in the conductivity of the formation when replacing 35mg/l saline water with 25mg/l saline water.

The electrical conductivities of the formation against time plotted for the laboratory static measurements for the Cottesloe Beach samples are shown in Figure 5.2.3. The Cottesloe static laboratory measurements also show unstable readings during Cottesloe samples (b) and (d) (Figures 5.2.3(b) and (d)). The recording of this erratic measurement was during replacement of 25mg/l saline water with 35mg/l saline water.

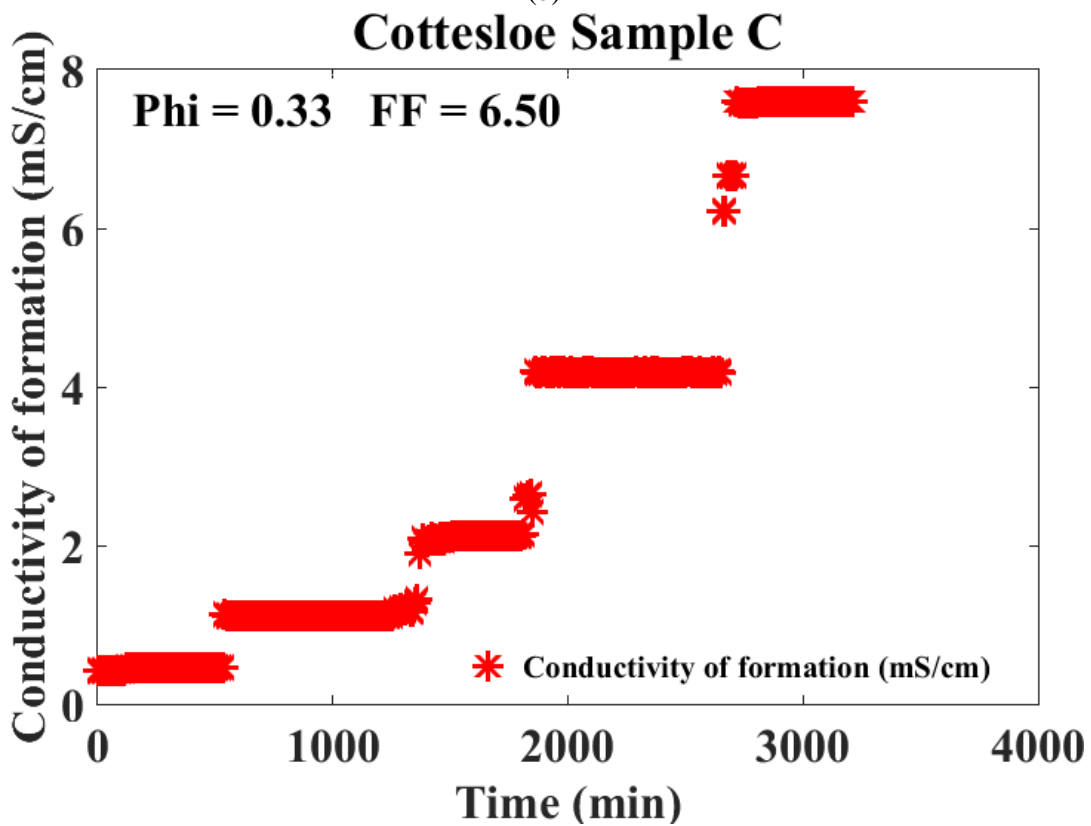
5.2.2.3 Cottesloe results



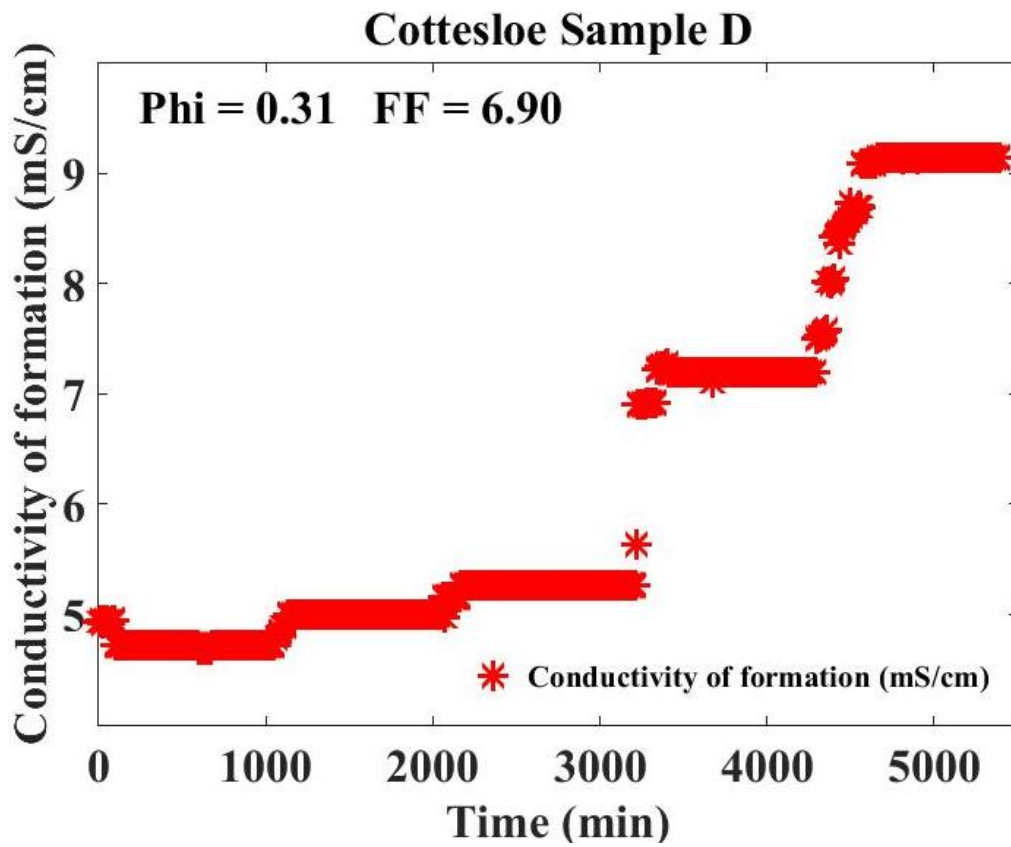
(a)



(b)

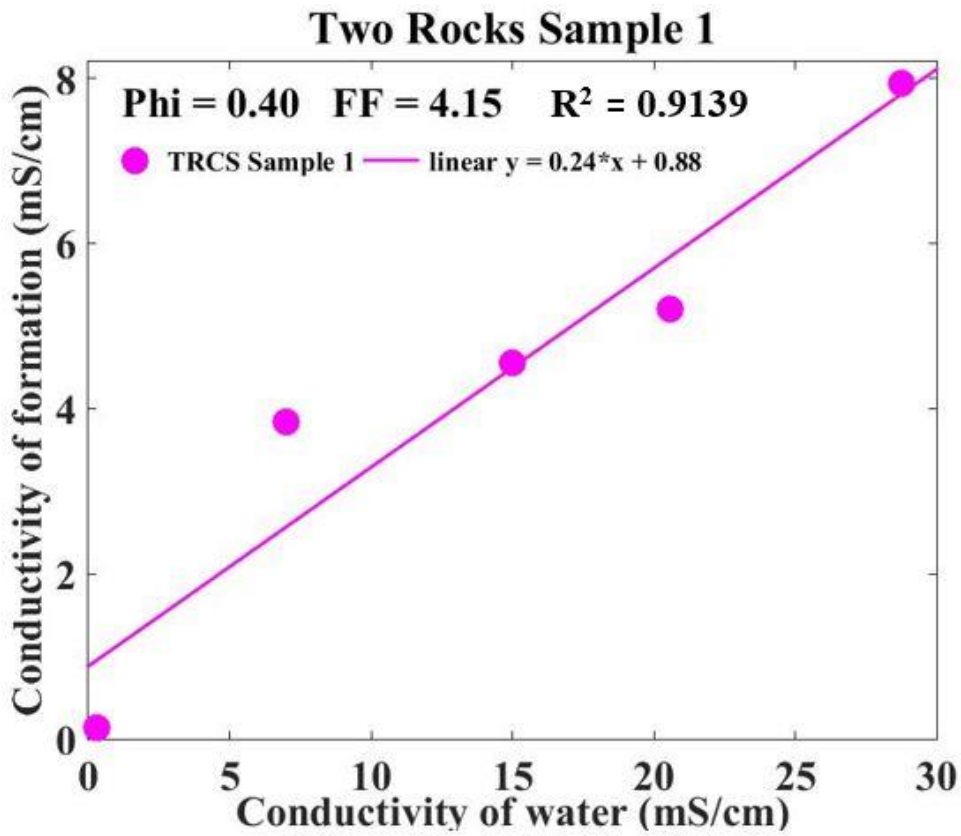


(c)

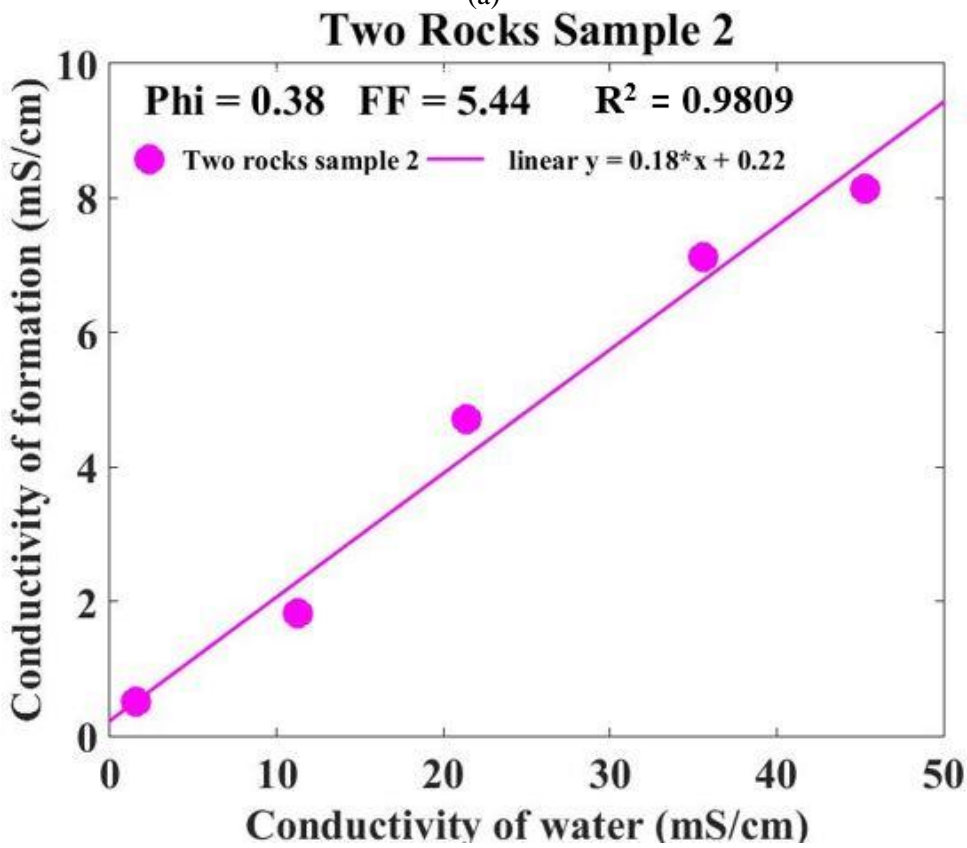


(d)

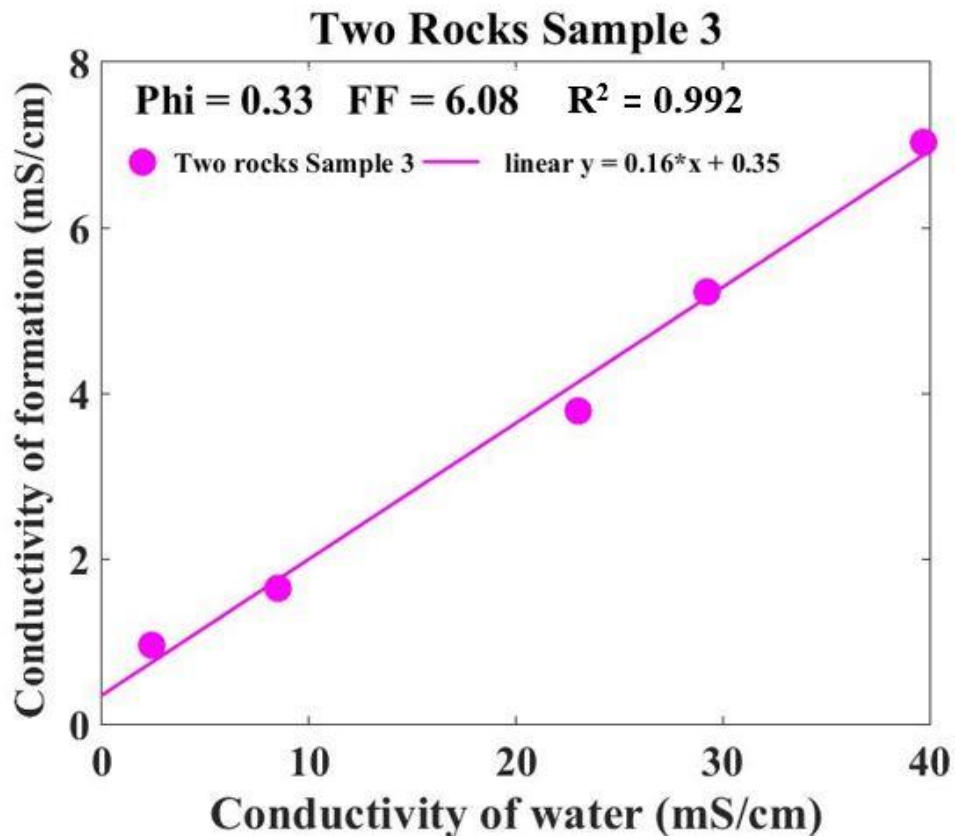
Figure 5.2.3: Graph of the electrical conductivity of the formation against time from static cell measurements of Cottesloe samples.



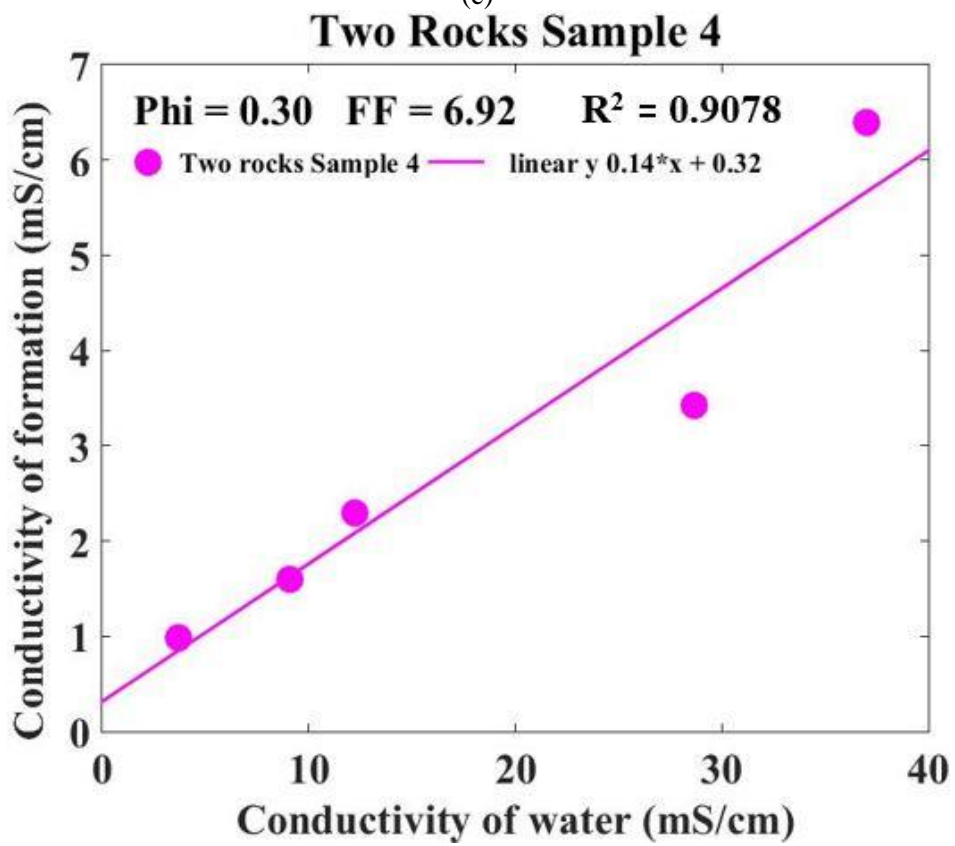
(a)



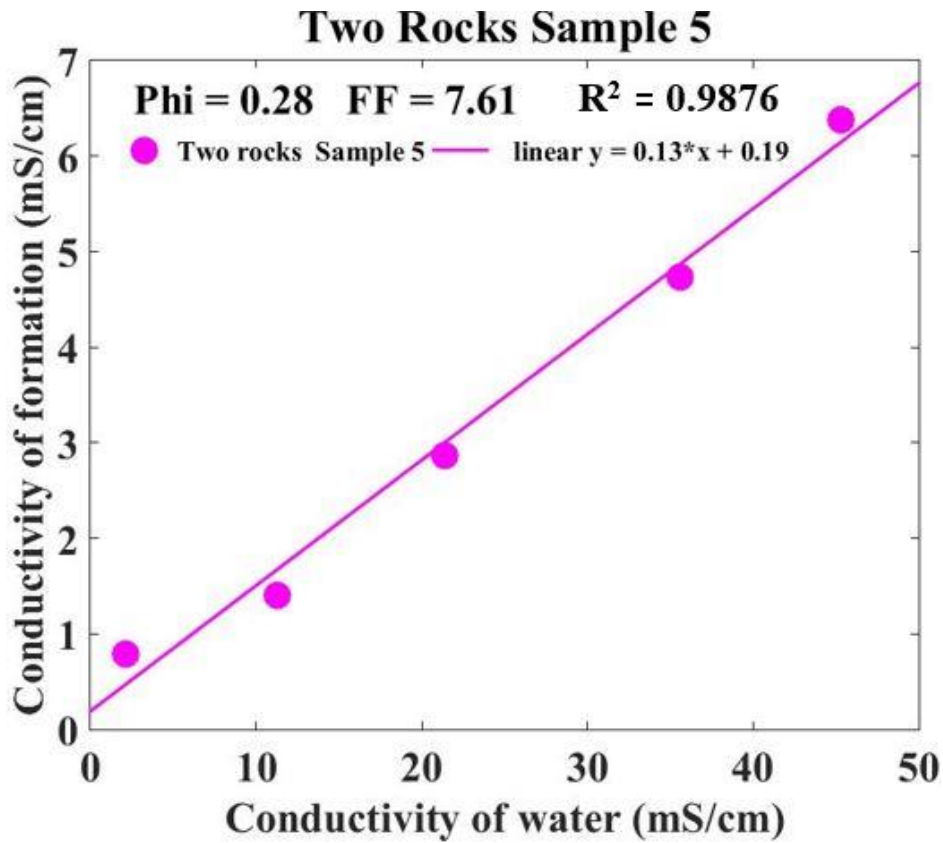
(b)



(c)



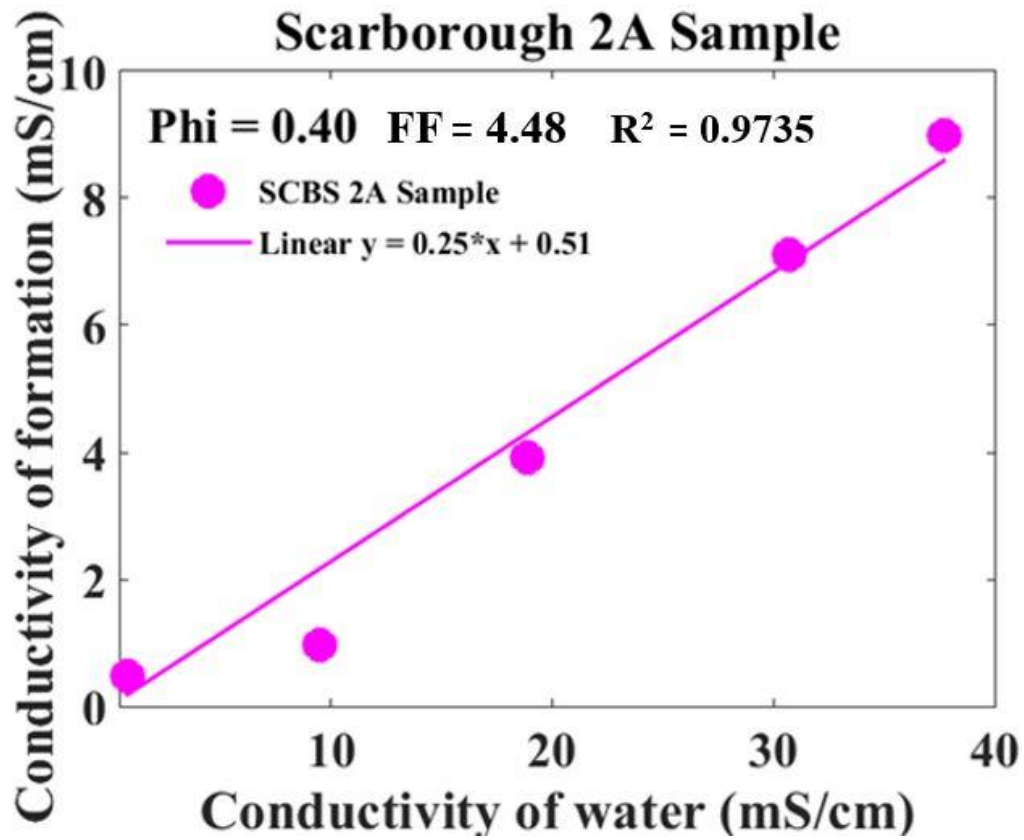
(d)



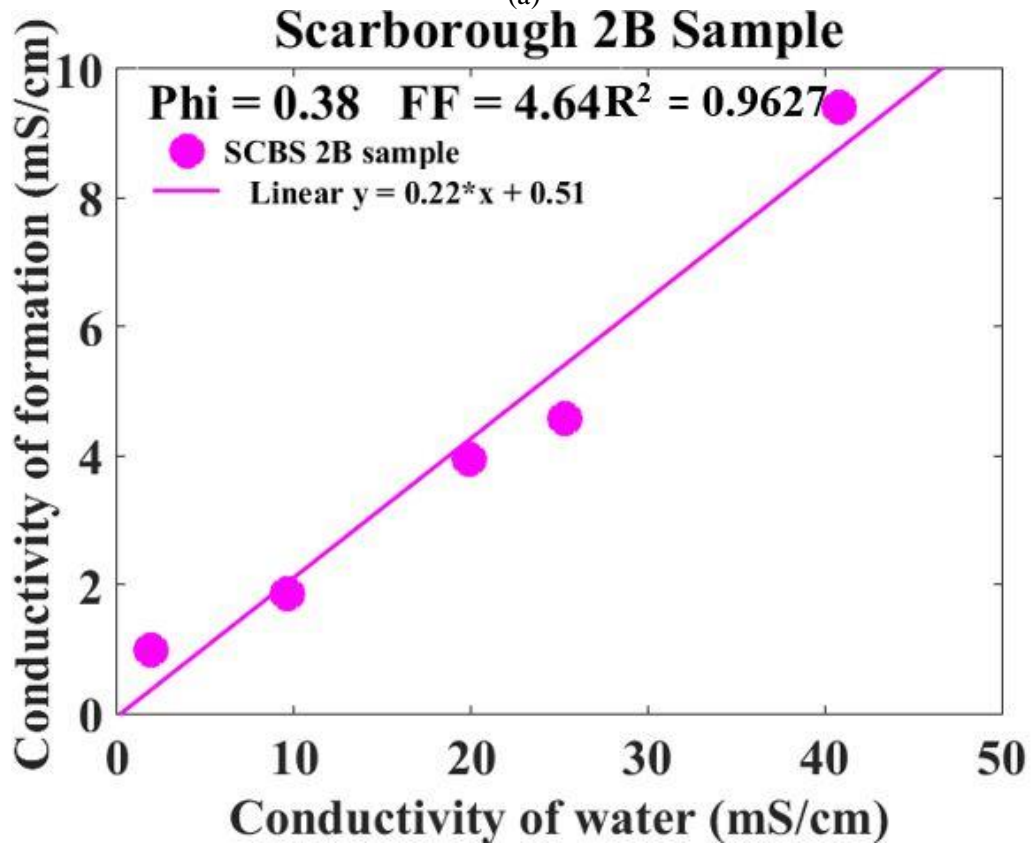
(e)

Figure 5.2.4: Graphs of the electrical conductivity of the formation against the electrical conductivity of water for static cell measurements of Two Rocks samples.

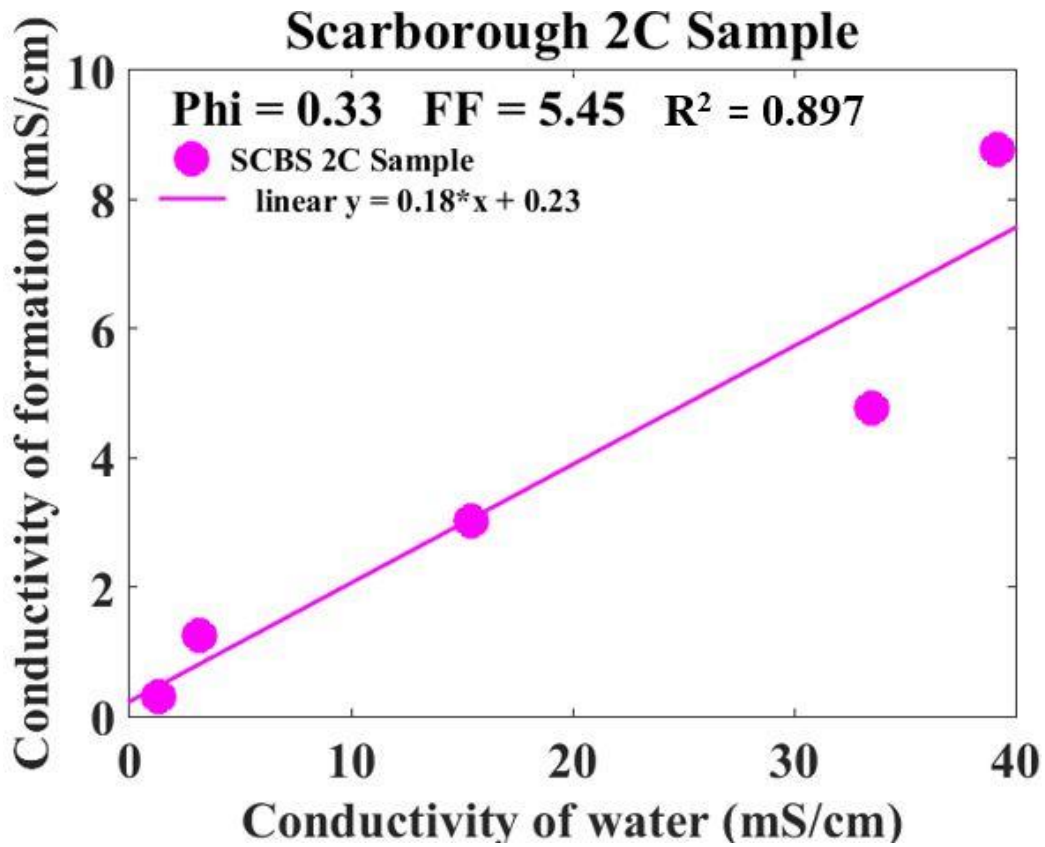
The graph of the electrical conductivity of the formation against the electrical conductivity of water for the static laboratory measurements from the Two Rocks samples shows a poor correlation especially in Two Rocks samples 1 and 4 during flushing of 5mg/l with 25mg/l and flushing 25mg/l for samples 1 and 4 respectively Figure 5.2.4(a) and Figure 5.2.4(d).



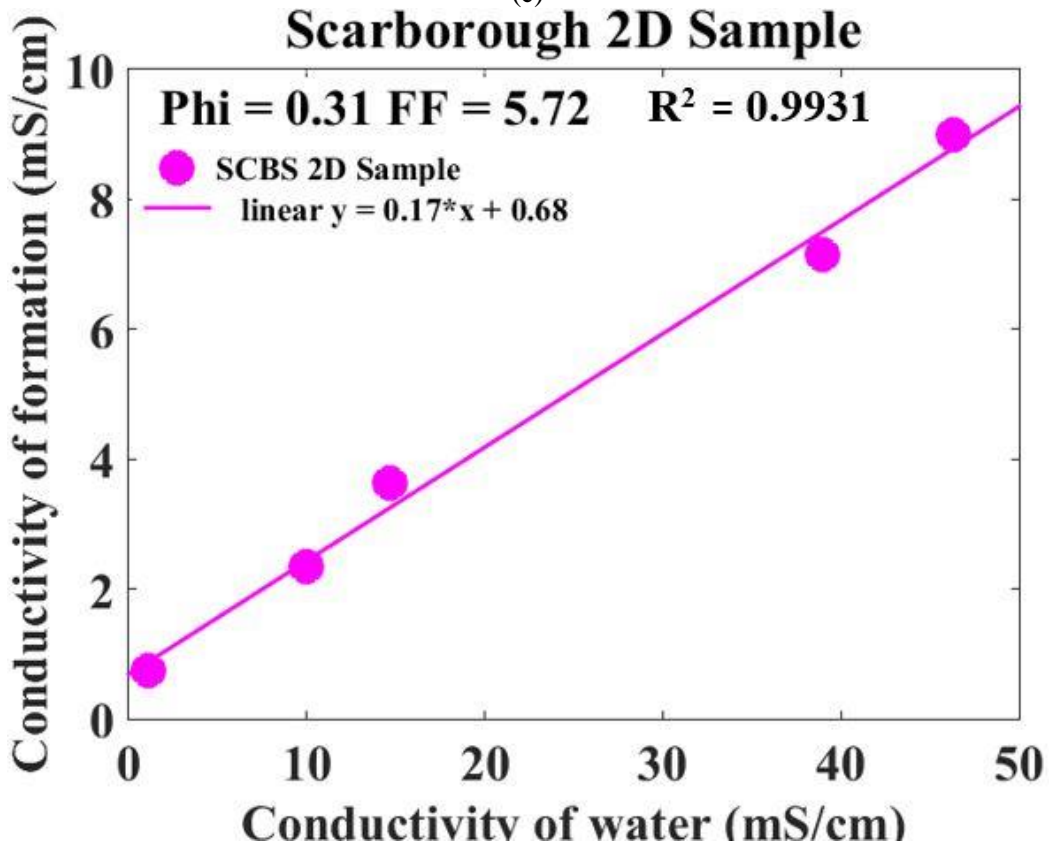
(a)



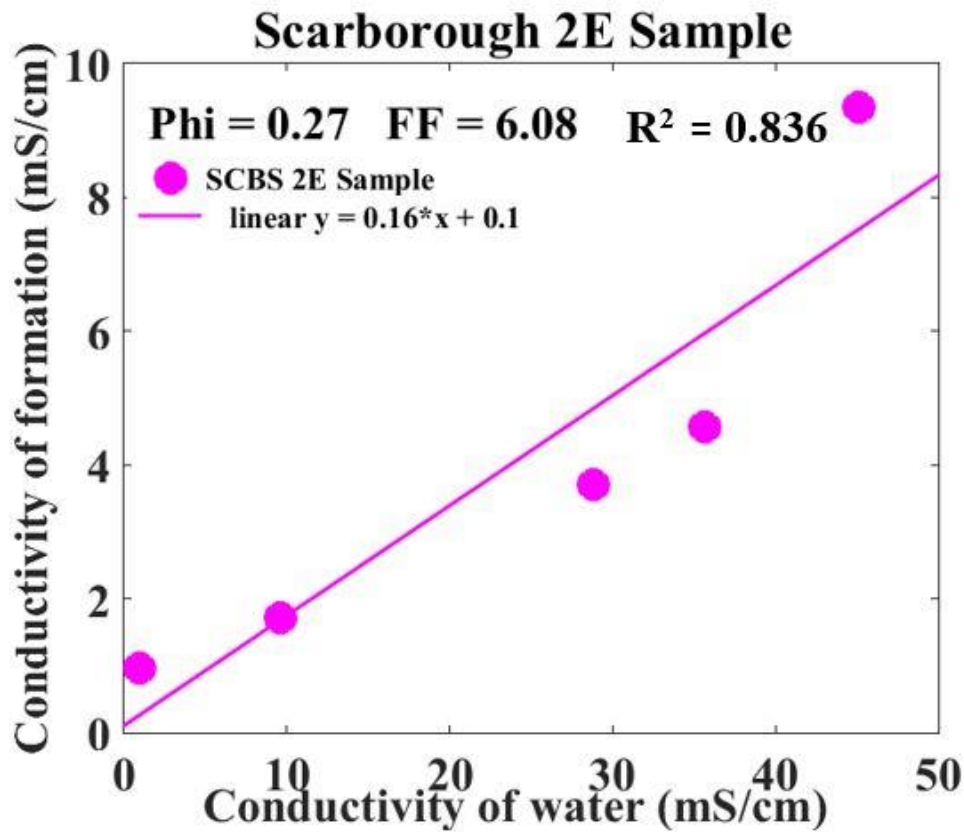
(b)



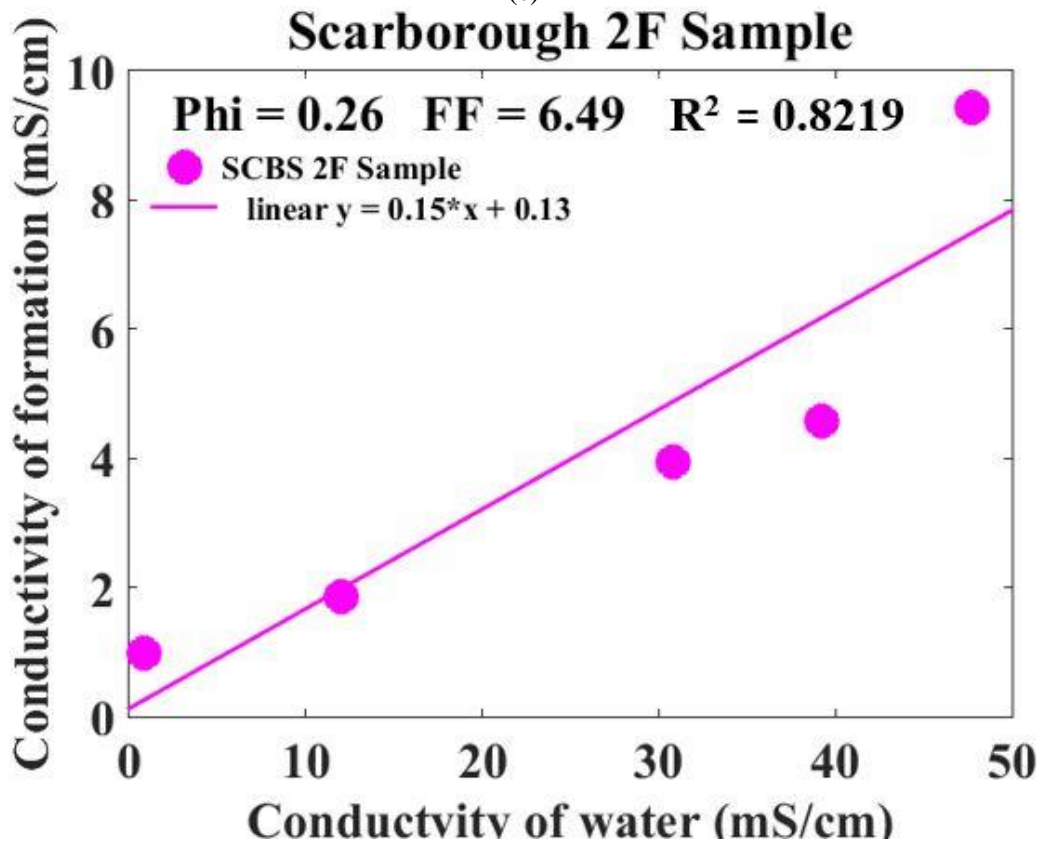
(c)



(d)

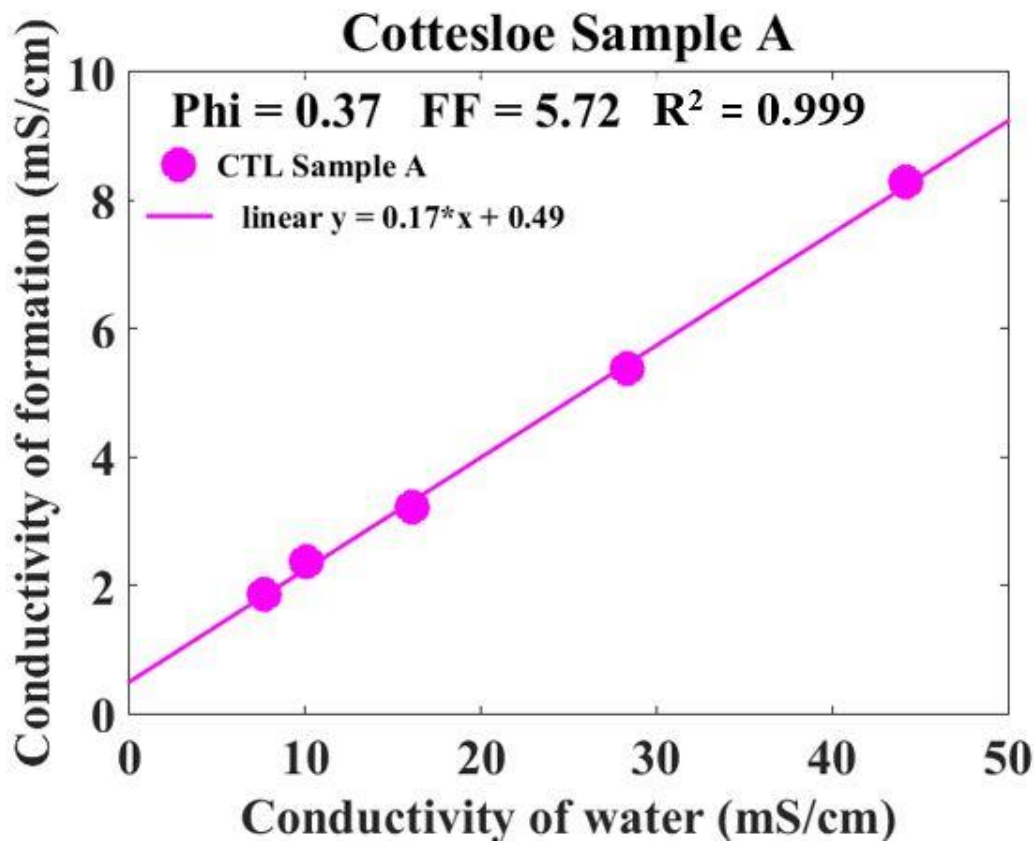


(e)

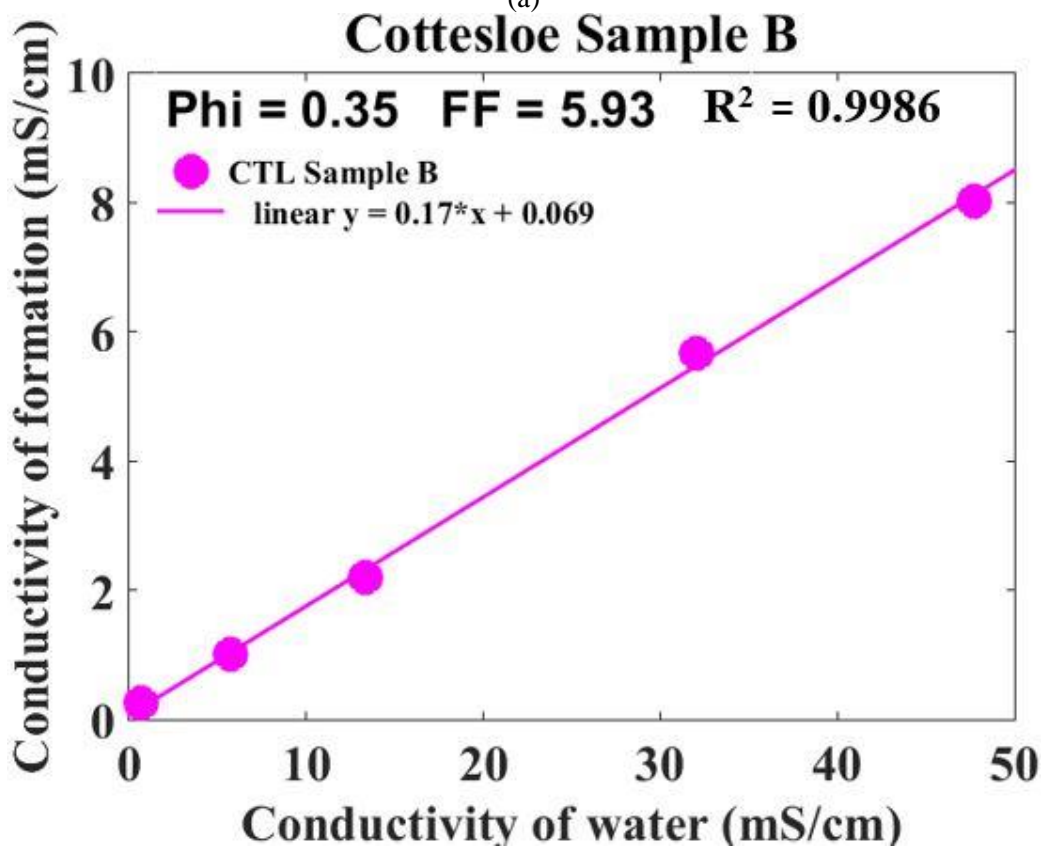


(f)

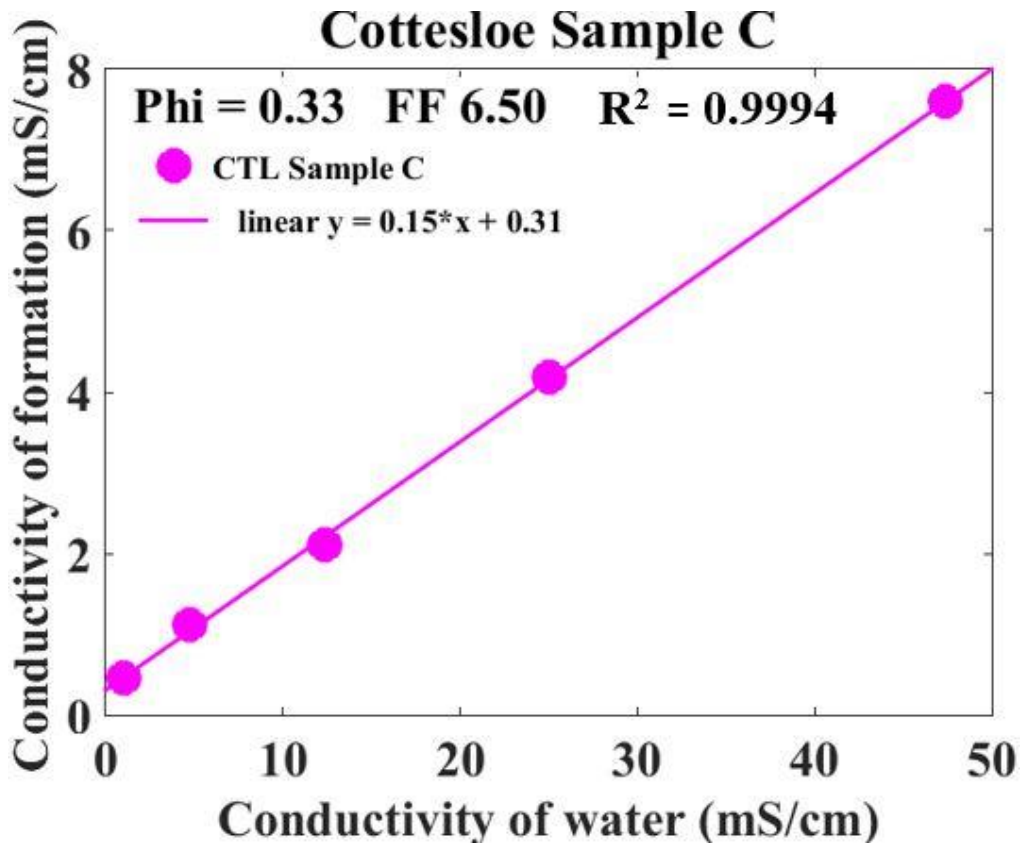
Figure 5.2.5: Graphs of the electrical conductivity of the formation against the electrical conductivity of water for static cell measurements of Scarborough sample 2.



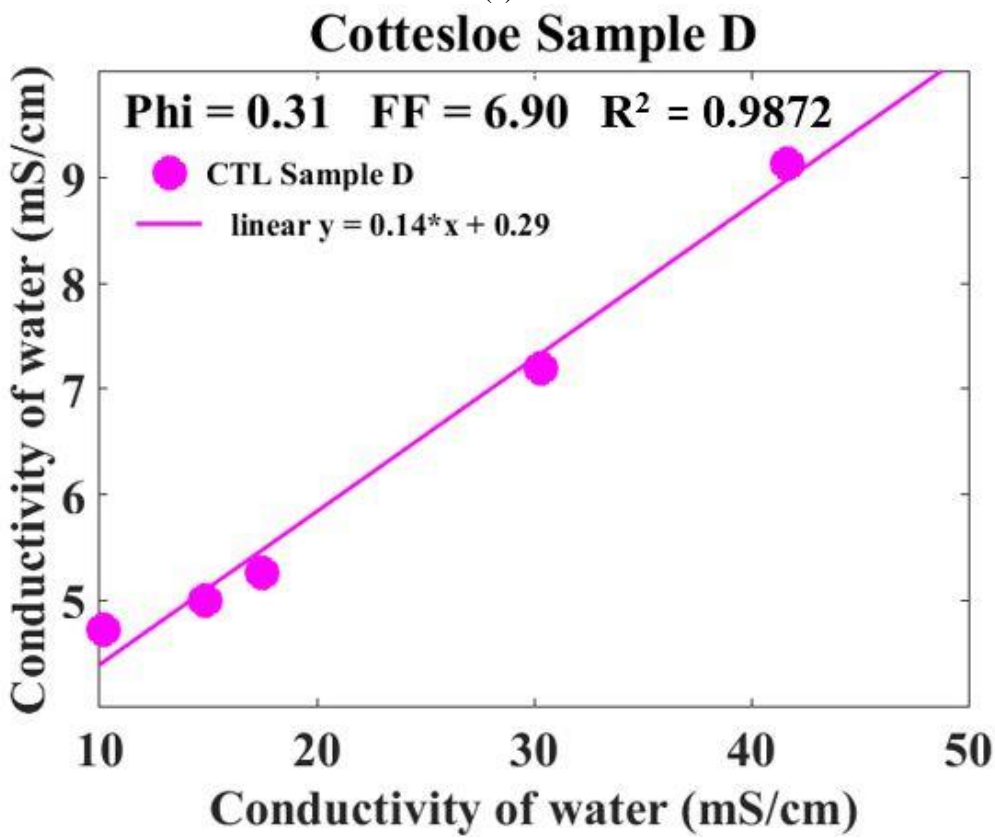
(a)



(b)



(c)



(d)

Figure 5.2.6: Graphs of the electrical conductivity of the formation against the electrical conductivity of water for static cell measurements of the Cottesloe samples.2

5.3 Error and possible experimental defects

- During the flow cell, experiment of Scarborough sample 1B sample Figure 5.1.2(b), there was decrease in conductivity of the formation. This decrease was due to partial contact between the electrodes and the crocodile clips which led to erratic readings; this problem was not noticed for about 40 minutes after the start of the experiment and was immediately rectified by firmly attaching the crocodile clip to the electrode.
- An unstable reading was also recorded during the flow cell experiment of Scarborough sample 2F Figure 5.1.3(f): however, it was noticed there was not much difference in the conductivity of formation at 25mg/l saline water and 35mg saline water.
- There was lack of significant change in the electrical conductivity of the formation when a higher saline solution replaced a lower saline solution especially when replacing fresh water with 0.5mg/l saline water during the Scarborough flow cell experiments. This might be because at the lower conductivity of fresh water to 0.5mg/l saline water, the difference in the electrical conductivity of both the water and the formation is not much (as seen in Figure 5.1.3(b), (d), and (f)).
- The graph of the conductivity of the formation against the conductivity of water for Cottesloe samples 1D Figure 5.1.8 shows scattered points. This is because there was instability as well as electrochemical effects, physical variations of environmental errors during the laboratory experiments of the samples, as shown in Figure 5.1.4.
- The graphs of the conductivity of the formation against conductivity of water for static laboratory measurements of Scarborough samples 2(c), (e) and (f) in Figure 5.2.5(c), (e), and (f) show scattered data this might be attributed to the instability of the reading during the experiment Figure 5.2.2(b), (d) and (f).

5.4 Micro CT-scan images

I used Avizo fire to analyse images of Scarborough and Cottesloe sand obtained from Micro CT scan. Ninety-six (96) cubes of micro CT-scans were produced, forty-four (44) for Scarborough and fifty-two (52) for Cottesloe, for the four (4) cubes (200^3 , 350^3 , 500^3 and 700^3). The calculation of porosity for the cubes of Scarborough and Cottesloe beaches is done in the following way:

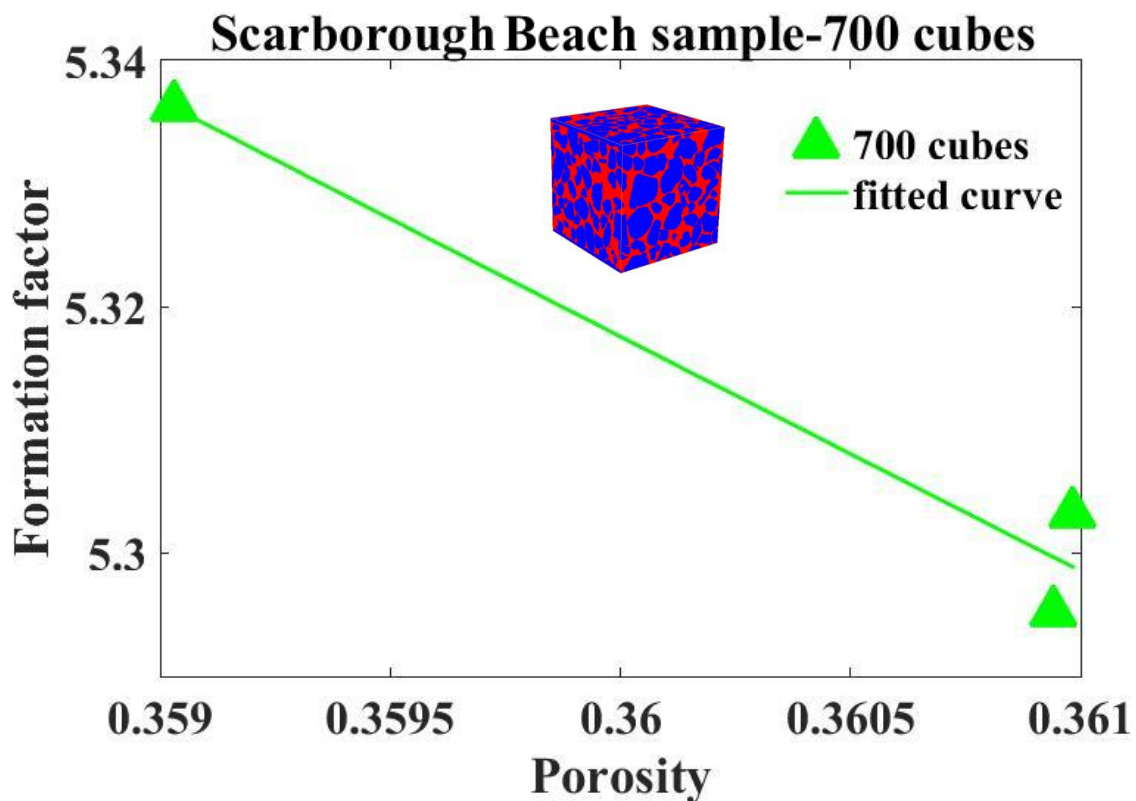
5.4.1 Porosity calculations from the images

The porosity calculations from the images were done using Avizo fire 9; this was achieved by loading the image and filtering it using a Local filter, which was followed by segmentation using threshold (2-phase) segmentation. The image was cropped into three and five $(700)^3$ cubes. The centre cube with coordinates x (min 144 and max 843), y (min 156, and max 855), and z (min 145, and max 844) was then cropped to cubes of eight and ten $(500)^3$ and 13 and $(350)^3$, and 20 and 24 $(200)^3$ from Scarborough and Cottesloe beaches respectively. I then calculated the porosity of each cube.

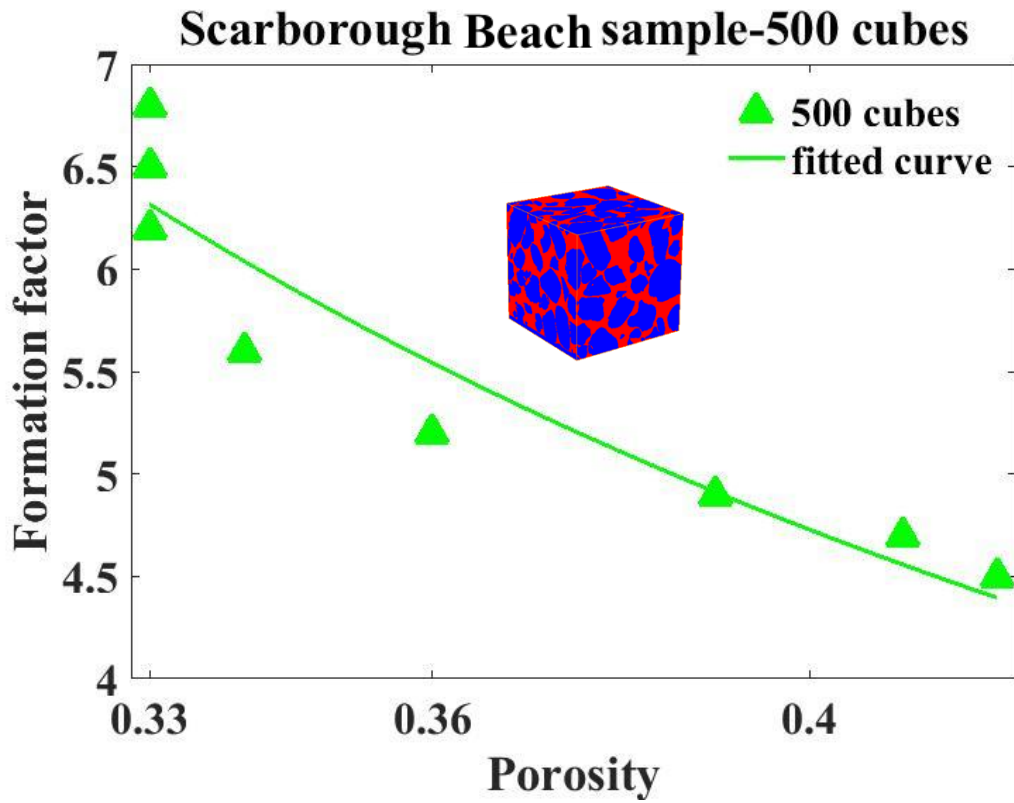
5.4.2 Formation factor calculation from the images

The electrical formation factor was calculated from the segmented images as explained in sections 5.5 (clean sand) and 5.8.3.3 (clay sand). The graphs of the formation factor were plotted against porosity for $(200)^3$, $(350)^3$, $(500)^3$, and $(700)^3$ as shown in Figures 5.3.1 and 5.3.4 Scarborough and Cottesloe Beach samples.

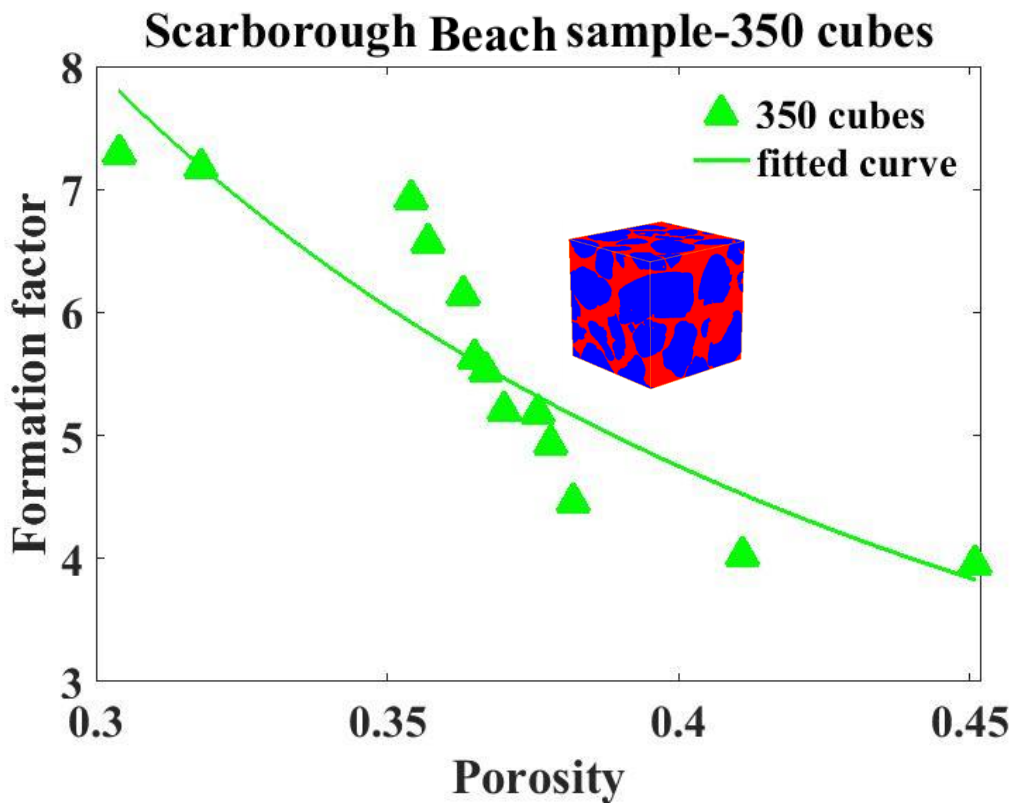
5.4.2.1 Scarborough results



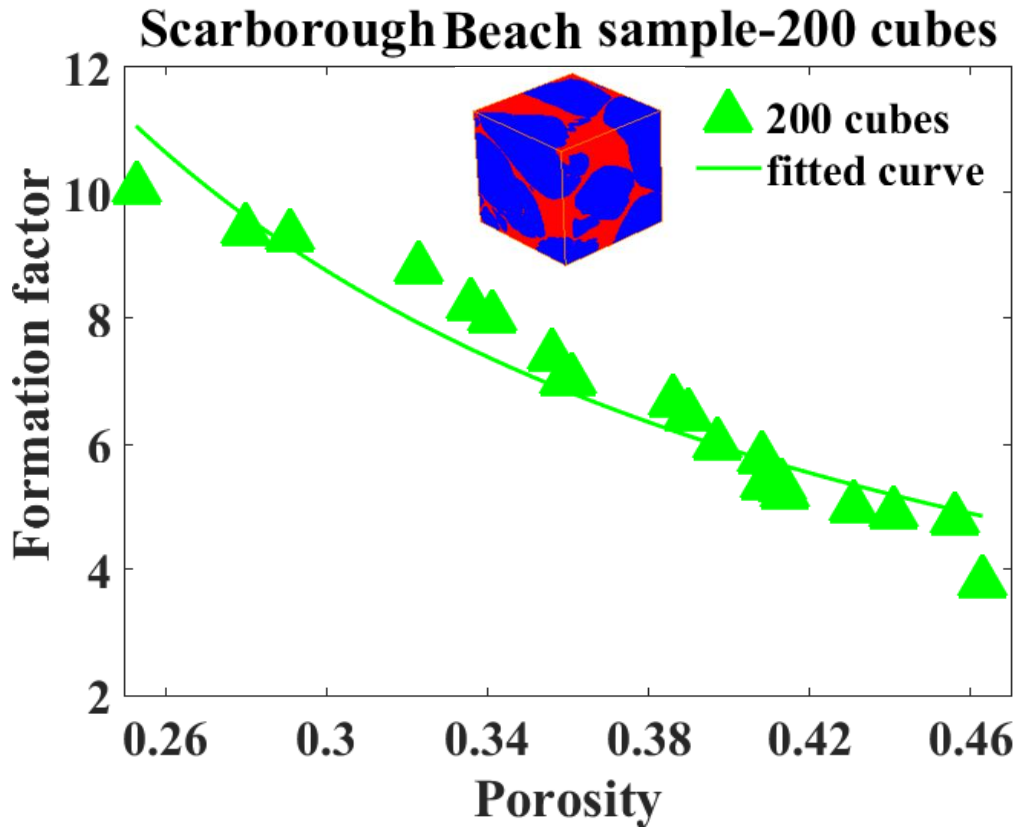
(a)



(b)



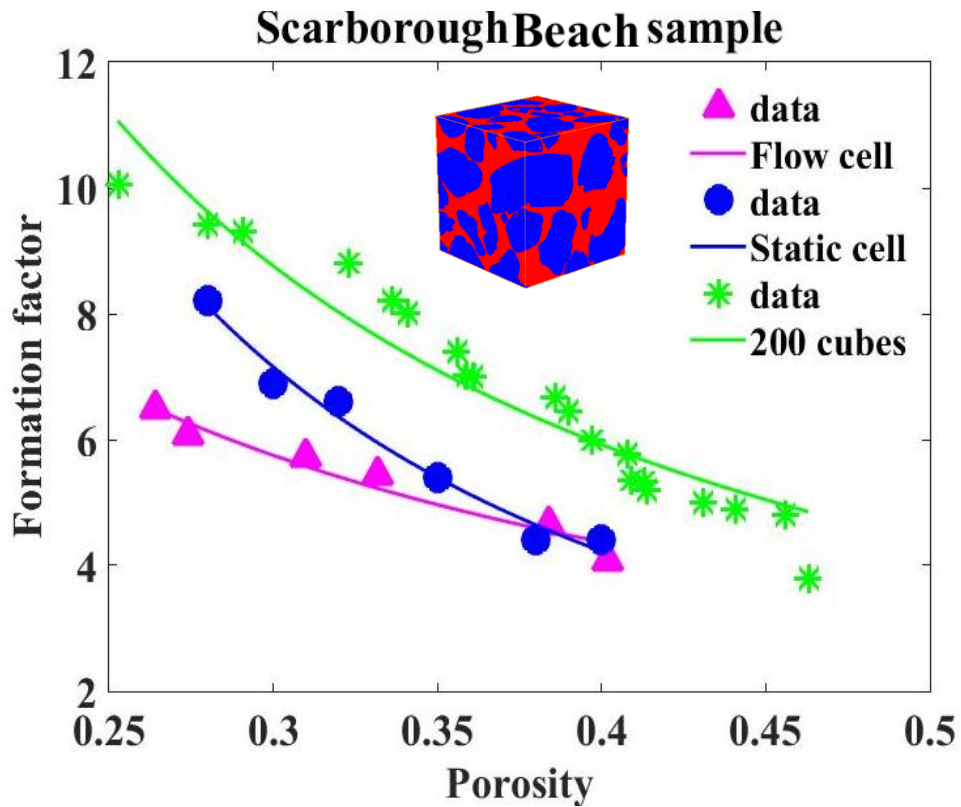
(c)



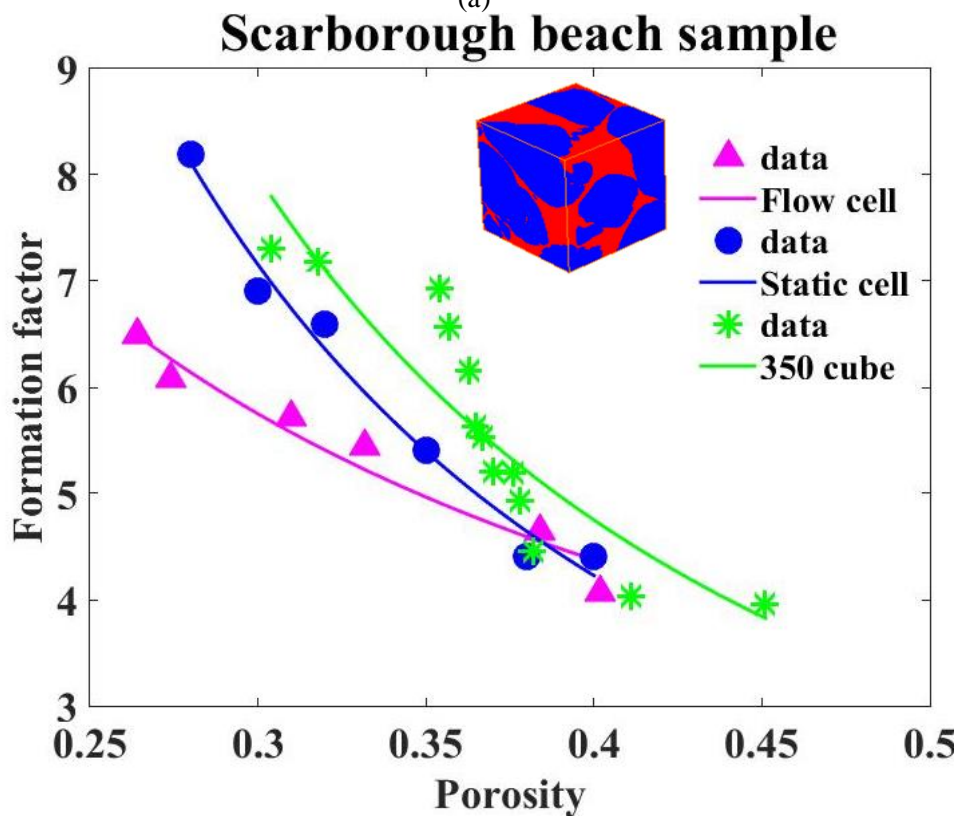
(d)

Figure 5.3.1: Electrical formation factor versus porosity for Scarborough micro CT-scan images.

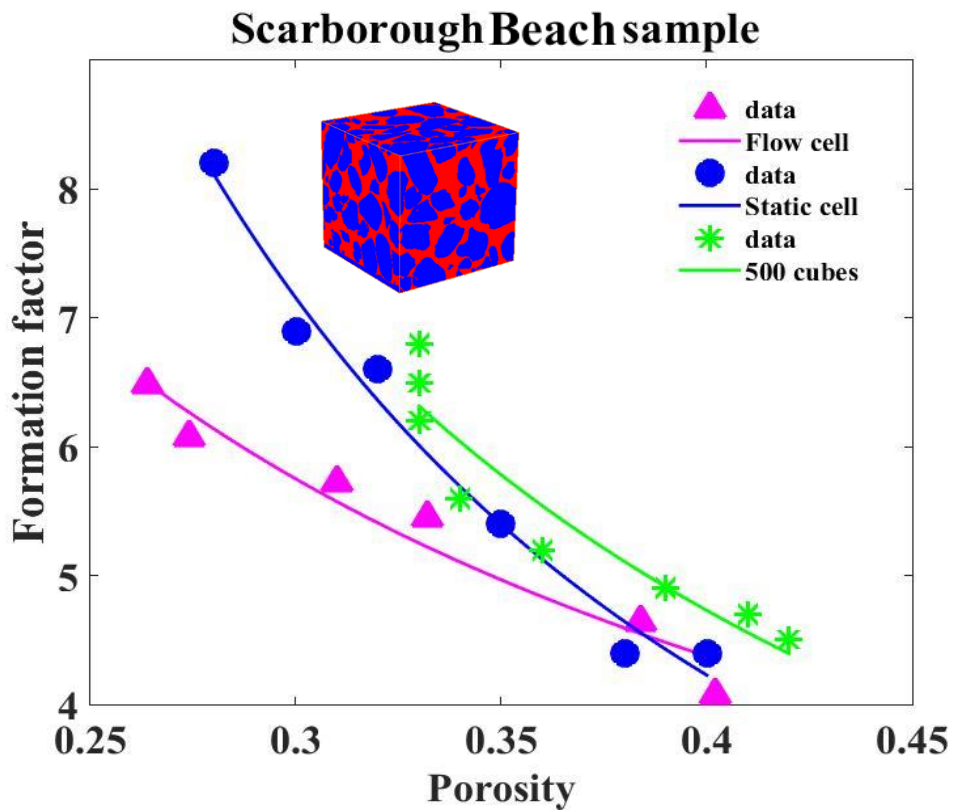
Although the formation factor trend was observed in $(200)^3$ Figure 5.3.1(d), the trend is scattered in cubes $(350)^3$ and $(500)^3$ while for cubes 500 the same porosity of 0.33 was found for 3 different cubes each having a different formation factor. The three cubes of $(700)^3$ have almost the same porosity and formation factor 0.35 and 5.3 respectively when the representative elemental volume was reached at about 500 voxels because the physical properties (porosity and formation factor) becomes stable.



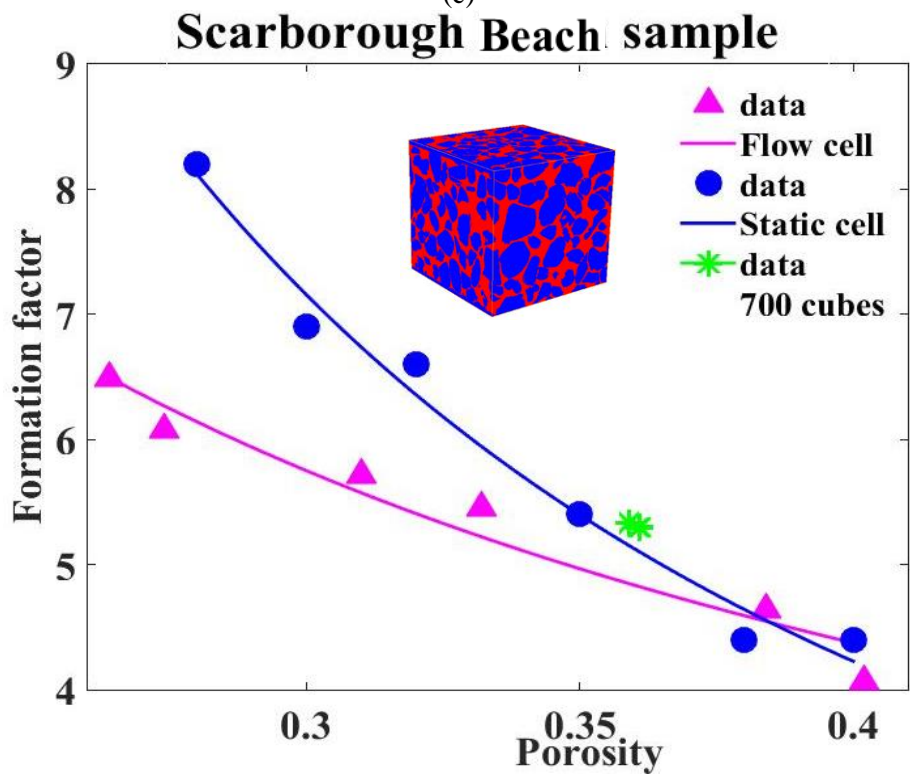
(a)



(b)



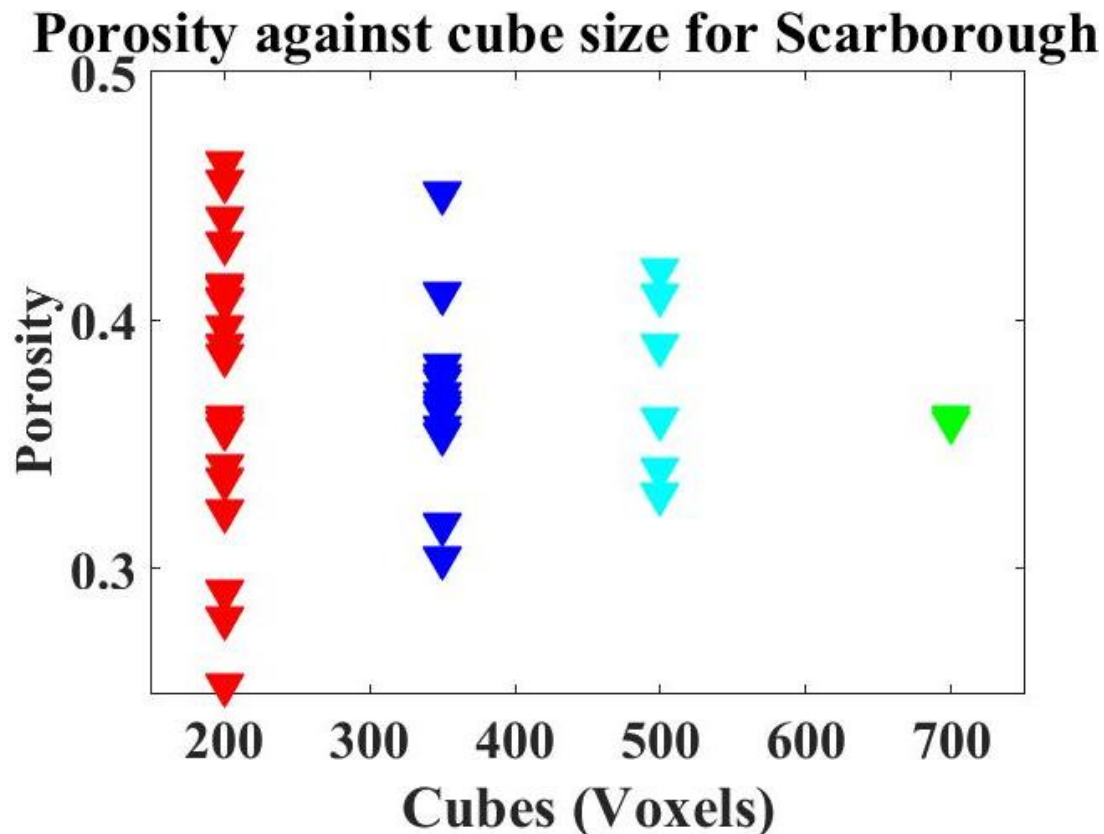
(c)



s(d)

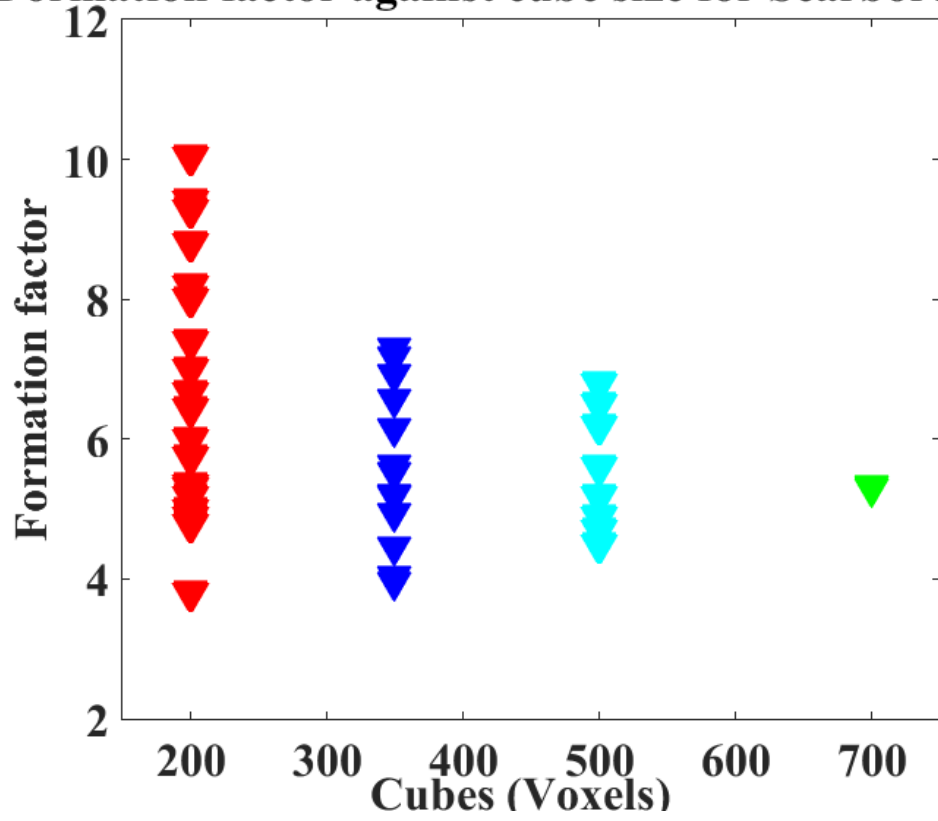
Figure 5.3.2: Scarborough Micro CT-scan images of cubes with measurements for the flow cell in pink and static in blue while green is for the cubes.

I was able to obtain only four different porosities during the laboratory static measurement of Cottesloe Beach and the flow cell measurements gave a complete deviation of formation factor when the least porosity of 0.26 was attained (Figure 5.2.4). Although there was consistency between the laboratory and micro CT-scan measurements of Cottesloe, there was, however, a cross between the 500 cubes and flow cell measurement as shown on figure 5.2.2(c). The graphs of porosity against cube size and formation factor against cubes sizes were plotted for $(200)^3$ in red, $(350)^3$ in blue, $(500)^3$ in cyan, and $(700)^3$ in green (Figures 5.3.3a and 5.3.3b for Scarborough and Cottesloe beaches respectively). For the plots of both Scarborough and Cottesloe clean sands for the porosities against cube sizes, the porosity has a very wide range especially when the cube sizes are small $(200)^3$ and $(350)^3$. The porosities range from 0.25 to 0.45 for 200 cubes of Scarborough, while it has a range of 0.26 to 0.39 for the Cottesloe clean sand sample. This wide porosity range tend to taper as the Representative Elemental Volume is approached at about $(500)^3$ as seen in Figure 5.3.3(a) and 5.3.6(a) for Scarborough and Cottesloe respectively. The summaries of the laboratory and micro-CT scan images from the Scarborough and Cottesloe Beach samples are presented in Tables 5.1 and 5.2.



(a)

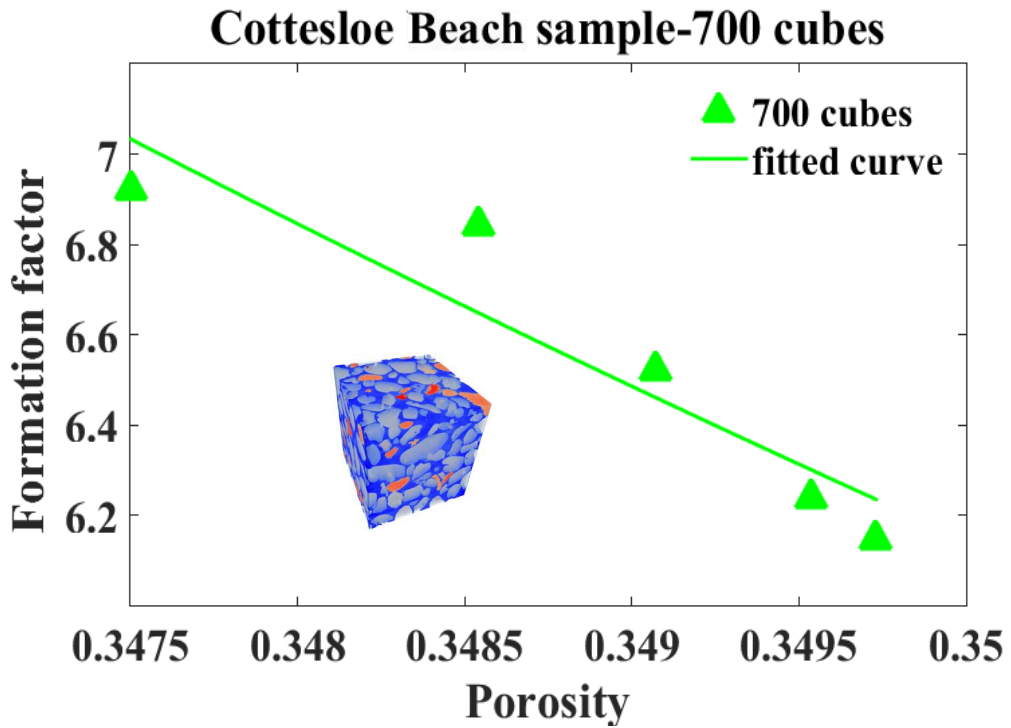
Formation factor against cube size for Scarborough



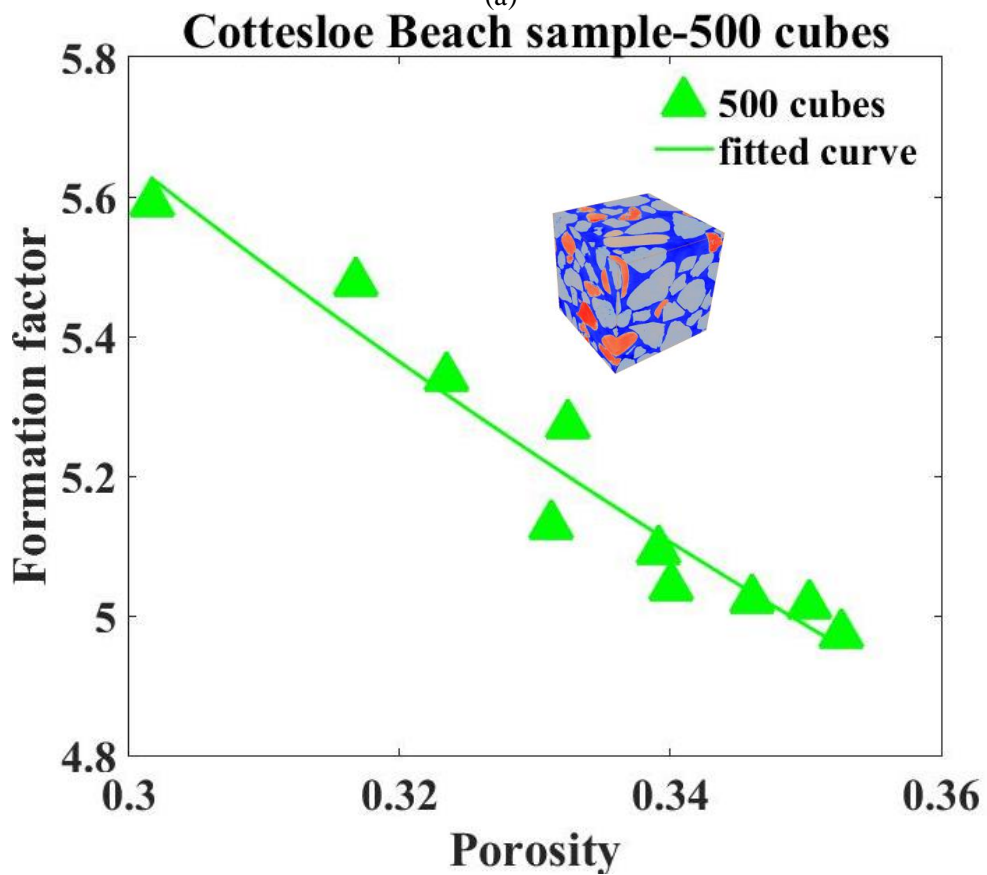
(b)

Figure 5.3.3: (a) Porosity against cube sizes and (b) formation factor against cube sizes for Scarborough Beach sample.

5.4.2.2 Cottesloe results



(a)



(b)

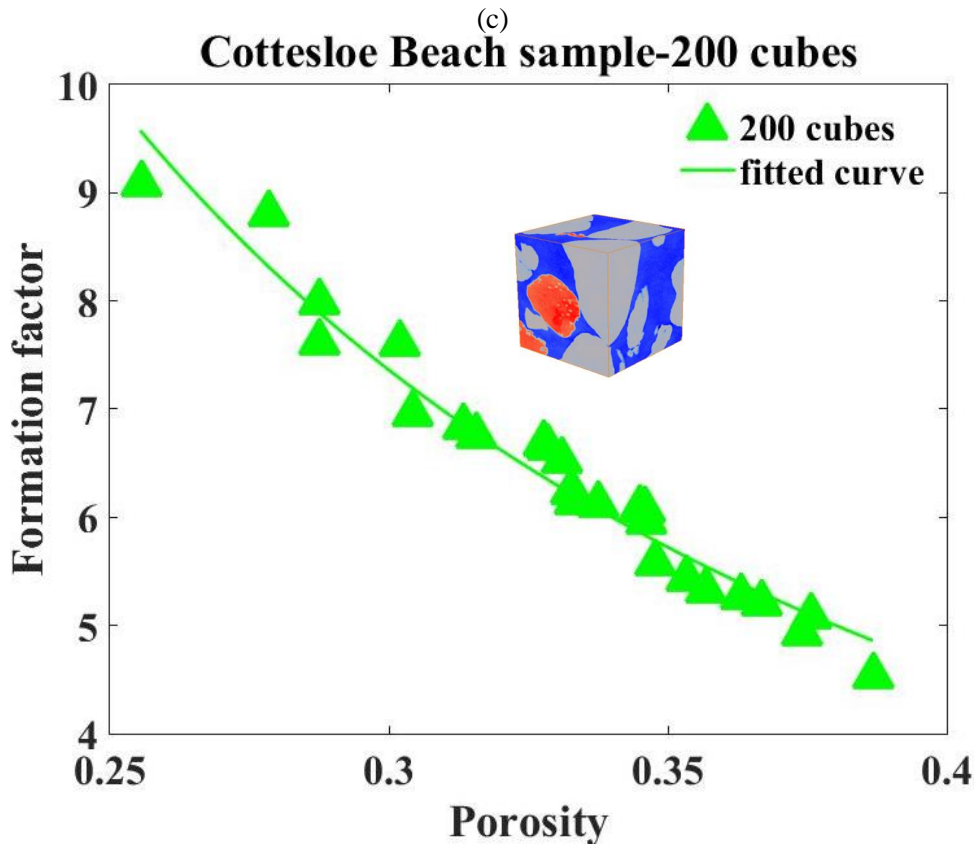
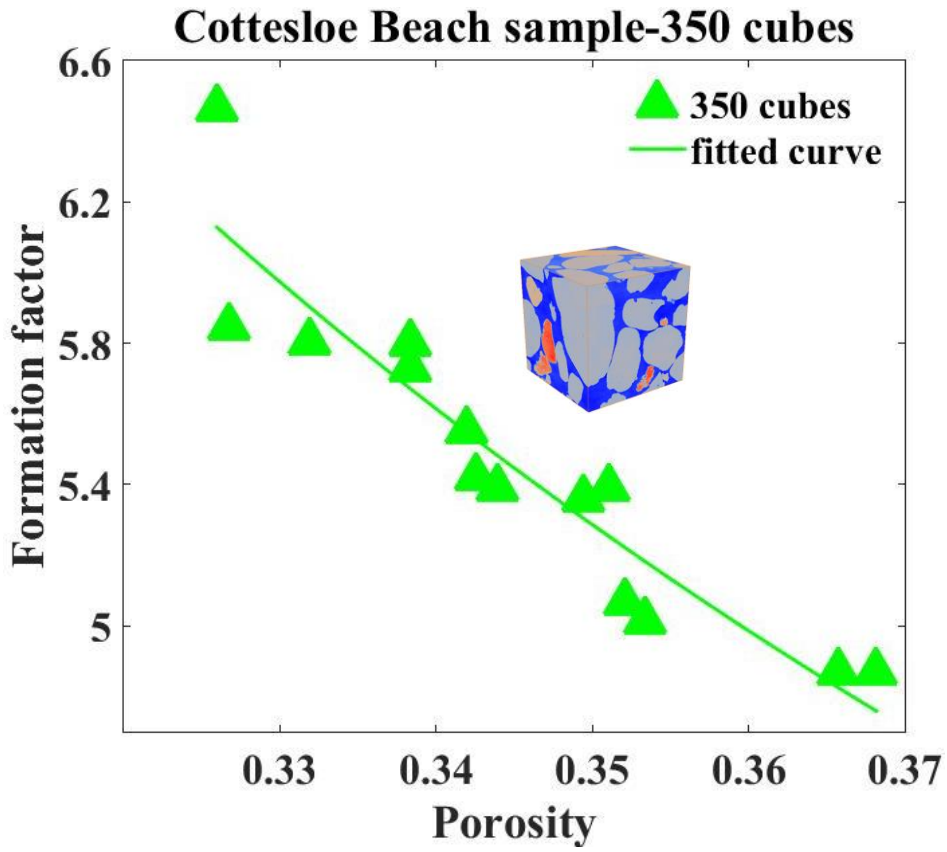
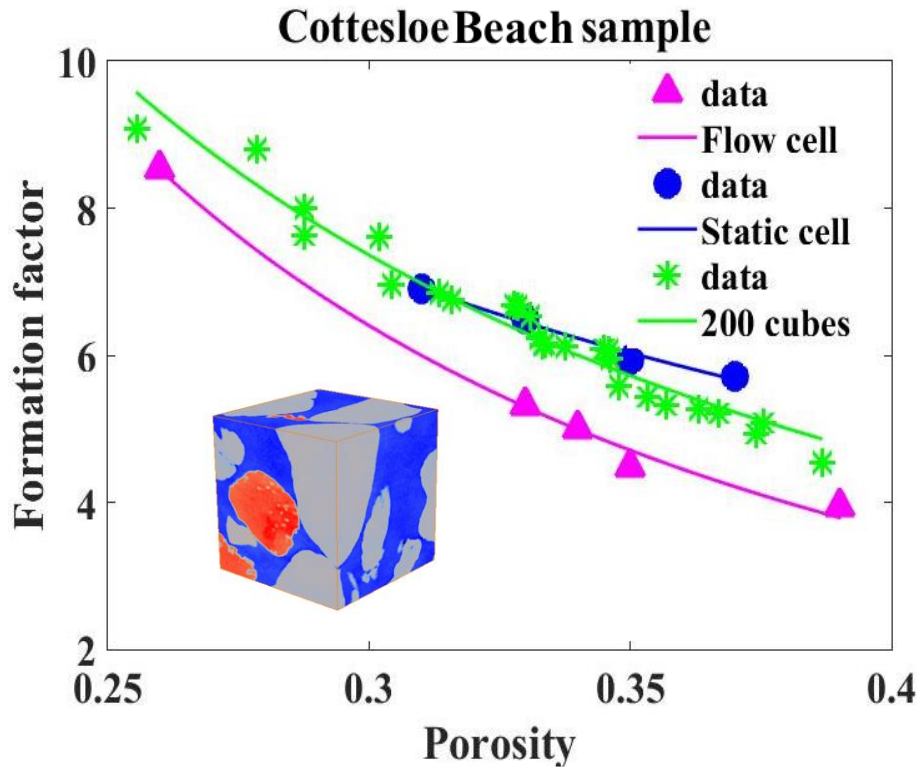


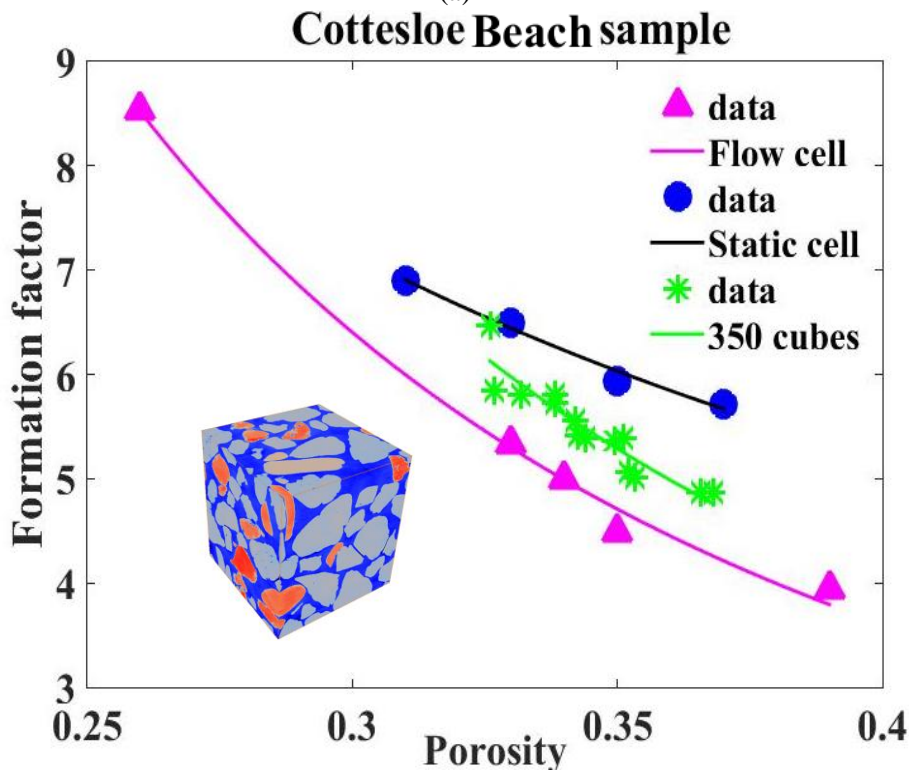
Figure 5.3.4: Electrical formation factor versus porosity for Cottesloe micro CT-scan images

The cubes of the Cottesloe Beach sand sample show a good trend of formation factor against porosity for all cubes $(200)^3$, $(350)^3$, $(500)^3$, and $(700)^3$.

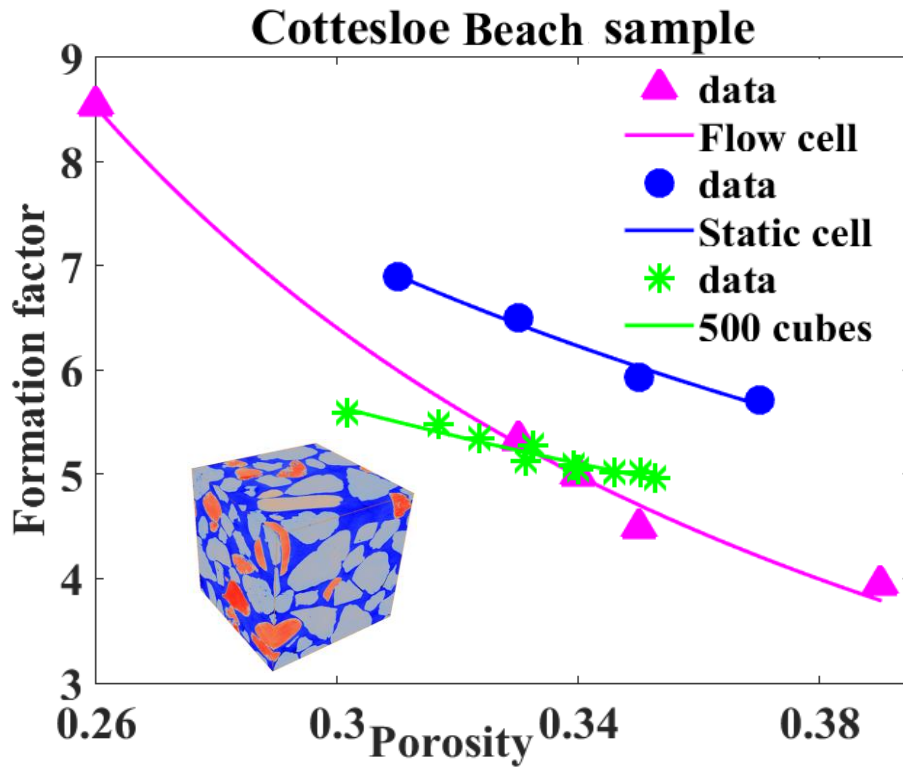
We can see how scattered the points are from $(200)^3$ to $(500)^3$ cubes when the Representative Elemental Volume is not reached.



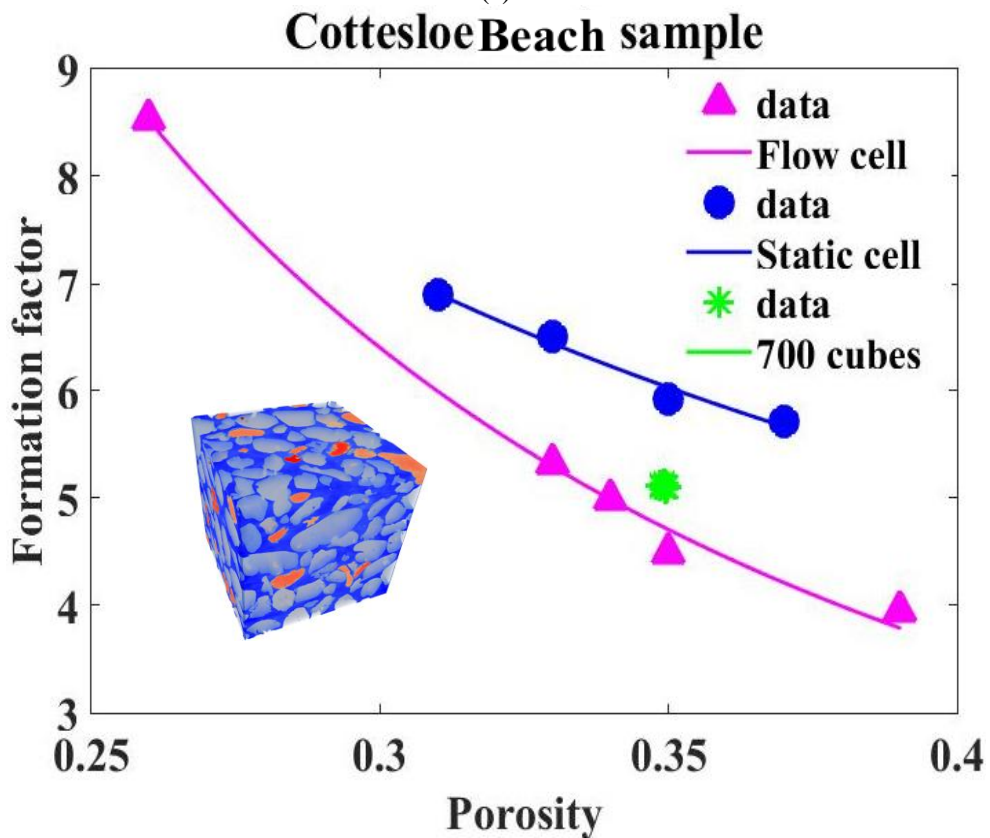
(a)



(b)

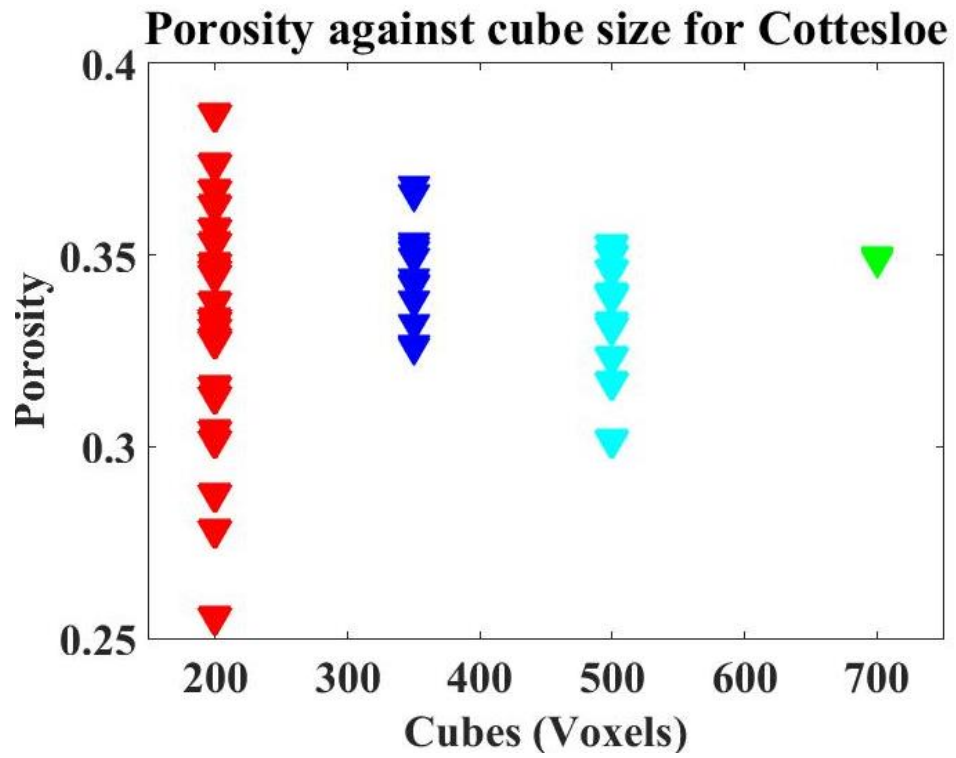


(c)

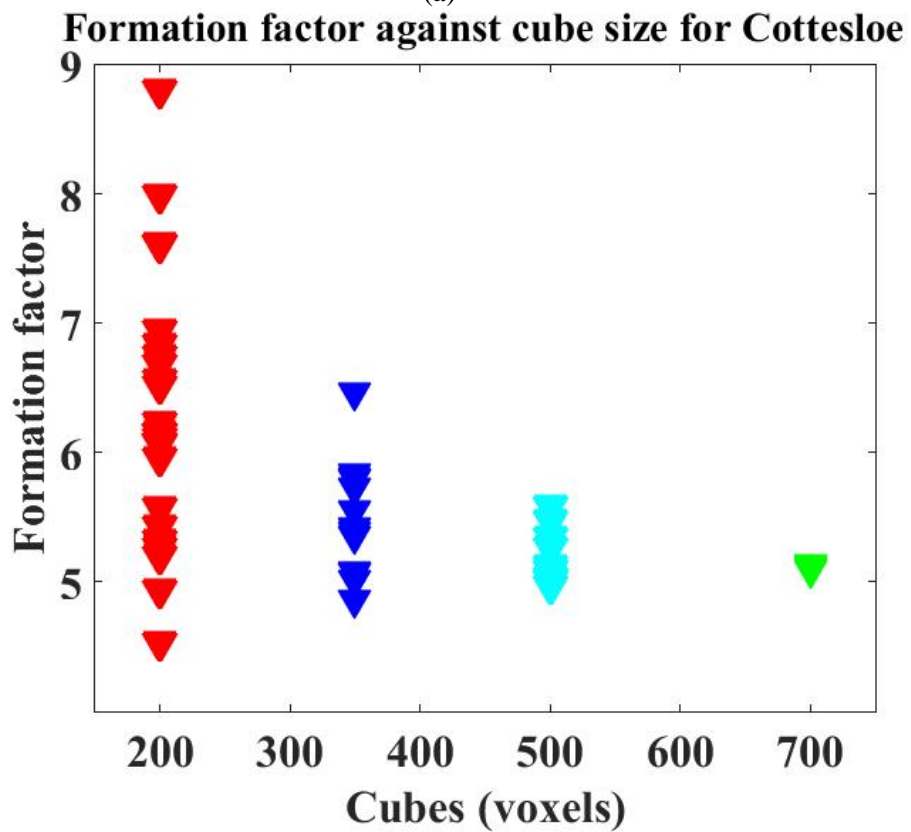


(d)

Figure 5.3.5: Cottesloe Micro CT-scan images of cubes with measurements for the flow cell in pink and static in blue while green is for the cubes.



(a)



(b)

Figure 5.3.6: (a) Porosity against cube sizes and (b) formation factor against cube sizes for Cottesloe Beach sample.

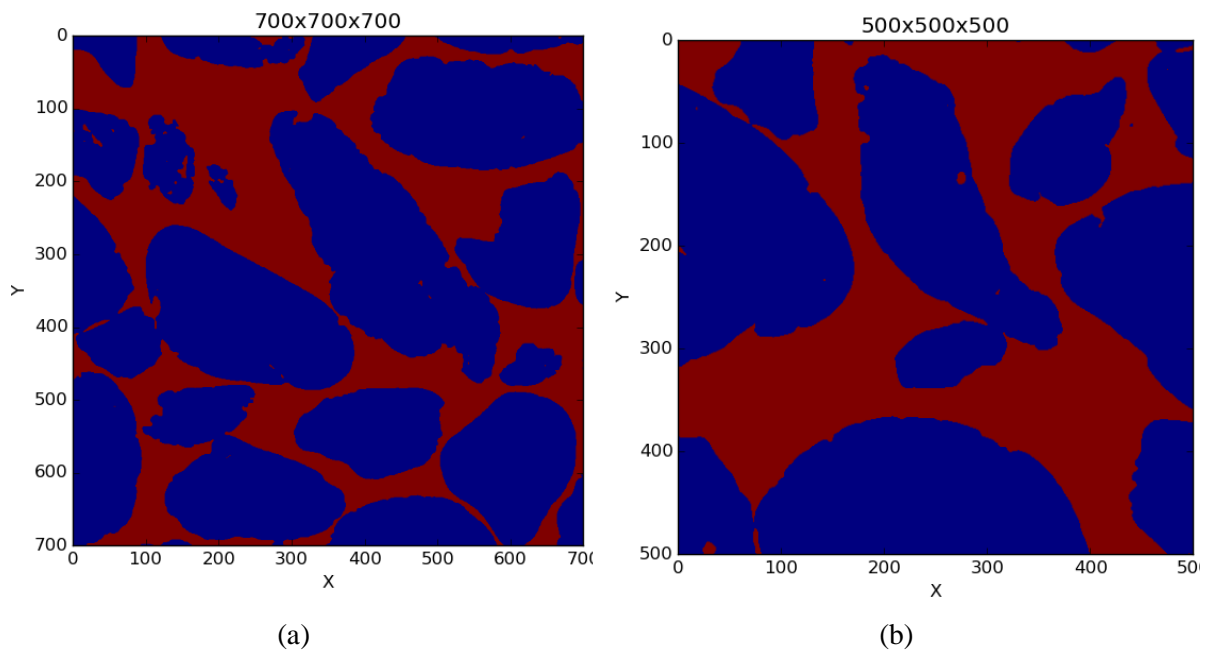
5.5 Electrical computations (clean sand)

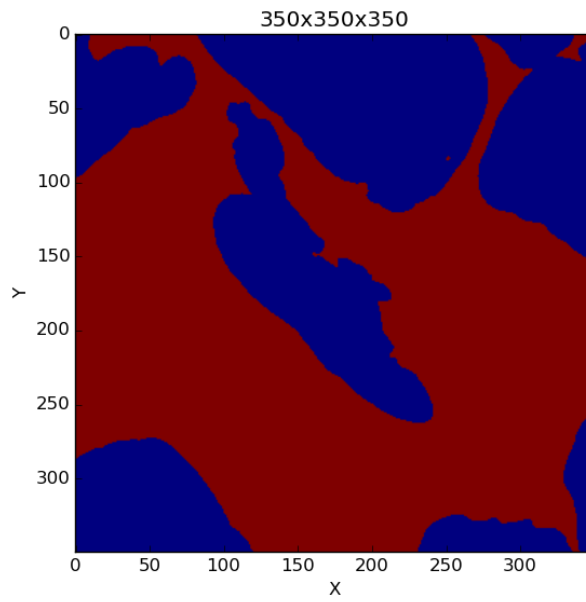
To estimate conductivity from micro-CT images, we assume the pores are electrically conductive, and the solid phases (matrix) are not conductive. This assumption compels the concept that the ions in the fluid in pores mainly drifted under the effect of external electric fields. After segmentation, we separated phases as solid (not conductive), and pore (conductive) for images of the Scarborough and Cottesloe samples pore and solid are shown as red and blue colours in Figure 5.4.1 and 5.4.2 for Scarborough and Cottesloe respectively.

To estimate the conductivity from the images, first we have to calculate an average current density that transports through the pore structures under applied external electrical fields. This is a typical electrical conductivity of porous media problem.

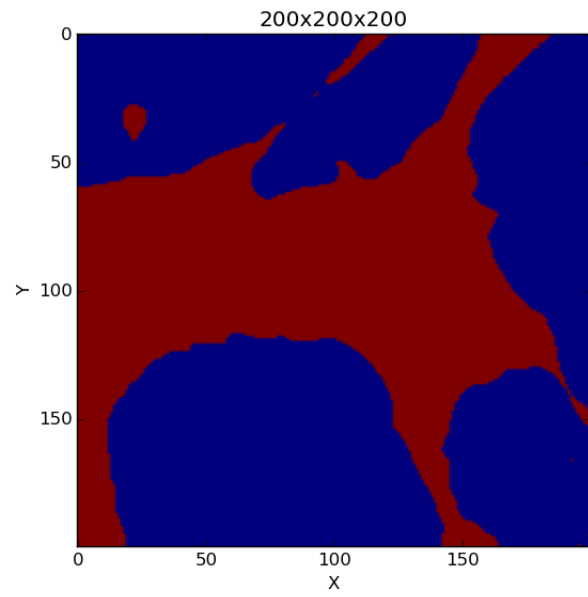
If we assume the conservation of charge is valid in the pore structure, volume and surfaces the net charges are not created nor annihilated. Therefore, the current density vector obeys the following equation as:

$$\nabla \cdot J = 0 \tag{5.2}$$



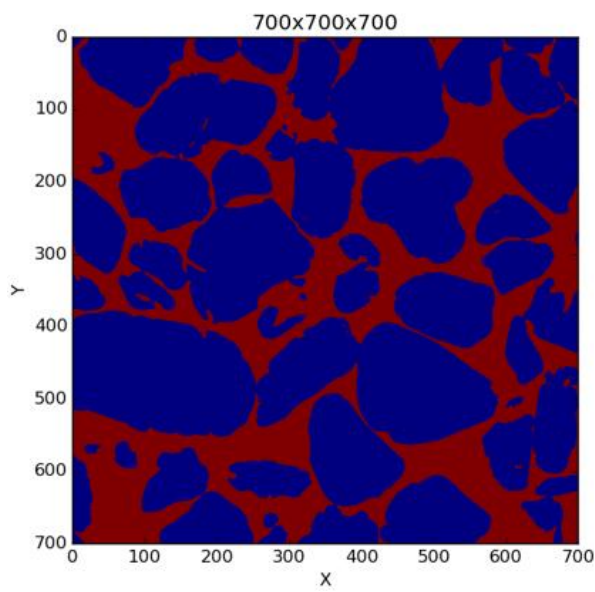


(c)

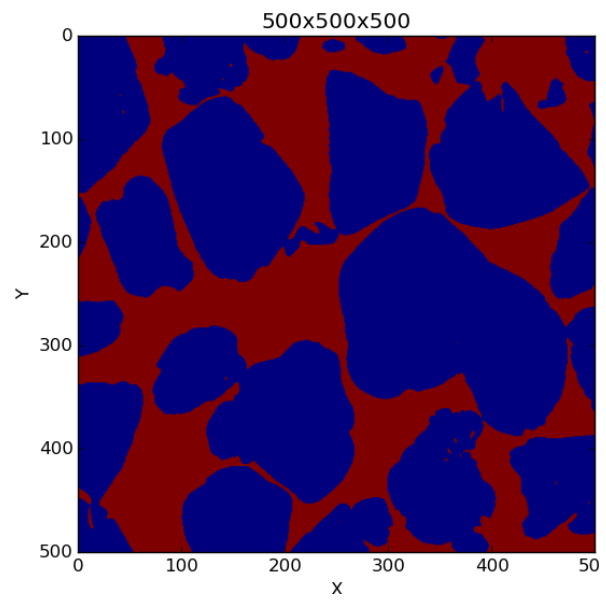


(d)

Figure 5.4.1: Binary images of Scarborough Beach sample



(a)



(b)

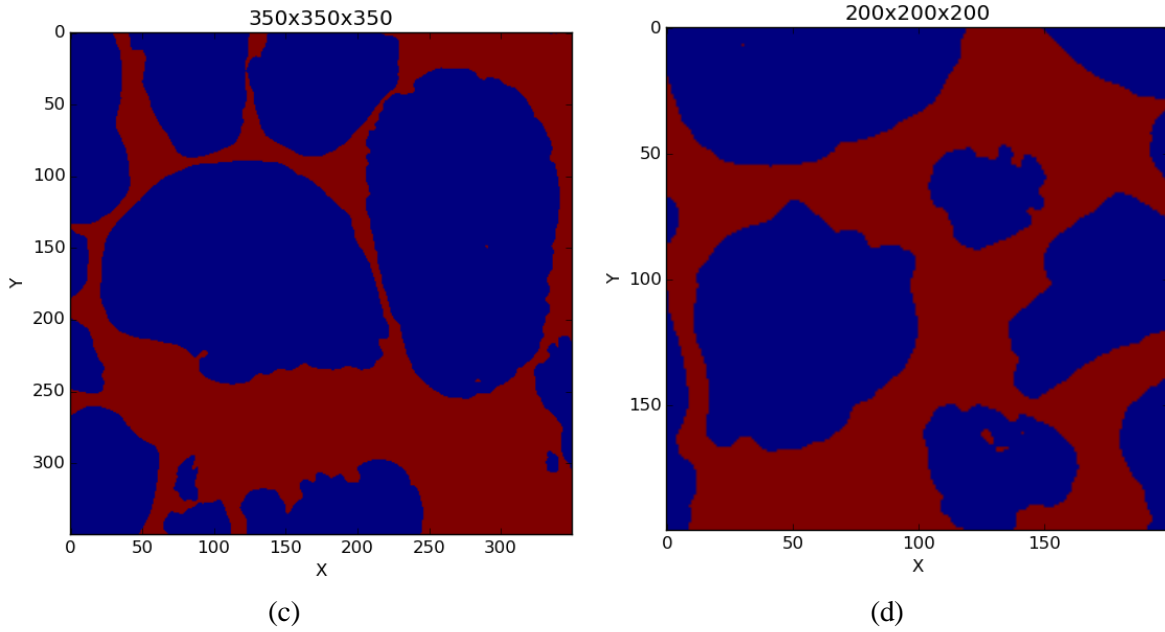


Figure 5.4.2: Binary image of Cottesloe Beach sample

On the other hand, in the Ohm's law in microscopic level assume the current density is proportional to electric fields.

$$J = \sigma_w \nabla V \quad 5.3$$

where J is the electrical current density, σ_w is the electrical conductivity of the fluid that fills the pore space, V is the electrical potential fields (voltage). By substituting equation (5.2) into equation (5.3), we have the Laplace equation as:

$$\nabla \cdot (\sigma_w \nabla V) = 0. \quad 5.4$$

The equation (5.4) can be solved numerically for pore structures by applying the external electric fields (\vec{E}_{ext}) on the boundaries. One of the most reliable numerical methods to estimate the average current density from 3D images is the finite element method (Dilsiz, 2011). By minimizing the electrical energy stored in volume, the finite element will estimate the local potential fields (V) at each coordinate system (pore and solid phases). Figure 5.4.3 and 5.4.4 show the potential field variations in samples from Scarborough and Cottesloe Beaches respectively. This can help us to evaluate the effective current density (\vec{J}_{av}) by using equation (5.4) and taking volume averaging of the local current density vectors (\vec{J}). On the other hand, the volume average of current density is defined as

$$\vec{J}_{av} = \langle \vec{J} \rangle = \sigma_{eff} \vec{E}_{ext} \quad 5.5$$

where S_{eff} is effective conductivity of micro-CT images. The effective conductivity is a 2nd rank tensor. By assuming the external electrical fields on any direction (let assume for x-direction, $\vec{E}_{ext} = E \hat{x}$); the current density, depending on the heterogeneity of pore network direction, can be:

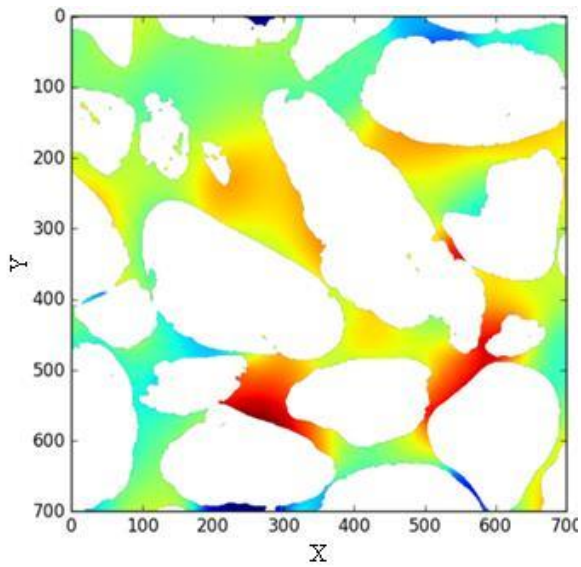
$$\vec{J}_{av} = \vec{J}_x \hat{x} + \vec{J}_y \hat{y} + \vec{J}_z \hat{z} \quad 5.6$$

Where from equation (5.6), the element of conductivity matrix is:

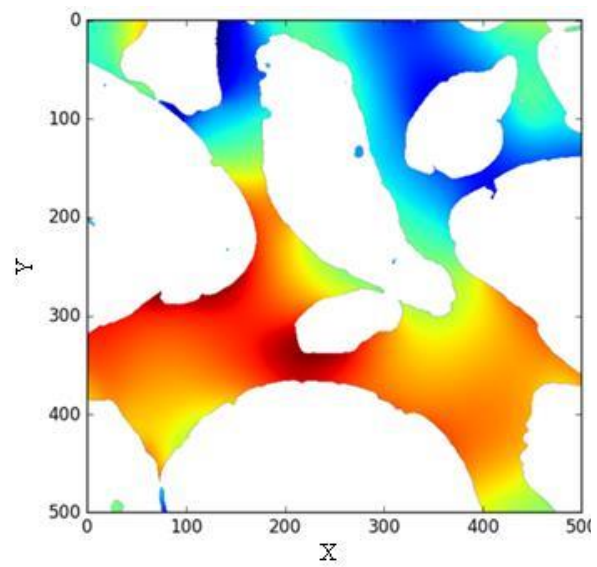
$$\vec{J} = \sigma_{xx} E \hat{x} + \sigma_{yx} E \hat{y} + \sigma_{zx} E \hat{z} \quad 5.7$$

This means the current density, depending on the heterogeneity of pore network one can calculate, in addition, the effective conductivity tensor as:

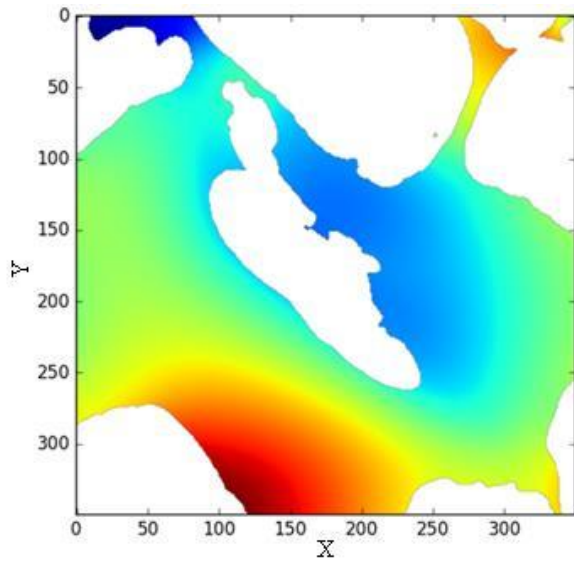
$$\sigma = \begin{pmatrix} \sigma_{xx} & \sigma_{xy} & \sigma_{xz} \\ \sigma_{yx} & \sigma_{yy} & \sigma_{yz} \\ \sigma_{zx} & \sigma_{zy} & \sigma_{zz} \end{pmatrix}. \quad 5.8$$



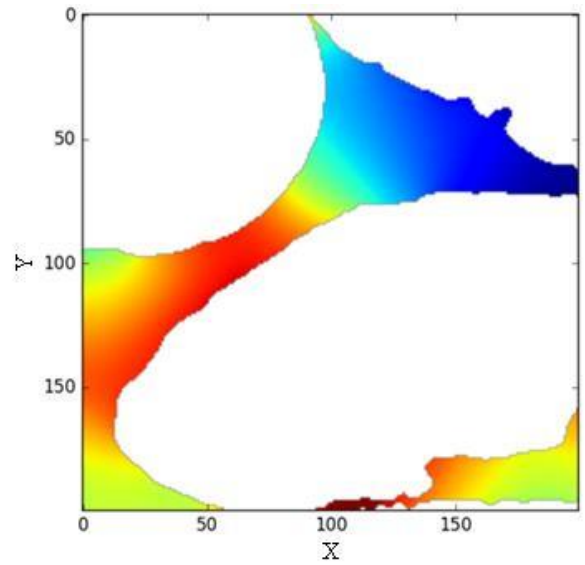
(a)



(b)

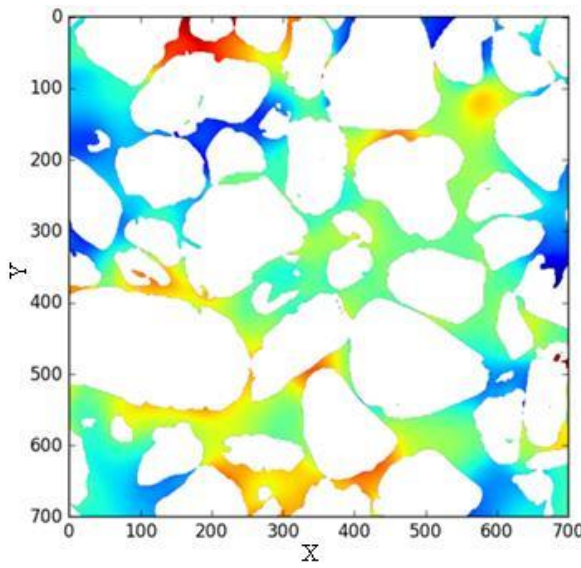


(c)

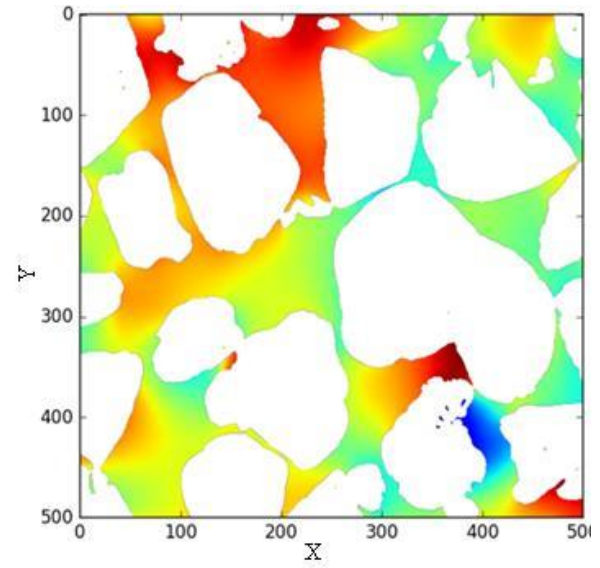


(d)

Figure 5.4.3: Potential field images of (a) $(700)^3$, (b) $(500)^3$, (c) $(350)^3$ and (d) $(200)^3$ cubes of Scarborough Beach sample.



(a)



(b)

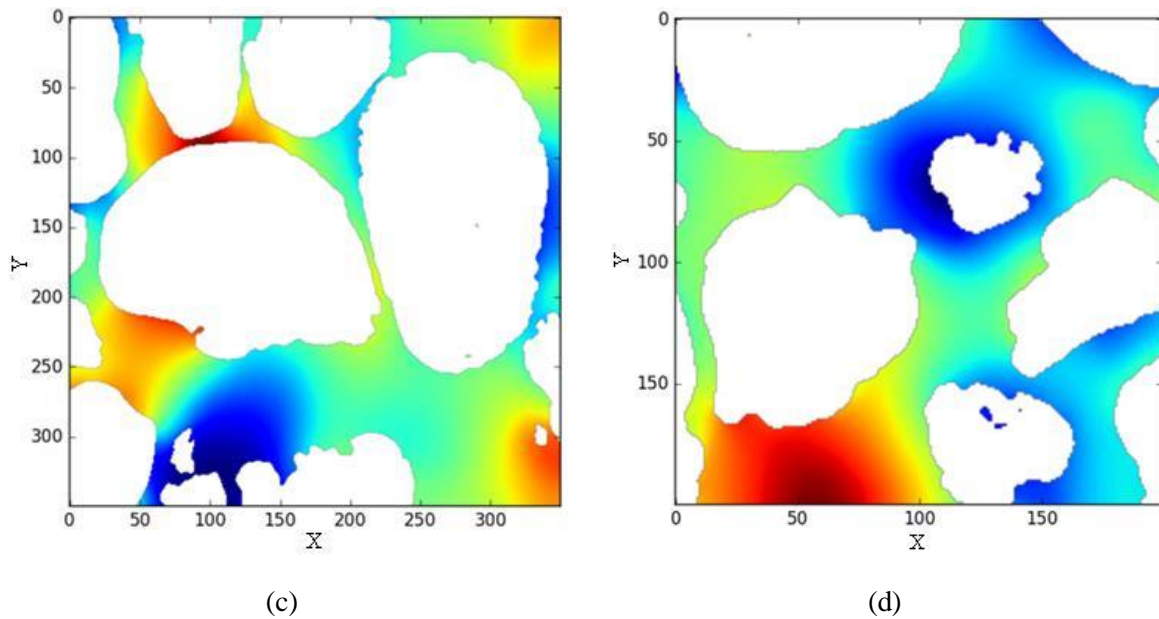


Figure 5.4.4: Potential field images of (a) $(700)^3$, (b) $(500)^3$, (c) $(350)^3$ and (d) $(200)^3$ cubes of Cottesloe beach sample.

The $(700)^3$ voxel from the Scarborough sample was analysed by applying the current in x, y and z-directions to find out whether the sample was homogeneity or heterogeneity Figure 5.4.5. The output of conductivity along x, y and z-directions are 0.1887, 0.2017 and 0.1967 mS/cm with an electrical formation factor of 5.30, 4.96 and 5.08 respectively. Hence, the difference in formation factor between x-direction and y-direction is 6% while the difference between x-direction and z-direction is 2%; therefore, the sample is isotropic in nature. For sure by decreasing the size of images, the pore structures became more anisotropic, but on the other hand, samples are not representative any more. Therefore, by having an isotropic conductivity of the representative volume, we just assume the isotropic pore structures and considering the conductivity as a scalar number for all images.

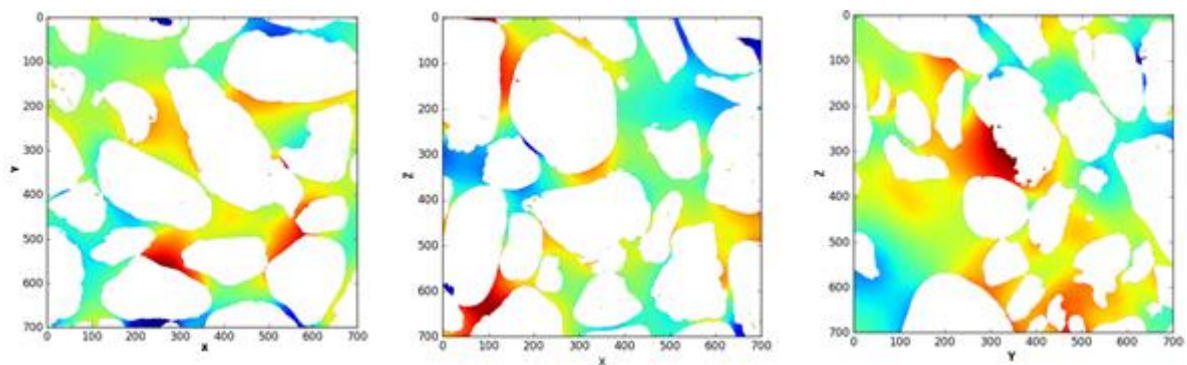


Figure 5.4.5: Conductivity images along x, y and z-axes.

To compute for the electrical formation factor F , the effective conductivity calculated from the micro-CT images as:

$$F = \frac{S_w}{S_{eff}}, \quad 5.9$$

where (S_w) is the electrical conductivity of pore fluids.

Details of the potential field variations for all the cubes is shown at appendixes (Figures A 3.1, 3.2, 3.3, 3.4, 3.5, 3.6, 3.7, 3.8 and 3.9)

Table 5.1: Summary of laboratory and micro-CT scan image results from Scarborough Beach samples.

Laboratory results	Flow cell	Porosity	0.40	0.38	0.35	0.32	0.30	0.27							
		F.F	4.4	4.4	5.4	6.6	6.8	8.2							
	Static cell	Porosity	0.40	0.38	0.33	0.31	0.27	0.26							
		F.F	4.0	4.6	5.5	5.7	6.1	6.5							
Micro-CT scan images	(700) ³ cubes	Porosity	0.36	0.36	0.36										
		F.F	5.3	5.3	5.3										
	(500) ³ cubes	Porosity	0.42	0.41	0.39	0.36	0.34	0.33	0.33	0.33					
		F.F	4.5	4.7	4.9	5.2	5.6	6.2	6.5	6.8					
	(350) ³ cubes	Porosity	0.45	0.41	0.38	0.38	0.38	0.37	0.37	0.37	0.36	0.36	0.36	0.32	0.30
		F.F	3.96	4.03	4.46	4.93	5.19	5.21	5.53	5.63	6.15	6.57	6.93	7.18	7.30
	(200) ³ cubes	Porosity	0.46	0.46	0.44	0.43	0.41	0.41	0.41	0.41	0.40	0.39	0.39	0.36	0.3
		F.F	3.8	4.8	4.9	5.0	5.2	5.3	5.4	5.8	6.0	6.5	6.7	7.0	7.0
			Porosity	0.36	0.34	0.34	0.32	0.29	0.28	0.25					
			F.F	7.4	8.0	8.2	8.8	9.3	9.4	10.1					

Table 5.2: Summary of laboratory and micro-CT scan image results from Cottesloe Beach samples.

Laboratory results	Flow cell	Porosity	0.39	0.35	0.34	0.33	0.26								
		F.F	3.96	4.50	5.00	5.33	8.54								
	Static cell	Porosity	0.37	0.35	0.33	0.31									
		F.F	5.72	5.93	6.50	6.90									
Micro-CT scan images	(700) ³ cubes	Porosity	0.35	0.35	0.35	0.35	0.35								
		F.F	5.1	5.1	5.1	5.1	5.1								
	(500) ³ cubes	Porosity	0.35	0.35	0.34	0.34	0.34	0.33	0.33	0.33	0.32	0.30			
		F.F	4.97	5.01	5.02	5.04	5.09	5.13	5.27	5.34	5.48	5.59			
	(350) ³ cubes	Porosity	0.368	0.366	0.353	0.352	0.351	0.349	0.344	0.343	0.342	0.338	0.332	0.327	0.326
		F.F	4.87	4.87	5.01	5.07	5.29	5.36	5.39	5.42	5.55	5.73	5.80	5.84	6.47
	(200) ³ cubes	Porosity	0.39	0.37	0.37	0.36	0.36	0.35	0.35	0.35	0.35	0.34	0.34	0.33	0.33
		F.F	4.5	4.9	5.2	5.3	5.3	5.4	5.6	6.0	6.1	6.1	6.1	6.1	6.2
			Porosity	0.33	0.33	0.33	0.32	0.31	0.30	0.30	0.29	0.29	0.28	0.26	
			F.F	6.2	6.5	6.6	6.7	6.7	6.8	7.0	7.6	7.6	8.0	8.8	

5.6 Volume analysis of the components

The volume of the components of Scarborough and Cottesloe beach samples were analysed, both samples show the percentage of quartz being the highest followed by the pore while the carbonate makes the least in percentage volume. The percentage volume distribution of the components is presented in

Table 5.3 for both the Scarborough Cottesloe clean sands. The Scarborough clean sample has 36.9 %, 51.7% and 11.4% of the volume of pore, quartz and carbonate respectively (Figure 5.4.6). While the Cottesloe clean sample has 35.9 %, 55.5% and 8.7% of the volume of pore, quartz and carbonates respectively (Figure 5.4.7).

Table 5.3: Percentage volume of components in Scarborough and Cottesloe clean Beach sand samples.

Beach	Components	Volume (%)
Scarborough sample	Pore	36.9
	Quartz	51.7
	Carbonate	11.4
Cottesloe sample	Pore	35.9
	Quartz	55.4
	Carbonate	7.7

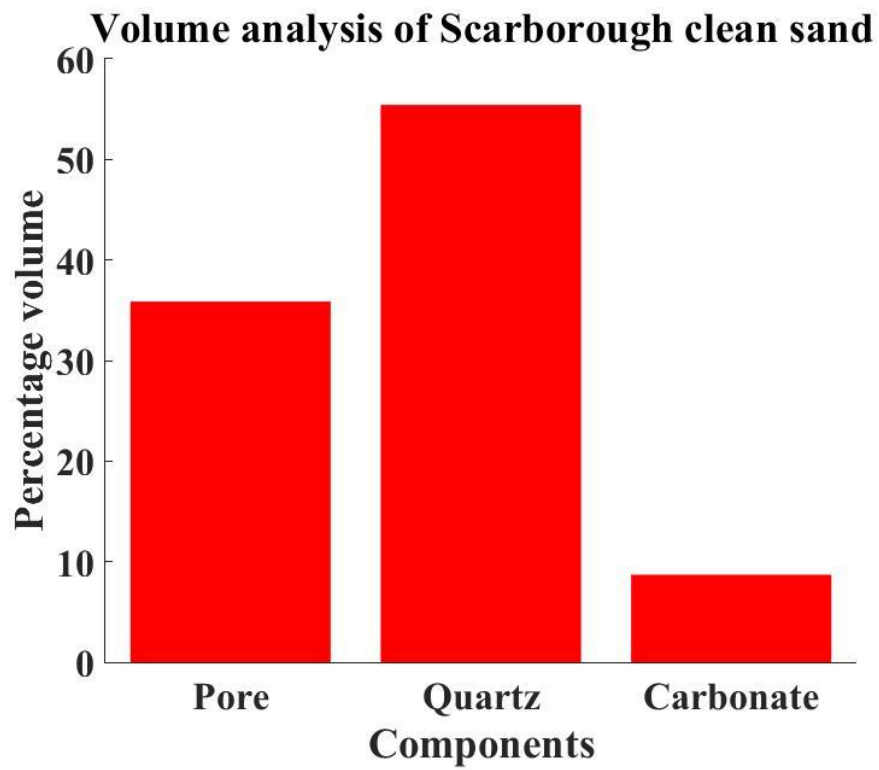


Figure 5.4.6: Percentage volume of components in Scarborough clean sand sample.

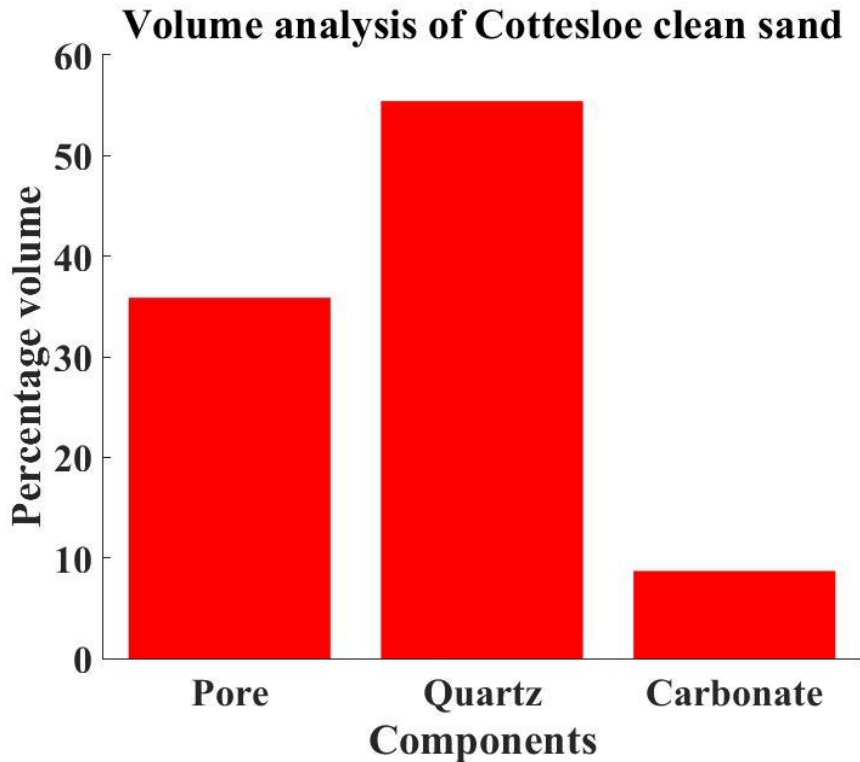


Figure 5.4.7: Percentage volume of components in Cottesloe clean sand sample.

5.7 Grain size analysis

The grain size analysis is very important because sand samples are heterogeneous at all scales and therefore physical properties such as porosity and formation factor vary between two points, so it is often invalid to assign a single physical property (such as porosity) to a volume. The natural sands of Scarborough and Cottesloe are of different grain sizes therefore, this range has to be grouped (or classified).

5.7.1 Label diameter distribution

Measurements were made on each particle size, in this calculation, touching particles are first opened and separated so that individual particles are identified, counted and measured. For a given particle, the equivalent diameter measure computes the diameter of the spherical particle of the same volume. This diameter was computed using the Avizo program after the watershed segmentation algorithm was applied on each of the micro-CT scan images of the Scarborough and Cottesloe samples. Applying opening follows this and separation for the individual materials (pore, quartz, and carbonate) was applied, the formula below computed the label analysis on the materials.

$$\text{EquiDiameter} = \sqrt[3]{\frac{6\text{Volume}3d}{\pi}} \quad 5.10$$

A particle frequency distribution shows the percentage of particles found in each size range (bin). For many applications, a volume-weighted size distribution is preferred. Image analysis of individual particles resulted primarily in a number-weighted size distribution (counting the number of particles/bin); this converted to an area-or volume-weighted distribution.

Table 5.4: Summary of EqDiameter of materials

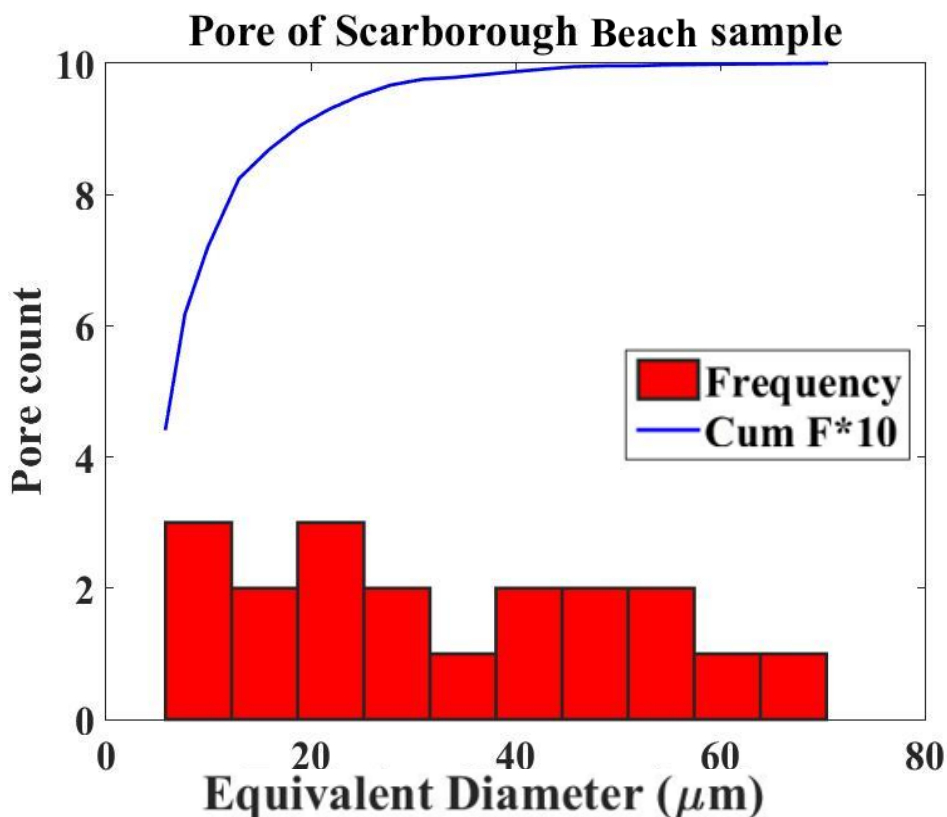
Beach	Material	Range(μm)	Average(μm)	
Scarborough	Pore	Min	18.57	199.4
		Max	693.9	
	Quartz	Min	16.11	120.0
		Max	794.0	
	Carbonate	Min	18.57	168.3
		Max	446.0	
Cottesloe	Pore	Min	15.26	172.8
		Max	415.5	
	Quartz	Min	15.26	159.2
		Max	606.4	
	Carbonate	Min	15.26	172.8
		Max	415.5	

There are 2,349 grains in the Scarborough Beach sand sample in total, with 1,583 grains of quartz, 384 grains of carbonate and 382 pores. The smallest grain size found within the quartz particles in the Scarborough Beach sample has a diameter of $3.98\mu\text{m}$ with the largest grain having a diameter of $393.81\mu\text{m}$. The range of the smaller grains from $3.98\mu\text{m}$ to $5.81\mu\text{m}$ constitutes 49% of the total grains of quartz in the Scarborough Beach sample, while the largest grains ranging from $100.4\mu\text{m}$ to $393.8\mu\text{m}$ constitute only 1% of the total quartz grains; the remaining quartz grains are constituted of the intermediary grain sizes. The smallest grain size found for carbonate in the Scarborough Beach sample is $3.98\mu\text{m}$ with the largest having a diameter of $804.80\mu\text{m}$. The range of smaller grains of carbonate from the Scarborough sand samples is $3.98\mu\text{m}$ to $5.81\mu\text{m}$; this constitute 56.4% of the total carbonate. The largest grains range from $490.7\mu\text{m}$ to $804.8\mu\text{m}$ and these grains constitute 1% of the total carbonate grains. Pores in the Scarborough Beach sand sample have a least pore diameter of $3.98\mu\text{m}$ with the largest pore of $64.2\mu\text{m}$. The smaller pores ranging from $3.98\mu\text{m}$ to $5.81\mu\text{m}$ constitute 44.3% of the total pore count, while the larger pores ranging from $54.7\mu\text{m}$ to $64.2\mu\text{m}$ constitute 1% of the total pore count.

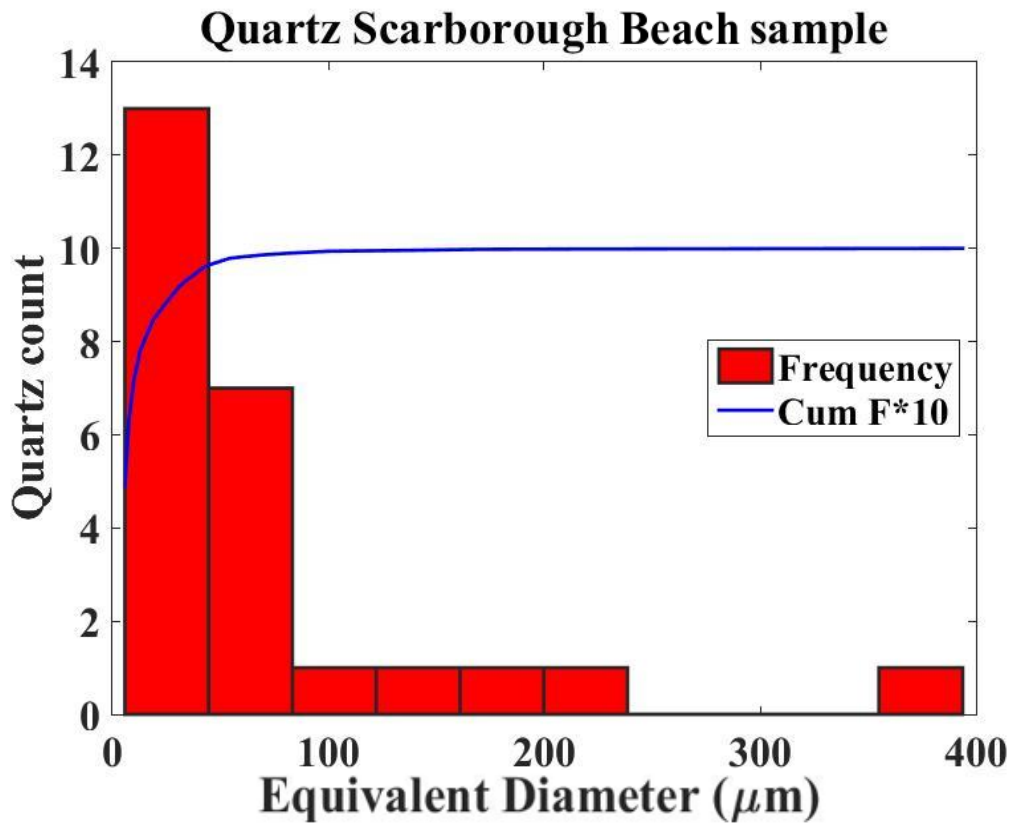
There are 3,301 grains in the Cottesloe Beach sand sample in total, with 2,192 grains of quartz, 566 grains of carbonate and 543 pores. The smallest grain size found within the quartz particles in the Cottesloe Beach sample has a diameter of $3.98\mu\text{m}$ with the largest grain having a

diameter of 200.62 μm . The range of the smaller grains from 3.98 μm to 3.99 μm constitutes 34% of the total grains of quartz in the Cottesloe Beach sample while the largest grains ranging from 100.2 μm to 200.6 μm constitute only 1% of the total quartz grains; the remaining quartz grains are constituted of intermediary grain sizes. The smallest grain size found for carbonate in the Cottesloe Beach sample is 3.98 μm with the largest having a diameter of 500.4 μm . The range of smaller grains of carbonate from Cottesloe sand samples is 3.98 μm to 3.99 μm ; this constitute 35% of the total carbonate. The largest grains range from 400.4 μm to 500.4 μm and these grains constitute 1% of the total carbonate grains. Pores in the Cottesloe Beach sand sample have a least pore diameter of 3.98 μm with the largest pore of 60.3 μm . The pores ranging from 3.98 μm to 5.81 μm constitute 44.3% of the total pore count, while the larger pores ranging from 400.3 μm to 500.4 μm constitute 1% of the total pore count.

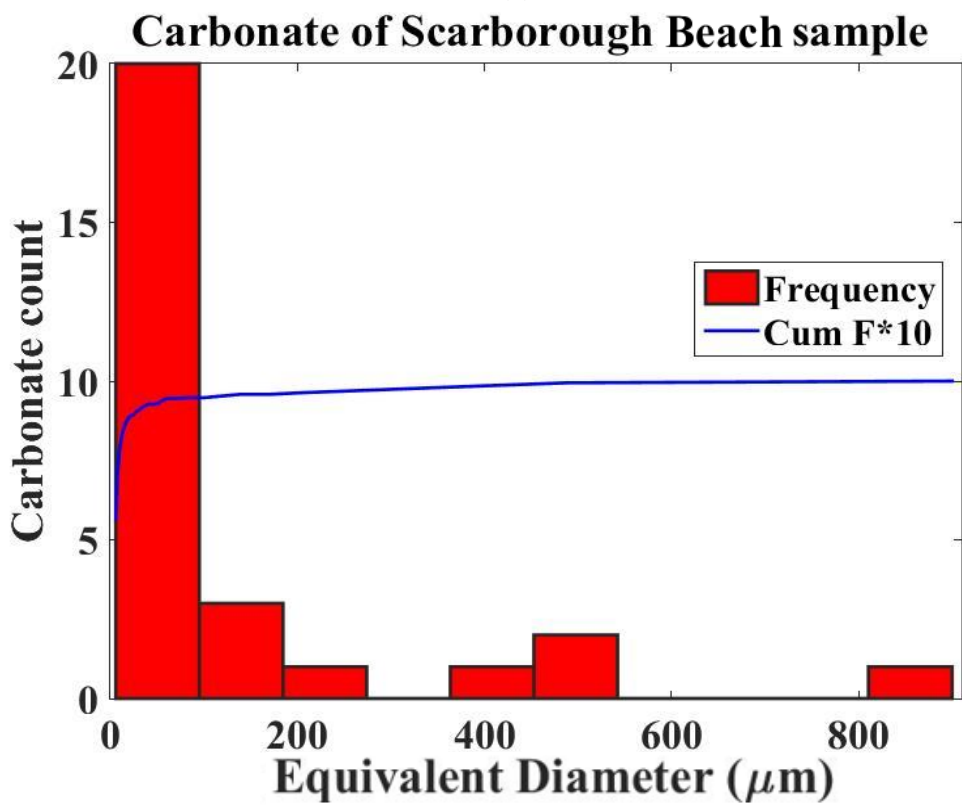
The total number of grains of 2,349 and 3,301 from Scarborough and Cottesloe Beaches respectively shows that Scarborough sand is coarser than Cottesloe since the same tube was use for scanning the images. The frequency and cumulative percentages for pore, quartz and carbonate from Scarborough and Cottesloe Beaches are presented in Figures 5.1.1 and 5.5.2 respectively.



(a)

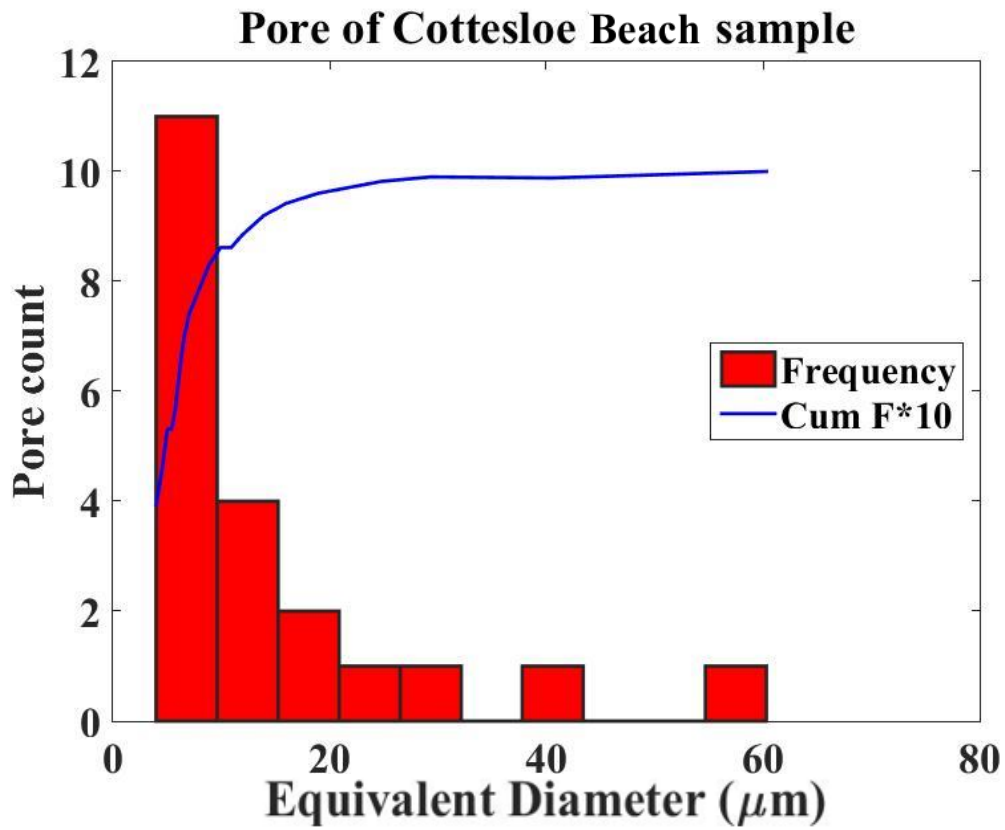


(b)

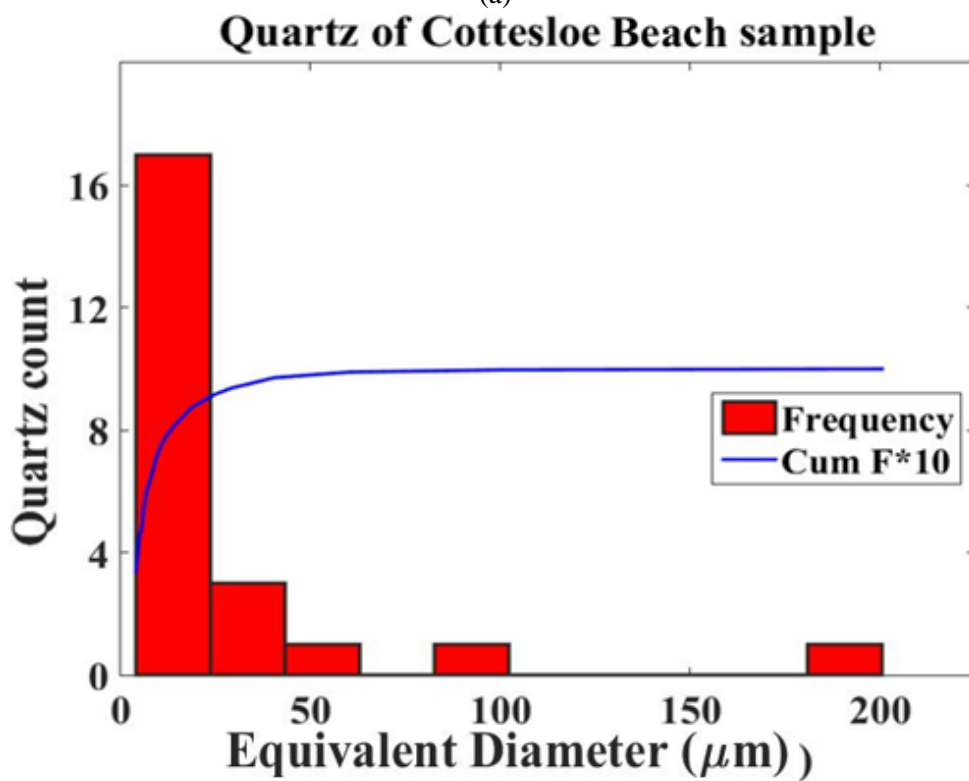


(c)

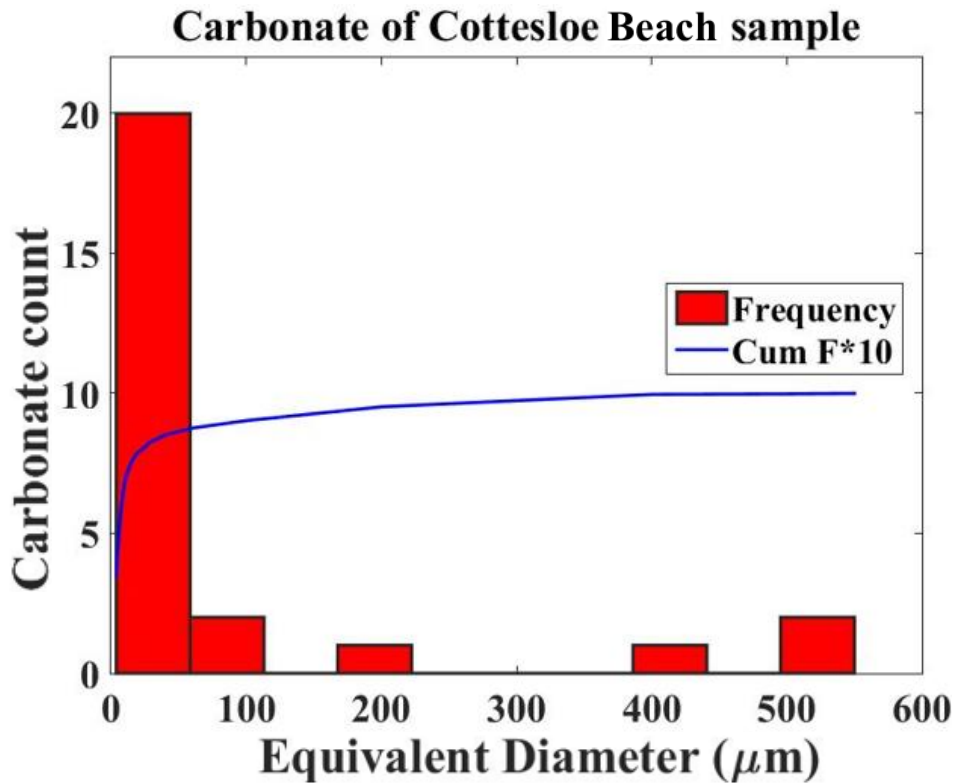
Figure 5.5.1: Graph of grain count and cumulative frequency of (a) pore (b) quartz and (c) carbonate from Scarborough Beach sample.



(a)



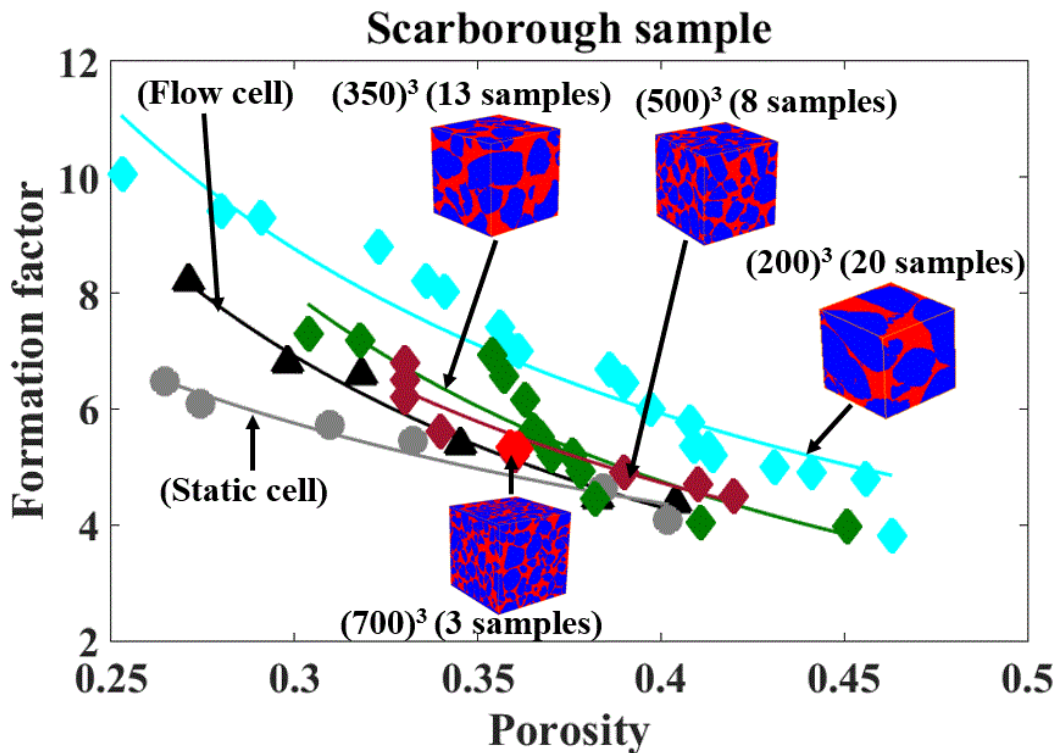
(b)



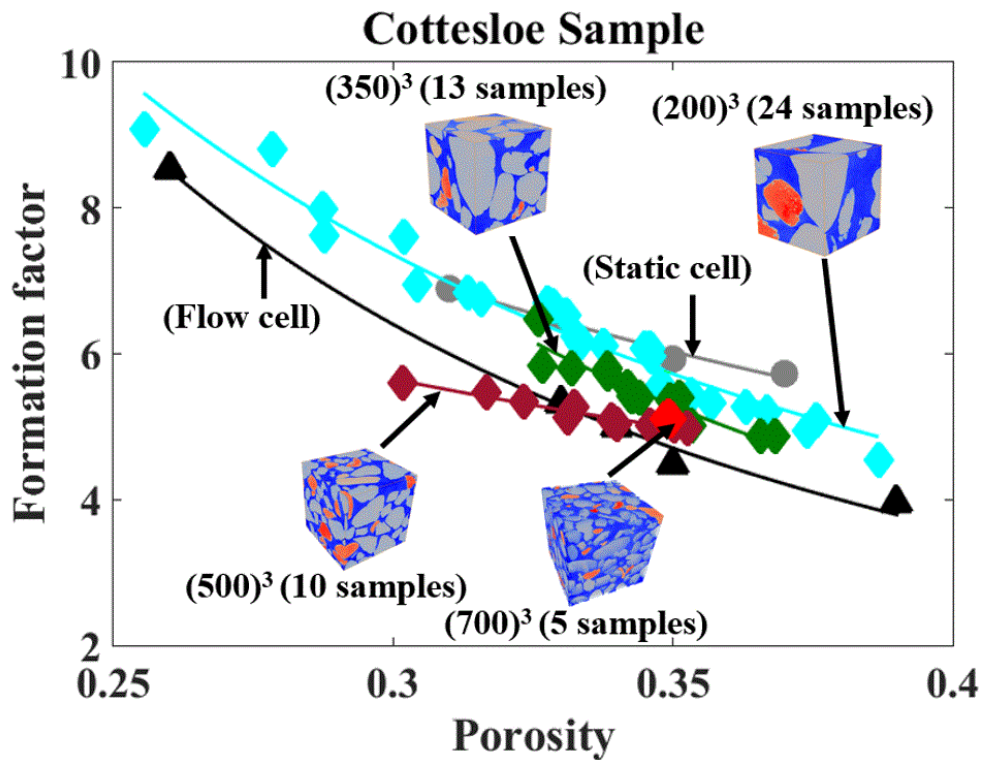
(c)

Figure 5.5.2: Graph of grain count and cumulative frequency of (a) pore (b) quartz and (c) carbonate from Scarborough beach sample.

The summary of the clean sands of Scarborough and Cottesloe beach sands from the laboratory (flow and static cells) as well as the Micro-CT scan images is presented in Figure 5.3.3.



(a)



(b)

Figure 5.5.3: Summary of measurements from laboratory and micro CT-scan images from Scarborough and Cottesloe Beaches.

5.8 Cottesloe clay sand results

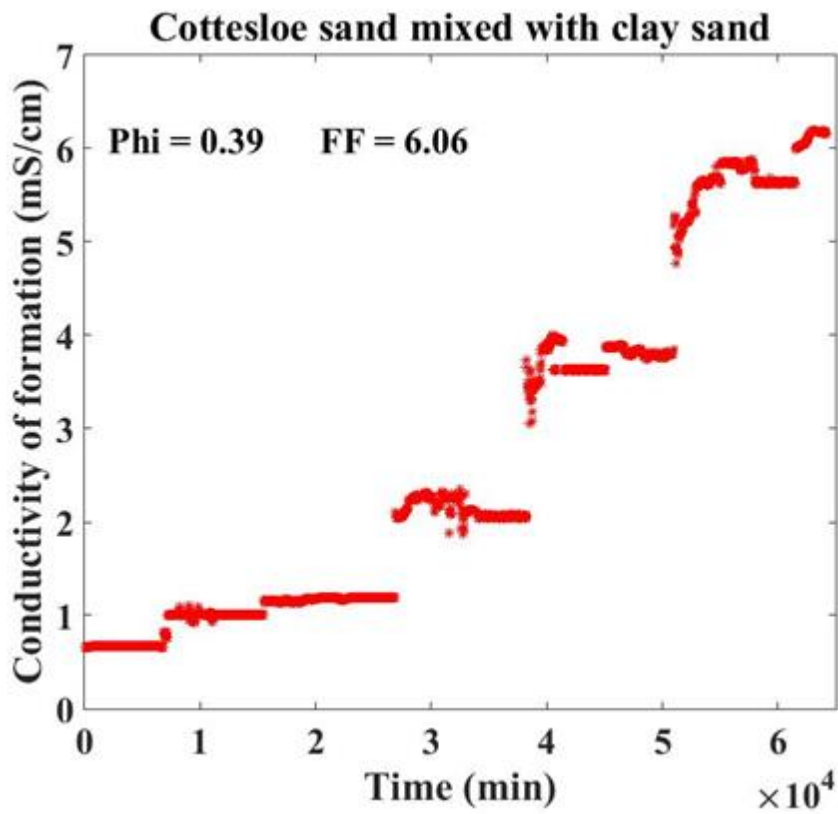
5.8.1 Introduction

In the case of clean sand, it is assumed that the saline water formation conductivity was uniform so that all the ions in the solution are evenly distributed throughout the pore space. But in the case of clay sand there is an additional charge carrier in the fluid phase, the Kaolinite clay added was 3% by weight of the sand sample, it is dried in an oven for seventy-two (72) hours at a temperature of 105°C, and then the dry clay was thoroughly mixed by hand for about forty (40) minutes. Kaolinite clay contains charged impurities like Al^{3+} substituting Si^{4+} ; the charge deficiency is compensated for cation adsorption on the mineral surface. This adsorption creates an electrical double layer near the mineral surface as shown in Figure 2.11 in chapter 2, with the concentration of ions in solution extending 30 to 80Å from the surface. Surface conduction is due to these ions in the diffuse double layer and is localized near the clay surface.

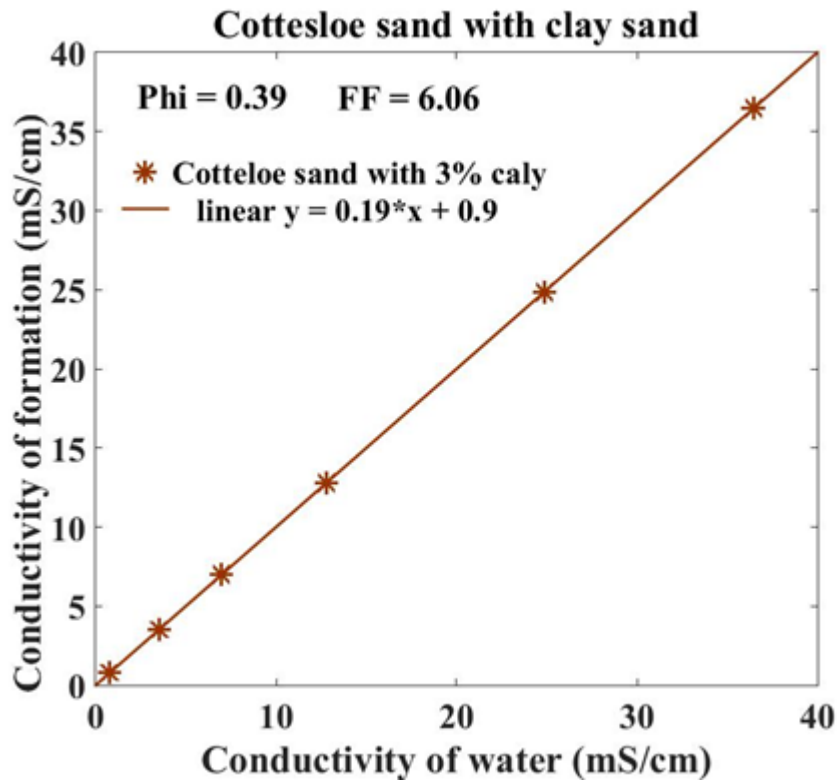
5.8.2 Laboratory result of clay sand

The graph of the electrical conductivity of the formation of the Cottesloe clay sand against time presented in Figure 5.6.1 show a very longer time of about 42 days to complete the experiment.

The graph of the conductivity of formation against the conductivity of water in Figure 5.6.1b shows how the readings became unstable especially at higher salinities of 25mg/l and 35mg/l saline solutions. The value of the porosity and formation factor computed from the laboratory measurements are 0.39 and 6.06 respectively.



(a)



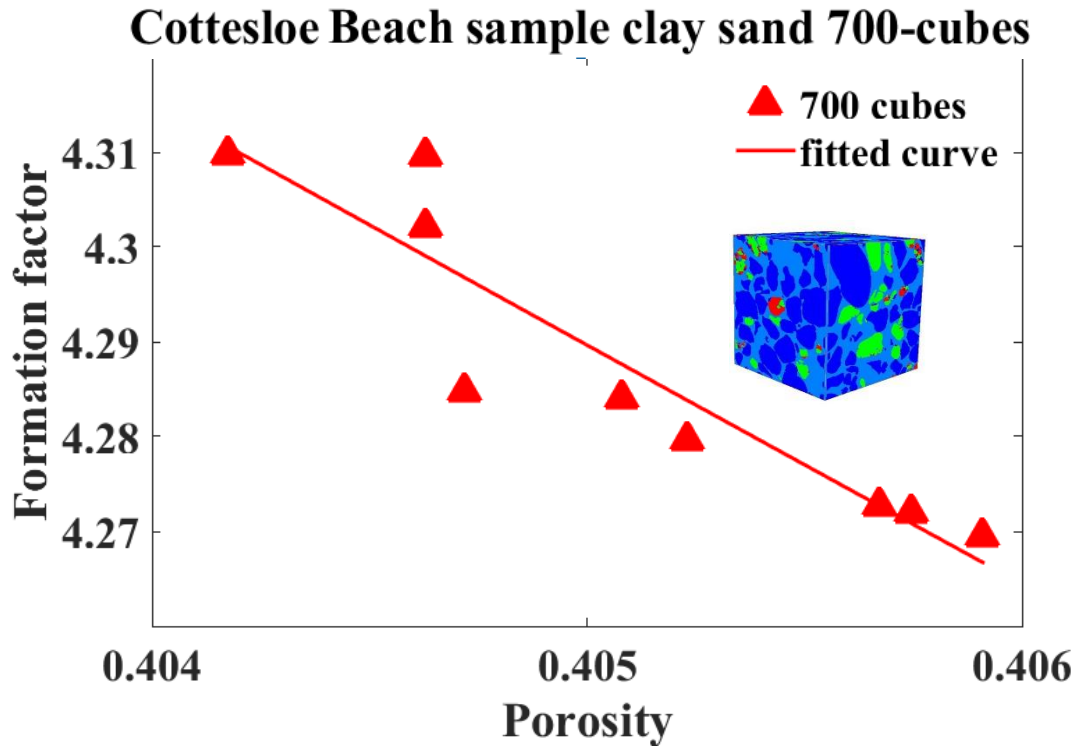
(b)

Figure 5.6.1: Cottesloe with 3% clay (a) conductivity of formation against time (b) conductivity of formation against conductivity of water.

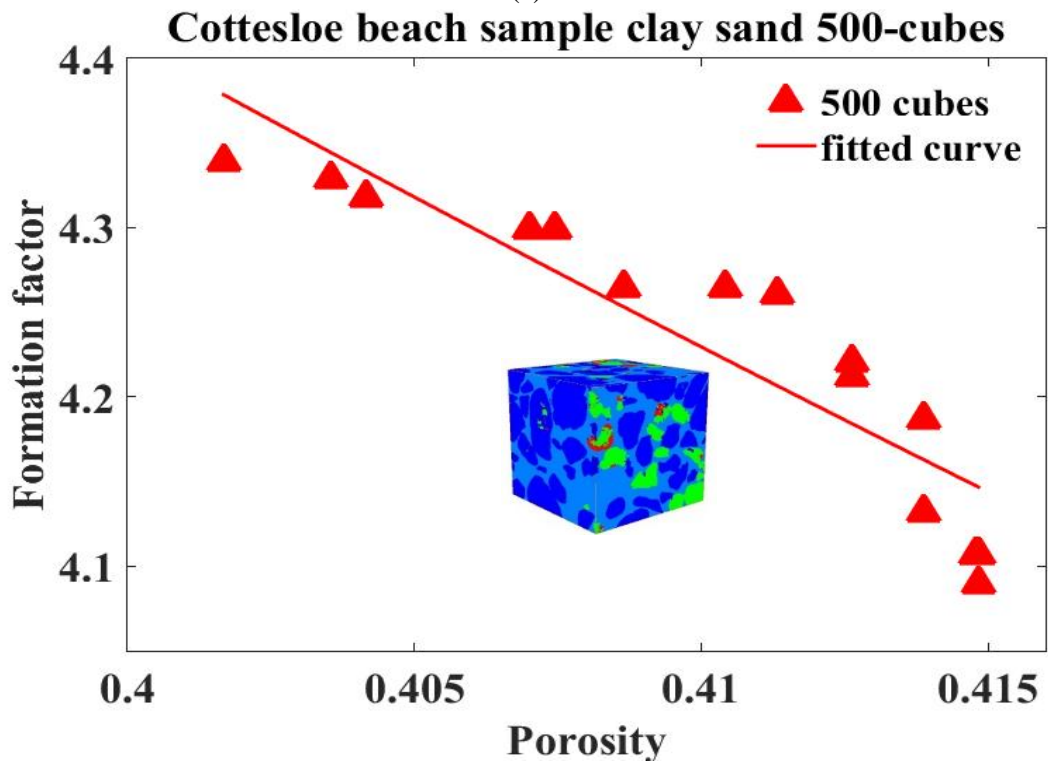
5.8.3 Micro CT-scan image result of clay sample

One sample from Cottesloe Beach was prepared for imaging with micro-CT: loose, moist was sand put in a cylindrical Pyrex glass tube of 6 mm in diameter and 6 cm in height. It was inserted into a core holder of a micro-tomograph, as in Figure 4.1a. The sample was scanned with a 3D X-ray Microscope Versa XRM 500 Zeiss – XRadia as shown in (Figure 4.1b) using X-ray energy of 60keV, a current of 70.66 μ A and energy of 5×10^6 Watts. The images were scanned using two different resolutions of 1.3739 μ m and 3.4348 μ m with a total number of 2D images of 990 and 992 respectively. The two images were acquired with exposure times of 9.48s and 9.51s with a total scanning time of 2 hrs 6 minutes and 2 hrs 6 minutes 2seconds for the two different images. Nominal voxel sizes of (1.3739 μ m)³ and (3.4348 μ m)³ were achieved with source-to-sample and detector-to-sample distances of 11mm and 11mm for both images. Initial cone-beam 3D image reconstruction was performed using initial software XM Reconstruction (XRadia).

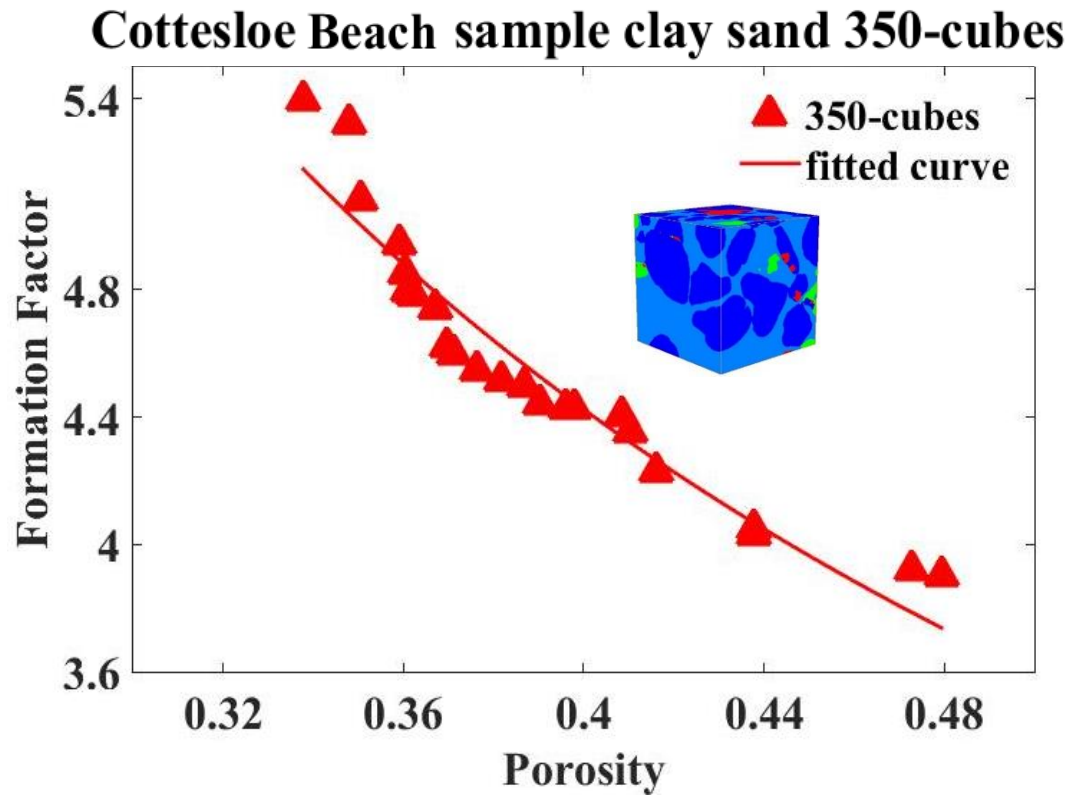
5.8.3.1 Clay sand result



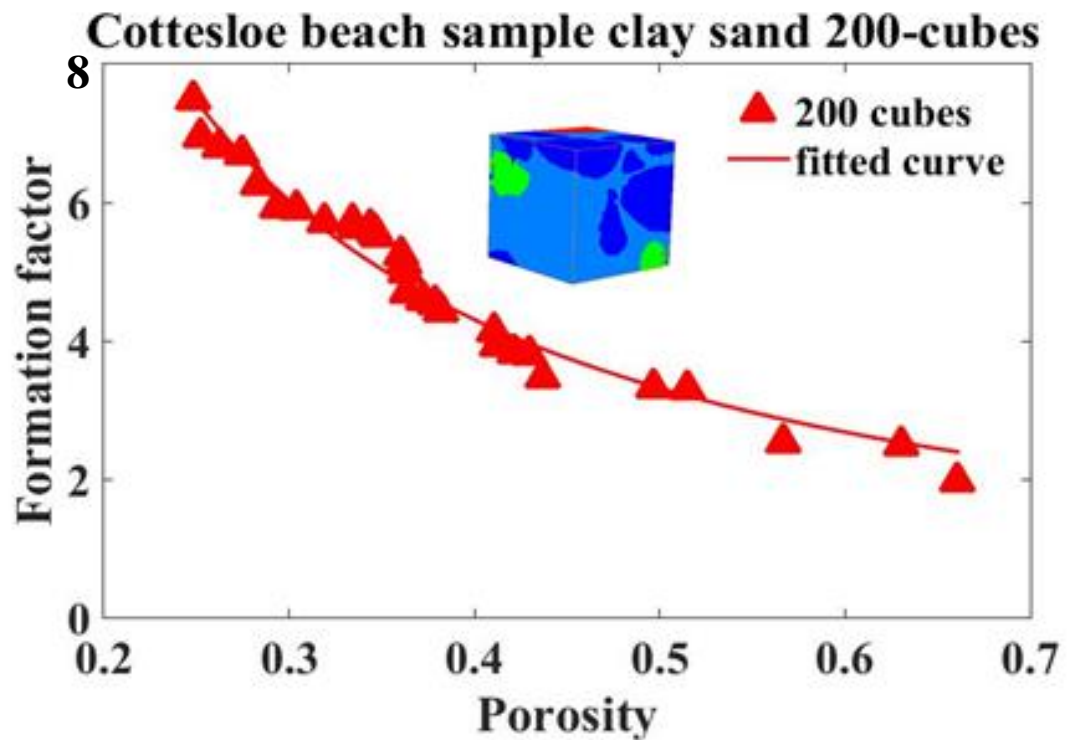
(a)



(b)



(c)



(d)

Figure 5.6.2: Formation factor against cube sizes of Cottesloe Beach samples with 3% clay (a) $(700)^3$ (b) $(500)^3$ (c) $(350)^3$ and (d) $(200)^3$ cubes.

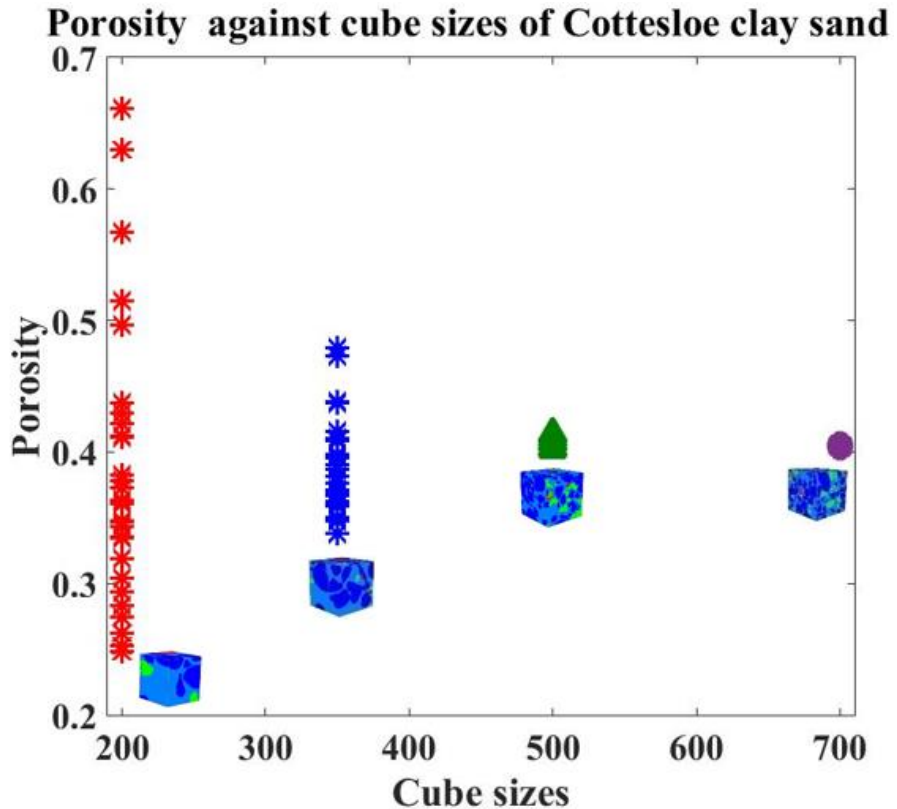


Figure 5.6.3: Porosity against cube sizes of Cottesloe Beach sand with 3% clay

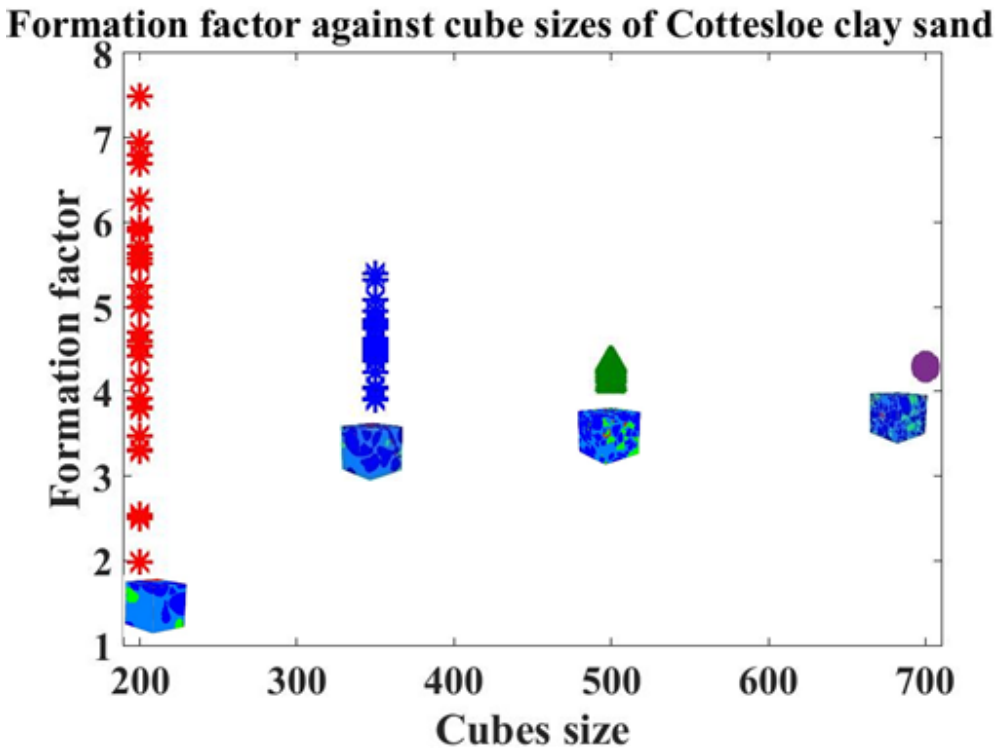
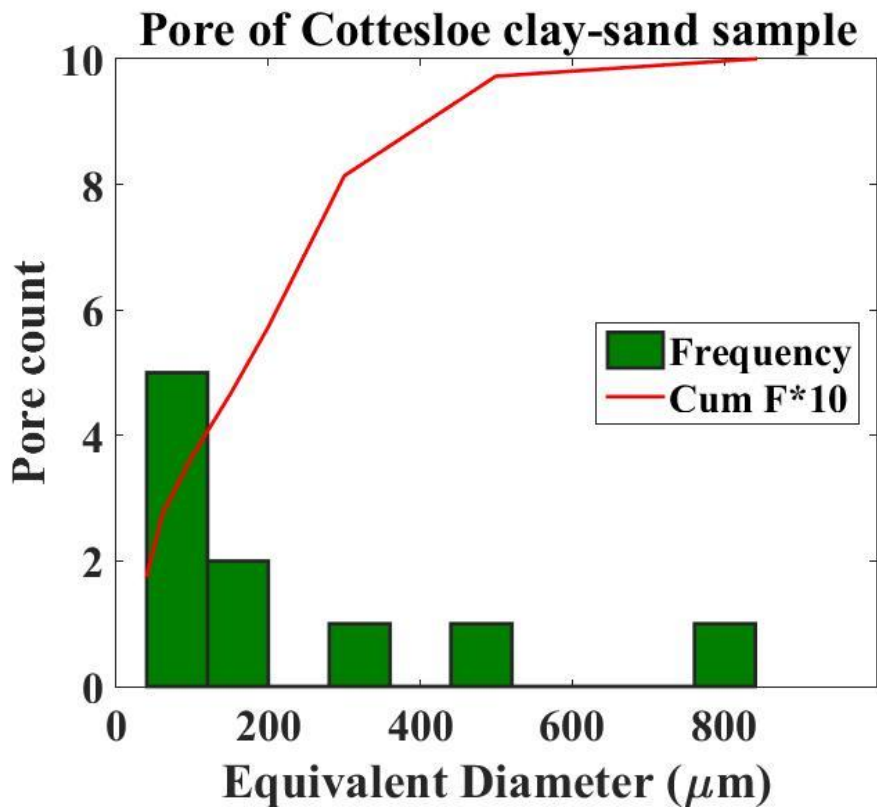


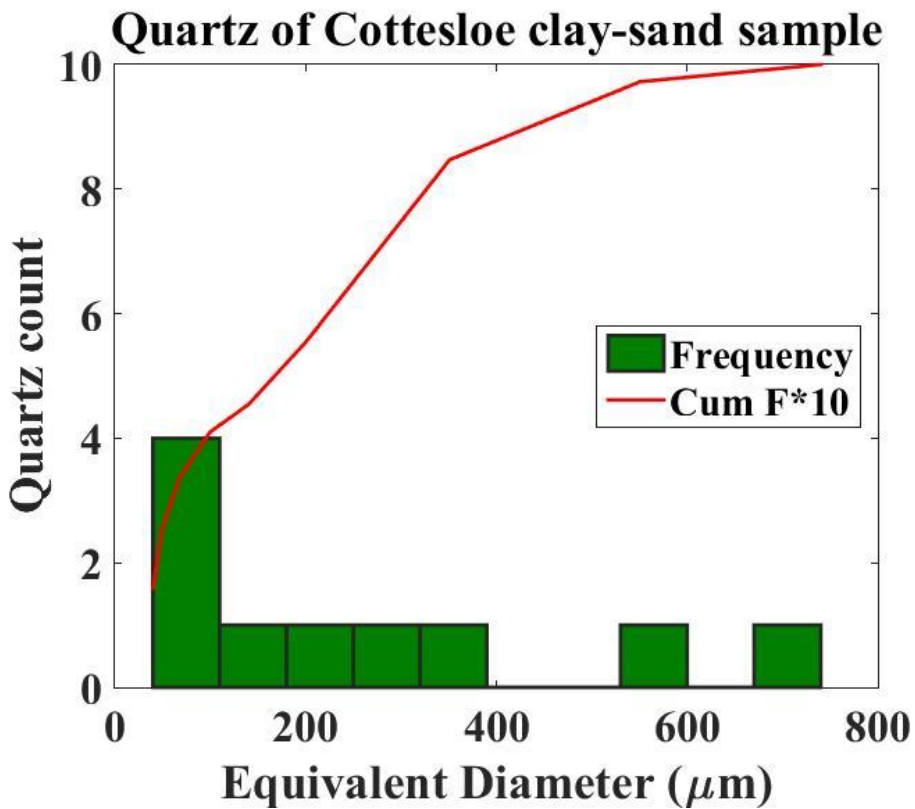
Figure 5.6.4 Formation factor against cube sizes of Cottesloe Beach sand with 3% clay

5.8.3.2 Grain size analysis

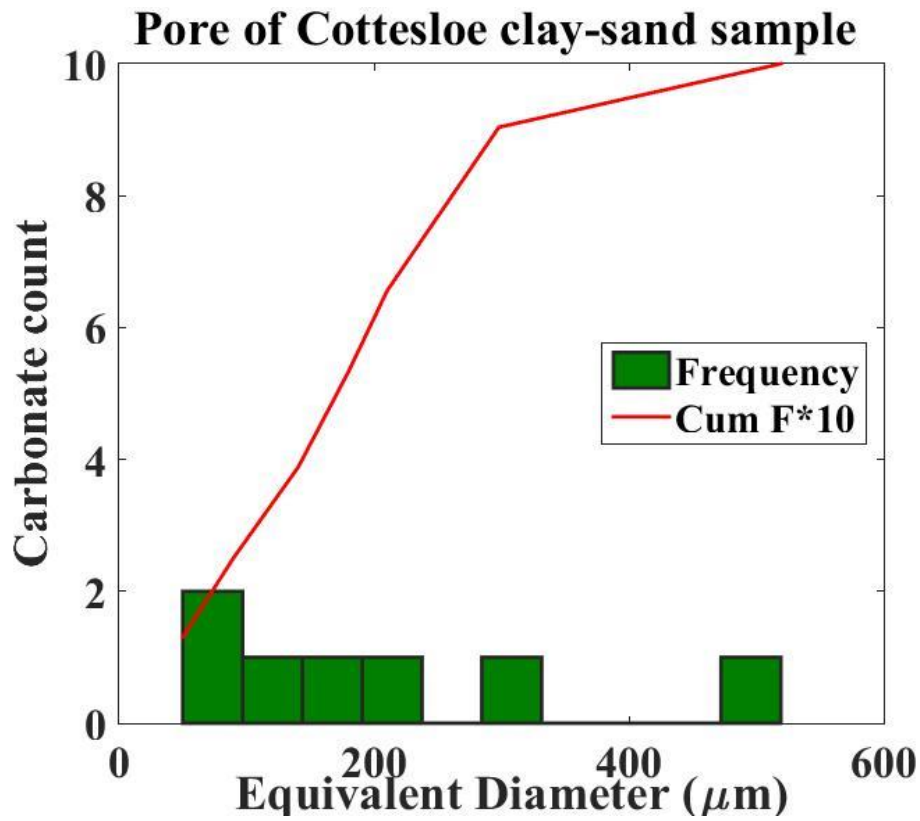
There are 1,604 grains in the Cottesloe Beach clay sand sample with 401 grains of quartz, 437 grains of clay, 473 grains of carbonate and 293 pores. The smallest grain size found within the quartz particles in the Cottesloe clay sand sample has a diameter of 14.2 μ m with the largest grain having a diameter of 840.9 μ m. The range of the smaller grains from 14.2 μ m to 29.8 μ m constitutes 15.9% of the quartz grains of the Cottesloe clay sand sample while the largest grains ranging from 550.6 μ m to 840.9 μ m constitutes only 2.8% of the total quartz grains. The remaining quartz grains are of intermediary grain sizes. The smallest grain size found for clay in the Cottesloe clay sample is 15.6 μ m with the largest having a diameter of 375.2 μ m. The range of smaller grains of clay from the Cottesloe clay sand samples is 15.6 μ m to 36.0 μ m constituting 24.7% of the total clay while the largest grains ranges from 199.5 μ m to 375.2 μ m and constitute 12.8% of the total clay grains. The smallest grain size found for carbonate in the Cottesloe clay sample is 14.5 μ m with the largest having a diameter of 519.3 μ m. The range of smaller grains of carbonate from the Cottesloe clay sample is 14.5 μ m to 50.0 μ m, constituting 12.9% of the total carbonate while the largest grain ranges from 298.0 μ m to 519.3 μ m and constitute 12.9% of the total carbonate grains. The pores in the Cottesloe clay sample have a least pore diameter of 8.2 μ m with the largest pore of 840 μ m. The smaller pores, ranging from 8.2 μ m to 39.9 μ m, constitute 26.3% of the total pore count while larger pores ranging from 499.3 μ m to 840.9 μ m constitute 27.6% of the total pore count Figure 5.6.5 and Table 5.5.



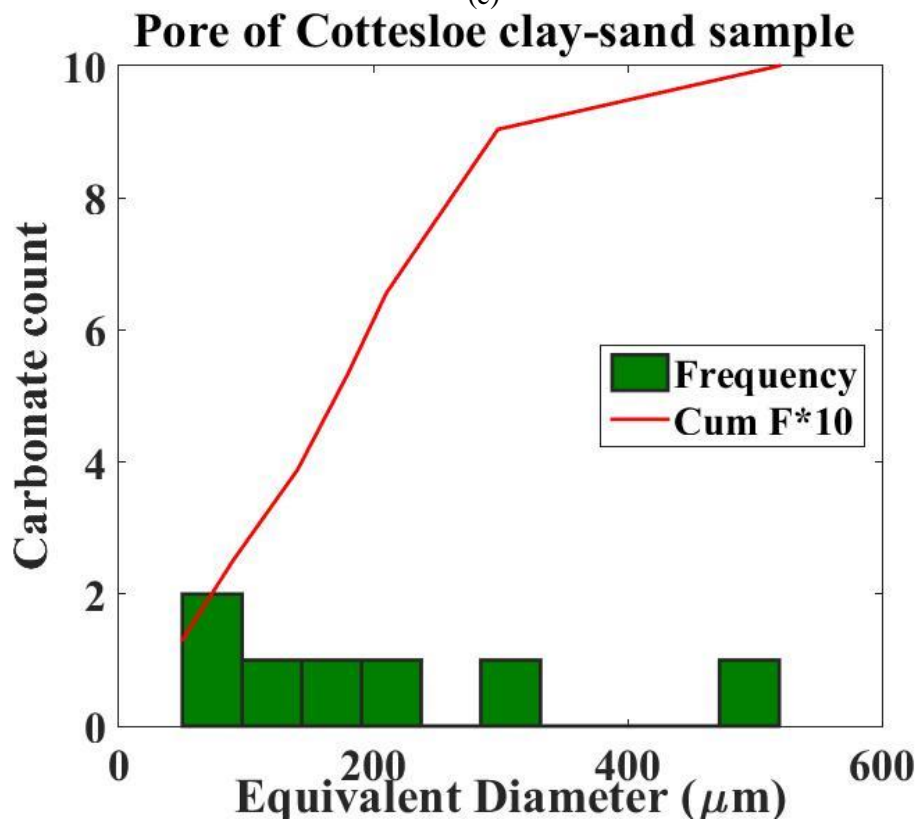
(a)



(b)



(c)



(d)

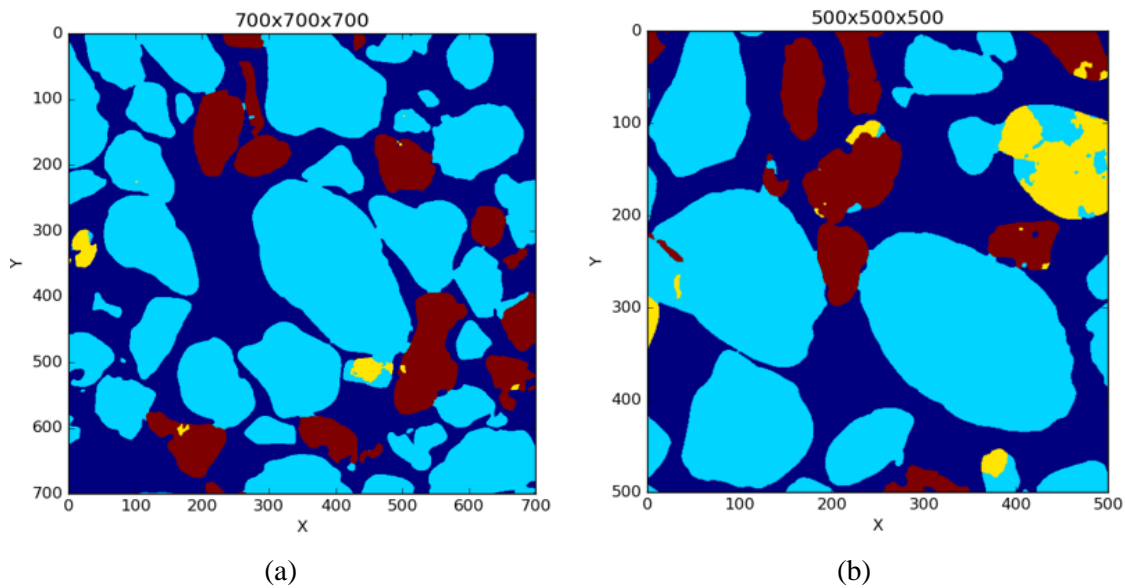
Figure 5.6.5: Frequency distribution of components in the Cottesloe sand with 3% clay (a) pore (b) quartz (c) clay and (d) carbonate

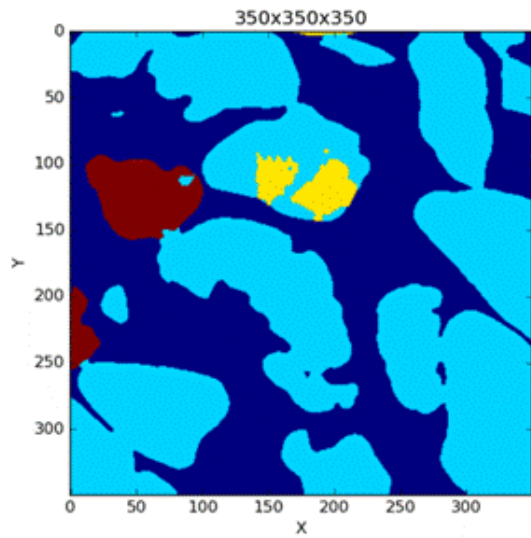
Table 5.5: Summary of EqDiameter of materials

Beach	Material	Range(μm)	Average(μm)
Cottesloe clay sand	Pore	Min	8.15
		Max	840.9
	Quartz	Min	14.2
		Max	740.2
	Clay	Min	15.6
		Max	375.2
	Carbonate	Min	14.5
		Max	519.3

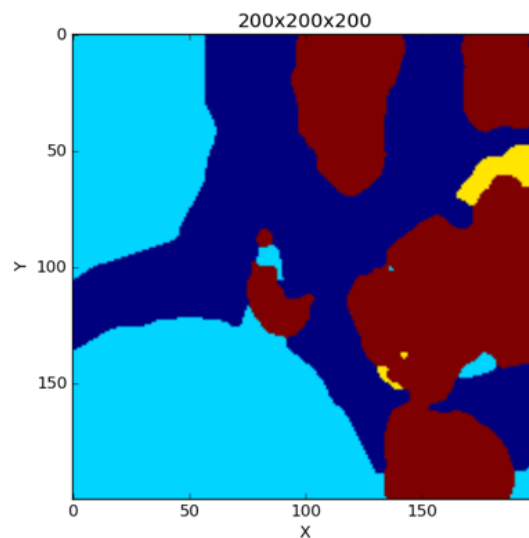
5.8.3.3 Plots of the electrical potential field after finite element code

Using free codes from National Institute of Standards Technology (NIST), I used the output file from the conductivity calculation of all 96 cubes (images shown in Figure 5.6.6) to plot the potential field variation of each cube. Shown below is an example of the result of the potential image (Figure 5.6.7) of the average conductivity.



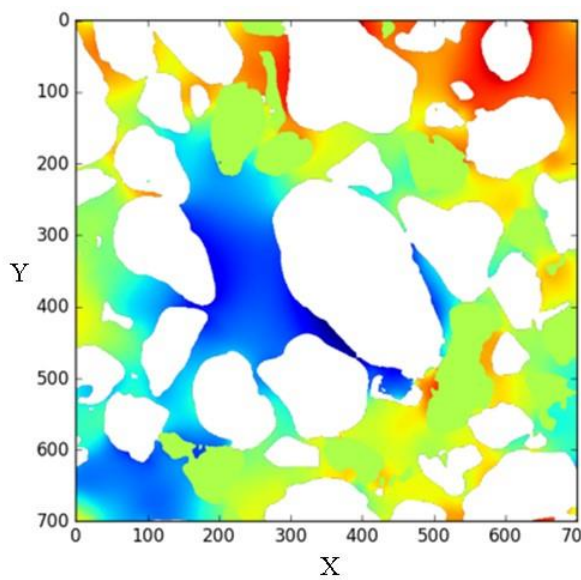


(c)

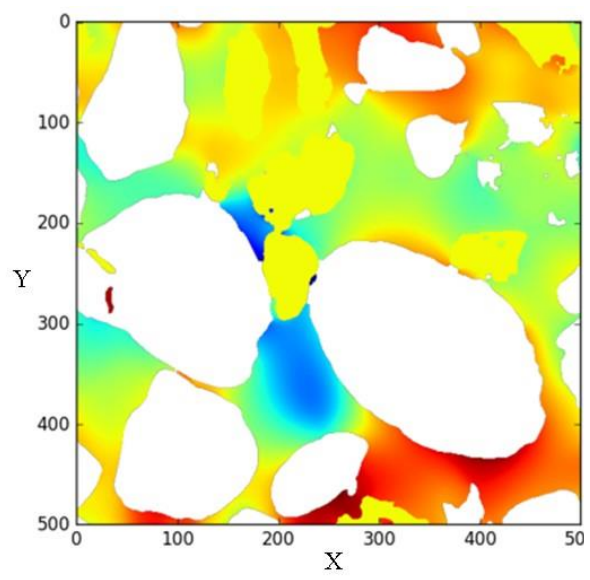


(d)

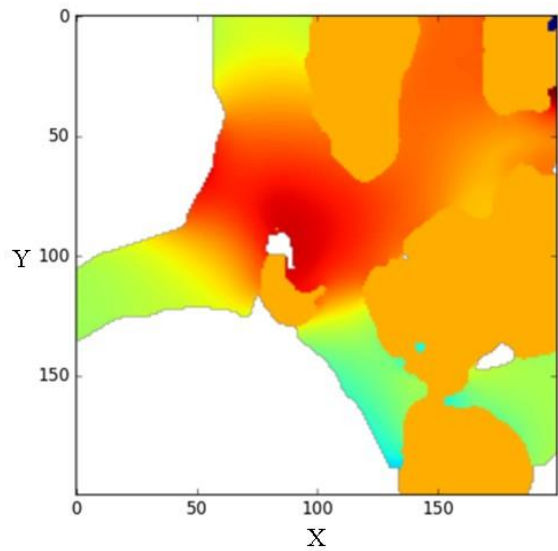
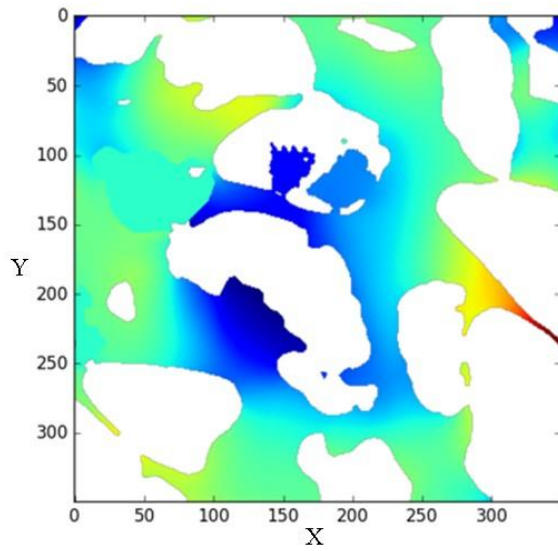
Figure 5.6.6: Cottesloe with 3% clay showing the components: deep blue (pore); sky blue (quartz); maroon (carbonate); and yellow (clay) of (a) $(700)^3$ (b) $(500)^3$ (c) $(350)^3$ and (d) $(200)^3$ cubes.



(a)



(b)



(c)

(d)

Figure 5.6.7: Cottesloe with 3% clay showing potential field variation of (a) $(700)^3$ (b) $(500)^3$ (c) $(350)^3$ and (d) $(200)^3$ cubes.

Table 5.6: General table for the Cottesloe clay sand mixture

Laboratory results	Static cell	Porosity	0.39													
		F.F	6.844													
Micro-CT scan images	(700) ³ cubes	Porosity	0.405	0.405	0.405	0.405	0.405	0.405	0.404	0.404	0.404	0.404	0.404			
		F.F	4.269	4.272	4.272	4.279	4.284	4.285	4.302	4.302	4.310	4.310				
	(500) ³ cubes	Porosity	0.414	0.414	0.414	0.414	0.414	0.413	0.413	0.411	0.410	0.409	0.407	0.407	0.404	
		F.F	4.090	4.107	4.107	4.132	4.187	4.212	4.221	4.260	4.265	4.265	4.299	4.299	4.318	
	(350) ³ cubes	Porosity	0.404	0.402												
		F.F	4.329	4.339												
		Porosity	0.479	0.473	0.438	0.438	0.416	0.410	0.408	0.400	0.400	0.390	0.387	0.382	0.376	
		F.F	3.902	3.922	4.032	4.051	4.231	4.355	4.407	4.426	4.429	4.441	4.498	4.516	4.546	
		Porosity	0.371	0.370	0.367	0.362	0.361	0.360	0.359	0.351	0.349	0.338				
		F.F	4.600	4.623	4.743	4.781	4.799	4.851	4.945	5.083	5.324	5.394				
		Porosity	0.661	0.630	0.567	0.515	0.497	0.437	0.430	0.422	0.412	0.411	0.382	0.378	0.373	
		F.F	1.978	2.495	2.537	3.297	3.313	3.472	3.795	3.817	3.923	4.134	4.421	4.538	4.603	
	(200) ³ Cubes	Porosity	0.363	0.362	0.362	0.361	0.348	0.346	0.344	0.336	0.334	0.319	0.304	0.293	0.283	
		F.F	4.695	4.996	5.106	5.246	5.517	5.671	5.631	5.635	5.715	5.717	5.902	5.934	6.268	
		Porosity	0.275	0.262	0.252	0.248										
		F.F	6.691	6.796	6.946	7.497										

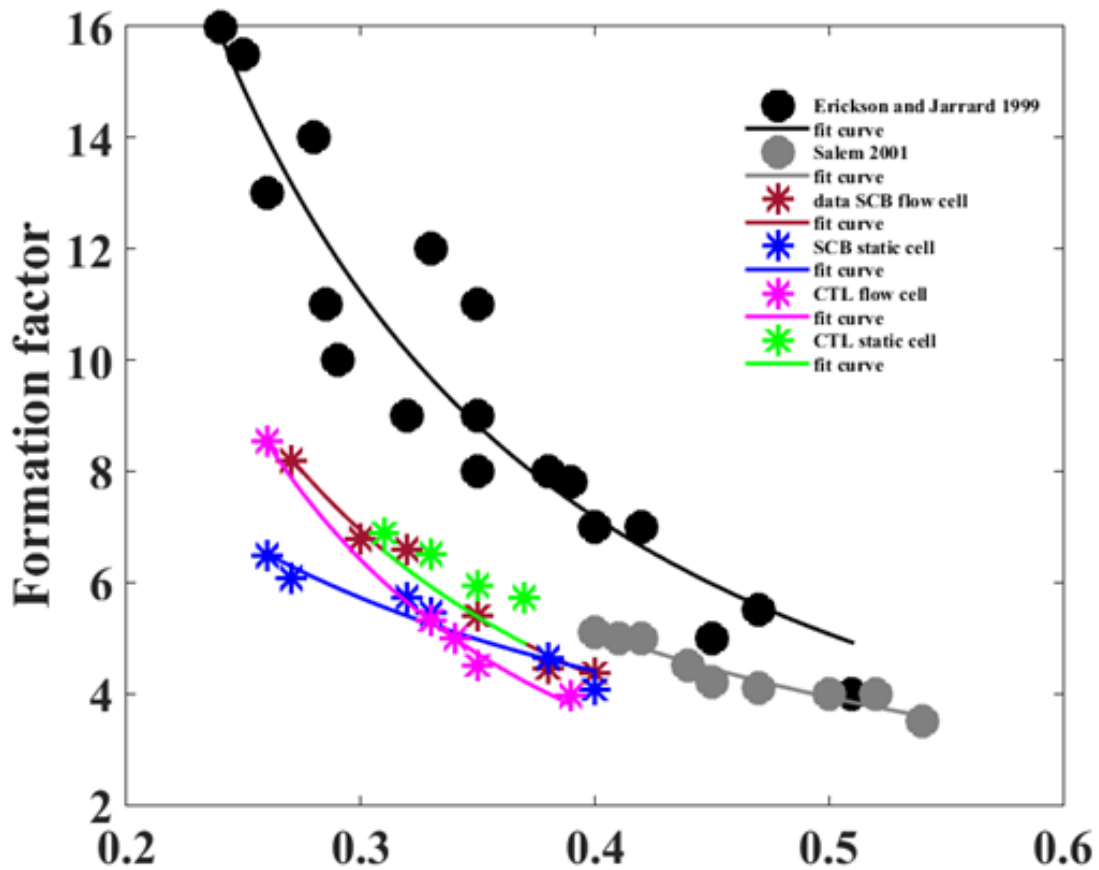


Figure 5.6.8: Summary of measurements from laboratory and micro CT-scan images from Cottesloe clay sand.

5.9 Conclusion

In this chapter, I have presented the results of the laboratory flow and static cells and the analysis of the 174 cubes of Scarborough, Cottesloe (clean sand) and Cottesloe (clay-sand) micro CT-scan images. Results of the pore and grain size analysis are also presented in this chapter from which the percentage composition of individual materials is shown. Finally, the results of the electrical computations of the 174 cubes cropped from the 174 cubes of Scarborough, Cottesloe (clean sand) and Cottesloe (clay-sand) micro CT-scan images as well as the formation factor is presented in this chapter. In the following chapter (Chapter 6), I will be discussing my results within the context of other research works in the laboratory and digital rock physics.

Chapter 6

Synthesis and future directions

6.1 Introduction

In this chapter, I will highlight the main results and key points that we can draw from this research work, as well as present the potentials of the methodology developed here for many fields in geoscience. In particular I will compare the results with previous studies, talk about the importance of the cube size used for computation from digital images and discuss the particular case of conductive materials (such as clay).

The main advantages of the computation of rock properties from digital images are essentially a gain of time (it can indeed take several weeks to measure the electrical properties of clay-rich rocks using classical laboratory equipment) and the possibility to alter the digital images (for example changing porosity by dissolving or precipitating some minerals or inducing any other diagenetic alteration) without actually performing the experiment and also to sub-sample my sample in order to create trends for a given rock or sand hence generating enormous amount of data that can be treated statistically.

6.2. Laboratory-measurement versus computed formation factor: the case of clean sand

In figure 6.1, the laboratory measurements of formation factor values for Scarborough and Cottesloe Beaches are displayed along with previous measurements made in various granular media, both natural (beach sand) and synthetic (made of regular shaped grains). Note that only the results obtained with the “flow cell have been reported as we already discussed in chapter 5 that they give more reliable result. If we draw a shaded zone bounded by two lines representing a formation factor versus porosity trend with a pre-exponential factor of 1 and cementation exponents of 1.35 and 1.75, which corresponds to the typical range of cementation exponents for unconsolidated media, we can see that all the data, including those measured in

this work, falls between these trends. It hence validates the quality of the laboratory measurements.

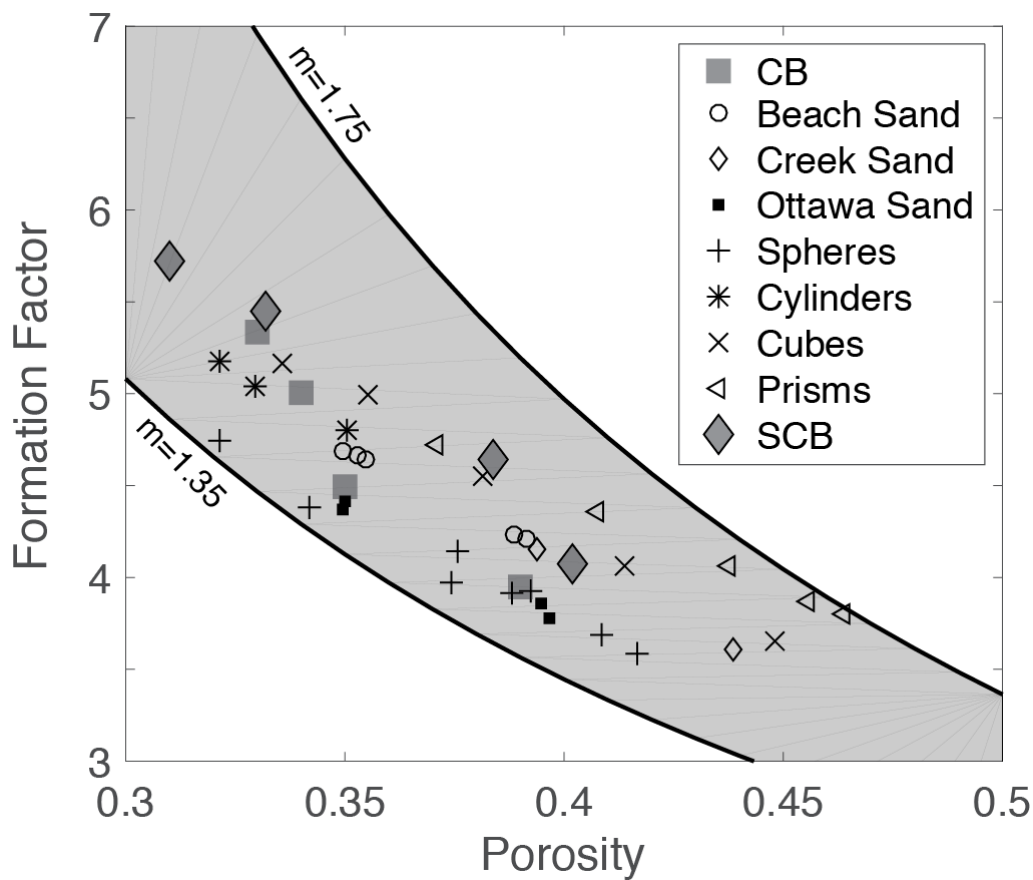


Figure: 6.1: Summary of laboratory and micro CT scan results with results from Research

Figure 6.2 and 6.3 summarize the laboratory-measured versus computed formation factor values, for both Scarborough and Cottesloe Beaches. Generally, the flow cell laboratory measurements are higher than the static cell measurements for both Scarborough and Cottesloe sand samples. Similarly, all micro CT scan measurements are higher than the laboratory measurements. The formation factor trends of laboratory measurements (flow and static cells) agree with the ones obtained from the micro-CT scan images; however, the best agreement was observed when the cube size became larger, reaching a volume generally referred to as the Representative Elemental Volume (REV). Figures 5.3.3 and 5.3.6 of Chapter 5, which display the computed values of porosity and formation factor as a function of cube size, for both studied beach sands, show that the computed values are very scattered for a small cube size $(200)^3$ and that this scatter becomes smaller and smaller when the cube size used for the computation increases; for all the cubes with size of $(700)^3$ all the computed values are the same, which

means that the REV is between $(500)^3$ and $(700)^3$. Note that the cube size in voxel units is meaningless as a voxel has dimensions that vary based on the scanning resolution: in my case one voxel is about $(2.6\mu\text{m})^3$. Hence REV is here between about $(1300\mu\text{m})^3$ and $(1820\mu\text{m})^3$, which, with an average grain size of $160\mu\text{m}$, is between 8 and 11 grains. An interesting observation is that, for porosity, the mean of all computed values for a given cube size is the same and equal to that of the $(700)^3$ cube, but for that formation factor, this is not the case, and in general the mean value becomes larger when the cube size becomes smaller. This translates to formation factor versus porosity trends that have an increasing cementation exponent for decreasing cube size (see Figure 6.2 and 6.3). Note also that the computed values are closer to the ones found from the laboratory measurements (flow cell) for cube size of $(700)^3$.

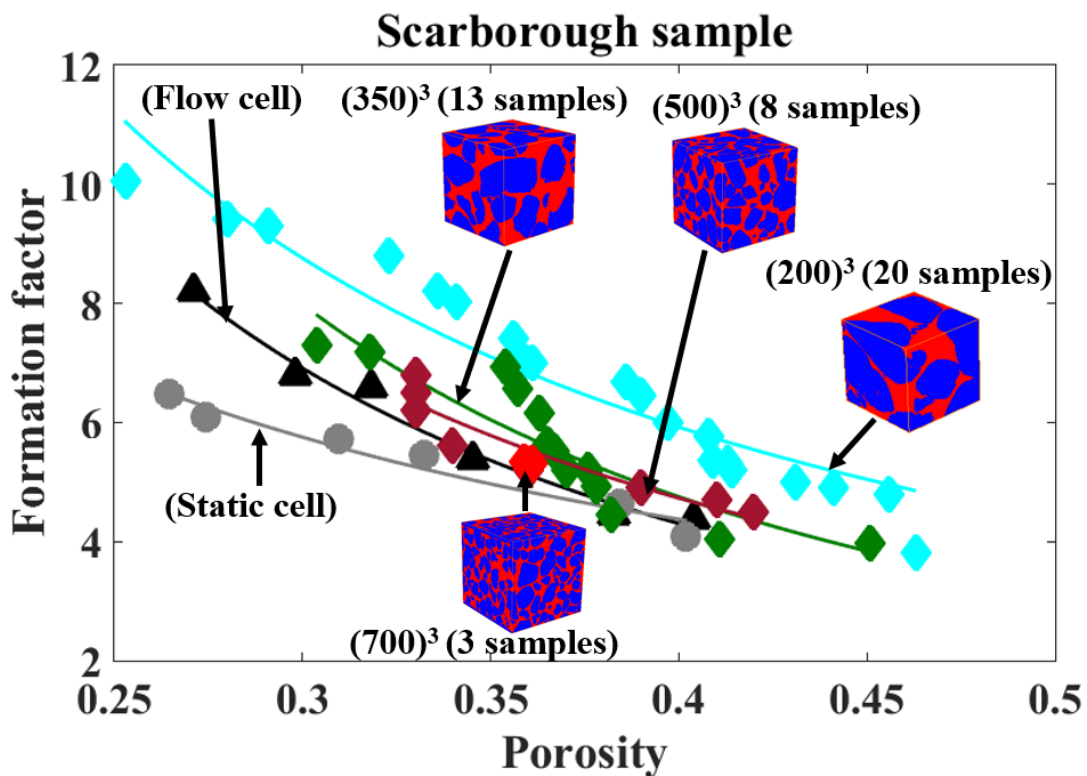


Figure: 6.2: Summary of laboratory and micro-CT scan image of Scarborough clean sand

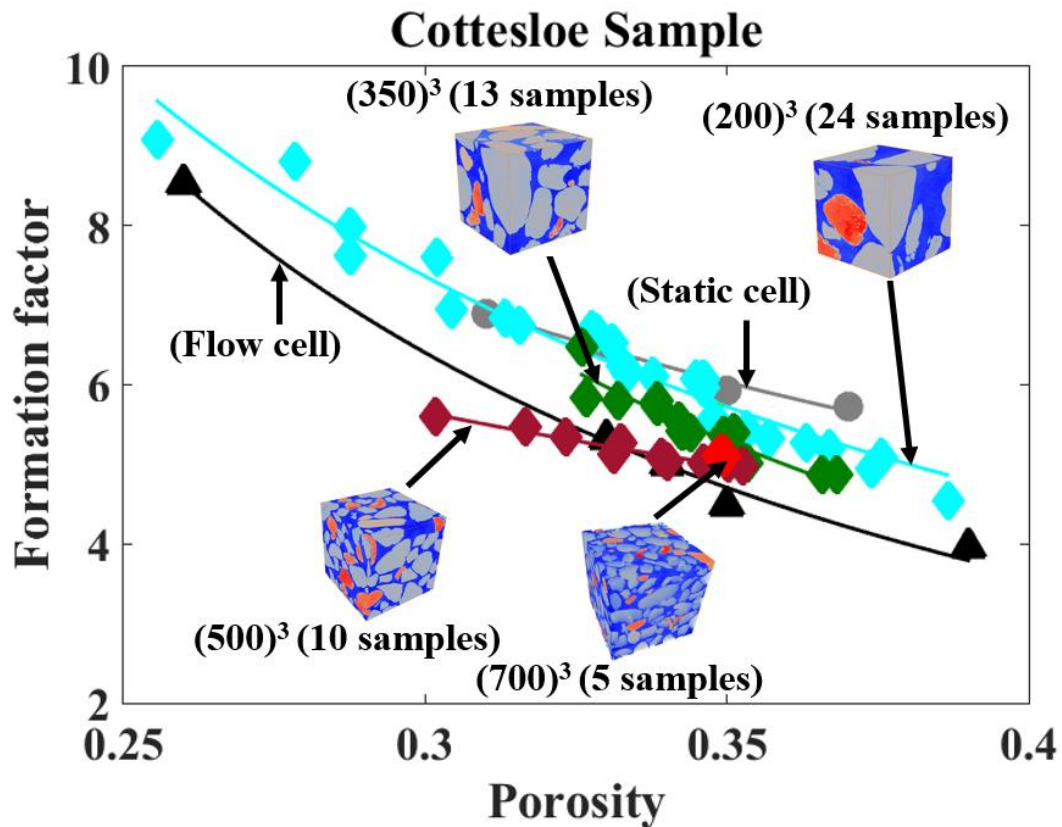


Figure: 6.3: Summary of laboratory and micro-CT scan image of Cottesloe clean sand

6.3 Laboratory-measured versus computed formation factor: the case of clay sand

The estimation of conductivity from the digital sample of clay-sand mixtures is not as robust as the clean sand mixtures. The main, and most important, step is the three-phase segmentation of the micro-CT image of these mixtures. The over- (or under-) segmentation of these samples can under-(or over-) estimate the percentage of pores, that can contribute to the electrical conductivity. The clay phase, as it has intrinsic porosity, in the grey scale images can be seen as an intermediate phase between solids and pores. Therefore, a simple threshold segmentation is not enough to segment the image correctly.

After clay segmentation, the electrical conductivity of the water-saturated clay mixture can be estimated from the finite element code, by assuming an effective electrical conductivity. We can assume the clay has an effective conductivity, related to its intrinsic porosity, which is lower than the resolution of the micro-CT images.

Obtaining formation factor from laboratory measurement of the clay-sand takes much longer than the measurement of the clean sand. At the beginning of the experiment, I started measuring the resistance of the clay-sand with deionized water, unlike that of the clean sand, which I started with fresh water; this was to take into account the effect of surface conduction contributed by the clay. At higher salinities of 25g/l and 35g/l, the measurements become much more unstable as seen in Figure 5.6.1. Presented in Table 5.6 are the values of the formation factor and porosity for the clay-sand laboratory and micro-CT scan images for the Cottesloe Beach sample. [Rezaei-Gomari \(2011\)](#) in their work used 20 siliciclastic reservoir rock samples and obtain porosity range of 0.15 to 0.30 and [Berg \(2012\)](#) in their research work on Bentheimer sandstone obtain a porosity range of 0.05 to 0.25 while [Lopez \(2012\)](#) worked on more than 100 carbonate reservoir core samples and obtain a porosity range of 0.11 to 0.35.

The formation factor trend from the laboratory measurement and micro-CT scan images (700, 500, 350 and 200 cubes) were plotted against their porosities as shown in Figure 5.6.2 for the clay-sand of Cottesloe Beach. A perfect agreement was achieved from the micro CT-scan images in all cases. However, the formation factor calculated from the laboratory measurement is higher than the formation factor calculated from the micro CT-scan images by over 30%; hence, I recommend a repeat of the experiment Figure 5.6.8.

6.4 Summary of key findings and perspectives

Electrical properties of rocks are important parameters for well log and reservoir interpretation. The main goal of this research study was to establish robust method of computing the electrical formation factor from micro-CT scan images. Laboratory measurements of such properties are time-consuming and, difficult, if not impossible in some cases.

I have successfully combined the scientific approach of laboratory measurements (as the benchmark) with micro-CT scan computational images. I have achieved the objectives of computing the variability of calculating formation factor as a function of porosity from laboratory measurements of three clean sand samples and two micro-CT scan images from the sand samples of Scarborough and Cottesloe Beaches of the Perth basin. In addition, I have also successfully computed the formation factor from a more complex clay-sand mixture of a Cottesloe Beach sand sample.

This approach is practical, easy and repeatable in real time (though expensive and time-wasting in the case of the clay-sand mixture), hence, it can be an alternative method for calculating the

formation factor when time is not on the side of the experimenter, which is always the case. In this research, a micro CT-scan images computational technique was employed to calculate properties such as porosity and formation factor on large, three- dimensional digitized images of sand samples. I demonstrated that for most of the parameters studied here, the values obtained by computing micro CT-scan images are in agreement with the classical laboratory measurements and results from the other research work [Berg \(2012\)](#); [Lopez et al. \(2012\)](#) and [Rezaei-Gomari \(2011\)](#).

In view of this, I have achieved the following:

- Although there are several works on both laboratory and micro-CT scan computations of the formation factor, there is not any literature that computed and compared for the agreement or otherwise of the formation factor from the “*same sample*” using the two different methods (flow and static cells).
- Generally, in the case of the clean sand, the static cell laboratory measurement shows a higher formation factor than the flow cell measurement and this is in line with reports of several authors, such as [Auzerais et al. \(1996\)](#); [Schwartz et al. \(1994\)](#); [Spanne et al. \(1994\)](#).
- This research work was able to address the issue of scaling. Although results obtained from laboratory scale (cm) with that of micro-CT the images is not of the same scale, but both results follow a similar trend. Therefore, extrapolating it to the field scale (m or even km) to follow the same trend is feasible. [Dvorkin and Wollner \(2017\)](#) recently presented a hypothesis using 1-D synthetic earth models and a real well data from an offshore field to show that results of physical measurement are “*scale independent*”.
- I have shown that for the micro-scale measurements to be valid, the Representative Elemental Volume (REV) “MUST” be attained in this case between $(500)^3$ and $(700)^3$ for the Scarborough and Cottesloe Beach samples respectively.
- This research work was able to compute for the formation factor of grains with intra-granular porosity (carbonates), as they are characteristic of the sands of both Scarborough and Cottesloe Beaches.
- Apart from computing the formation factor of clean sand using the free online NIST code, I was also able to alter the code to compute for the formation factor of clay-sand.
- I envisage that, computing the formation factor of more complex samples, such as sands with disseminated conductive grains (e.g. ores), could be achieved by accurate alteration of the NIST code.

- A robust method of obtaining the formation factor from CT-scan images that takes a shorter time (1 day) from that of laboratory measurements (that take a much longer time of 3-7 days for a clean sand to 30-65 days (in case of clay-sand) was established.

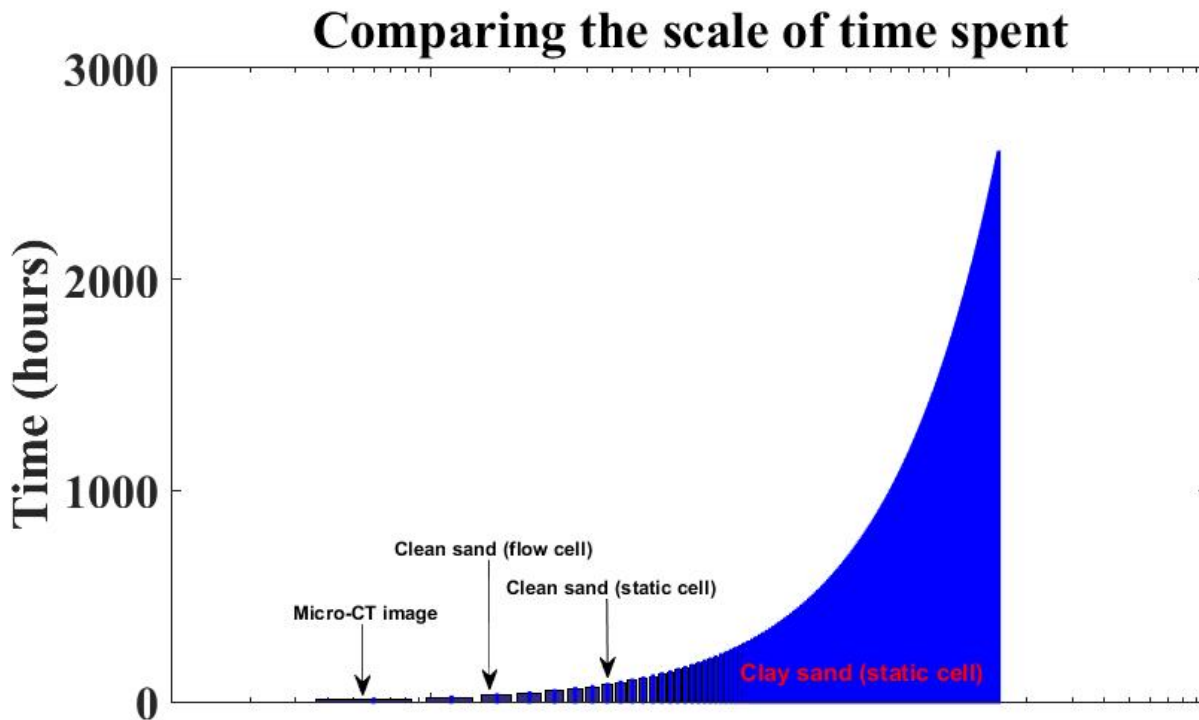


Figure: 6. 4: Comparing the scale of time spent for micro-CT image, clean sand using flow cell, clean sand using static cell and clay sand using static cell.

This work is a comprehensive workflow comparing laboratory measurements with micro CT scan measurements of the same sample and that it can find applications in many fundamental and applied areas. Hence, fields such as groundwater recharge, ore discovery, oil & gas technology, and geothermal studies could benefit from the use of digital computation of rock properties.

This work flow can work on other lithology types.

6.5 Remaining questions

Some of the remaining questions are but limited to

- This thesis focus based on establishing a workflow and was performed with three unconsolidated samples.
- There is need to perform more laboratory and digital image scan analysis of more sand samples to have a more representative of a data set.
- There is need to do this type of a work with a wide range of clay content.
- The focus of this thesis is on formation factor, other parameters such as tortuosity and cementation factor need to be done.
- Another interesting aspect is to do the laboratory measurement using various frequencies to look at the permittivity and the imaginary path.
- if this research work will be extended to include metals it will be of interest to exploration geophysics to look for metals in mineral exploration.

References

- Adler, P., C. Jacquin, and J. Quiblier, 1990, Flow in simulated porous media: *International Journal of Multiphase Flow*, **16**, 691-712.
- Adler, P. M., C. G. Jacquin, and J. F. Thovert, 1992, The formation afctor of reconstructed porous media: *Water Resources Resaerch*, **28**, 1571-1576.
- Aharony, A., and D. Stauffer, 2003, *Introduction to percolation theory*: Taylor & Francis.
- Andrä, H., N. Combaret, J. Dvorkin, E. Glatt, J. Han, M. Kabel, Y. Keehm, F. Krzikalla, M. Lee, and C. Madonna, 2013, Digital rock physics benchmarks—Part I: Imaging and segmentation: *Computers & Geosciences*, **50**, 25-32.
- Archie, G. E., 1942, The electrical resistivity log as an aid in determining some reservoir characteristics: *Transactions of the AIME*, **146**, 54-62.
- Arns, C. H., M. A. Knackstedt, W. V. Pinczewski, and K. R. Mecke, 2001, Euler-Poincaré characteristics of classes of disordered media: *Physical Review E*, **63**, 031112.
- Avizo User's guide 2014, Konrad-Zuse-Zentrum ftr informatiostechnik. Berlin (ZIB) Germany, 1-715.
- Bear, J., 1972, *Dynamics of fluids in porous media*—American Elsevier pub: Comp., inc. New York, 764p.
- Bell, F. G., 2013, *Engineering properties of soils and rocks*: Elsevier.
- Berg, C. F., 2012, Re-examining Archie's law: Conductance description by tortuosity and constriction: *Physical Review E*, **86**, 046314.
- Börner, F., M. Gruhne, and J. Schön, 1993, Contamination indications derived from electrical properties in the low frequency RANGE1: *Geophysical Prospecting*, **41**, 83-98.
- Börner, F., F. Jung, and J. Schön, 1991, Complex Electrical Conductivity of KTB Samples in the Frequency Range Between 10– 3 and 10 4 Hz-First Results: *Scientific Drilling*, **2**, 101-104.
- Buades, A., B. Coll, and J.-M. Morel, 2005, A review of image denoising algorithms, with a new one: *Multiscale Modeling & Simulation*, **4**, 490-530.
- Bulling, T., and J. Breyer, 1989, Exploring for subtle traps with high-resolution paleogeographic maps: Reklaw 1 interval (Eocene), south Texas: *AAPG bulletin*, **73**, 24-39.
- Carothers, J. E., and C. R. Porter, 1971, Formation factor-porosity relation derived from well log data: *The Log Analyst*, **12**.
- Chaouachi, M., A. Falenty, K. Sell, F. Enzmann, M. Kersten, D. Haberthür, and W. F. Kuhs, 2015, Microstructural evolution of gas hydrates in sedimentary matrices observed with synchrotron X-ray computed tomographic microscopy: *Geochemistry, Geophysics, Geosystems*, **16**, 1711-1722.
- Corey, A. T., 1994, *Mechanics of immiscible fluids in porous media*: Water Resources Publication.
- De Witte, L., 1955, *A study of electric log interpretation methods in shaly formations*.
- Dilsiz, G., 2011, *Determination of aggregate shapes using X-ray computed tomography and making virtual concrete*.
- Diment, W., R. Wilcox, G. Keller, E. Dobrovolny, F. Kracek, J. Roller, L. Peseinick, E. Robertson, A. Lachenbruch, and C. Bunker, 1959, *Properties of Oak Spring formation in Area 12 at the Nevada Test Site*.
- Drugan, W., and J. Willis, 1996, A micromechanics-based nonlocal constitutive equation and estimates of representative volume element size for elastic composites: *Journal of the Mechanics and Physics of Solids*, **44**, 497-524.
- Dullien, F. A., 2012, *Porous media: fluid transport and pore structure*: Academic press.

- Dvorkin, J., N. Derzhi, E. Diaz, and Q. Fang, 2011, Relevance of computational rock physics: *Geophysics*, **76**, E141-E153.
- Dvorkin, J., and U. Wollner, 2017, Rock-physics transforms and scale of investigation: *Geophysics*, **82**, MR75-MR88.
- Fang, H.-Y., 2013, *Foundation engineering handbook*: Springer Science & Business Media.
- Freudenthal, A. M., 1950, *The inelastic behavior of engineering materials and structures*: Wiley.
- Guichet, X., L. Jouniaux, and J. P. Pozzi, 2003, Streaming potential of a sand column in partial saturation conditions: *Journal of Geophysical Research: Solid Earth*, **108**.
- Guyed, H., and P. Wichmann, 1971, *Theoretical Notes On The Resistivity Of Shaly Sands*: SPWLA 12th Annual Logging Symposium, Society of Petrophysicists and Well-Log Analysts.
- Hashin, Z., 1983, Analysis of composite materials: *J. appl. Mech*, **50**, 481-505.
- Jackson, P., D. T. Smith, and P. Stanford, 1978, Resistivity-porosity-particle shape relationships for marine sands: *Geophysics*, **43**, 1250-1268.
- Jackson, P. D., 1975, An electrical resistivity method for evaluating the in-situ porosity of clean marine sands: *Marine Georesources & Geotechnology*, **1**, 91-115.
- Johnson, D. L., and P. N. Sen, 1988, Dependence of the conductivity of a porous medium on electrolyte conductivity: *Physical Review B*, **37**, 3502.
- Jones, P. H., and T. B. Buford, 1951, Electric logging applied to ground-water exploration: *Geophysics*, **16**, 115-139.
- Kamel, M. H., 2001, An approach for estimating formation factor parameter from transit time data in clean sand formation: *Journal of Petroleum Science and Engineering*, **30**, 83-89.
- Keller, G., 1971, Electrical characteristics of the earth's crust: *Electromagnetic probing in geophysics*, 13.
- Keller, G. V., and F. C. Frischknecht, 1966, *Electrical methods in geophysical prospecting*.
- Knight, R. J., and A. Nur, 1987, The dielectric constant of sandstones, 60 kHz to 4 MHz: *Geophysics*, **52**, 644-654.
- Kulenkampff, J., and J. Schopper, 1988, Low frequency complex conductivity—A means for separating volume and interlayer conductivity: *Trans. 11th Eur. Form., Eval. Symp.*, Paper P.
- Leva, M., M. Weintraub, M. Grummer, M. Polchik, and H. Storch, 1951, *Fluid flow through packed and fluidized systems*: US Government Printing Office.
- Lindeberg, T., 1998, Edge detection and ridge detection with automatic scale selection: *International Journal of Computer Vision*, **30**, 117-156.
- Lopez, O., A. Mock, P. E. Øren, H. Long, Z. Kalam, V. Vahrenkamp, M. Gibrata, S. Seraj, S. Chacko, and M. Al Hammadi, 2012, Validation of fundamental carbonate reservoir core properties using digital rock physics: *International Symposium of the Society of Core Analysts held in Aberdeen, Scotland, UK, SCA2012-19*.
- Lynch, E. J., 1962, *Formation evaluation*: Harper & Row.
- McNeill, J., 1980, *Electrical conductivity of soils and rocks*: Geonics Limited.
- Miller, M. N., 1969, Bounds for effective electrical, thermal, and magnetic properties of heterogeneous materials: *Journal of Mathematical Physics*, **10**, 1988-2004.
- Ogolo, N. A., O. G. Akinboro, J. E. Inam, F. E. Akpokere, and M. O. Onyekonwu, 2015, Effect of Grain Size on Porosity Revisited: *Society of Petroleum Engineers*.
- Olhoeft, G., 1985, Low-frequency electrical properties: *Geophysics*, **50**, 2492-2503.
- Olhoeft, G. R., 1981, Electrical properties of rocks: *Physical properties of rocks and minerals*, **2**, 257-297.
- Ostoja-Starzewski, M., 2002, Microstructural randomness versus representative volume element in thermomechanics: *Journal of Applied Mechanics*, **69**, 25-35.

- Patnode, H., and M. Wyllie, 1950, The presence of conductive solids in reservoir rocks as a factor in electric log interpretation: *Journal of petroleum technology*, **2**, 47-52.
- Powers, M. C., 1953, A new roundness scale for sedimentary particles: *Journal of Sedimentary Research*, **23**.
- Pryor, W. A., 1973, Permeability-porosity patterns and variations in some Holocene sand bodies: *AAPG Bulletin*, **57**, 162-189.
- Revil, A., and P. Glover, 1997, Theory of ionic-surface electrical conduction in porous media: *Physical Review B*, **55**, 1757.
- Rezaei-Gomari, S. S. B., F.; Mock, A.; Øren, P. E.; Petersen Jr, E. B.; Rustad, A. B.; Lopez, O., 2011, Electrical and petrophysical properties of siliciclastic reservoir rocks from pore-scale MODELING
- Roberts, A. J., 1994, A one-dimensional introduction to continuum mechanics: World Scientific.
- Rogers, J. J., and W. B. Head, 1961, Relationships between porosity, median size, and sorting coefficients of synthetic sands: *Journal of Sedimentary Research*, **31**.
- Ruffet, C., M. Darot, and Y. Gueguen, 1995, Surface conductivity in rocks: a review: *Surveys in Geophysics*, **16**, 83-105.
- Saarenketo, T., 1998, Electrical properties of water in clay and silty soils: *Journal of applied geophysics*, **40**, 73-88.
- Saenger, E., C. Madonna, N. Tisato, and B. Quintal, 2014, Towards a representative rock model from a micro-CT image: Second EAGE Workshop on Rock Physics.
- Schock, R. N., A. G. Duba, and T. J. Shankland, 1989, Electrical conduction in olivine: *Journal of Geophysical Research: Solid Earth*, **94**, 5829-5839.
- Schwartz, L. M., P. N. Sen, and D. L. Johnson, 1989, Influence of rough surfaces on electrolytic conduction in porous media: *Physical Review B*, **40**, 2450.
- Schwartz, R., S. Evett, M. Pelletier, and J. Bell, 2009, Complex permittivity model for time domain reflectometry soil water content sensing: I. Theory: *Soil Science Society of America Journal*, **73**, 886-897.
- Shan, J., F. Wang, E. Knoesel, M. Bonn, and T. F. Heinz, 2003, Measurement of the frequency-dependent conductivity in sapphire: *Physical review letters*, **90**, 247401.
- Slawinski, A., 1926, Conductivity of an Electrolyte Containing Dielectric Bodies: *Jour. Chem. Phys*, **23**, 710.
- Sweeney, S., and H. Jennings, 1960, The electrical resistivity of preferentially water-wet and preferentially oil-wet carbonate rock: *Producers Monthly*, **24**, 29-32.
- Torsæter, O., and M. Abtahi, 2000, Experimental Reservoir Engineering Laboratory Work Book, Department of Petroleum Engineering and Applied Geophysics: Norwegian University of Science and Technology.
- Vialle, S., 2008, Etude expérimentale des effets de la dissolution (ou de la précipitation) de minéraux sur les propriétés de transport des roches, Paris 7.
- Vincent, L., and P. Soille, 1991, Watersheds in digital spaces: an efficient algorithm based on immersion simulations: *IEEE transactions on pattern analysis and machine intelligence*, **13**, 583-598.
- Vinegar, H., and M. Waxman, 1984, Induced polarization of shaly sands: *Geophysics*, **49**, 1267-1287.
- Walls, J. D., and S. Sinclair, 2011, Eagle Ford shale reservoir properties from digital rock physics: first break, **29**, 97-101.
- Wang, D., 1997, A multiscale gradient algorithm for image segmentation using watershed: *Pattern recognition*, **30**, 2043-2052.
- Waxman, M., and L. Smits, 1968, Electrical conductivities in oil-bearing shaly sands: *Society of Petroleum Engineers Journal*, **8**, 107-122.

- Waxman, M. H., and E. Thomas, 1974, Electrical conductivities in Shaly Sands-I. The relation between hydrocarbon saturation and resistivity index; II. The temperature coefficient of electrical conductivity: *Journal of petroleum technology*, **26**, 213-225.
- Westman, A. R., and H. Hugill, 1930, The packing of particles: *Journal of the American Ceramic Society*, **13**, 767-779.
- Winsauer, W., and W. McCardell, 1953, Ionic double-layer conductivity in reservoir rock: *Journal of Petroleum Technology*, **5**, 129-134.
- Wyllie, M., and A. Gregory, 1953, Formation factors of unconsolidated porous media: Influence of particle shape and effect of cementation: *Journal of petroleum technology*, **5**, 103-110.
- Wyllie, M. R. J., 1957, *The fundamentals of electric log interpretation*: Academic Press.
- Wyllie, M. R. J., A. R. Gregory, and L. W. Gardner, 1956, Elastic wave velocities in heterogeneous and porous media: *Geophysics*, **21**, 41-70.
- Zhang, W., K. E. Thompson, A. H. Reed, and L. Beenken, 2006, Relationship between packing structure and porosity in fixed beds of equilateral cylindrical particles: *Chemical Engineering Science*, **61**, 8060-8074.

Appendix 1: Volume rendering of Scarborough and Cottesloe clean sand samples

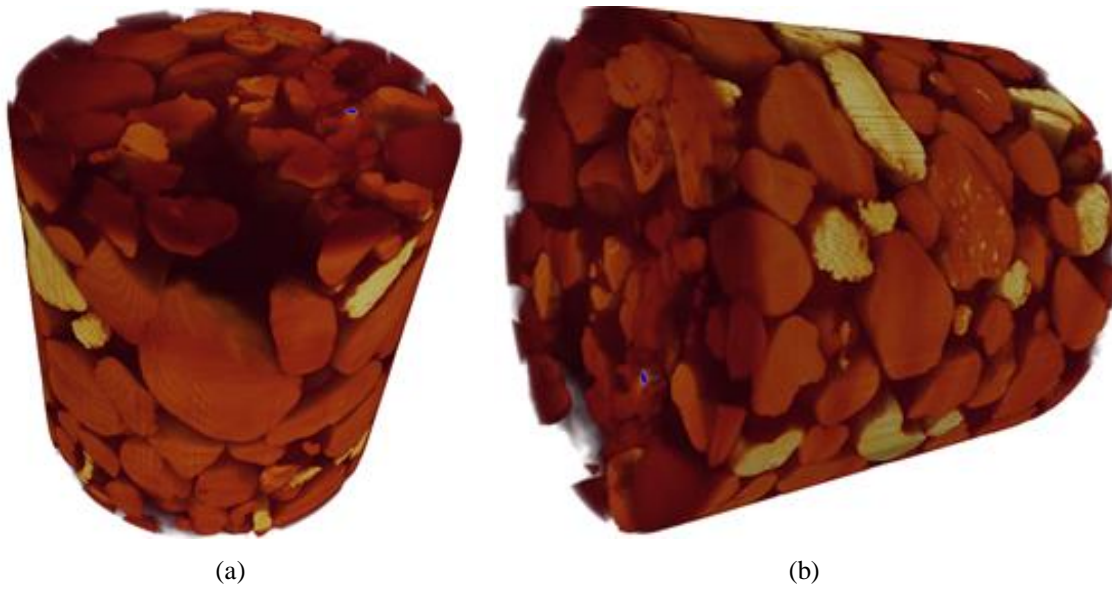


Figure A1.1: Rendered volume of Scarborough clean sand sample.

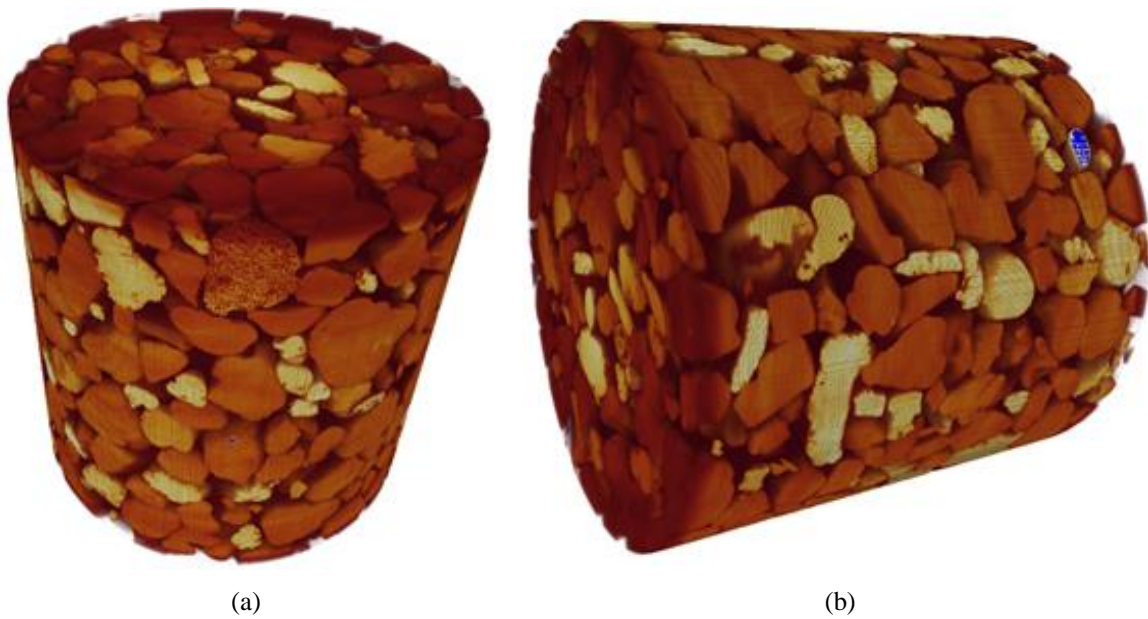


Figure A1.2: Rendered volume of Scarborough clean sand sample.

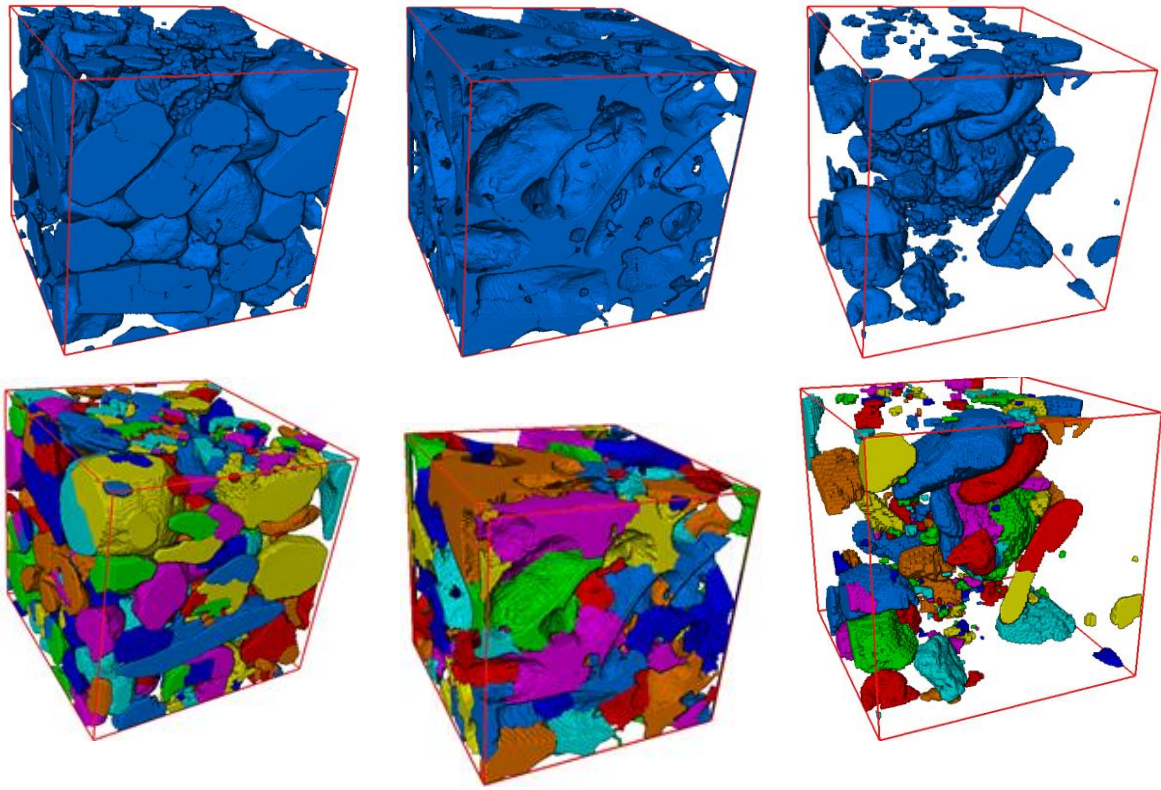


Figure A1.3: Rendered volume of $(700)^3$ of Scarborough clean sand images of carbonate, pores and quartz.

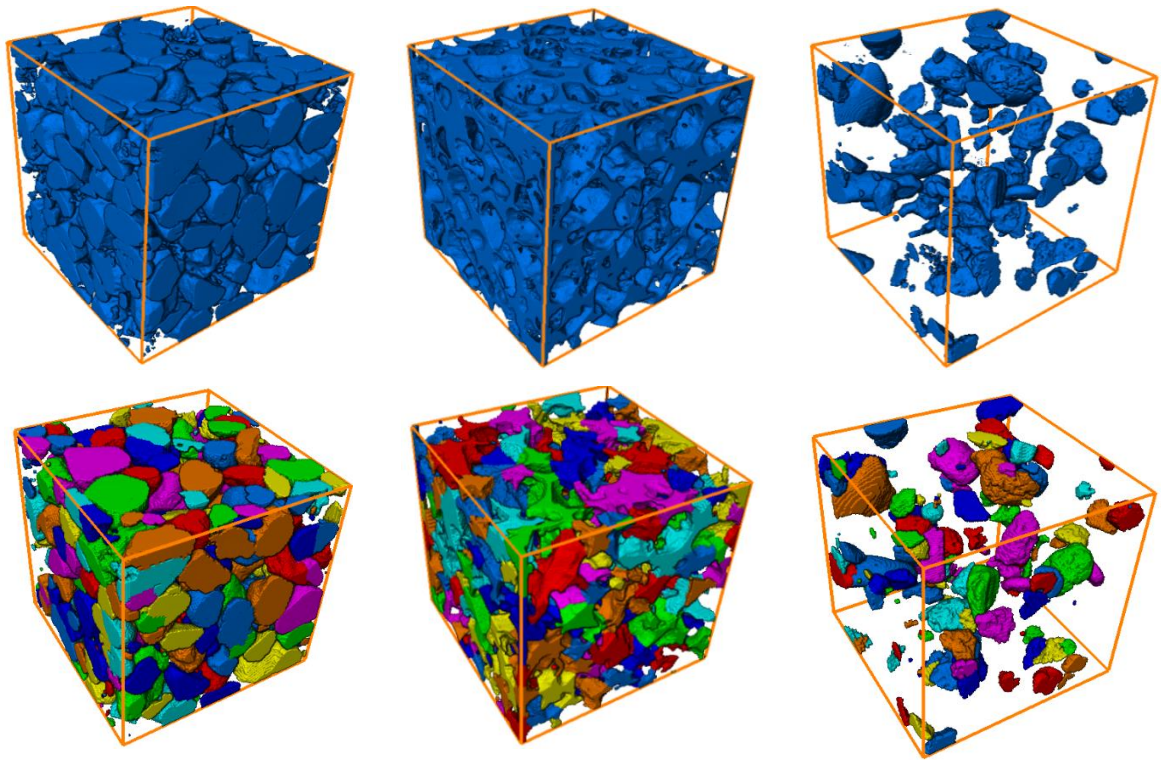


Figure A1.4: Rendered volume of $(700)^3$ of Cottesloe clean sand images of carbonate, pores and quartz.

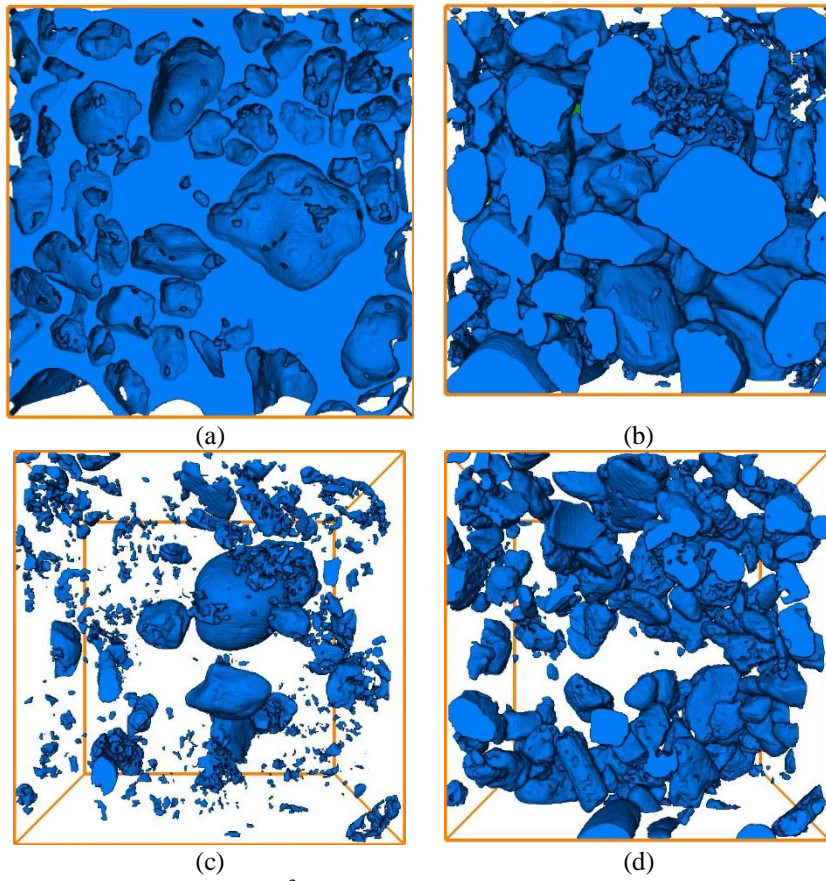


Figure A 1.5: Rendered volume of $(700)^3$ of Cottesloe with clay-sand sample (a) pore (b) quartz (c) clay and (d) carbonate.

Appendix 2: Binary images of Scarborough and Cottesloe beach clean samples

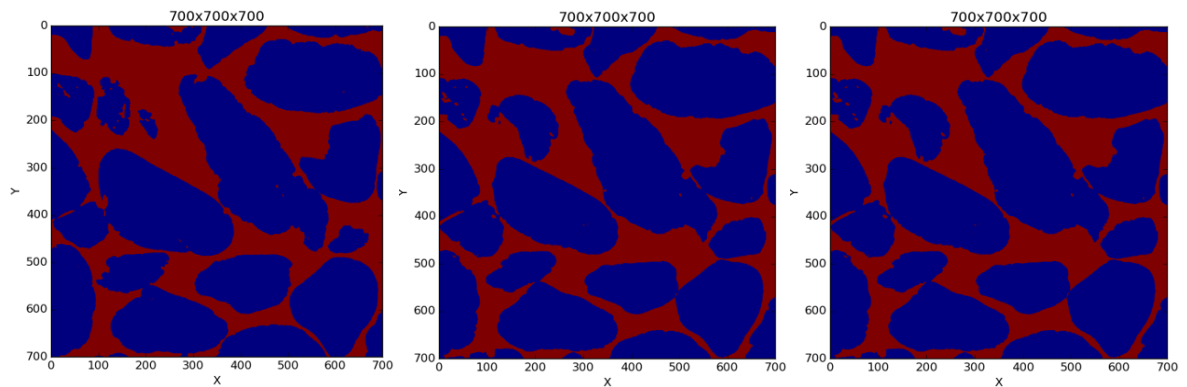


Figure A 2.1: Binary image of $(700)^3$ cubes f or Scarborough clean sand sample.

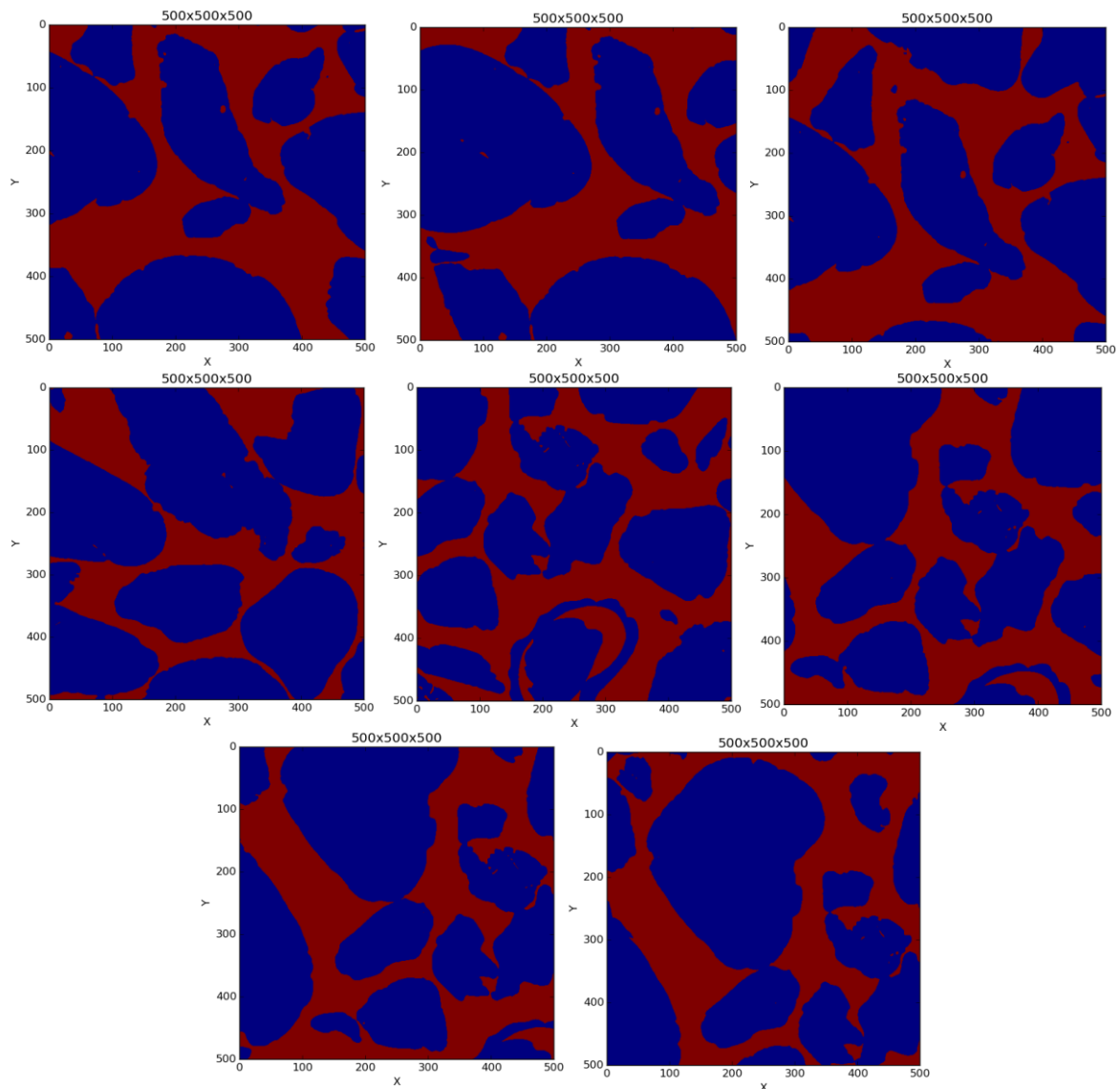


Figure A 2.2: Binary image of $(500)^3$ cubes f or Scarborough clean sand sample.

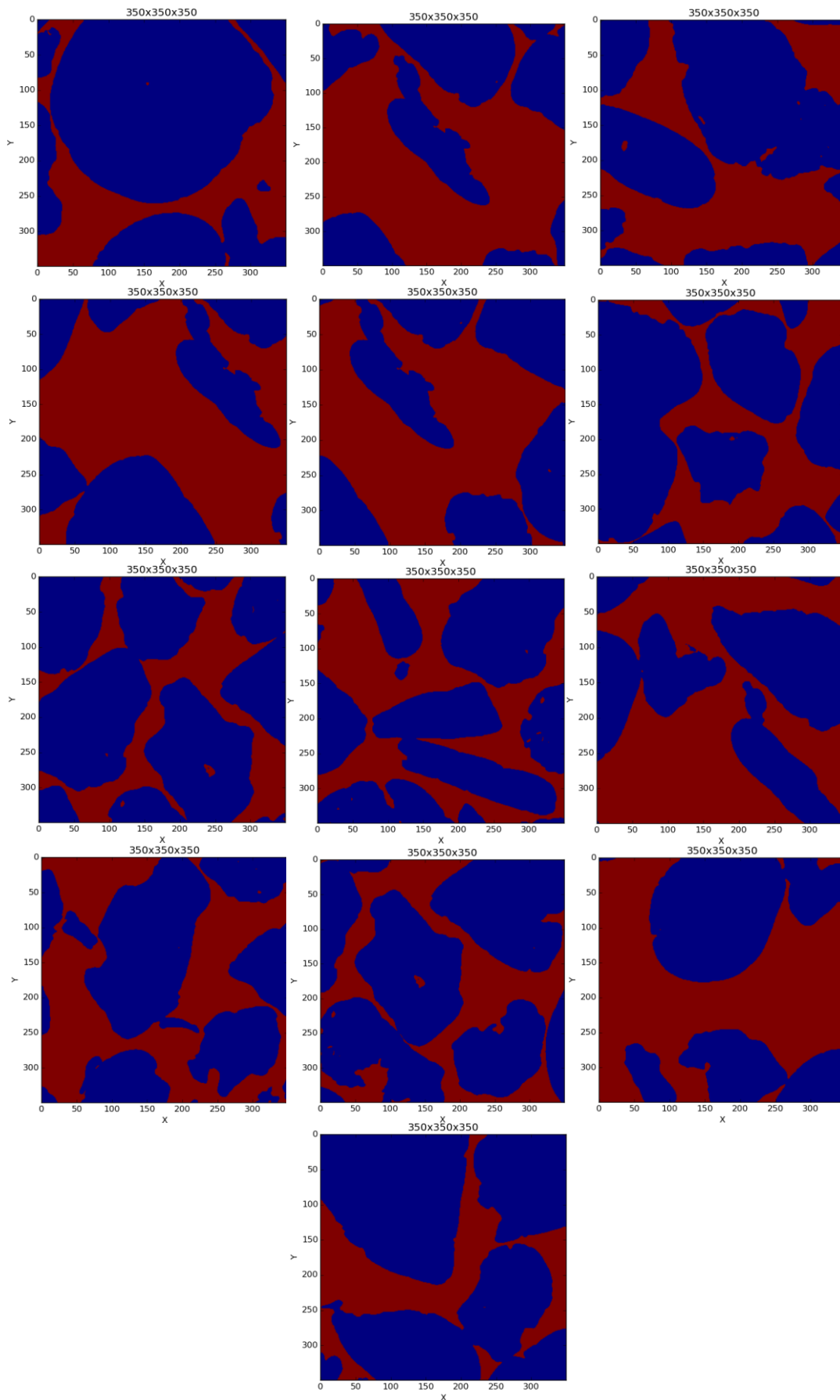
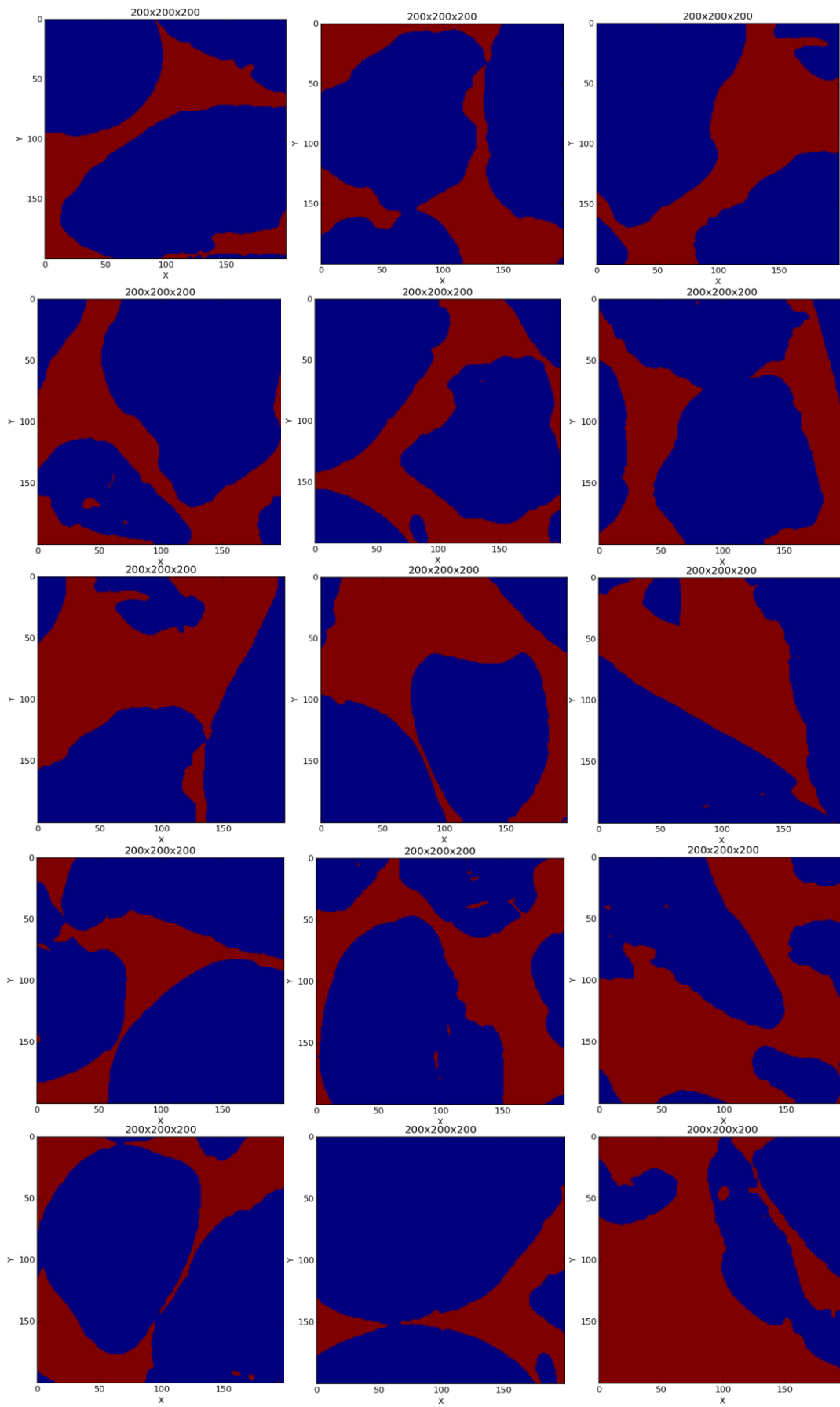


Figure A 2.3: Binary image of $(350)^3$ cubes of Scarborough clean sand sample.



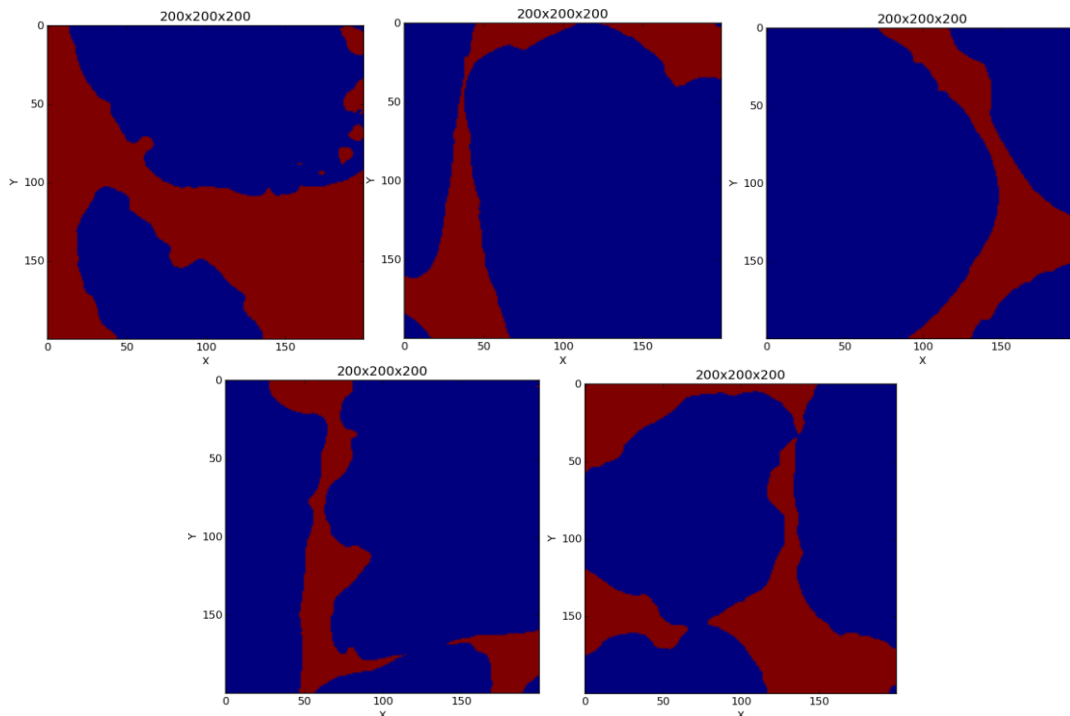


Figure A 2.4: Binary image of $(200)^3$ cubes for Scarborough clean sand sample.

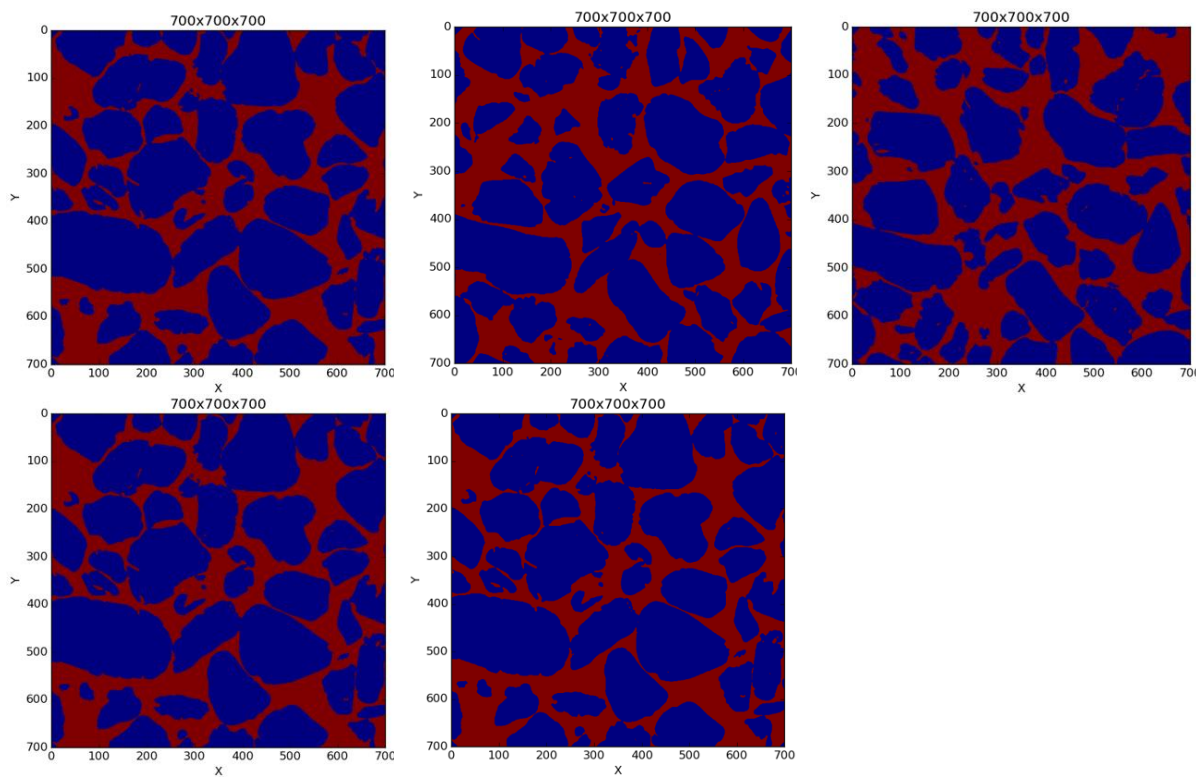


Figure A 2.5: Binary image of $(700)^3$ cubes for Cottesloe clean sand sample.

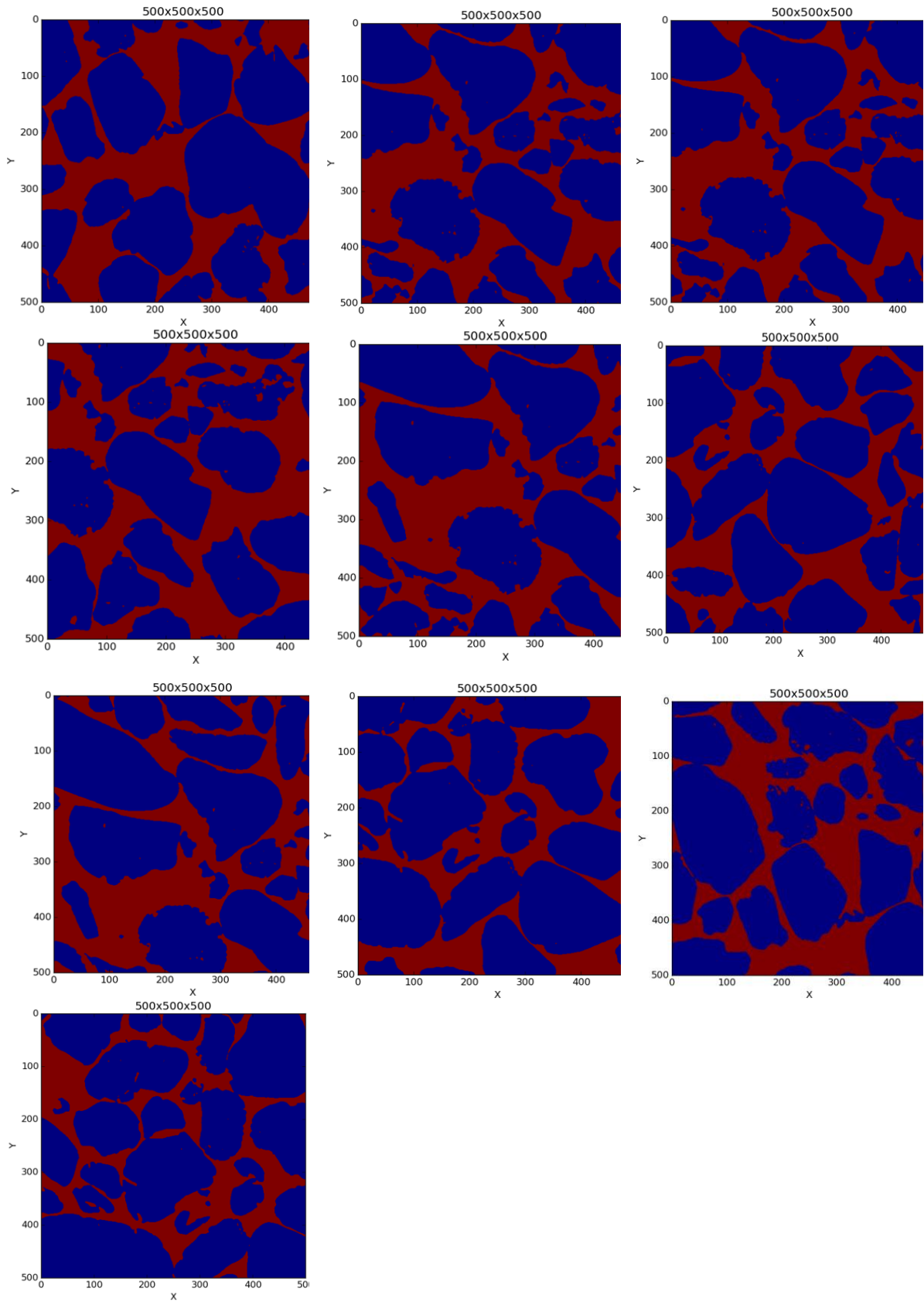
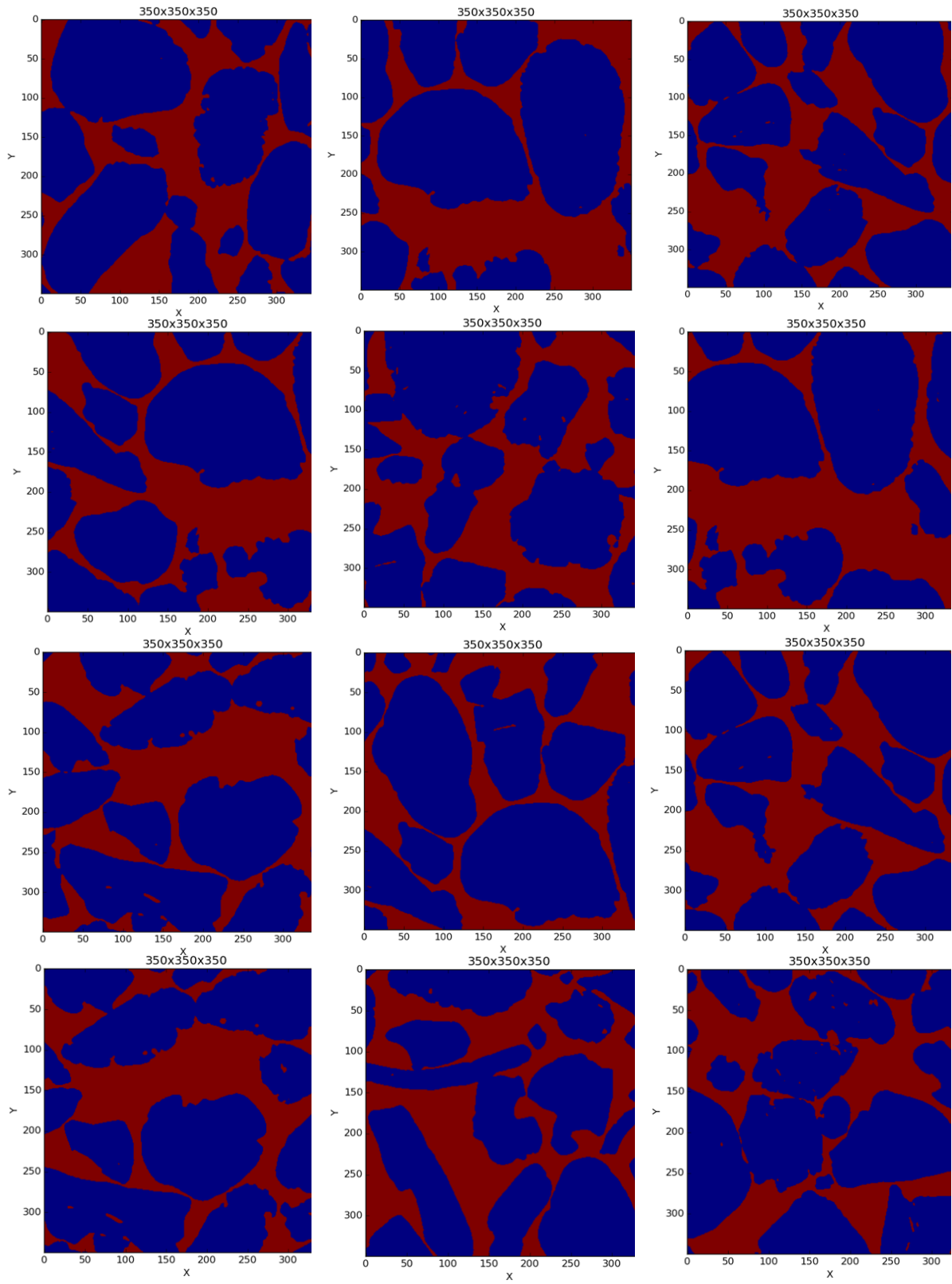


Figure A 2.5: Binary image of $(500)^3$ cubes f or Cottesloe clean sand sample.



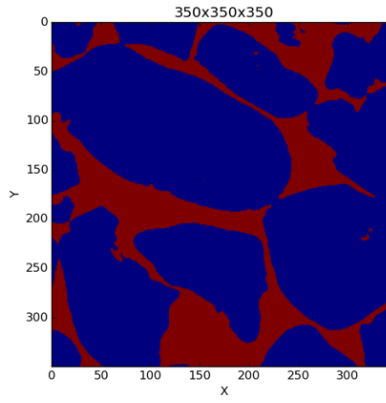
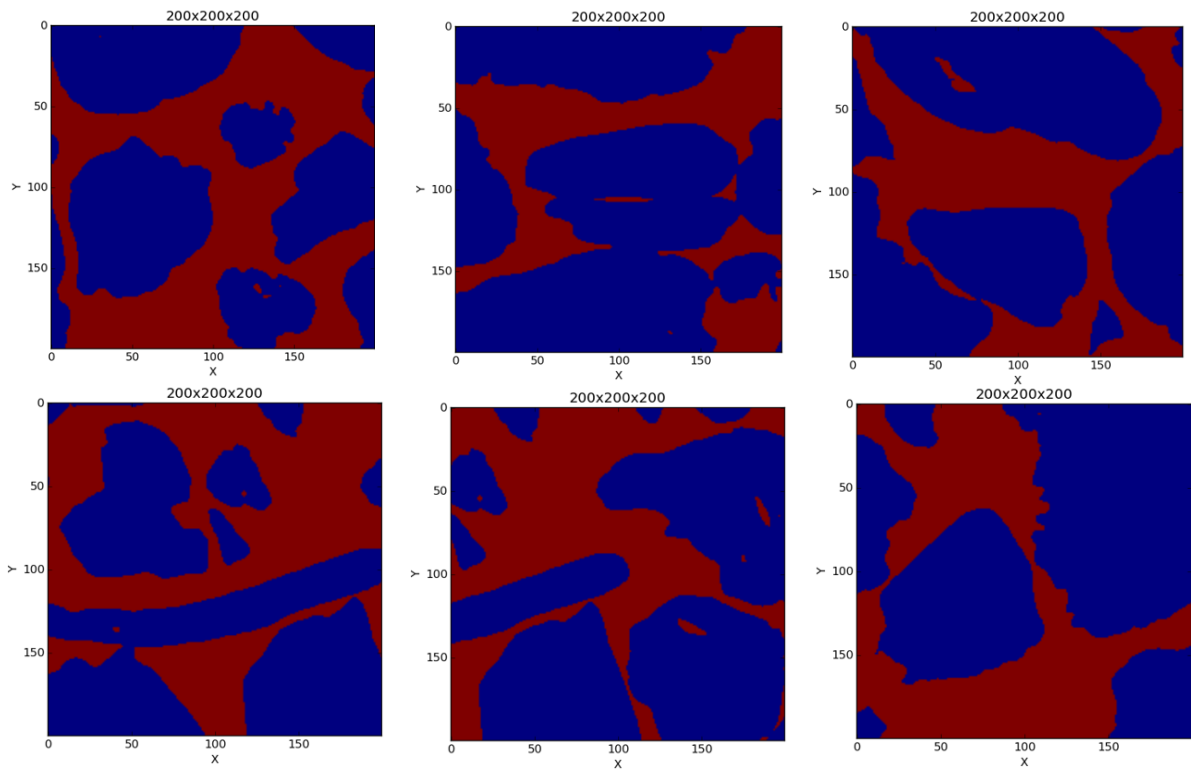
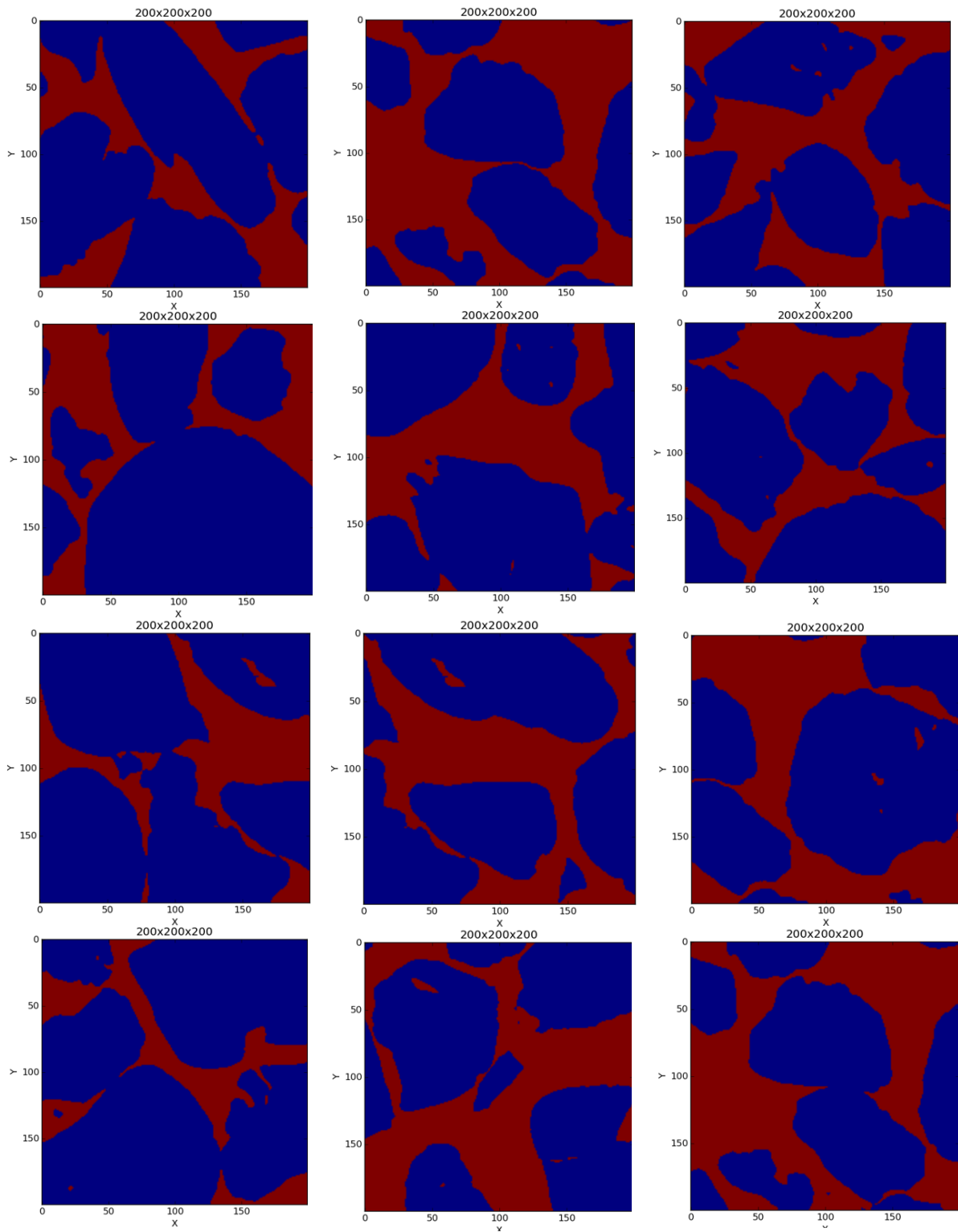


Figure A 2.6: Binary image of $(350)^3$ cubes for Cottesloe clean sand sample.





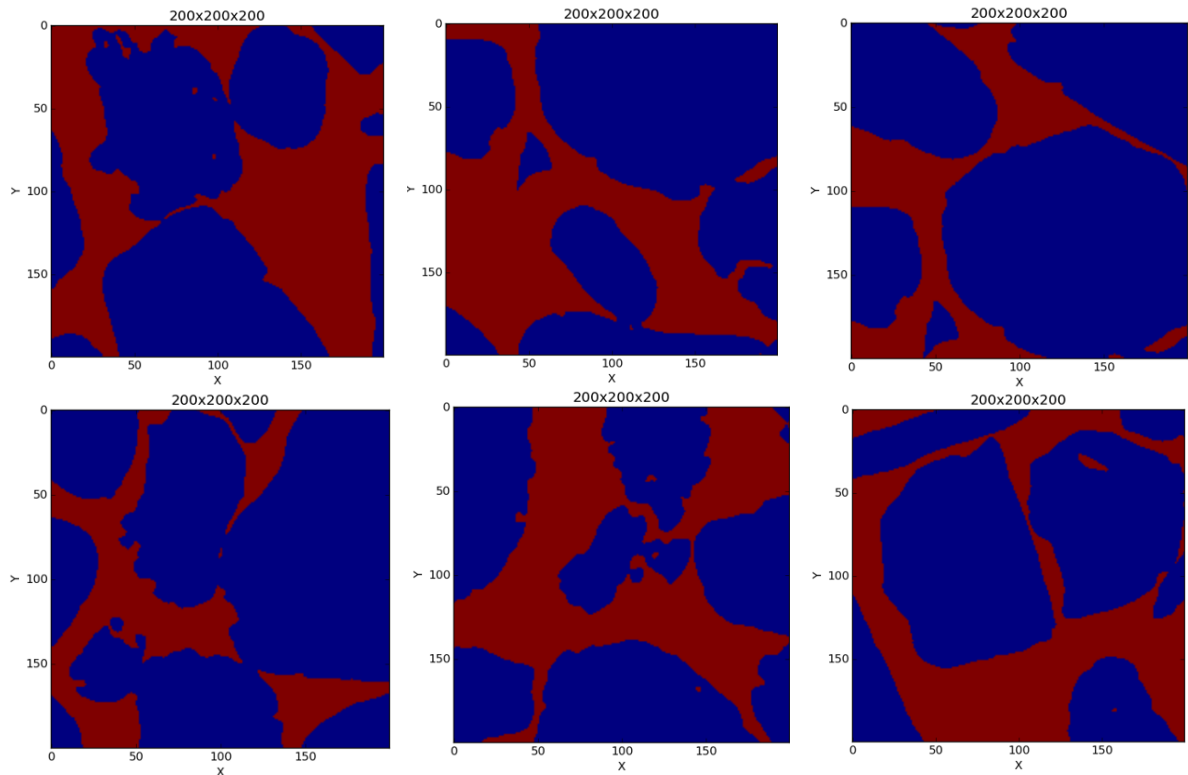


Figure A 2.7: Binary image of $(200)^3$ cubes for Cottesloe clean sand sample.

Appendix 3: Potential field variations of Scarborough and Cottesloe clean sand samples.

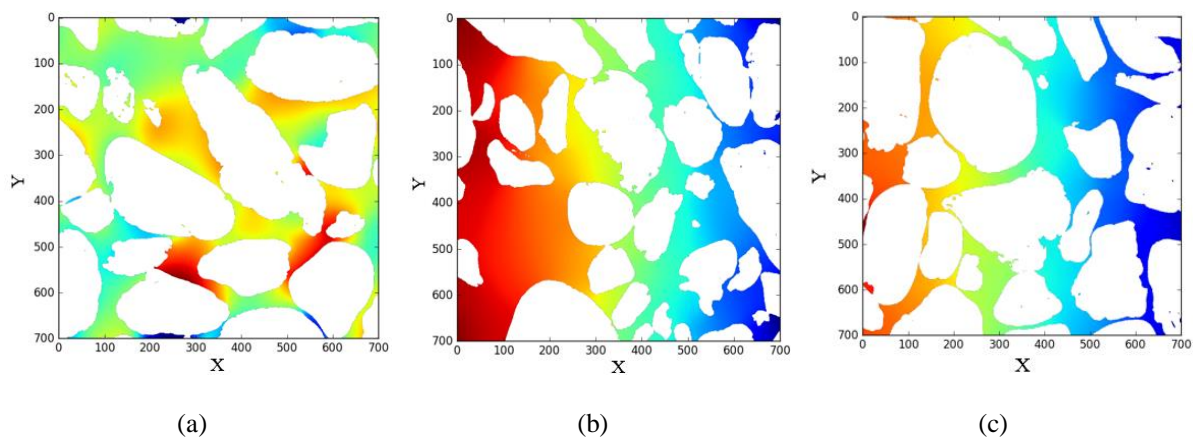


Figure A 3.1: Potential field variation of clean sand of Scarborough sand sample (a) x (b) y and (c) z directions.

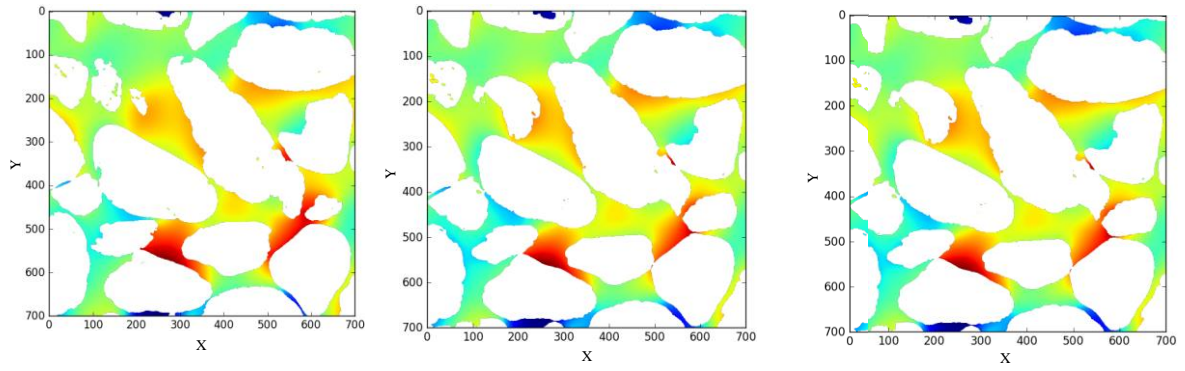


Figure A 3.2: Potential field variation of $(700)^3$ from Scarborough clean sand sample.

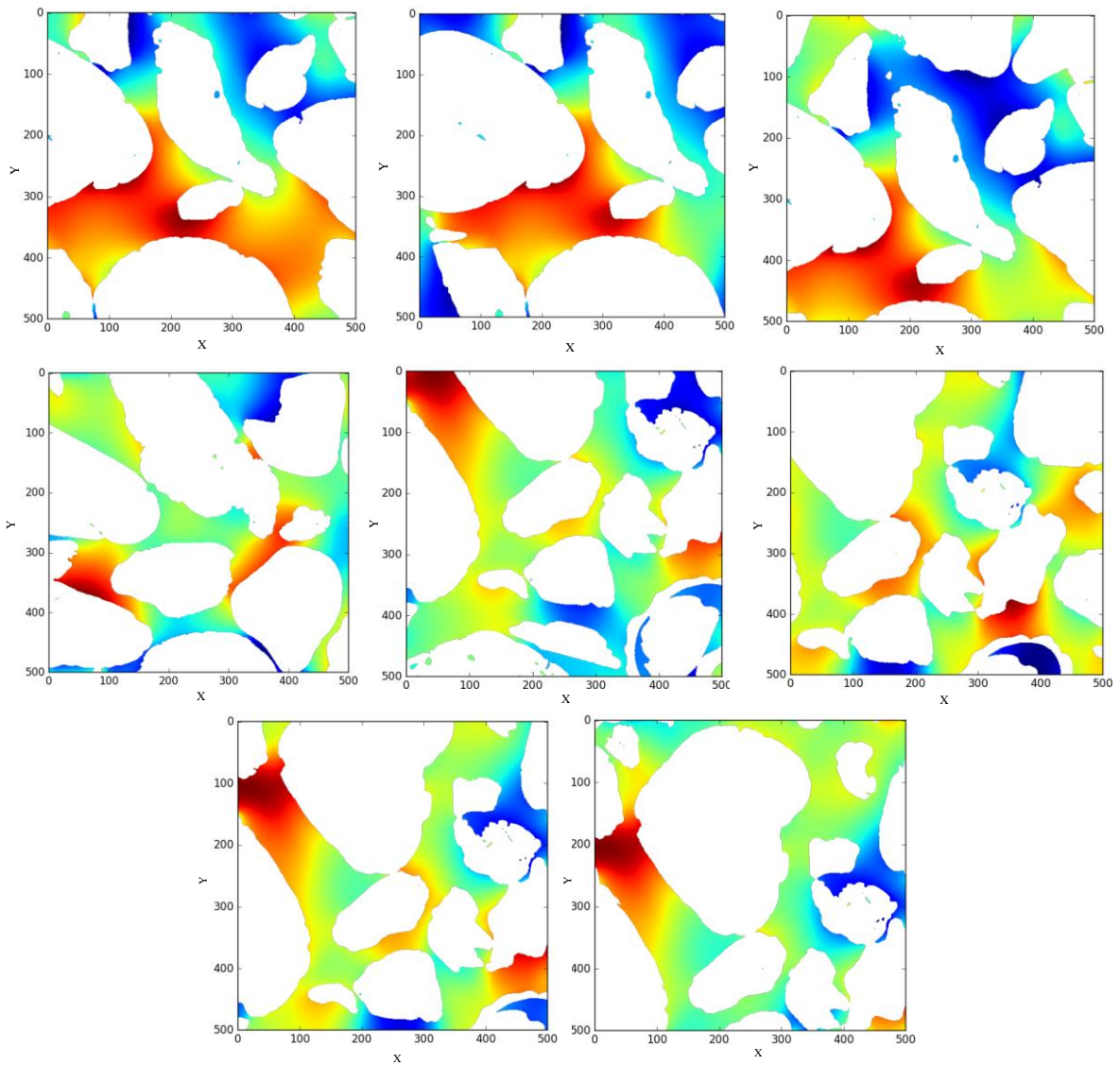


Figure A 3.3: Potential field variation of $(500)^3$ from Scarborough clean sand sample.

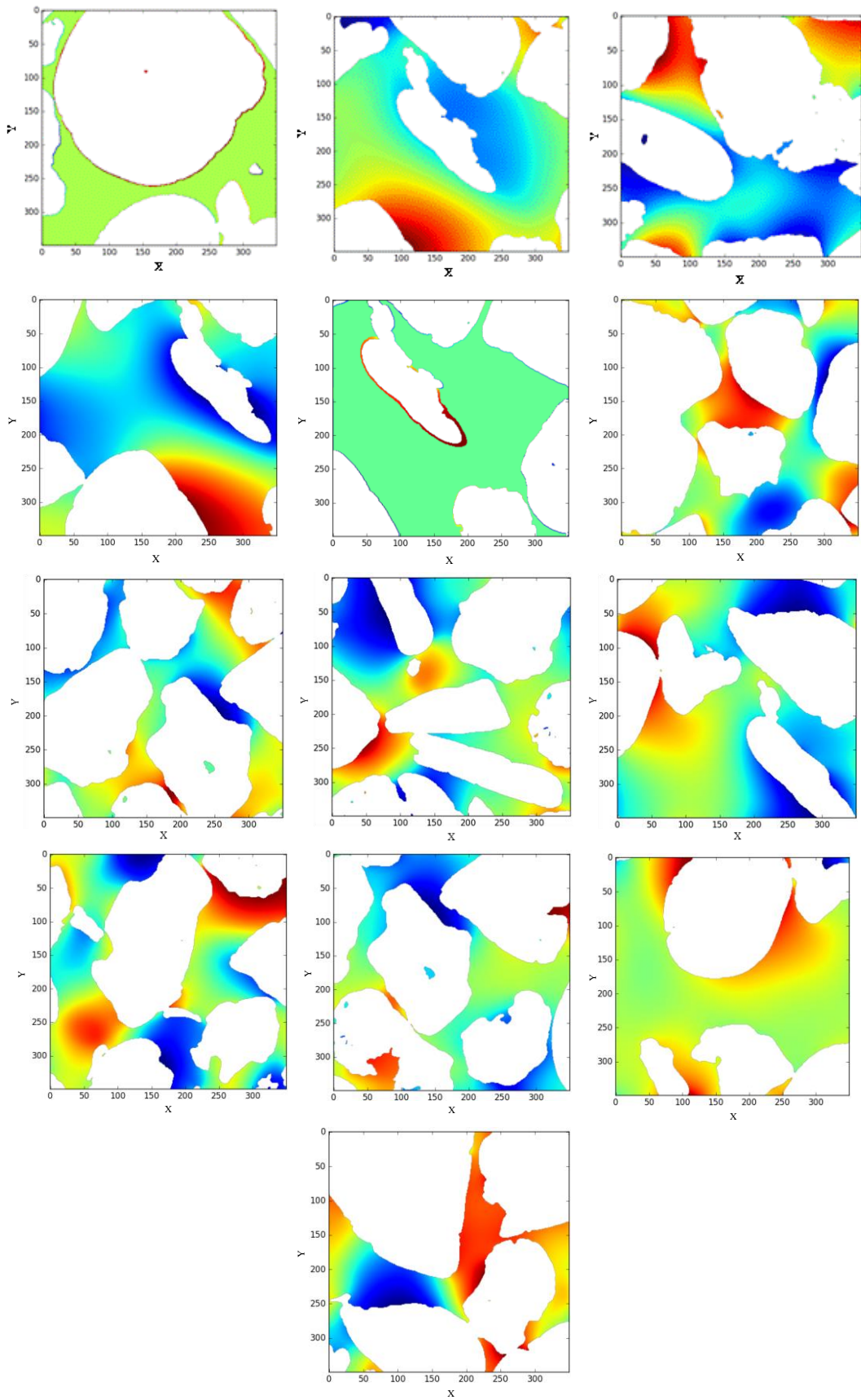
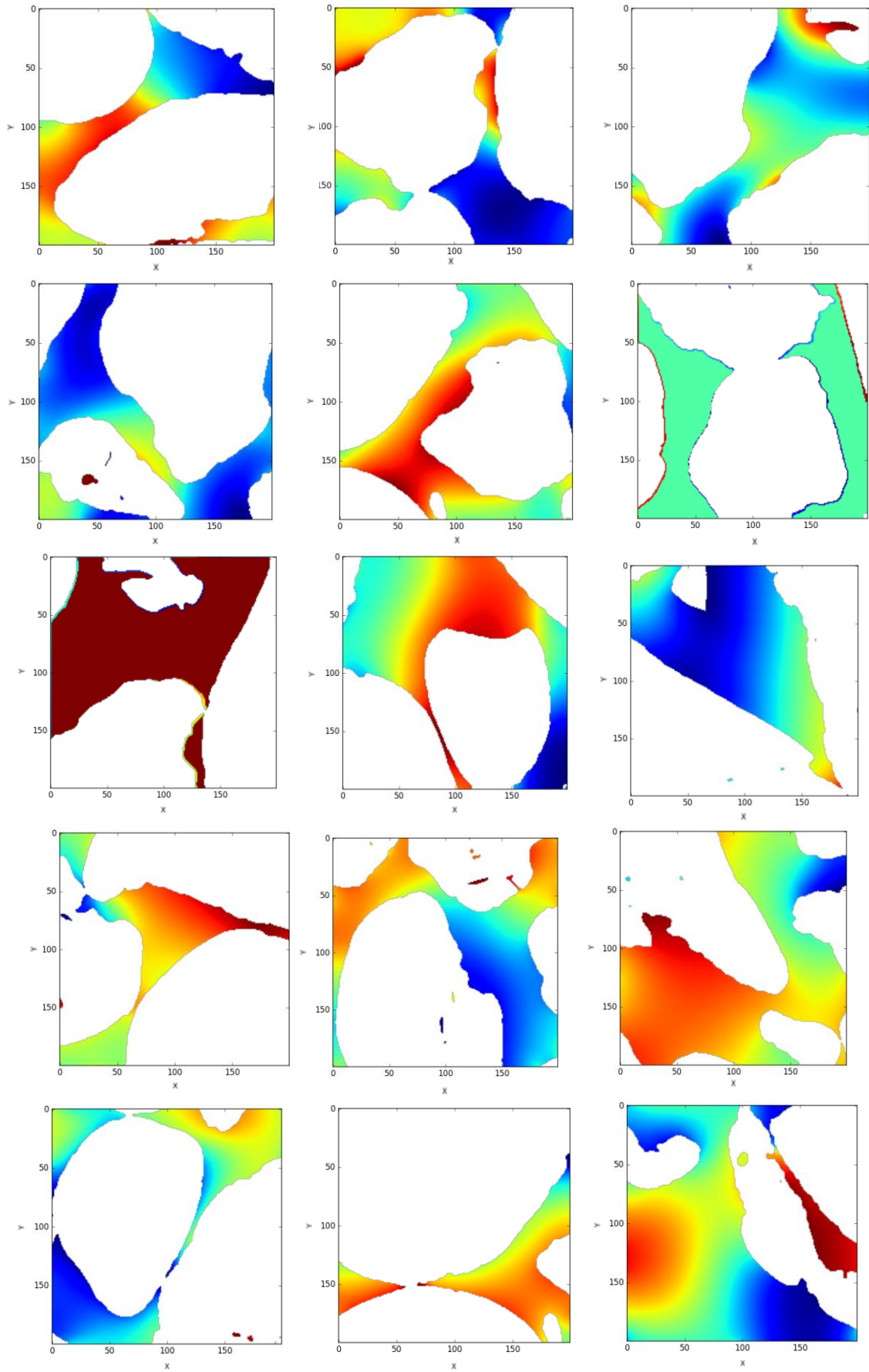


Figure A 3.4: Potential field variation of $(350)^3$ from Scarborough clean sand sample.



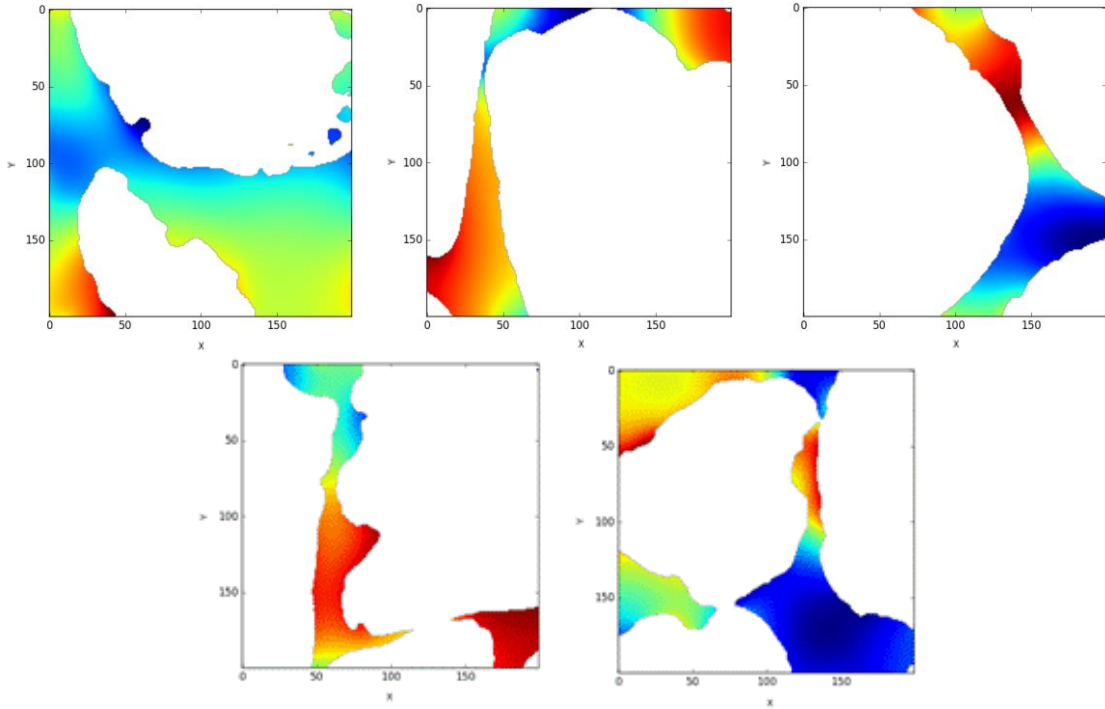


Figure A 3.5: Potential field variation of $(200)^3$ from Scarborough clean sand sample.

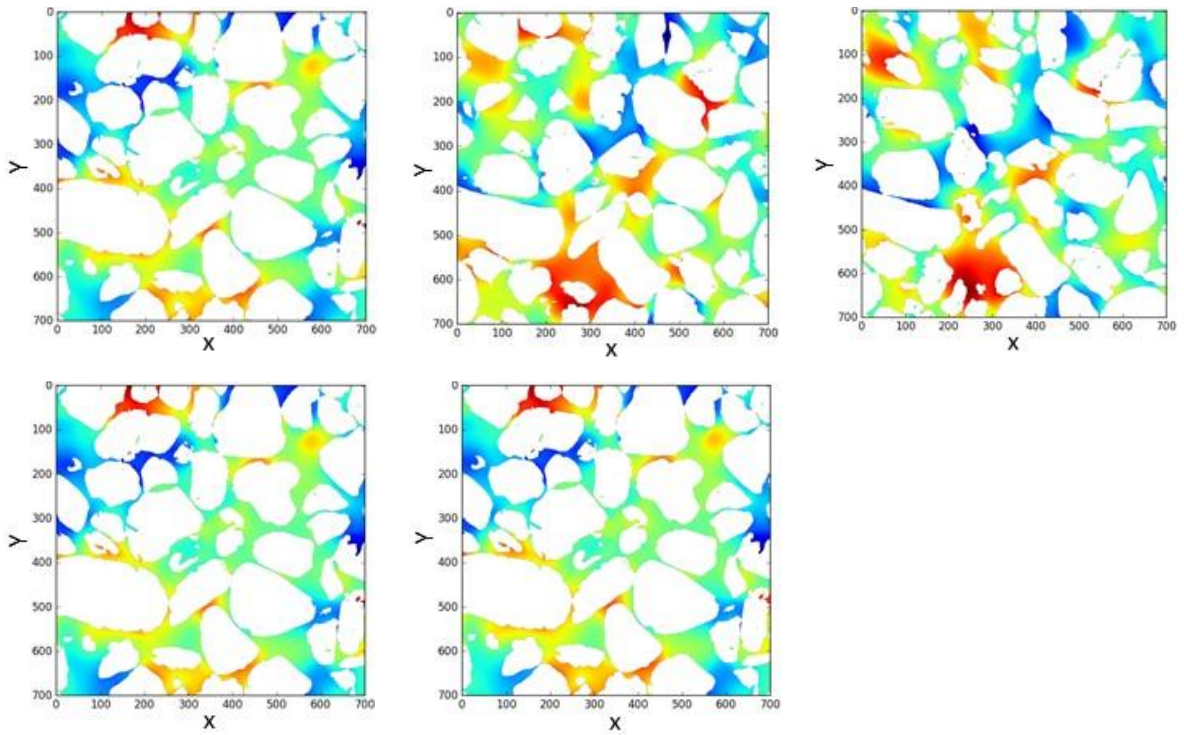


Figure A 3.6: Potential field variation of $(700)^3$ from Cottesloe clean sand sample.

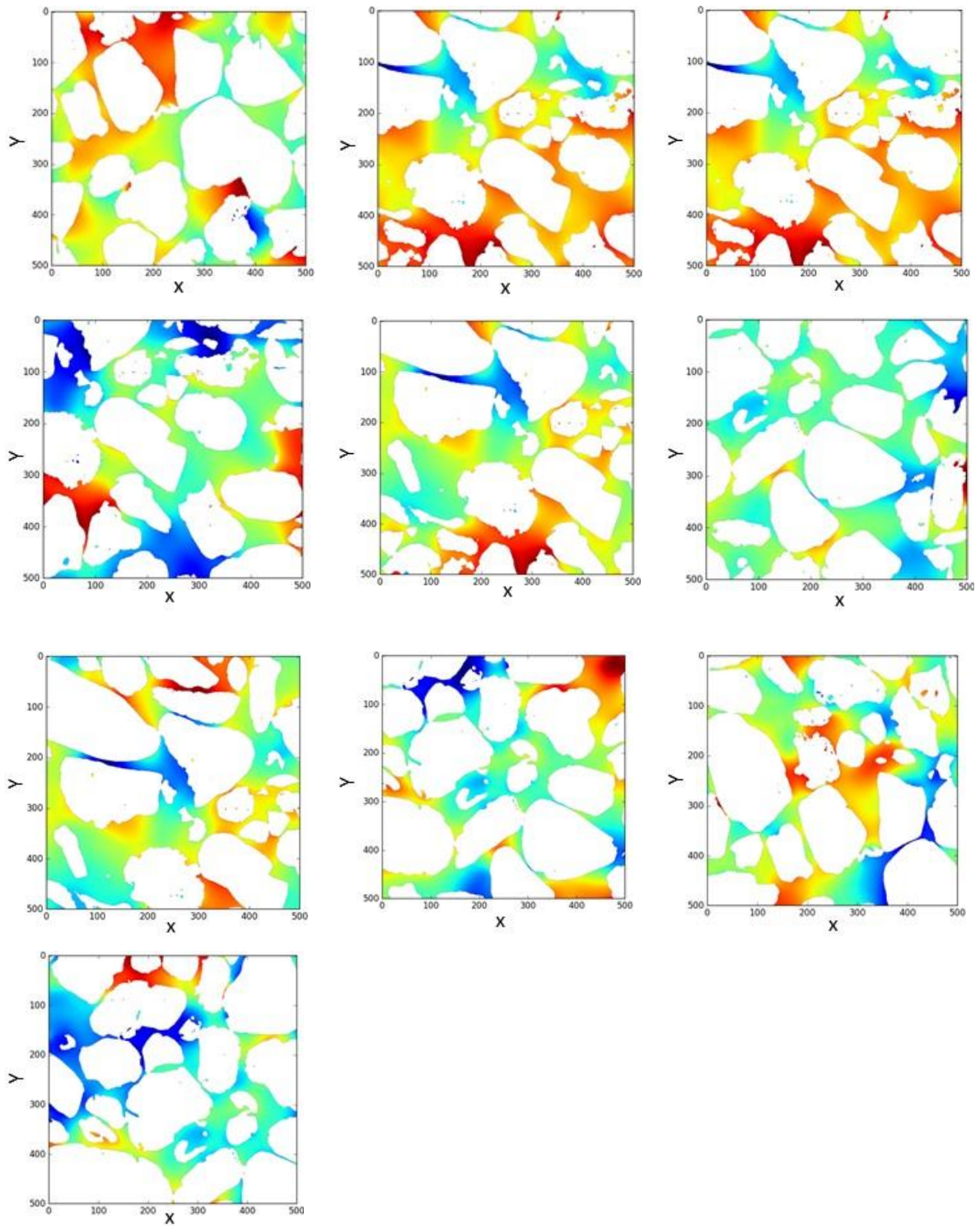
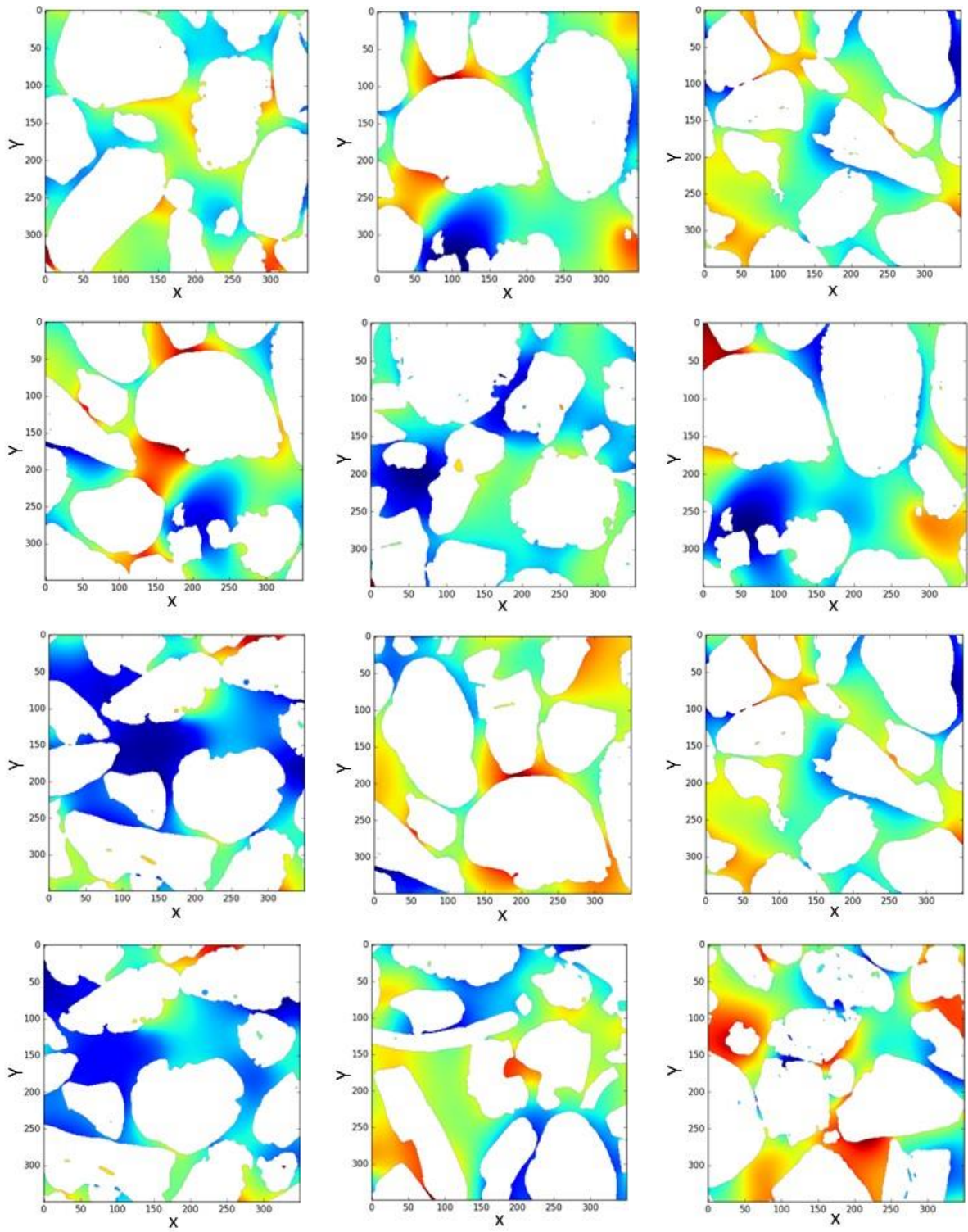


Figure A 3.7: Potential field variation of $(200)^3$ from Cottesloe clean sand sample.



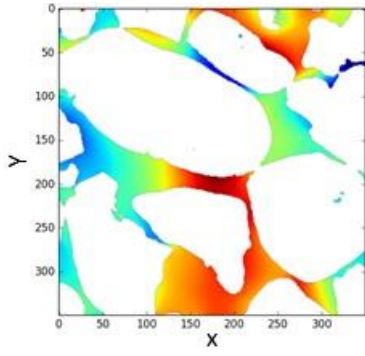
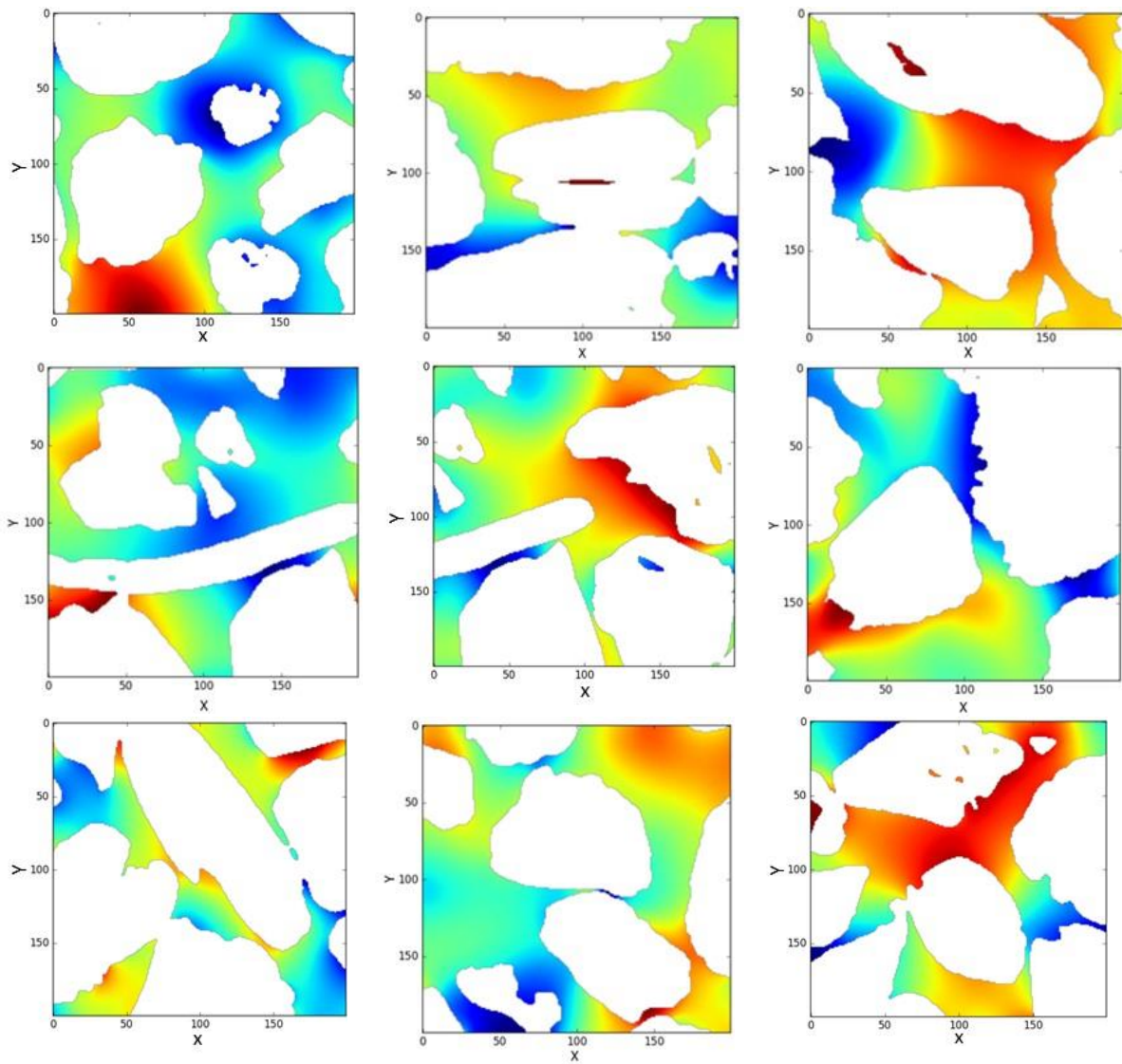
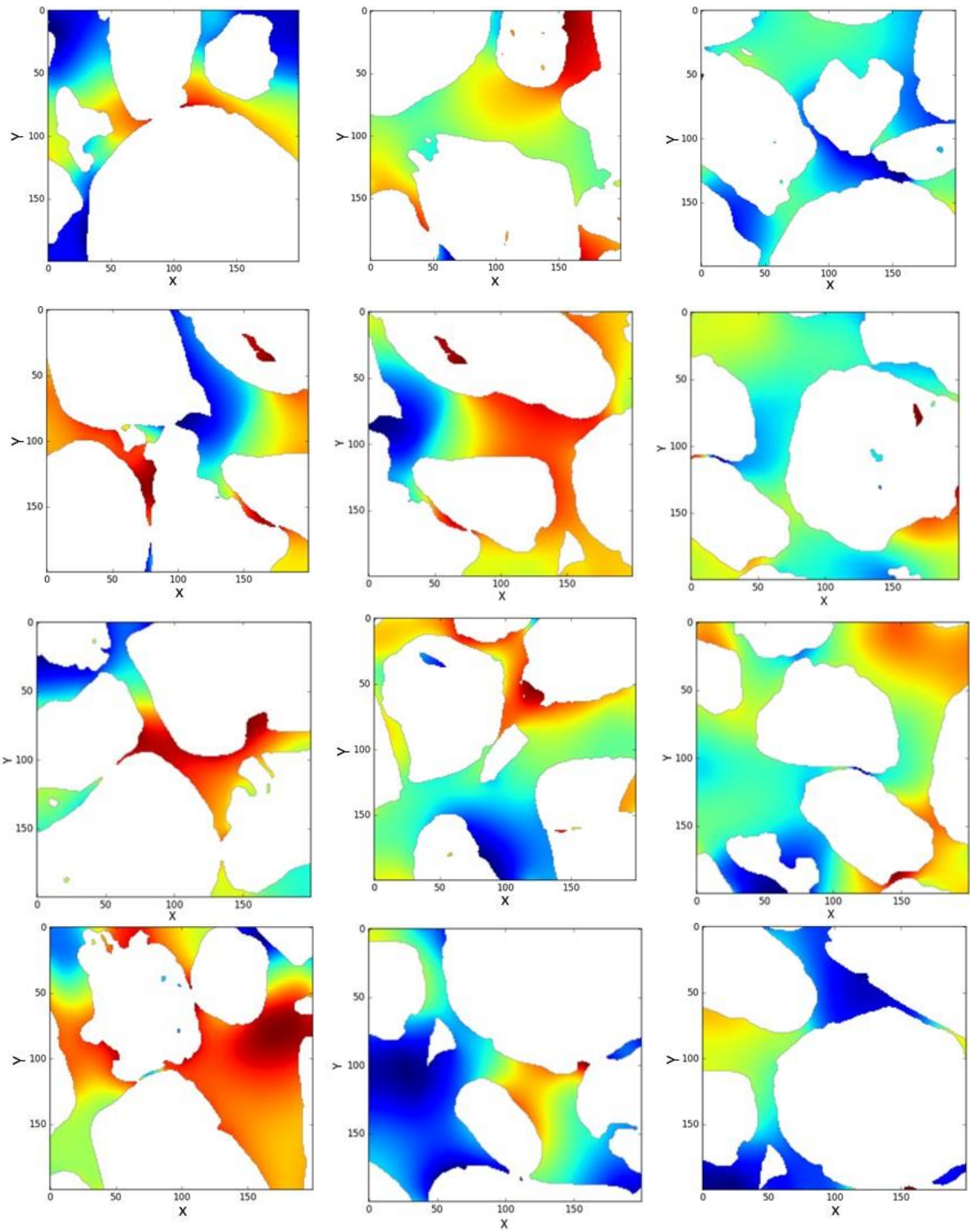


Figure A 3.8: Potential field variation of $(350)^3$ from Cottesloe clean sand sample





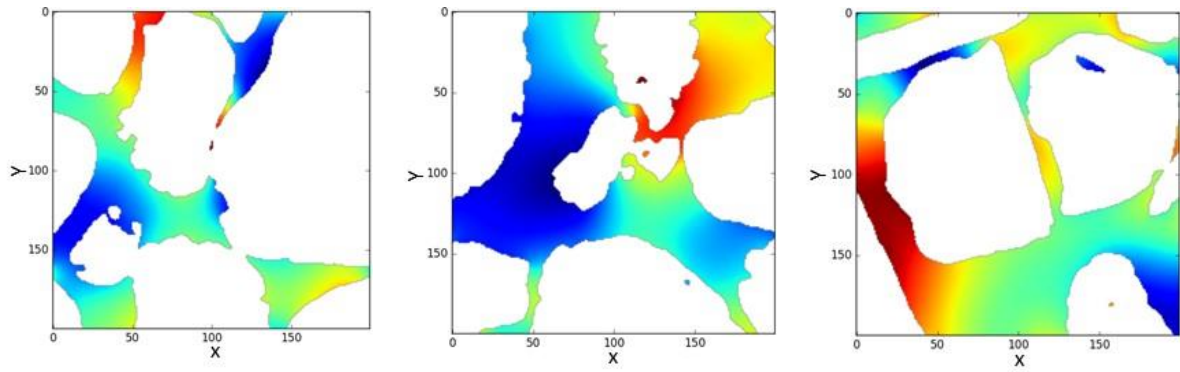


Figure A 3.9: Potential field variation of $(200)^3$ from Cottesloe clean sand sample

Appendix 4: Grain size analysis and image processing

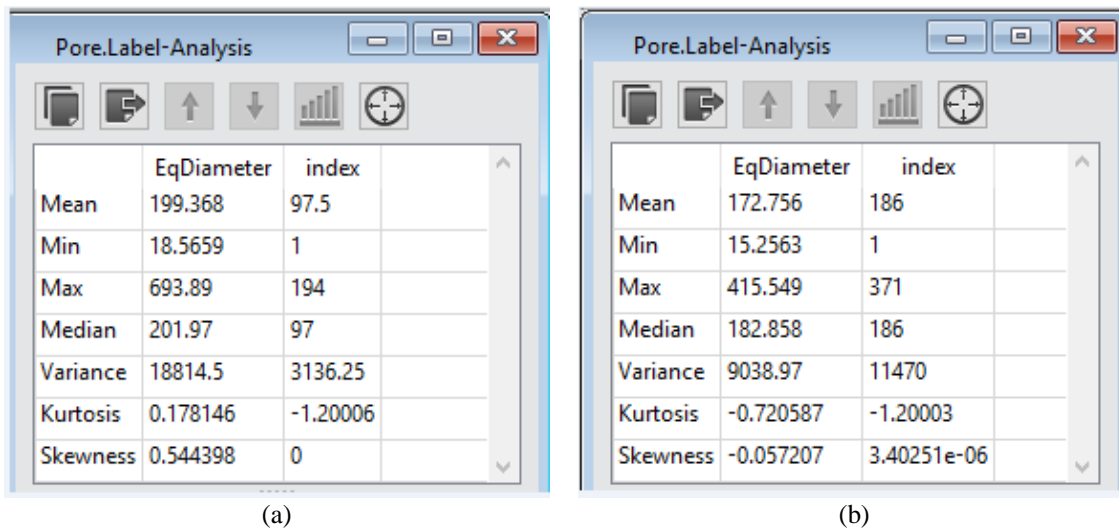


Figure A 4.1: Pore label analysis of (a) Scarborough and (b) Cottesloe beach sample

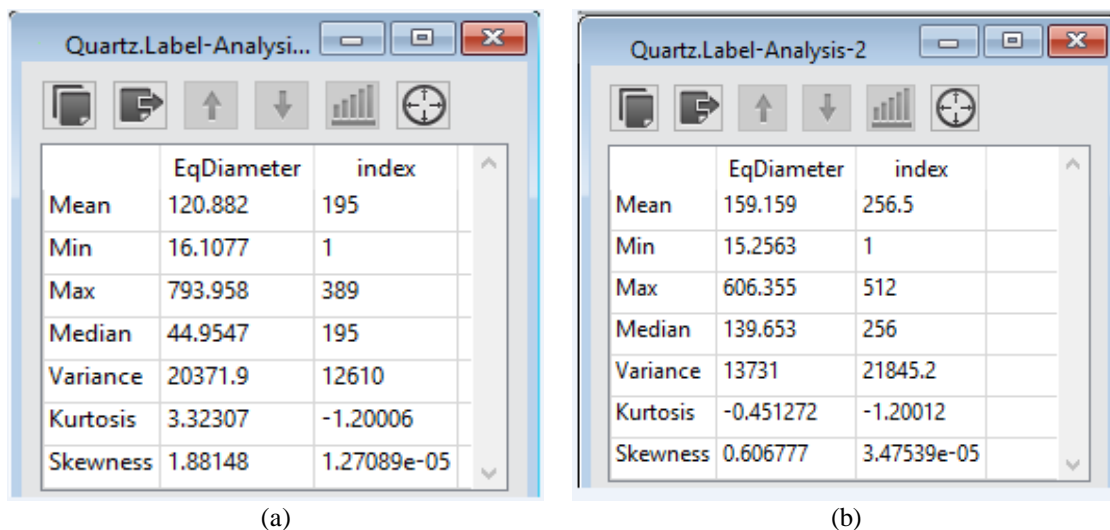


Figure A 4.2: Quartz label analysis of (a) Scarborough and (b) Cottesloe beach sample

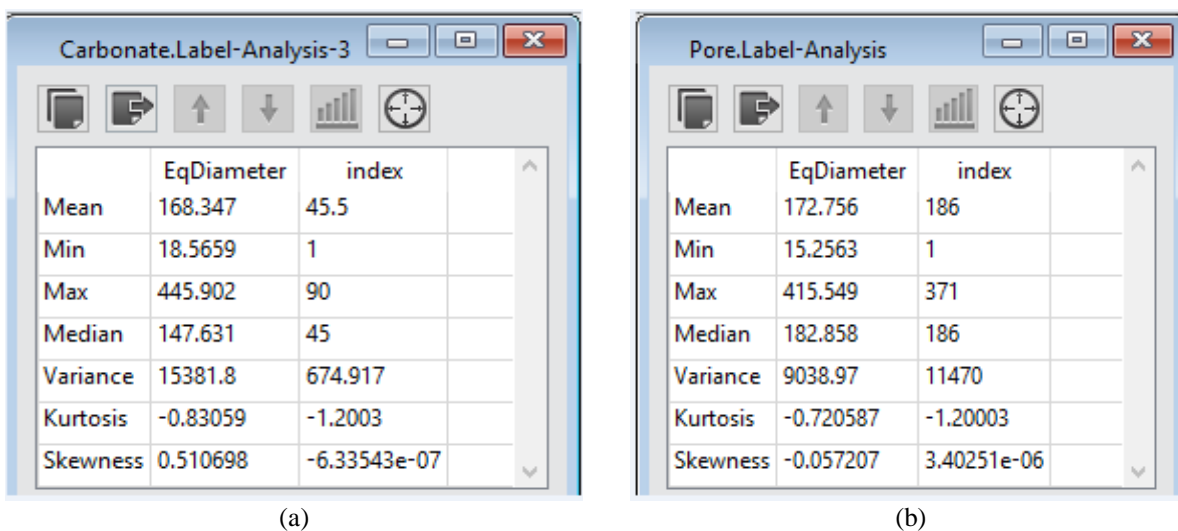


Figure A 4.3: Carbonate label analysis of (a) Scarborough and (b) Cottesloe beach sample

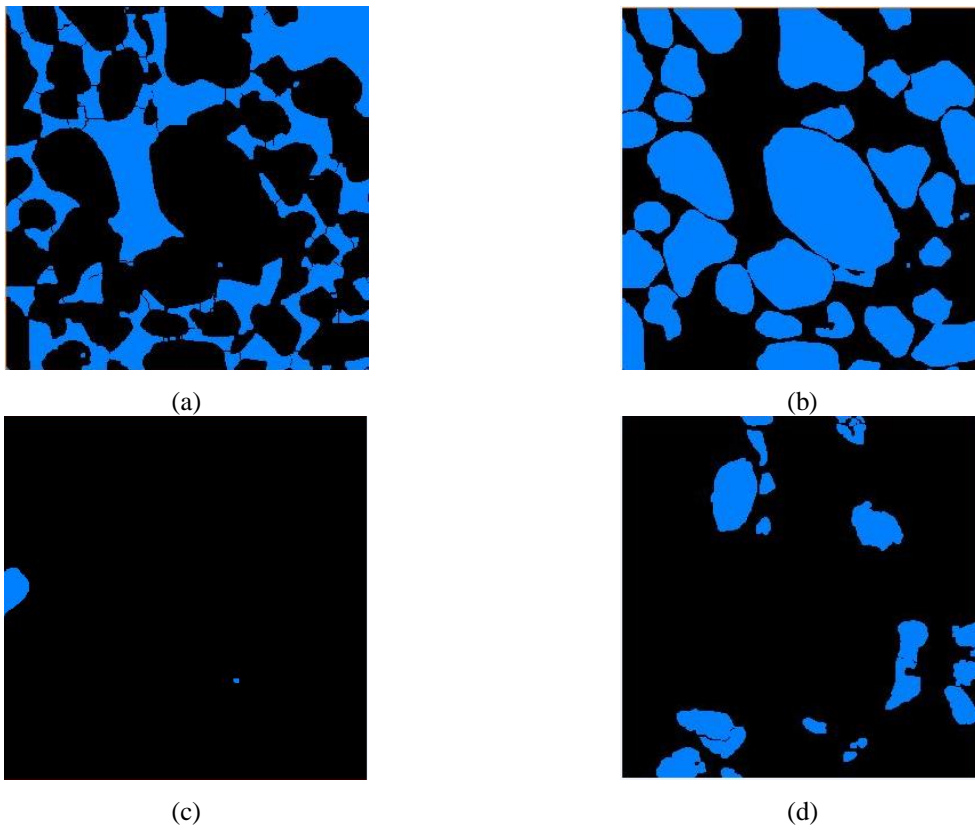


Figure A 4.4: Separate of $(700)^3$ cube of Cottesloe clay sand sample (a) pore (b) quartz (c) clay and (d) carbonate.

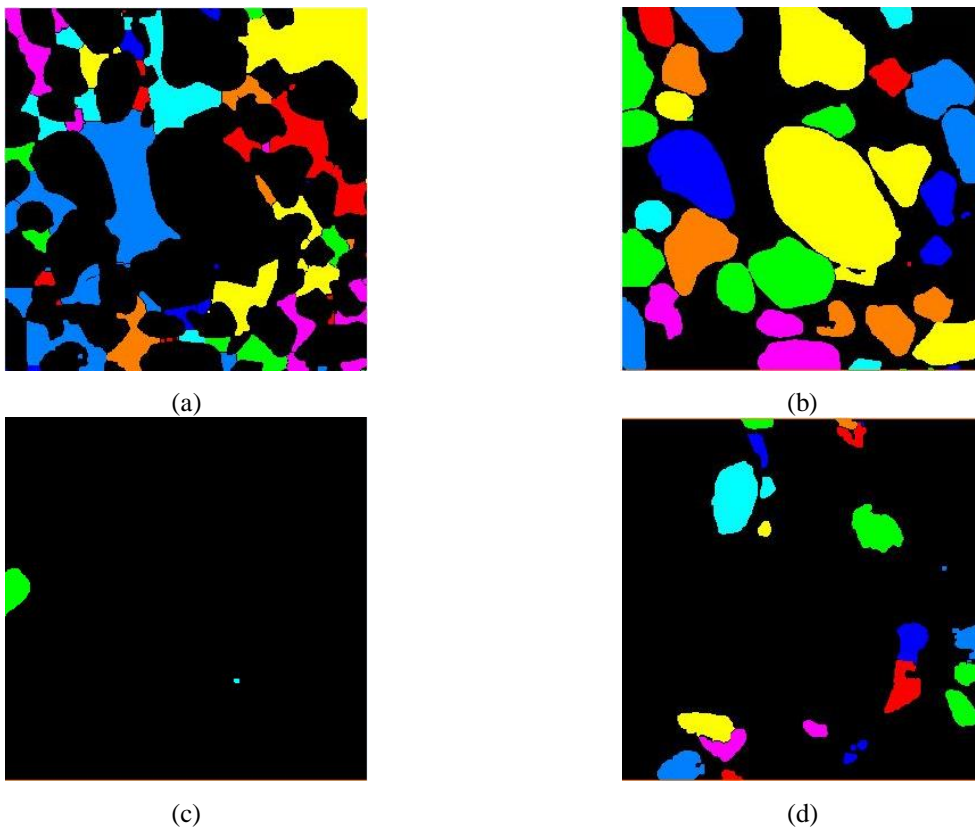


Figure A 4.5: 2-D label field of $(700)^3$ cube of Cottesloe clay-sand sample (a) pore (b) quartz (c) clay and (d) carbonate.

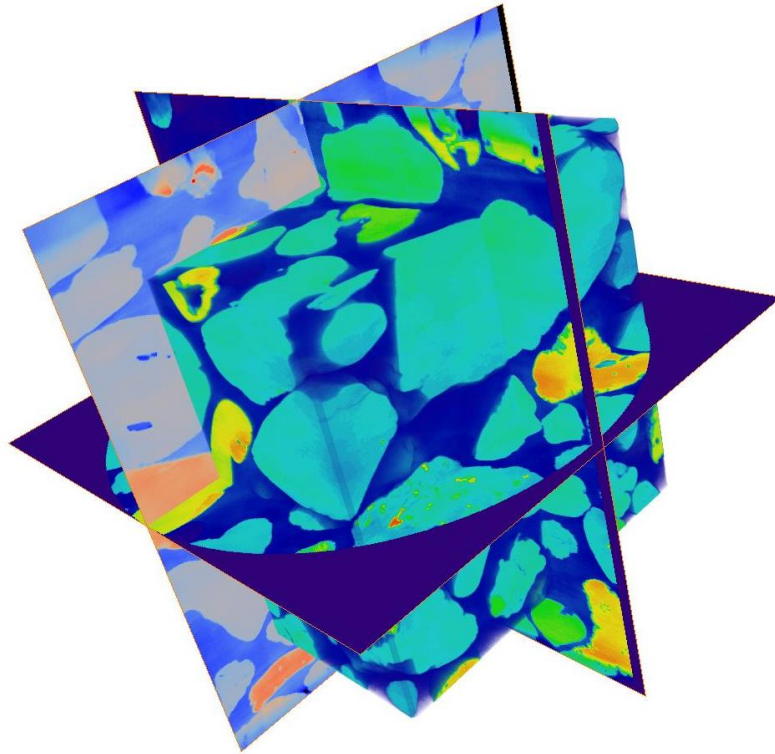


Figure A. 4.6: Scarborough clean sand sample showing the x, y and z planes of the $(700)^3$ cube inside 500 cube.

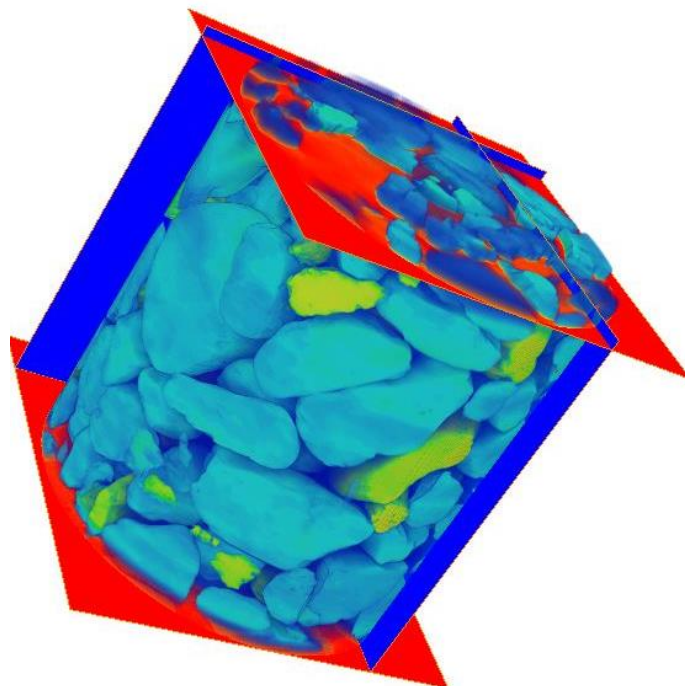


Figure A 4.7: The whole image of clean sand sample of Scarborough showing the x, y, and z planes.